

Experimental Study of Water Jet Impingement Cooling of Hot Steel Plates

Experimentelle Untersuchung der Prallkühlung von heißen Stahlplatten mittels Wasserstrahlen
Zur Erlangung des akademischen Grades Doktor-Ingenieur (Dr.-Ing.)
genehmigte Dissertation von M.Tech. Nitin Karwa aus Churu (Indien)
July 2012 — Darmstadt — D 17



TECHNISCHE
UNIVERSITÄT
DARMSTADT

FACHBEREICH
MASCHINENBAU



Technische Thermodynamik

Experimental Study of Water Jet Impingement Cooling of Hot Steel Plates

Experimentelle Untersuchung der Prallkühlung von heißen Stahlplatten mittels Wasserstrahlen

Vom Fachbereich Maschinenbau an der Technischen Universität Darmstadt
zur Erlangung des akademischen Grades eines Doktor-Ingenieurs (Dr.-Ing.)
genehmigte Dissertation von M.Tech. Nitin Karwa aus Churu (Indien)

1. Gutachten: Prof. Dr.-Ing. Peter Stephan
2. Gutachten: Prof. Dr.-Ing. Cameron Tropea
3. Gutachten: Prof. Dr.-Ing. Karl-Hermann Tacke

Tag der Einreichung: 07. März 2012

Tag der Prüfung: 30. Mai 2012

Darmstadt — D 17

This thesis is online available at:

Universitäts- und Landesbibliothek Darmstadt
tuprints (<http://tuprints.ulb.tu-darmstadt.de>)

*Dedicated to
Bapu's message of "universal brotherhood and peaceful coexistence"*

Ehrenwörtliche Erklärung zur Dissertation

Ich erkläre hiermit ehrenwörtlich, dass ich die vorliegende Arbeit selbstständig angefertigt habe. Sämtliche aus fremden Quellen direkt oder indirekt übernommenen Gedanken sind als solche kenntlich gemacht. Die Arbeit wurde bisher keiner anderen Prüfungsbehörde vorgelegt und noch nicht veröffentlicht.

Darmstadt, den 07. März 2012

Nitin Karwa

Acknowledgments

The ability of humans to leverage the forces of the nature for its benefit has been the most important reason for the prosperity of mankind. Up till the late 17th century, naturally occurring event were theologically described as divine interventions and miracles. Then came the age of enlightenment, when using scientific philosophy, intellectuals started to understand and appreciate the beautiful order in nature and the underlying physiochemical forces that drive it. Solutions to complex problems evolved with this scientific approach. I am glad to have got an opportunity to walk on this path of scientific enlightenment and make my tiny contribution to the scientific knowledge. In all honestly, I must acknowledge that this effort has been an intense learning phase, at the end of which I only managed to raise more questions than I have provided answers to.

In October 2007, when I was offered this opportunity at TU Darmstadt, I accepted it with great pleasure. In retrospect, coming to Darmstadt was one of the best decisions that I ever made. In the years that I worked at TU Darmstadt, I have been indebted to many individuals who have contributed to the completion of this thesis. This voyage has been a success mostly because of the guidance of one person, Prof. Peter Stephan. His constant encouragement and support, to add to his scientific guidance, are the major reasons for the achievements of this work. His mentoring has helped reinvent the scientist in me and gave me the confidence to reflect upon my work with positivity. No words can describe my indebtedness towards him, though my actions in the years to come would reflect the inspiration that I drew from him.

I thank Prof. Cameron Tropea, firstly, for recommending my candidature for the project position and, secondly, for accepting to be the thesis examiner. A special indebtedness is extended to Dillinger Hütte GTS (Dillingen, Germany) for funding this research program. I acknowledge the technical inputs and the critical examination of Prof. Dr. Karl-Hermann Tacke, which has greatly helped in shaping this thesis. In fact, this thesis provided me the rare opportunity to closely interact with both the examiners since the very beginning of this project work. The discussions with the technical team at Dillinger Hütte (Dr. Roland Schorr, Mr. Hans-Jürgen Kirsch and Mr. Klaus Eberwein) were always enriching and I am very thankful to them for their valuable inputs. I am indebted to Prof. Masanori Monde and Dr. Peter Woodfield for providing the inverse heat conduction analysis tool. I would also like to acknowledge the guidance and scientific knowledge that I received from the published works of other researchers.

I would like to thank Dr. Tatiana Gambaryan-Roisman, Prof. Suad Jakirlic and Dr. Ilia Roisman for their scientific inputs. I appreciate the cooperation of Roland Berntheisel and his team at the workshop for manufacturing precise parts for my test setup in quick time. Thanks are due to the Mr. Resourceful, Robert Schrod, for the laboratory organization and making sure that working in the laboratory was risk-free. In addition, I would like to thank Gaby Gunkel and Ingrid Benz for their help with the administrative work. Hearty thanks to all my past and present colleagues at the

institute for providing an enriching environment during my stay at the institute, and extending their help and support on various occasions. Especially, I would like to appreciate the fine company of my dearest colleagues and friends: Bo, Jagan, Khalid and Mete. I also thank my students, Lukas Schmidt and Ulrich Kruse, for demonstrating great patience and motivation in finishing their task.

The biggest motivating factor for me has been the love and support of my family. Prof. Rajendra Karwa, my father, who played the dual roles of a scientific guide and a philosopher. Mrs. Kusum Karwa, my mother, for imbibing in me the virtues of truthfulness and patience. Raina and Praveen for constantly reminding me of the pride they take in my success. My best teammate in this journey has been my wife, Minakshi. While I used to work for extended hours at the university, she patiently made sure that I forgot all my worries while at home. The best way for me to express my gratitude to my family will be by living up to their ideals in all walks of my life.

To sign off, I quote the final few lines from the famous poem "Stopping by woods on a snowy evening" by Robert Frost:

*"The woods are lovely, dark and deep,
But I have promises to keep,
And miles to go before I sleep,
And miles to go before I sleep."*

Darmstadt, den 07. März 2012

Nitin Karwa

Abstract

Liquid jet impingement cooling is critical in many industrial applications. Principle applications include extracting large heat flux from metal parts, such as hot fuel bundle post-loss-of-coolant-accident in nuclear reactors, heat treatment of steel plates post-hot-processing, etc. The ability of liquid jets to extract high heat flux at controlled rates from metal parts, with temperatures as high as 800-1000 °C, at moderate flow rates has made them indispensable in these applications. Due to the complexity of the process, the mechanism of flow boiling heat transfer during jet impingement cooling is not well understood. Resultantly, the presently used design approaches are based more on experience and rule of thumb than science. The principle challenge in the study of jet impingement cooling for these high temperature applications has been the lack of reliable instrumentation for measuring the cooling rates. To add to this, the conjugate nature of boiling heat transfer, especially on low conductivity metal like steel, makes this problem very complicated to understand. Thus, much of the state of art on this subject has been limited to experiments where either the conjugate problem has not been addressed or the tests have been performed at temperatures that are much lower than in the above mentioned applications.

The basic objective of the present work is to contribute to the understanding of the thermohydrodynamic phenomenon occurring during the cooling of a hot steel plate with an impinging water jet. This work also complements a parallel study being conducted at the Institute of Fluid Mechanics and Aerodynamics (Technische Universität Darmstadt), in which the complex transport processes are being treated theoretically and validated against the experimental results of this work.

To achieve the objective, transient cooling experiments have been performed on an instrumented stainless steel AISI-type 314 cylinder. To measure the temperature variation within the stainless steel cylinder during the transient cooling, fast-response thermocouples have been embedded within holes that are precisely drilled through its bottom flat face. The cylinder is induction heated to a homogeneous initial temperature of 900 °C and is subsequently cooled by means of an axisymmetric subcooled free-surface water jet that impinges on its top flat face (impingement surface). During the cooling, each thermocouple output has been recorded at the rate of 100 samples per second. A two-dimensional axisymmetric inverse heat conduction analysis using these measured temperature data has been performed to estimate the temporospatial variation of temperature and heat flux on the impingement face. Both low and high speed images have been recorded to visualize the two-phase flow. These images and the estimated heat transfer distribution are used to understand the boiling mechanism. The effect of jet parameters, namely subcooling and impingement velocity, on the heat transfer process has been studied. Additionally, the effect of spent liquid accumulation over the impingement surface has been studied in few exploratory plunging jet experiments.

This study presents a systematic methodology for the measurement and estimation of the temporospatial variation of heat transfer on the impingement surface of a hot steel plate. Three distinct

regions, with difference in the extent of liquid-wall contact, have been identified on the impingement surface from the recorded images.

- i) A wetted region surrounds the jet stagnation region. Nucleate boiling is the principle heat transfer mode in this region. The outer periphery of this region is called the wetting front. No boiling activity has been observed in the high speed images, most likely because the bubbles were small and were unable to reach the liquid free-surface. The maximum heat flux position is determined to be within this region. As the wetted region grows in size with time, the maximum heat flux position also moves radially outwards. The wetting front and maximum heat flux position velocity reduce with increasing radial distance from the impingement point because the liquid velocity and subcooling reduce at the wetting front. Likewise, the wetting front velocity increases with jet velocity and subcooling.
- ii) The liquid gets deflected at the wetting front due to the efflux of large vapor bubbles beyond the maximum heat flux position. A term “wetting front region” has been coined in this thesis to describe this region. The width of this region could not be determined from the high speed images. Transition boiling within a thin superheated liquid film that is continuously replenished by the bulk flow is proposed to be the probable reason for the high heat flux in this region. Further, the radial heat conduction to the wetted region is also significant here.
- iii) The impingement surface outside the wetting front region is dry. The dry surface slowly cools down due to film boiling and radial heat conduction to the wetting front region. The film boiling rate is very low in the impingement region. After deflecting away from the impingement surface in the wetting front region, the liquid film breaks into droplets over this region. Looking from the side, droplet deflection angle is observed to be small; still these droplets do not come into direct contact with the impingement surface, as has been confirmed by looking down from the top.

The velocity of the splashed droplets has been determined by analyzing the high speed images. It has been found that the drop velocity is much lower than the liquid film velocity calculated at the wetting front position using single-phase flow relations suggested by Watson. It has been hypothesized that the liquid film in the wetted region is decelerated by the bubbles growing on the impingement surface. Further, measurements reveal that the drop velocity increases with decreasing subcooling, which means that the film and the droplet are accelerated in the radial outward direction by the vapor released in the wetting front region.

It has been shown that the rewetting temperature (analogous to the Leidenfrost temperature for a sessile droplet), which refers here to the temperature below which the direct liquid-wall contact is re-established and the heat flux increases, in both the impingement and radial flow regions is significantly higher than that reported in the literature for pool boiling. Removal of bubbles by the flowing liquid in the early stages of their growth and then their rapid condensation within the subcooled liquid avoids the buildup of vapor near the hot wall, which is the likely reason for the enhancement of the rewetting temperature. This observation confirms that high heat fluxes can be removed at large wall superheats by impinging liquid jets, as practiced in the industry.

The boiling curve shifts to higher heat flux and superheat with the increase in the jet velocity and subcooling. The maximum heat flux and surface temperature at maximum heat flux increase with both the jet velocity and subcooling. Area-weighted average boiling curves have been determined, which clearly show the enhancement in the heat transfer with jet velocity over the average surface

superheat of 100 to 800 K. The enhancement in jet subcooling is, however, noticeable only in the wall superheat range of 300 to 700 K. The maximum heat flux and surface temperature at maximum heat flux decrease with radial distance from the stagnation point before reaching a constant value. The radial distribution of maximum heat flux condition has been classified into three regions based on the relative size of the hydrodynamic/thermal boundary layer and the liquid film.

In the plunging jet impingement studies, it has been found that the wetting front growth slightly slows down due to accumulation of the spent liquid over the impingement surface. Area-weighted average boiling curves show that the heat transfer reduces due to accumulation.

Keywords

Free-surface jet impingement

Plunging jet impingement

Quenching

Inverse heat conduction solution

Boiling

Maximum heat flux condition

Rewetting temperature

Zusammenfassung

In vielen industriellen Anwendungen hat die Kühlung mit Hilfe von Flüssigkeitsstrahlen eine große Bedeutung. Diese Kühltechnik wird hauptsächlich dann verwendet, wenn hohe Wärmestromdichten abgeführt werden müssen wie z.B. zur Notkühlung von Brennstabbündeln bei Kühlmittelverluststörfällen in Kernreaktoren oder Abschreckung bzw. Wärmebehandlung von Metallbauteilen. Die Flüssigkeitsstrahlkühlung ist unerlässlich, da mit moderaten Volumenströmen hohe Wärmestromdichten von heißen Metallbauteilen, welche Temperaturen weit über 800 bis 1000 °C haben, abgeführt werden können. Aufgrund der hohen Komplexität der Wärmeübertragung in einem solchen Kühlprozess, sind die physikalischen Mechanismen nicht vollständig verstanden. Die gegenwärtigen Auslegungen solcher Kühlsysteme basieren daher mehr auf Erfahrungen und Faustformeln als auf Wissenschaft. Die grundsätzliche Herausforderung im Bezug auf die Untersuchung der Wärmeübertragung beim Aufprall von Flüssigkeitsstrahlen in Hochtemperaturanwendungen, ist der Mangel an betriebssicheren und zuverlässigen Messgeräten zur Bestimmung der Abkühlraten. Darüber hinaus wird dieses Problem durch den Charakter der gekoppelten Wärmeübertragung während des Siedevorgangs auf schwach wärmeleitenden Metallen wie Stahl sehr kompliziert. Daher ist die Forschung auf diesem Gebiet zum großen Teil auf Experimente begrenzt, in denen das gekoppelte Wärmeübertragungsproblem nicht adressiert wird oder die Versuche bei geringeren Temperaturen durchgeführt werden als die, die in den oben genannten Anwendungen vorliegen.

Das grundlegende Ziel dieser wissenschaftlichen Arbeit ist es, einen Beitrag zum besseren Verständnis über das thermo-hydrodynamische Phänomen, welches während des Abschreckens einer heißen Edelstahlplatte mit einem Wasserstrahl eintritt, zu leisten. Um dieses Ziel zu verwirklichen, sind transiente Abschreckexperimente an einem auf die Anfangstemperatur von 900 °C homogen aufgeheizten, instrumentierten Edelstahlzylinders (AISI 314) durchgeführt worden, auf dessen Oberfläche ein unterkühlter, zylindrischer Wasserstrahl achsensymmetrisch aufprallt. Die Abkühlraten wurden während der Abschreckvorgänge von Thermoelementen erfasst. An Hand der gemessenen Temperaturdaten wurde eine zwei-dimensionale, achsensymmetrische, inverse Analyse der Wärmeleitung vorgenommen, um die zeitliche und örtliche Änderung der Oberflächentemperatur und der Wärmestromdichte an der Aufprallfläche zu bestimmen. Um den Siedemechanismus zu verstehen, wurde zusätzlich die Zweiphasenströmung mit niedriger und hoher Kamergeschwindigkeit visualisiert und mit der Verteilung der Wärmeübertragung verglichen. Der Einfluss der Unterkühlung und der Aufprallgeschwindigkeit des Wasserstrahls auf den Wärmetransportprozess wurde untersucht.

Drei verschiedene Bereiche mit unterschiedlichen Ausmaßen des Flüssigkeit-Wand-Kontaktes wurden auf der Aufprallfläche identifiziert.

- i) Ein zentraler, benetzter Bereich, in dem einphasige Konvektion und Blasensieden die grundlegenden Wärmetransportmechanismen sind. In den Hochgeschwindigkeitsaufnahmen wurden

jedoch keine Siedeaktivitäten beobachtet, da die Bläschen sehr klein sind und die freie Oberfläche der Flüssigkeit nicht erreichen. Die Position der maximalen Wärmestromdichte befindet sich innerhalb dieses Bereiches. Wenn der benetzte Bereich mit der Zeit wächst, so wandert auch die Position der maximalen Wärmestromdichte radial nach außen. Die Wachstumsrate des benetzten Bereichs steigt mit zunehmender Geschwindigkeit des unterkühlten Wasserstrahls.

- ii) Die Flüssigkeit wird am äußeren Umfang des benetzten Bereichs aufgrund des Abflusses von verhältnismäßig großen Dampfbläschen nahe der Position der maximalen Wärmestromdichte verformt. Übergangssieden innerhalb eines dünnen Flüssigkeitsfilmes, der kontinuierlich mit Flüssigkeit nachgespeist wird, wird als der Wärmetransportmechanismus im benetzten Frontbereich angenommen.
- iii) Die Aufprallobерfläche außerhalb des zentralen, benetzten Bereichs ist trocken und der Wärmeübergang ist hier sehr gering. Nach der Ablösung, weg von der Aufprallobерfläche, zerfällt der Flüssigkeitsfilm in Tröpfchen.

Die Geschwindigkeit fort spritzender Tröpfchen wurde an Hand der Hochgeschwindigkeitsaufnahmen analysiert. Dabei wurde eine viel geringere Tropfengeschwindigkeit ermittelt als die Geschwindigkeit des Flüssigkeitsfilms, die mit der von Watson vorgeschlagenen Korrelation für einphasige Strömungen errechnet wurde. Es wird vermutet, dass Dampfbläschen, die auf der Aufprallobерfläche innerhalb des benetzten Bereiches wachsen, den Flüssigkeitsfilm abbrem sen.

Es wird gezeigt, dass die Wiederbenetzungstemperatur in den Bereichen des Aufpralls und der radialen Strömung deutlich höher ist als die, die in der Literatur für das Behältersieden berichtet wird. Wahrscheinlich erfolgt durch die strömende Flüssigkeit eine Ablösung mit anschließend schneller Kondensation der ausfliegenden Dampfbläschen in ihrer frühen Wachstumsphase innerhalb des unterkühlten Flüssigkeitsfilmes. Dies verhindert die Entstehung von Dampf nahe der heißen Wand und führt schließlich zu einer Erhöhung der Wiederbenetzungstemperatur. Diese Beobachtung bestätigt, dass, wie in der Industrie angewendet, hohe Wärmestromdichten bei sehr großen Wandüberhitzungen durch den Aufprall von Flüssigkeitsstrahlen abgeführt werden können.

Der maximale Wert der Wärmestromdichte und die zugehörige Temperatur nehmen mit wachsendem Abstand vom Staupunkt ab bevor sie einen konstanten Wert erreichen. Im Gegensatz dazu, steigen sie mit zunehmender Wasserstrahlgeschwindigkeit und -unterkühlung. Mit Erhöhung der Unterkühlung und der Geschwindigkeit des Wasserstrahls verschiebt sich die Siedekurve zu höheren Wärmestromdichten und Wandüberhitzungen.

Contents

Abstract	XI
Zusammenfassung	XV
Nomenclature	XXIX
1. Introduction	1
1.1. Motivation	1
1.2. Fundamentals of quenching	2
1.3. Historical overview of jet impingement quenching research	5
1.4. Scope and outline of the present thesis	6
1.5. Closure	6
2. State of the Art	9
2.1. Flow boiling	9
2.1.1. Stage I: bubble nucleation	10
2.1.2. Stages II and III: bubble detachment from cavity, lift-off and condensation . .	11
2.1.3. Quantitative assessment of bubble dynamics in flow boiling	13
2.1.4. Summary	14
2.2. Rewetting process	15
2.3. Fundamentals of jet impingement heat transfer	17
2.3.1. Jet impingement hydrodynamics on an unheated surface	18
2.3.2. Single-phase jet impingement heat transfer	19
2.4. Hydrodynamics of jet impingement quenching	21
2.5. Techniques for determining the heat transfer rate during quenching	23
2.5.1. Steady state measurements	24
2.5.2. Transient measurements	24
2.5.2.1. The inverse heat conduction solution and its non-uniqueness	25
2.5.2.2. Transient measurement setups	27
2.6. Jet impingement quenching heat transfer	28
2.6.1. Steady state measurement results	29
2.6.1.1. Onset of nucleate boiling and fully developed nucleate boiling . . .	29
2.6.1.2. Critical heat flux	31
2.6.2. Transient measurement results	31
2.6.2.1. Effect of initial plate temperature on the boiling curve	31

2.6.2.2.	Heat transfer in the impingement region	32
2.6.2.3.	Heat transfer in the radial flow region	35
2.7.	Comments	37
2.8.	Objectives of the present thesis	38
2.9.	Closure	39
3.	Experimental Methodology	41
3.1.	Concept of the experiment	41
3.2.	Overall experimental setup	42
3.2.1.	Jet nozzle	44
3.2.2.	Test cell	45
3.2.3.	Heating system	47
3.2.4.	The data acquisition system	47
3.2.5.	Visual observation	48
3.2.6.	Plunging jet setup	48
3.3.	Experimental conditions	50
3.3.1.	Free-surface jet impingement quenching	50
3.3.2.	Plunging jet impingement quenching	50
3.4.	Closure	51
4.	Data Analysis and Uncertainty Estimation	53
4.1.	Inverse heat conduction analysis	53
4.1.1.	The inverse heat conduction model Inverse2D	54
4.1.2.	Model parameters for Inverse2D	57
4.1.2.1.	Thermal properties	57
4.1.2.2.	Degree of half-polynomial to approximate the measured temperature history	57
4.1.2.3.	Number of eigenfunctions to approximate the measured radial temperature distribution	57
4.2.	Uncertainty in the heat transfer estimations	58
4.2.1.	Time resolution and time shift	59
4.2.2.	Error in determining high frequency disturbances	63
4.2.3.	Space resolution	65
4.2.3.1.	Stationary heat sink	65
4.2.3.2.	Heat sink of constant width moving radially outwards at a constant speed	65
4.2.4.	Effect of temperature dependent properties	69
4.2.5.	Summary	70
4.3.	Image analysis	70
4.4.	Closure	70
5.	Results and Discussion	73
5.1.	Free-surface jet impingement quenching: hydrodynamics	73
5.1.1.	Flow patterns	74

5.1.2. Wetting front dynamics	77
5.1.3. Boiling activity and wetting limits	78
5.1.4. Summary	85
5.2. Free-surface jet impingement quenching: heat transfer	85
5.2.1. Uncertainty in the heat transfer estimations	85
5.2.2. Measured temperature	86
5.2.3. Surface temperature and heat flux	88
5.2.3.1. Maximum heat flux position	89
5.2.3.2. Effect of jet velocity and subcooling	94
5.2.3.3. Mechanism of heat transfer near the wetting front	95
5.2.4. Boiling curves	96
5.2.4.1. Impingement region	97
5.2.4.2. Radial flow region	104
5.2.4.3. Area-weighted average boiling curves	106
5.2.5. Maximum heat flux condition	106
5.2.5.1. Variation of maximum heat flux condition with radial position . . .	107
5.2.5.2. Variation of maximum heat flux condition with jet velocity and sub- cooling	110
5.2.6. Rewetting temperature	111
5.2.7. Summary	114
5.3. Plunging jet impingement heat transfer	116
5.4. Closure	120
6. Summary and Outlook	121
6.1. Summary	121
6.2. Outlook	122
Bibliography	132
A. Thermophysical Properties of Materials	133
Publications	135
Résumé	137

List of Figures

Figure 1.1: Schematic of the impingement condition on the top and bottom faces of a wide plate.	2
Figure 1.2: A schematic boiling curve showing the dependence of heat flux on surface temperature in the various boiling regimes. The schematics of the bubble dynamics in the various boiling regimes have been adapted from [62].	3
Figure 1.3: A quench curve schematically showing the variation of cooling rate and heat flux.	4
Figure 2.1: Subcooled flow boiling in a channel heated from beneath [106].	10
Figure 2.2: Three stages of vapor bubble departure from a surface in shear flow: (I) instant of departure from the nucleation site, (II) sliding bubble, and (III) lift-off (Adapted from [126]).	10
Figure 2.3: Forces on a vapor bubble growing in shear flow (adapted from [58]).	11
Figure 2.4: Schematic of the bubble ebullition cycle observed in [8].	12
Figure 2.5: Effect of (a) heat flux [96] and (b) surface superheat [56] on bubble growth.	14
Figure 2.6: Schematic of jet impingement configurations relevant to this study.	18
Figure 2.7: Schematic of a circular free-surface jet impingement showing the three flow regions along with the inviscid pressure and velocity distributions within the impingement region. These distributions are based on the equations for single-phase flow [60].	19
Figure 2.8: Development of viscous and thermal boundary layers on an uniformly heated flat surface (adapted from [68]). Based upon the relative size of the liquid film and the boundary layers, four heat transfer regions can be identified in the schematic.	20
Figure 2.9: Comparison of the local Nusselt number predicted using the model by Ma et al. [75] with the experimental data by Stevens [31]).	21
Figure 2.10: Schematic of a hot steel plate quenched by an impinging circular free-surface jet.	21
Figure 2.11: Schematic of observed flow patterns, with (a) to (d) arranged in the order of decreasing surface temperature (adapted from [50]).	23
Figure 2.12: Temperature variation at the surface ($z = 0$ mm) and at a depth ($z = 0.6$ mm) for (a) a 1 Hz sinusoidal heat flux signal, and (b) a 1 Hz sinusoidal heat flux signal with a superimposed 100 Hz sinusoidal heat flux signal [63].	26
Figure 2.13: Effect of source width on heat flux estimation for three different materials with two rows of sensors at depths of 1.9 and 5 mm below the surface and a radial pitch of 5 mm [123].	28
Figure 2.14: Boiling curve at the stagnation point of a planar free-surface impinging jet ($v_N = 0.8$ m/s, $w_N = 1$ mm, $S = 6$ mm and $\Delta T_{sub} = 16$ K) [98].	29
Figure 2.15: Boiling curves for spray cooling of a steel plate with different initial temperatures [67].	32

Figure 2.16: Comparison of predictions from various nucleate boiling correlations for stagnation point obtained by steady state measurements with the boiling data obtained by transient measurements [127].	35
Figure 2.17: Effect of jet mass flow rate on the boiling curves at stagnation point [127].	35
Figure 3.1: Identification of an unit cell.	41
Figure 3.2: Schematic of the test specimen.	42
Figure 3.3: Block diagram showing the various components of the test setup.	43
Figure 3.4: Schematic of the test section showing the arrangement of the test cell, jet nozzle and cameras.	43
Figure 3.5: A schematic of the experimental setup.	44
Figure 3.6: The test cell assembly for free-surface jet impingement quenching studies.	45
Figure 3.7: Measured temperature at $r = 24$ mm and calculated cooling rate at the thermocouple depth. For details of experiments F2 and F4, see Table 3.1.	47
Figure 3.8: The test cell assembly for plunging jet impingement quenching studies.	49
Figure 3.9: A snapshot of the test section with a ceramic cylinder of $h_p = 30$ mm assembled on top of the test cell.	49
Figure 4.1: A schematic of the test specimen showing the boundary conditions.	54
Figure 4.2: Data ranges used to calculate surface temperature and heat flux at time t	55
Figure 4.3: Effect of number of eigenfunctions used to approximate the radial temperature distribution at depth z_m for experiment F2.	58
Figure 4.4: A schematic of the heat flux variation, $q_{s,real}(t)$, given by Eq. (4.17) and time resolution, t_{res} , described by Eq. (4.14).	59
Figure 4.5: A schematic representation of the time shift, t_{shift} , described mathematically by Eq. (4.16).	60
Figure 4.6: Effect of time duration Δ on the accuracy of the inverse heat conduction solution.	61
Figure 4.7: Error in estimating $q_{s,max}$ of a thermal wave.	62
Figure 4.8: Comparison of $q_{s,real}(t)$ and $q_{s,inv}(t)$ showing the time shift in estimating a triangular thermal wave that is asymmetric at t_{max}	62
Figure 4.9: Limitations of the experiment in detecting high frequency components in thermal wave.	63
Figure 4.10: Effect of frequency, f , of the sinusoidal thermal wave on the accuracy of the inverse heat conduction solution.	64
Figure 4.11: Error in estimation of the amplitude of a sinusoidal thermal wave.	64
Figure 4.12: Comparison of $q_{s,real}(r)$, $q_{s,inv}(r)$ and $q_{s,int}(r)$ for different source widths w	66
Figure 4.13: Uncertainty in the estimation of a stationary heat sink of width w	67
Figure 4.14: Comparison of $q_{s,real}$, $q_{s,inv}$ and $q_{s,int}$ when the peak of the radially outwards moving heat sink defined by Eq. (4.23) is at $r = 10$ mm.	68
Figure 4.15: Error in the inverse heat conduction solution due to the use of constant thermal properties.	69
Figure 5.1: Formation of dark zone on the surface at time $t = 0.04$ s in experiment F1.	74
Figure 5.2: Formation of a wetted zone in experiment F1.	75

Figure 5.3: Heat flux, $q_s(t)$, at the stagnation point, $r = 0$ mm, in experiment F1. Since the time resolution of the inverse heat conduction solution is of the same order as the film boiling duration, the film boiling regime could not be identified.	75
Figure 5.4: Low speed image sequence showing the wetted region growth in experiment F1. .	76
Figure 5.5: Identified heat transfer regions on the surface during quenching in experiment F6.	76
Figure 5.6: High-speed image showing the deflection of liquid film at time $t = 0.955$ s ($d_N = 3$ mm, $v_J = 2.85$ m/s, $\Delta T_{sub} = 80$ K) [57].	77
Figure 5.7: Lamella breakup and formation of secondary jets at time $t = 0.18$ s in experiment F6. The secondary jets are marked by enclosing black dotted circles.	78
Figure 5.8: Effect of jet velocity, v_J , and subcooling, ΔT_{sub} , on wetting front growth.	79
Figure 5.9: Heat flux, $q_s(r)$, and surface temperature, $T_s(r)$, at time $t = 0.5$ s in experiment F6.	80
Figure 5.10: Splashed droplet velocity, v_d , in experiment F6 and its comparison with the theoretically determined single-phase film velocity, $v_f(r_w)$	81
Figure 5.11: Variation of the velocity deficit, $(v_d - v_f)$, with the wetting front position, r_w , for $v_J = 5$ m/s.	82
Figure 5.12: Heat transfer in experiment F6. Up to a radial position of 6 mm, the maximum heat flux, $q_{s,MHF}$, is reached when time $t < 0.3$ s. The maximum heat flux, $q_{s,MHF}$, reduces with radius after $r = 6$ mm, which means that the latent heat transfer increases with distance from the stagnation point.	82
Figure 5.13: Variation of velocity deficit, $(v_d - v_f)$, in experiment F5 ($v_J = 2.5$ m/s). Here, the velocity deficit is much lower compared to that in experiment F6 ($v_J = 5$ m/s).	84
Figure 5.14: Variation of wetting front radius, $r_w(t)$, and droplet velocity, $v_d(t)$ ($T_I = 900$ °C, $v_J = 5$ m/s and $\Delta T_{sub} = 30$ K).	84
Figure 5.15: Variation of measured temperature, $T_m(t)$, and cooling rate, $\frac{ \Delta T_m }{\Delta t}(t)$, at various radial positions in experiment F2. The temperature drops much faster within the impingement region as compared to the radial flow region. The maximum cooling rate at $r = 0$ mm is almost nine times of that at $r = 20$ mm.	87
Figure 5.16: Comparison of measured temperature, $T_m(r)$, in experiments F1 and F4. The best fit lines have been approximately drawn and are just for assistance in reading the chart. .	88
Figure 5.17: Effect of jet velocity, v_J , on the measured temperature, $T_m(t)$, at $r = 10$ mm. The jet velocities are 2.5 m/s, 5.1 m/s and 9.75 m/s in experiments F1, F2 and F4, respectively. .	89
Figure 5.18: Effect of jet velocity, v_J , on the measured cooling rate, $\frac{ \Delta T_m }{\Delta t}(t)$, at $r = 0$ mm. The jet velocities are 2.5 m/s, 5.1 m/s and 9.75 m/s in experiments F1, F2 and F4, respectively.	89
Figure 5.19: Surface temperature, $T_s(t)$, and heat flux, $q_s(t)$, at a radial position of $r = 20$ mm in experiments F2 and F4. Tangents to the surface temperature variation have been approximately drawn to illustrate that changes in the heat transfer mechanism can be interpreted from the change in the slope of the temperature history.	89
Figure 5.20: Measured cooling rate, $\frac{ \Delta T_m }{\Delta t}(t)$, surface cooling rate, $\frac{ \Delta T_s }{\Delta t}(t)$, and heat flux, $q_s(t)$, at $r = 8$ mm in experiment F2. The maximum heat flux (MHF) condition is delayed with respect to the estimated maximum surface cooling rate.	90
Figure 5.21: Heat flux, $q_s(r)$, and surface temperature, $T_s(r)$, at time $t = 0.37$ s in experiment F2. At this time instant, $r_{MHF} = 6$ mm and $r_w = 8$ mm.	91

Figure 5.22: Comparison of wetting front radius, r_w , and maximum heat flux position, r_{MHF} , showing that the maximum heat flux position is within the wetted region.	91
Figure 5.23: A snapshot of the quenching process with the instantaneous local boiling modes shown on schematic boiling curves.	92
Figure 5.24: A schematic of the jet quenching process showing the boiling activity in the wetted region and the liquid deflection in the wetting front region.	92
Figure 5.25: Surface temperature, $T_s(r)$, and heat flux, $q_s(r)$, at various time instants in experiment F2. The wetting front positions at the same instants are marked with closed symbols. Local peaks near the wetting front position are seen in the heat flux distribution.	93
Figure 5.26: Heat flux, $q_s(r)$, at different time instants during quenching of an AISI type 314 stainless steel specimen ($T_I = 900\text{ }^\circ\text{C}$) with an impinging water jet ($v_J = 2.85\text{ m/s}$, $d_J = 2.8\text{ mm}$ and $\Delta T_{sub} = 80\text{ K}$) [57]. Heat flux, $q_s(r)$, at same time instants in experiment F1 is shown for comparison. For almost similar experimental conditions, the local peaks near the wetting front cannot be identified in the study of Karwa et al. [57] because of inferior space and time resolution compared to this study.	94
Figure 5.27: A schematic representation of the error arising due to the time and space resolutions of the inverse solution. Here, a snapshot from experiment F2 at $t = 0.5\text{ s}$ is shown along with the estimated heat flux distribution. If the time and space resolutions of the inverse solution were almost negligible, the real heat flux distribution (schematically shown here) would have had a sharper peak just inside the wetting front boundary than is estimated in this study.	94
Figure 5.28: Effect of difference in thermocouple time response on the inverse solution at $t = 1.5\text{ s}$ in experiment F1.	95
Figure 5.29: Effect of jet velocity, v_J , on heat flux, $q_s(r, t)$	96
Figure 5.30: Effect of jet subcooling, ΔT_{sub} , on heat flux, $q_s(r, t)$	96
Figure 5.31: Schematic of the flow structure near the wetting front region.	97
Figure 5.32: Boiling curve for the stagnation point in experiment F1. Critical heat flux, $q_{s,CHF}$, calculated using Eq. (2.24) is also shown for comparison.	98
Figure 5.33: Boiling curve for the stagnation point, $r = 0\text{ mm}$, with different initial test specimen temperature, T_I , but same jet velocity and subcooling ($v_J = 2.5\text{ m/s}$ and $\Delta T_{sub} = 75\text{ K}$). The curve's slope during the initial cooling period is similar in both the experiments.	98
Figure 5.34: A schematic representation of the possible oscillations of the impingement surface temperature and liquid-vapor interface temperature during the initial cooling period.	99
Figure 5.35: Comparison of boiling curves for the impingement region in experiment F1 and correlations for nucleate boiling compiled in [116]. These correlations, obtained from steady state measurements, overpredict the slope of the nucleate boiling curve.	102
Figure 5.36: Comparison of the measured cooling rate, $\frac{ \Delta T_m }{\Delta t}$, at the stagnation point, $r = 0\text{ mm}$, with the noise in the measured temperature. The noise level in the temperature measurement is determined to be $3\sigma = 0.33\text{ K}$. The cooling rate becomes comparable to noise in the measurement after about $t = 1.5\text{ s}$. As a result, the heat flux estimates for $\Delta T_{sup} < 200\text{ K}$ are of doubtful accuracy.	102

Figure 5.37: Boiling curves for the stagnation point, $r = 0$ mm, in experiments F1, F2, F3 and F4. The boiling curves for different jet velocities merge upon each other in the initial cooling and nucleate boiling regime. Contrary to the observation of Liu et al. [72], the maximum heat flux decreases with increasing jet velocity.	103
Figure 5.38: Boiling curves for the stagnation point, $r = 0$ mm, in experiments F2 and F7. The boiling curve for different jet velocity merge in the initial cooling and nucleate boiling regime, while the the maximum heat flux increases with jet subcooling.	104
Figure 5.39: Boiling curves for the impingement and radial flow regions. The boiling curve shifts to lower surface superheat and heat flux with distance from the stagnation point.	105
Figure 5.40: Heat flux, $q_s(t)$, and surface temperature, $T_s(t)$, at $r = 10$ mm in experiment F1.	105
Figure 5.41: Boiling curve for experiment F1 clearly showing film boiling in the radial flow region.	106
Figure 5.42: Heat transfer coefficient, $h_s(\Delta T_{sup})$ at various radial positions.	107
Figure 5.43: Effect of jet velocity, v_J , on heat transfer coefficient, $h_s(\Delta T_{sup})$, at various radial positions.	108
Figure 5.44: Variation of area-weighted average heat transfer, $\bar{q}_{s,MHF}$ and \bar{h}_s , with area-weighted average surface superheat, $(\bar{T}_s - T_L)$	109
Figure 5.45: Effect of jet velocity, v_J , on maximum heat flux condition, $q_{s,MHF}(r)$ and $T_{s,MHF}(r)$. For clarifying the trend, tentative best fit lines have been drawn here, while ignoring the sudden changes in $q_{s,MHF}(r)$ and $T_{s,MHF}(r)$ when $r \geq 22$ in experiments F2, F3 and F4.	110
Figure 5.46: Distribution of maximum heat flux, $q_{s,MHF}(r)$. Three regions have been marked based on the relative size of boundary layer to the liquid film. Region I (Impingement region, $0 \leq \bar{r} < 1.28$), Region II (Boundary layer region, $1.28 \leq \bar{r} < 0.5554 \cdot Re_J^{1/3} / (50 - 5.147 \cdot Pr_L)^{1/3}$), Region III (Similarity region, $\bar{r} > 0.5554 \cdot Re_J^{1/3} / (50 - 5.147 \cdot Pr_L)^{1/3}$). Tentative best fit lines have also been drawn here.	111
Figure 5.47: Distribution of surface temperature at maximum heat flux, $T_{s,MHF}(r)$. Three regions have been marked based on the relative size of boundary layer to the liquid film. Region I (Impingement region, $0 \leq \bar{r} < 1.28$), Region II (Boundary layer region, $1.28 \leq \bar{r} < 0.5554 \cdot Re_J^{1/3} / (50 - 5.147 \cdot Pr_L)^{1/3}$), Region III (Similarity regions, $\bar{r} > 0.5554 \cdot Re_J^{1/3} / (50 - 5.147 \cdot Pr_L)^{1/3}$). Tentative best fit lines have also been drawn here.	112
Figure 5.48: Variation of maximum heat flux, $q_{s,MHF}$, in the radial flow region with jet Reynolds number, Re_J , at $\Delta T_{sub} = 75$ K.	113
Figure 5.49: Variation of temperature at maximum heat flux, $T_{s,MHF}$, in the radial flow region with jet Reynolds number, Re_J , at $\Delta T_{sub} = 75$ K.	113
Figure 5.50: Effect of jet subcooling, ΔT_{sub} , at $v_J = 5$ m/s on the variation of maximum heat flux condition, $q_{s,MHF}(r)$ and $T_{s,MHF}(r)$, with radial position. Tentative best fit lines have been drawn here for better visualization of the variation, while ignoring the sudden drop in $q_{s,MHF}(r)$ or the sudden rise in $T_{s,MHF}(r)$ when $r \geq 22$	114
Figure 5.51: Effect of jet velocity, v_J , on the rewetting temperature, $T_{s,rewet}$	114
Figure 5.52: Effect of liquid accumulation on the evolution of surface temperature, $T_s(r, t)$. Based on the mass flow rate of the jet, the filling time in experiments P1 and P2 are calculated to be 1.7 s and 4.5 s, respectively.	116

Figure 5.53: Effect of coolant accumulation over the impingement surface on the heat flux, $q_s(r)$	117
Figure 5.54: Comparison of the boiling curves for the radial flow region of the plunging jet and free-surface jet impingement quenching experiments shows that no clear trend regarding the variation of boiling heat transfer rate with the accumulated liquid height can be made. . .	118
Figure 5.55: Comparison of the maximum heat flux condition, $q_{s,MHF}(r)$ and $T_{s,MHF}(r)$, for the plunging jet and free-surface jet impingement quenching experiments. It can be seen that the effect of accumulation is not considerable.	119
Figure 5.56: Comparison of the maximum heat flux condition, $q_{s,MHF}(r)$ and $T_{s,MHF}(r)$, for the plunging jet and free-surface jet impingement quenching experiments. While the deterioration of maximum heat flux, $q_{s,MHF}$, due to accumulation can be seen, no such effect on the temperature at maximum heat flux is seen.	119
Figure 5.57: Variation of area-weighted average heat transfer coefficient, $\overline{h_s}$, with area-weighted average surface superheat, $(\overline{T_s} - T_L)$	120

List of Tables

Table 2.1: Compilation of reported rewetting condition during quenching with flowing water at atmospheric pressure (arranged chronologically).	17
Table 2.2: Compilation of reported maximum heat flux condition, $q_{s,MHF}$ and $T_{s,MHF}$, for water jet impingement quenching at atmospheric pressure (chronologically arranged).	33
Table 3.1: Experimental conditions for the free-surface jet impingement quenching studies. . .	50
Table 3.2: Experimental conditions for the plunging jet impingement quenching studies	50
Table 4.1: Effect of the time duration Δ on the time resolution, t_{res}	60
Table 4.2: Variation of space resolution with the width of the heat sink, w	67
Table 4.3: Effect of the movement of heat sink on the time resolution and shift.	69
Table 5.1: Compilation of reported surface superheat at maximum heat flux, $\Delta T_{sup,MHF}$, during quenching with impinging water jet at atmospheric pressure (arranged chronologically). .	101
Table 5.2: Compilation of reported rewetting temperature, $T_{s,rewet}$, during quenching with flowing water at atmospheric pressure (arranged chronologically).	115
Table A.1: Thermophysical properties of water [113].	133
Table A.2: Elemental composition of stainless steel AISI-type 314 (as per the supplier's report). .	133
Table A.3: Thermophysical properties of stainless steel AISI-type 314 at select temperatures. .	134

Nomenclature

Roman Symbols

Symbol	Meaning	SI unit
c	specific heat	$[\text{J}/(\text{kg} \cdot \text{K})]$
D	diameter of test specimen	$[\text{m}]$
d_b	bubble diameter	$[\text{m}]$
d_J	jet diameter at the impingement surface position calculated assuming that the test specimen is absent $= d_N \cdot \sqrt{v_N/v_J}$	$[\text{m}]$
d_N	jet diameter at jet nozzle exit	$[\text{m}]$
f	frequency of a sinusoidal thermal wave, Eq. (4.19)	$[\text{Hz}]$
F	force on a bubble growing on a heated surface during flow boiling, Eqs. (2.3) and (2.4)	$[\text{N}]$
g	gravitational acceleration	$[\text{m}/\text{s}^2]$
$G_{i,j,k}$	coefficient for the IHCP solution, Eqs. (4.7) and (4.11)	$[-]$
h_{fg}	latent heat of vaporization	$[\text{J}/\text{kg}]$
h_p	maximum height of spent coolant accumulated over the impingement surface in the plunging jet experiment, see Fig. 3.8	$[\text{m}]$
h_s	heat transfer coefficient on impingement surface	$[\text{W}/(\text{m}^2 \cdot \text{K})]$
\bar{h}_s	area-weighted average heat transfer coefficient on the impingement surface, Eq. (5.4)	$[\text{W}/(\text{m}^2 \cdot \text{K})]$
$J_0(r), J_1(r)$	Bessel function, see Eq. (4.10)	$[-]$
l	length	$[\text{m}]$
m_j	j th eigenvalue [root of $J_1(m_j) = 0$], Eq. (4.10)	$[-]$
m_J	jet mass flow rate	$[\text{kg}/\text{s}]$
\dot{m}_J	jet mass flux on the impingement surface $= m_J/(\pi \cdot R^2)$	$[\text{kg}/(\text{m}^2 \cdot \text{s})]$
N_{corr}	number of corrections applied to the polynomial approximating the measured temperature history, Eqs. (4.6) and (4.10)	$[-]$
N_j	number of eigenfunctions in the polynomial approximating the measured radial temperature distribution minus one, Eqs. (4.6) and (4.10)	$[-]$
N_k	number of terms in the polynomial approximating the measured temperature history minus one, Eqs. (4.6) and (4.10)	$[-]$
p	pressure	$[\text{N}/\text{m}^2]$
p_a	atmospheric pressure	$[\text{N}/\text{m}^2]$

Roman Symbols

Symbol	Meaning	SI unit
$P_{i,j,k}$	coefficient of the polynomial approximating the measured temperature, Eq. (4.10)	[-]
q_s	heat flux on the impingement surface, with the positive sign used as a convention for heat extracted from the test specimen	[W/m ²]
$\overline{q_s}$	area-weighted average heat flux on the impingement surface, Eq. (5.2)	[W/m ²]
$q_{s,int}$	interpreted heat flux, which is a time and/or radial average of the actual heat flux distribution, Eq. (4.15)	[W/m ²]
$q_{s,inv}$	heat flux on the impingement surface estimated by solving the IHCP (Chapter 4)	[W/m ²]
$q_{s,MHF}$	maximum heat flux on the impingement surface	[W/m ²]
$q_{s,ONB}$	heat flux at the onset of nucleate boiling	[W/m ²]
$q_{s,real}$	real or actual heat flux (Chapter 4)	[W/m ²]
$q_{s,rewet}$	rewetting heat flux	[W/m ²]
r	radial coordinate of the test specimen, see Fig. 3.2	[m]
R	test specimen radius, see Fig. 3.2	[m]
\bar{r}	non-dimensional radius = r/d_J	[-]
r_c	cavity radius	[m]
$r_{c,min}, r_{c,max}$	minimum and maximum active cavity radius, respectively, Eq. (2.2)	[m]
r_{MHF}	maximum heat flux position	[m]
r_{res}	radial resolution of the inverse heat conduction solution	[m]
r_{shift}	radial shift of inverse heat conduction solution with respect to actual heat flux distribution	[m]
r_w	radial position of wetting front	[m]
s	characteristic axial dimension of a solid	[m]
S	spacing between the jet nozzle exit and the impingement surface	[m]
t	time	[s]
T	temperature	[°C]
T_{cr}	thermodynamic critical temperature of a fluid	[°C]
t_f	finishing time of the data window for the approximating polynomial, see Fig. 4.2	[s]
t_i	starting time of the data window for i th correction to the approximating polynomial, see Fig. 4.2	[s]
T_I	initial temperature of the test specimen	[°C]
T_L	jet temperature at the jet nozzle exit	[°C]
T_m	measured test specimen temperature	[°C]
t_{res}	time resolution of the inverse heat conduction solution, Eq. (4.14)	[s]
T_s	temperature of the impingement surface	[°C]
$\overline{T_s}$	area-weighted average temperature of the impingement surface, Eq. (5.3)	[°C]
T_{sat}	saturation temperature	[°C]

Roman Symbols

Symbol	Meaning	SI unit
t_{shift}	time shift of the inverse heat conduction solution with respect to actual heat flux variation, Eq. (4.16)	[s]
$T_{s,MHF}$	impingement surface temperature at maximum heat flux	[°C]
$T_{s,rewet}$	rewetting temperature	[°C]
T_z	temperature of the test specimen at an axial position z	[°C]
v	velocity	[m/s]
v_d	splashed drop velocity	[m/s]
v_f	velocity of liquid film calculated using Eqs. (2.6) and (2.7)	[m/s]
v_J	jet velocity at impingement surface position = $\sqrt{v_N^2 + 2 \cdot g \cdot S}$	[m/s]
v_N	jet velocity at the jet nozzle exit = $m_J / (\rho_L \cdot \pi \cdot d_N^2 / 4)$	[m/s]
v_w	wetting front velocity	[m/s]
v_∞	free-surface velocity of the liquid film	[m/s]
x, y	space coordinates in Cartesian system, see Section 2.1	[m]
z	axial coordinate measured from the impingement surface, see Fig. 3.2	[m]
Z	test specimen thickness, see Fig. 3.2	[m]
z_m	axial position of the embedded thermocouple junction's geometric center from the impingement surface, see Fig. 3.2	[m]

Greek Symbols

α	thermal diffusivity = $\lambda / (\rho \cdot c)$	[m ² /s]
$\Gamma()$	gamma function	[-]
δ	film thickness	[m]
$\bar{\delta}$	non-dimensional film thickness = δ / d_J	[-]
Δ	time duration	[s]
Δ_t	thermal boundary layer thickness	[m]
Δ_h	hydrodynamic or momentum boundary layer thickness	[m]
Δr_m	radial pitch of thermocouples arranged within the test specimen, see Fig. 3.2	[m]
ΔT_{sub}	liquid subcooling at the jet nozzle exit = $(T_{sat} - T_L)$	[K]
ΔT_{sup}	surface superheat = $(T_s - T_{sat})$	[K]
λ	thermal conductivity	[W/(m · K)]
ν	kinematic viscosity	[m ² /s]
ρ	density	[kg/m ³]
σ	surface tension	[N/m]
ω	angular frequency of the thermal wave = $2 \cdot \pi \cdot f$	[1/s]

Dimensionless Groups

Symbol	Meaning
Fo	Fourier number = $\alpha \cdot t / s^2$
Nu_J	Nusselt number = $h_s \cdot d_J / \lambda_L$
Pr	Prandtl number = $\mu \cdot c / \lambda$
Re_J	Reynolds number of the jet = $(v_J \cdot d_J) / \nu_L$

Subscripts

Symbol	Meaning
f	liquid film
J	jet
L	liquid
m	temperature measurement plane within the test specimen
N	nozzle
$real$	real or actual surface boundary condition
s	top surface of the test specimen, also referred to as the impingement surface
sat	saturated
sub	subcooled
sup	superheat
T	test specimen
V	vapor

Abbreviations

Symbol	Meaning
AISI	American iron and steel institute
BRF	bottom reflooding
CHF	critical heat flux
CJI	circular jet impingement
CS	carbon steel
IHCP	inverse heat conduction problem
IHCS	inverse heat conduction solution
MHF	maximum heat flux
ONB	onset of nucleate boiling
PJI	planar jet impingement
SS	stainless steel
WJ	wall jet

1

Introduction

This chapter introduces briefly the issues related to thermal management and processing of hot metal parts when cooled in a forced flow of liquid. Here, the emphasis is given on the jet impingement cooling process, also called as the jet impingement quenching process, and is the focus area of this work. The basics of pool boiling process are presented in the next section. The quenching process is a conjugate heat transfer problem of flow boiling and conduction heat transfer, and is more complex compared to a steady state pool boiling problem; the complexity of flow boiling and jet impingement quenching compared to pool boiling is being dealt in much detail in Chapter 2. Further, an overview of the previous research on the subject of this thesis is presented in this chapter, which aided in defining the aim of this work. Thereafter, the scope and the structure of the thesis are given.

1.1 Motivation

Rapid cooling of extremely hot metal parts is widely encountered in various industrial applications, e.g. metal processing [90], loss-of coolant-accident [21], etc. At the beginning of the cooling, the temperatures of these parts can be as high as 800–1000 °C. Small parts are cooled in air, while large parts are cooled in liquids. When cooling with liquids, boiling happens due to the high temperature of the part. To control the boiling process and thereby the cooling rate, the following flow configurations are used: directly submerging in a pool, falling film, bottom reflooding, sprays and impinging jets. In metal processing industry, impinging jets are widely used where very intense cooling is required, while spray cooling is used where moderate but uniform cooling is required. Considerable information on spray cooling is available, but efforts to understand and characterize the jet impingement quenching process have been scarce. Therefore, this work is focused on the quenching of metal parts by impinging jets.

The parts may get distorted due to thermal stresses induced by non-homogeneous cooling, especially in the case of jet impingement cooling. For example, when cooling thick and wide flat plates, large water flux is used. The spent liquid from the top surface of the plate is drained from the edges

by gravity. If the draining rate is less than the rate at which the water arrives on the plate surface, then the plate top surface gets flooded. A schematic of the jet impingement condition on the top and the bottom face of the plate is shown in Fig. 1.1. Typical water mass flux is up to about 1.6–20 kg/(m² · s) [93, 125]. In many cases, the retained water height can be up to 200 mm for large plates [14, 48, 93], and it strongly influences the cooling rate [48]. On the other hand, the bottom surface of the plate has no accumulated water. Thus, the orientation of the surface with respect to gravity has significant influence on the heat transfer rates and hence the quality of the product. The key challenges for the process designer and operator are [41]:

- control of the part temperature at the end of the cooling process,
- controlled cooling rate on the surface and the interior of the part,
- homogeneous cooling from all the faces of the part.

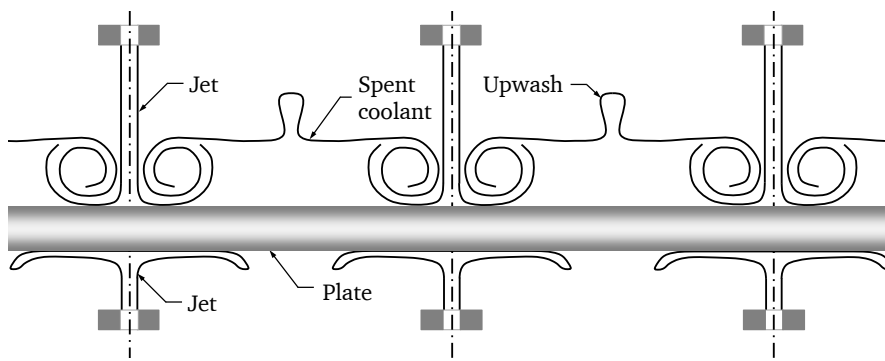


Figure 1.1. Schematic of the impingement condition on the top and bottom faces of a wide plate.

In jet impingement cooling, the jets are equally spaced in the form of an array. This results in hydrodynamic variations within the coolant stream on the surface; as a result, the heat transfer rate on the surface of the quenched part is non-uniform. The understanding of the cooling process during jet impingement cooling is difficult because of the simultaneous presence of all the modes of boiling (stable film boiling to partially developed nucleate boiling through transition boiling and critical heat flux), besides single-phase forced convection. The boiling process is further complicated by the transient cooling process. The boiling heat transfer rate is influenced by the coolant temperature, flow rate, the retained coolant height on the plate, plate thermal properties, to name a few. Bogdanic et al. [9] commented that performing boiling experiments in the very high temperature region are difficult due to technological problems. The likely technological problems faced by the researcher are lack of appropriate sensors and materials for these high temperatures, corrosion at high temperature, etc. As a result, scarce experimental data is available in literature concerning this process. Due to the lack of enough knowledge of the mechanism and scarcity of appropriate correlations, the process control is a challenging task. Current industry practices for designing and operating such cooling systems are generally based on empirical relations developed from experience and rule of thumb.

1.2 Fundamentals of quenching

Quenching refers to the rapid cooling of a high temperature metal part resulting from its sudden contact with a lower temperature liquid. Since the metal part temperature is much higher than the

saturation temperature of the liquid at atmospheric pressure, heat transfer occurs by boiling. Here, first a quick insight into the boiling process is necessary before discussing the quenching process.

Boiling is a two-phase heat transfer process in which heat is transferred from a solid (wall) to a saturated or superheated liquid in contact with its surface. The heat transfer occurs by phase change processes, which results in rapid vapor bubble formation, their growth and departure from the wall. At any time, numerous bubbles grow and depart from the wall. Schweizer [102] listed the following reasons for the enhancement in the heat transfer rate during boiling as compared to that for single-phase convection:

- A thin liquid microlayer is formed on the wall at the bubble foot, which significantly enhances the heat transfer rate.
- The bubble motion near the wall significantly enhances the single phase convection rates by churning the liquid.
- The thermal boundary layer is removed during each bubble cycle and the resulting thermal resistance is low.

A typical pool boiling curve is shown in Fig. 1.2. First constructed by Nukiyama for pool boiling of water, the boiling curve is also referred to as Nukiyama's curve. Dhir et al. [20] describe four distinct heat transfer regimes in the Nukiyama curve obtained during quenching:

1. Film boiling: This boiling regime occurs when surface temperature $T_s \geq T_{s,rewet}$, and is characterized by a stable layer of vapor that forms between the heated wall and the liquid. Vapor is generated at the liquid-vapor interface, which then escapes into the liquid above. Radiation heat transfer between the wall and the liquid also becomes significant during the film boiling process. The end of this regime is referred to as the Leidenfrost point [4] or the minimum heat flux point or the rewetting point. The heat flux and surface temperature at this point are referred to as the rewetting heat flux, $q_{s,rewet}$, and the surface rewetting temperature, $T_{s,rewet}$, respectively.
2. Transition boiling: This is an unstable intermediate regime between nucleate boiling and film boiling, which is encountered during quenching or during temperature feedback-controlled steady state boiling. This boiling regime occurs in the surface temperature range $T_{s,CHF} \leq$

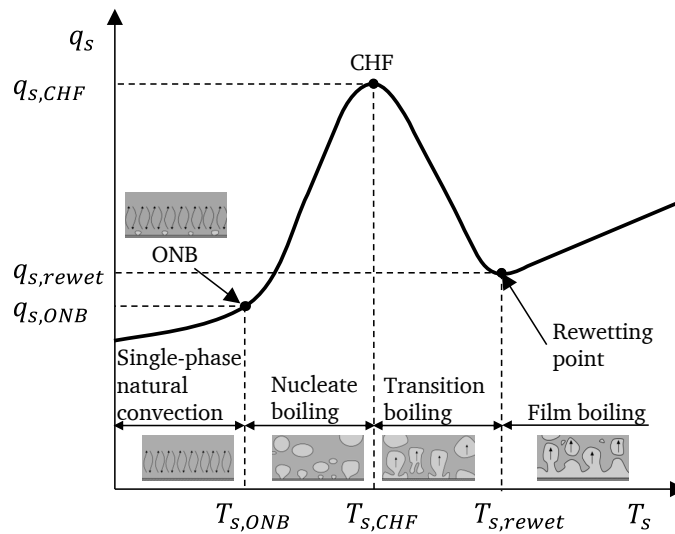


Figure 1.2. A schematic boiling curve showing the dependence of heat flux on surface temperature in the various boiling regimes. The schematics of the bubble dynamics in the various boiling regimes have been adapted from [62].

$T_s \leq T_{s,rewet}$. The boiling mode fluctuates between nucleate boiling and film boiling, with both the incidences of liquid-wall contact and the contact period increasing with decreasing surface temperature. In this regime, the heat flux increases as the surface temperature decreases. At the end of this regime, the heat flux reaches its maximum value. This maximum is termed as the critical heat flux (CHF).

3. Nucleate boiling: This is a two-phase natural convection process in which bubbles nucleate, grow and depart from the heated wall. The end of this zone is marked by the onset of nucleate boiling (ONB) point.
4. Single-phase natural convection: This regime exists once the wall superheat is low. At low wall superheat, any vapor bubble, if generated, would immediately condense in the subcooled liquid around it. The main mode of heat transfer here is natural convection.

During the later part of the thesis, various terminologies used to describe the Nukiyama's curve for pool boiling would be used to explain the jet impingement quenching phenomenon.

Pool boiling refers to boiling under natural convection conditions, liquid flow over the hot wall whereas in forced flow boiling is imposed by external means [20]. In the case of forced convection boiling, the heat flux is a function of the local liquid velocity and subcooling in all the regimes, though the representative features of the boiling curve are still similar to the Nukiyama's curve for pool boiling. Hence, during jet impingement cooling, the boiling condition is different from pool boiling. The effect of hydrodynamics of the jet on the heat transfer is significant, and it must be taken into account when analyzing the boiling process. Flow boiling is discussed in detail in Section 2.1.

Figure 1.3 shows a cooling curve or quench curve for quenching of a hot metal part with initial temperature $T_I > T_{s,rewet}$. The variation of boiling heat flux during the quenching process is also shown. Since the initial temperature of the part is greater than the rewetting temperature, heat transfer happens by film boiling and the cooling rate is low. As the wall temperature reduces below $T_{s,rewet}$, partial wetting of the surface occurs and rapid cooling commences. Once the surface is rewetted, various modes of boiling occur with decreasing surface temperature and the rate of cooling varies significantly during these modes of boiling. Importantly, in the case of quenching, the maximum achievable heat flux value is generally different than the critical heat flux of a steady state measurement. Therefore, the equivalent of the critical heat flux condition in a transient measurement is termed as the maximum heat flux condition (MHF). The heat flux and surface temperature at this condition are $q_{s,MHF}$ and $T_{s,MHF}$, respectively. The boiling regime is transition boiling when

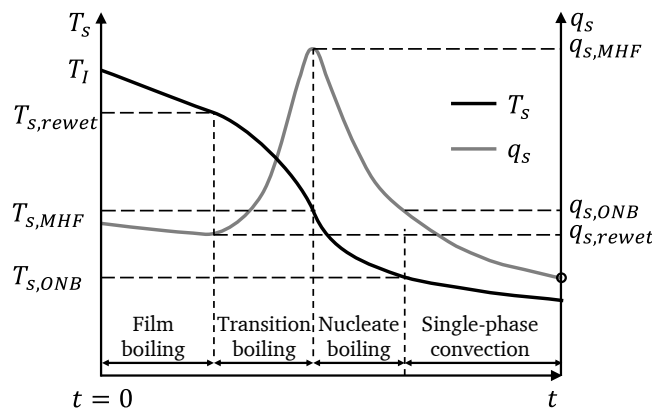


Figure 1.3. A quench curve schematically showing the variation of cooling rate and heat flux.

the surface temperature is between $T_{s,rewet}$ and $T_{s,MHF}$, while nucleate boiling occurs in the surface temperature range of $T_{s,MHF}$ and $T_{s,ONB}$. Once the surface temperature reduces to $T_{s,ONB}$, the boiling activity is suppressed and the heat transfer occurs by single-phase convection. The boiling dynamics depends on the thermal properties of the metal part, as is being discussed later on in Chapter 2. Thus, the jet impingement quenching process under consideration here is a conjugate heat transfer problem.

1.3 Historical overview of jet impingement quenching research

This section gives a historical overview of the research related to jet impingement quenching over the past few decades. While this technique has been used extensively across the steel industry since 1970's, very little published research work is available.

Preliminary research during 1970's and 1980's was mostly published in Japanese research journals [42–44, 48]. In these studies, jet impingement quenching of stainless steel plates heated to an initial temperature of 900 °C was investigated. These earlier works provided some basic insight into the phenomenon, though the given correlations and heat transfer estimates have limited applicability as the measurement methods adopted were inadequate to estimate the heat transfer during the various boiling regimes.

Both analytical and experimental contributions were made by the researchers at Purdue University (USA) [25–29, 37, 38, 111, 117, 129–131]. Their research focus was on analytical and experimental prediction of heat transfer in the jet impingement and parallel/radial flow regions, including the effect of moving surface [26, 28, 29, 129–131]. Also, the quenching of copper blocks heated to an initial temperature in the range of 600–800 °C with a wall jet [25, 27] and an impinging free-surface jet [37, 38] were experimentally studied. Wolf et al. [117] and Vader et al. [111] studied the boiling heat transfer during planar jet impingement under steady state heat transfer conditions. These studies provided an insight into the boiling phenomenon and also gave an estimate of the magnitude of heat transfer during boiling.

Auracher and co-workers [9, 98, 99] studied jet impingement heat transfer under steady state conditions. While Robidou et al. [98] investigated the wall temperature fluctuations in the various boiling regimes, Bogdanic et al. [9] performed measurements of two-phase structures in the jet stagnation region and for the first time reported the vapor thickness in the stagnation region of an impinging jet during film boiling.

Monde and co-workers [39, 50, 86–88, 122, 123] at Saga University (Japan) have recently made significant contributions to this subject. These studies were done on three different materials (copper, brass and carbon steel) with the initial temperature in the range of 250–600 °C. Using high speed visualization methods, the flow patterns during jet quenching were studied. Interesting insight into the wetting front region and wetting behavior of the surface were provided.

A full-scale pilot runout table facility exists at University of British Columbia (Canada) [69]. Top jet impingement [45, 78], bottom jet impingement [127] and multiple top jets impinging on a moving plate [30] were studied at the facility with plate temperature similar to that in plate mill.

1.4 Scope and outline of the present thesis

As stated earlier, the jet impingement boiling process is very complex and more insight into the physical phenomenon is essential for better mathematical description of the quenching process. Limited research has happened in this field and much more experimental research is necessary, especially for conditions similar to that in the aforementioned applications.

The aim of this work is to study jet impingement quenching of steel plates with conditions comparable to that encountered in the actual industrial applications. Using high resolution measurement techniques, more insight into the complex thermo-hydrodynamic phenomenon is to be gained. Along with this, the work includes the development of a high fidelity experimental database for validation of the results of mathematical modeling work being simultaneously performed at the Institute of Fluid Mechanics and Aerodynamics, Technische Universität Darmstadt.

This thesis is organized as follows:

Chapter 1: This introductory chapter describes the jet impingement quenching process occurring in the industrial applications. The boiling process occurring during this process is briefly introduced, following which a historical overview of the jet impingement quenching research is given. Finally, the scope and organization of the thesis are described.

Chapter 2: This chapter introduces flow boiling, with particular emphasis on the effect of flow on the bubble dynamics. The rewetting phenomenon, which is of particular interest in quenching studies, has been discussed at length. An extensive discussion on the research methodologies and key observations in jet impingement studies follows this section. The objectives of this thesis are presented at the end.

Chapter 3: The experimental setup has been described in this chapter, followed by the design of experiment.

Chapter 4: The inverse analysis model is described in this chapter followed by a note on the choice of appropriate model parameters. The uncertainties in the results are determined mathematically and are discussed in the next section.

Chapter 5: This chapter mainly focuses on the free-surface jet impingement quenching results. The observed hydrodynamics is described and quantitative assessments of splashed droplet velocity are made. Next the boiling heat transfer results are discussed. Few exploratory plunging jet impingement quenching experiments for determining the effect of spent coolant accumulation over the impingement surface have been performed; the results of these studies are reported in the last section.

Chapter 6: Concluding remarks from this study are given here. The open questions are outlined and an outlook for future studies is presented.

1.5 Closure

The need for thermal management of very hot metal parts has been the driving force for significant industrial development in the field of quenching technology. However, a need is felt for a science based approach to the design and control of these processes. With the advancement in measurement instrumentation, it is now possible to understand the complex processes happening during a quenching process. In this light, this chapter presented the motivation of the present work and established the need for research on the subject of jet impingement quenching. With this insight, the

state of the art on this subject will be reviewed in the next chapter and a critical assessment of the effectiveness of different experimental approaches adopted in previous studies will be made, with the aim to frame the objectives of the present research.

2

State of the Art

In Chapter 1, the quenching process and its requirements have been discussed in brief. A historical overview of the research relating to jet impingement quenching has also been presented. A more extensive discussion on the research methodologies and key observations of the previous studies is included in this chapter. This chapter has been divided into eight sections. The flow boiling phenomenon, with emphasis on the effect of the flow on the bubble dynamics during nucleate boiling, is described in the first section. In the second section, the rewetting condition, which determines the boundary size of the wetted zone, is discussed. In the following section, the thermohydraulics of jet impingement on surfaces with temperature less than the boiling point is briefly described. In the next section, the hydrodynamics of jet impingement quenching of very hot surfaces is discussed, thereby portraying the generally observed flow features. In the next section, a discussion on the measurement methodologies adopted in previous studies to estimate the quenching rates is presented along with a discussion on the shortcoming of each technique. In the sixth section, the jet impingement boiling heat transfer results from previous studies are discussed. Here, a comparison of reported influences of the flow and the thermal properties of the solid on the quenching heat transfer rate is presented. Thereafter, key inferences drawn based on the review of the state of the art are presented in the form of comments and the objectives of this thesis are outlined.

2.1 Flow boiling

Jet impingement quenching can be classified as a flow boiling process. A flow boiling phenomenon differs significantly from the pool boiling phenomenon owing to the forced convection effect of the flow. In this section, the key flow features of flow boiling are discussed. Specifically, the state of the art related to isolated bubble flow regime is presented. A schematic of the subcooled flow boiling region on a wall heated from beneath is shown in Fig. 2.1. In the subcooled region extending between positions A and B, the surface temperature, T_s , is sufficient to initiate and sustain nucleate boiling, while the temperature of the bulk liquid, T_L , remains below the saturation temperature,

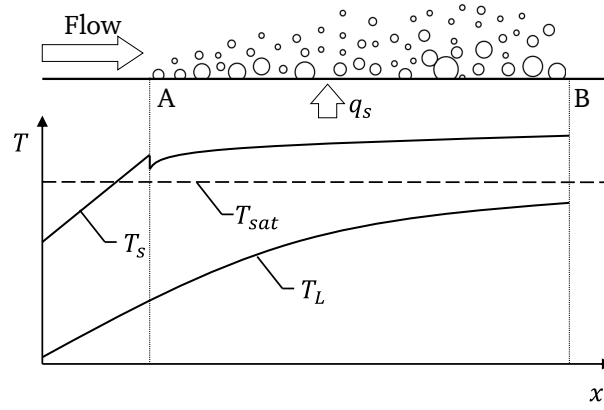


Figure 2.1. Subcooled flow boiling in a channel heated from beneath [106].

T_{sat} . Bubble dynamics is altered by the presence of a subcooled thermal boundary layer. This aspect of flow boiling is reviewed next.

Zeng et al. [126] hypothesized that the process of vapor bubble detachment in flow boiling evolves in three different stages, as schematically shown in Fig. 2.2. During stage I, the bubble nucleates and is thereafter pinned to its nucleation site. Due to the hydrodynamic forces, the bubble is inclined in the flow direction by an angle θ . Kandlikar et al. [53] also experimentally observed bubble inclination during stage I, with the inclination angle increasing with the liquid flow velocity. However, at higher flow rates, as the bubbles become smaller in size due to early removal, the surface tension force becomes dominant and the bubble retains its spherical shape [53]. At the end of stage I, the bubble starts to slide along the heated wall in an upright position ($\theta = 0^\circ$). During stage II, the bubble still keeps growing in size until it reaches a critical bubble volume, where the buoyancy force is sufficiently high to make the bubble lift-off from the wall. This marks the beginning of stage III. During stage III, the bubble condenses inside the subcooled bulk liquid and disappears.

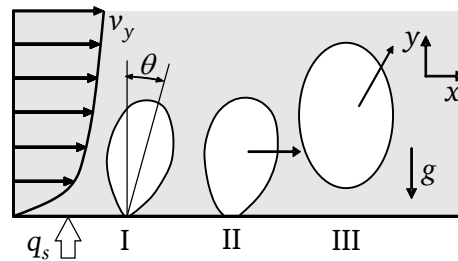


Figure 2.2. Three stages of vapor bubble departure from a surface in shear flow: (I) instant of departure from the nucleation site, (II) sliding bubble, and (III) lift-off (Adapted from [126]).

2.1.1 Stage I: bubble nucleation

During manufacturing, small cavities are formed on the surface of a metal part. When the surface is wetted, the liquid is unable to enter these cavities due to surface tension forces and gas gets trapped inside these cavities. Under suitable thermodynamic conditions, these cavities may serve as nucleation sites. The basis for analyzing nucleating characteristics of cavities in flow boiling has been

discussed by Kandlikar et al. [56]. Various relations for the range of active cavities in flow boiling are available [5, 17, 47] and these relations are based upon the condition that a vapor bubble would grow if the surrounding liquid temperature is equal to or more than the saturation temperature of the vapor inside the bubble, $T_{sat}(p_V)$.

$$T_{sat}(p_V) = T_{sat}(p_L) \cdot \left[1 + \frac{4 \cdot \sigma_L}{d_b \cdot \rho_V \cdot h_{fg}} \right]. \quad (2.1)$$

Kandlikar et al. [55] studied the nucleation characteristics of cavities on a polished aluminum surface in flow boiling of water at atmospheric pressure. Observations of nucleation activity were made using high speed photography with capture rates of up to 6000 frames per second. For subcooled flow boiling, the following observations were made:

- With the increase in flow velocity, surface temperature required to activate a cavity increased. This resulted in an increase in the onset of nucleate boiling temperature, $T_{s,ONB}$.
- With the increase in flow velocity, the range of active cavities shifted towards smaller sizes.
- As the surface superheat increased, smaller cavities were activated.

For subcooled flow boiling with velocity in the range of 0.47–0.77 m/s, subcooling of 40 K and a surface superheat of ≤ 8 K, they observed that the active cavity radius was in the range of 2–5.8 μm . Kandlikar et al. [56] numerically simulated liquid flow around a nucleating bubble and found that the streamline at $0.55 \cdot d_b$ swept over the bubble. With the receding contact angle, ϕ_r , as a variable, they derived the following equation for the range of active cavity size.

$$\{r_{c,min}, r_{c,max}\} = \frac{\Delta_t \cdot \sin \phi_r}{2.2} \cdot \frac{\Delta T_{sup}}{T_s - T_L} \cdot \left[1 \mp \sqrt{1 - \frac{9.2 \cdot \sigma_L \cdot T_{sat}(p_L) \cdot (T_s - T_L)}{\rho_V \cdot h_{fg} \cdot \Delta_t \cdot \Delta T_{sup}^2}} \right]. \quad (2.2)$$

This equation also provides the lower limit of surface superheat, ΔT_{sup} , required to nucleate a cavity in subcooled flow boiling.

2.1.2 Stages II and III: bubble detachment from cavity, lift-off and condensation

An important aspect of flow boiling is the sliding of bubbles on the wall before lift-off, i.e. stage II described in Fig. 2.2. Figure 2.3 shows a schematic of a bubble growing on a heated surface in the presence of shear. The bubble would be acted upon by various forces, which can be resolved in

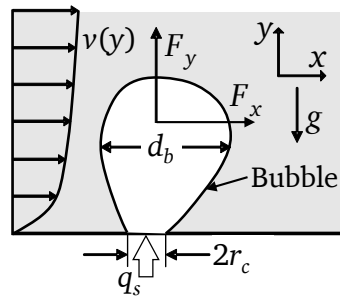


Figure 2.3. Forces on a vapor bubble growing in shear flow (adapted from [58]).

components parallel (x -direction) and normal (y -direction) to the heated surface [58]. The forces on the bubble are:

$$\sum F_x = F_{s,x} + F_{qs} + F_{du,x}, \quad (2.3)$$

$$\sum F_y = F_{s,y} + F_{du,y} + F_{sl} + F_b + F_h + F_{cp}, \quad (2.4)$$

where F_s is the surface tension force, F_{qs} is the quasi-steady drag in the flow direction, F_{du} is the unsteady drag due to asymmetrical growth of the bubble and dynamic effect of the unsteady liquid flow, F_{sl} is the shear lift force, F_b is the buoyancy force, F_h is the hydrodynamic pressure, and F_{cp} is the contact pressure with a wall. Detailed mathematical formulation of the various forces is presented by Klausner et al. [58]. They showed that the shear force has a major influence on the growth and detachment of the bubbles on the wall. Depending on the liquid flow, the following three scenarios may exist:

1. $\sum F_x = 0$ and $\sum F_y = 0$: The bubble remains attached to the nucleation site, i.e. stage I;
2. $\sum F_x > 0$ and $\sum F_y = 0$: the bubble will slide along the hot surface before lifting off, i.e. stage II;
3. $\sum F_x = 0$ and $\sum F_y > 0$: the bubble will lift-off from the hot surface without sliding, i.e. stage III.

Experimental evidence of the hypothesis by Zeng et al. [126] was presented by Bibeau and Salcudean [8]. Bubble activity was visualized during subcooled ($\Delta T_{sub} = 10\text{--}60$ K) boiling of water at flow velocity ranging from 0.08 to 1.2 m/s. Their experiments revealed two phases in a bubble cycle: (1) bubble sliding phase that starts immediately after the bubble inception at nucleating cavity, and (2) bubble ejection phase that leads to a normal detachment of the bubbles from the hot surface and subsequent collapse in the cooler bulk fluid. The two phases of a bubble cycle are shown in Fig. 2.4. During the sliding phase, the bubble first grows to its maximum diameter, $d_{b,max}$, after which the bubble changes from a flattened shape to an inverted pear shape. After ejection, the bubble condenses rapidly in the liquid bulk.

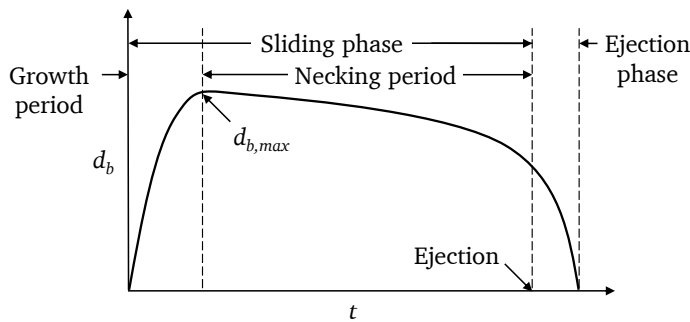


Figure 2.4. Schematic of the bubble ebullition cycle observed in [8].

Similar to the observations of Bibeau and Salcudean [8], Prodanovic et al. [96] also observed a two-phase bubble cycle at pressure of 1.05 to 3 bars, subcooling of 10 to 30 K and bulk liquid velocity ranging from 0.08 to 0.8 m/s. They reported that at low heat flux, nearly spherical bubbles were observed. These bubbles slid along the wall, occasionally detaching from the wall and then reattaching soon after. At much larger subcooling, the bubbles grew and collapsed while sliding along the wall, but never left the wall [103].

Cornwell and Schüller [16] showed that sliding bubbles can cause enhancement of heat transfer due to microlayer evaporation process. Tsung-Chang and Bankoff [110] presented an analysis for heat transfer with a moving bubble at constant wall temperature, and showed that the formation of a fresh microlayer at the foot of the moving microlayer can lead to more than 2 times increase in heat transfer compared to a stationary bubble's continuous microlayer. They also commented that under large subcooling, the microlayer evaporation process could become an important contributor to the heat transfer. Houston and Cornwell [46] and Thorncraft and Klausner [108] suggested that sliding bubble induces bulk liquid turbulence, which also contributes significantly to the macroscale heat transfer.

Situ et al. [104] studied flow boiling of water at atmospheric pressure and flow velocity of 0.5 m/s, but at low subcooling of up to 6.6 K. They observed that the bubble dynamics varied over time. Some bubble would collapse before departing from the nucleation site, some would slide before lift-off, while some would directly lift-off from the nucleation site. Moreover, the bubble frequency varied over the measurement period. They believed that the liquid superheat close to the heated surface does not remain stable. Del Valle and Kennings [19] observed that the activation of nucleation sites does not proceed in a regular manner with surface superheat. Some cavities which are active at low heat flux become inactive at higher heat flux, but some of these again become active at a still higher heat flux. Klausner et al. [58] expressed the bubble growth and departure during saturated flow boiling in terms of probability density function. Based on the observations in [19, 58, 104], it can be concluded that the bubble dynamics during flow boiling is rather chaotic, which might be partially responsible for the stochastic nature of flow boiling.

2.1.3 Quantitative assessment of bubble dynamics in flow boiling

Using an analytical force balance model, Klausner et al. [58] showed that increase in lift force due to shear and drag, reduces bubble departure diameter during saturated flow boiling. The bubble size and lifetime decrease with the increase of flow velocity, subcooling and heat flux [8, 35, 58, 96, 106, 126]. To show the strong effect of heat flux on the bubble diameter and lifetime, a typical result of Prodanovic [96] is replotted in Fig. 2.5(a). The bubble population increases strongly as the burnout/CHF condition is approached [3, 19]. Kandlikar et al. [54] observed that the bubble growth rate and frequency increases sharply with surface superheat. In Fig. 2.5(b), replotted from Kandlikar et al. [56], it can be seen that the bubble lifetime reduces from 130 ms to 5 ms with just 1.5 K increase in the surface superheat. Further, when the surface superheat increases to around 10 K, the bubble growth period reduces to less than 2 ms. Kandlikar et al. [54] commented that at very large superheat, camera frame rate of the order of 10^3 frames/s might be insufficient to capture a bubble lifetime. Consequently, flow boiling with large subcooling and velocity may appear as bubbleless.

Del Valle and Kennings [19] reported mean bubble lifetime and diameter of 0.2 ms and 0.4 mm, respectively, during boiling of water at atmospheric pressure and at liquid velocity of 1.7 m/s, subcooling of 84 K and 95% of CHF. Kandlikar et al. [54] examined bubble growth at high shear rates inside a rectangular channel of 3 mm height (Reynolds number as high as 5160) and at surface superheat of up to 20 K. They reported that the bubble departure diameter decreased with the increase in near-wall shear rates and was less than 60 μm at the highest Reynolds number of their study. Mean

bubble lifetime and diameter of 0.3 ms and 0.38 mm, respectively, in a flow with velocity of 3 m/s and subcooling of 72 K have been reported elsewhere [103].

In all the above mentioned studies on single bubble dynamics in flow boiling, the shear rates are at least an order of magnitude lower those that encountered in jet impingement quenching. As mentioned earlier, a high shear rate has a major influence on the growth and detachment of the bubbles on the wall. Omar et al. [91] examined bubble dynamics during nucleate boiling in the jet stagnation region of a planar water jet impinging with a velocity of 0.75 m/s and subcooling of 10 K. At a surface superheat of 15 K, the mean bubble diameter is reported to be in the range of 0.1 to 0.4 mm. Even though the velocity and subcooling are much lower in their study as compared to that in the study of Del Valle and Kennings [19], the bubble departure diameters are comparable. Thus, it is expected that the bubbles in jet impingement quenching will be much smaller than that observed in flow boiling inside channels. Further, with increase in the subcooling and impingement velocity, the departure diameters are expected to be significantly smaller than that measured by Omar et al. [91].

2.1.4 Summary

Based upon the above review of the state of art, the following can be concluded about the subcooled flow boiling process.

1. The bubbles slide on the wall before departing.
2. The microlayer evaporation process is enhanced due the bubble sliding phenomenon.
3. The bubble departure diameter and lifetime strongly reduce with increase in flow velocity, shear rates, subcooling, heat flux and superheat.
4. It is expected that the bubble departure diameter and lifetime are smaller in jet impingement flow than in flow boiling inside channels.
5. The bubble dynamics is rather chaotic and might be partially responsible for the stochastic nature of flow boiling.

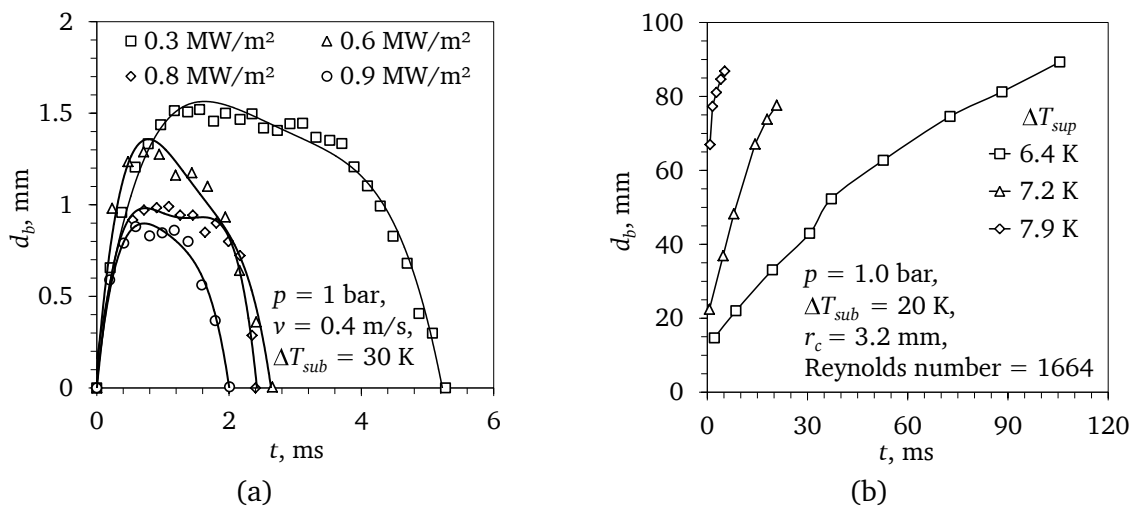


Figure 2.5. Effect of (a) heat flux [96] and (b) surface superheat [56] on bubble growth.

2.2 Rewetting process

In Section 1.2, the four regimes typically occurring during the quenching of a hot metal part in liquid have been briefly described. It is obvious from the description of the transient cooling process that rapid cooling occurs once the surface of the metal part cools down to the rewetting temperature, $T_{s,rewet}$. This condition is discussed in details in this section.

Leidenfrost effect is a phenomenon occurring when a volatile droplet is brought into contact with the upward facing face of a wall whose temperature is much above the liquid's saturation temperature. It is observed that drop does not touch the wall but is levitated on a vapor film, and that the droplet takes appreciable time to evaporate. A lower threshold temperature exists for this phenomenon to occur, below which the evaporation rate is insufficient to sustain a stable vapor film and the drop would touch the wall and evaporate rapidly. This threshold is classically referred to as the *Leidenfrost temperature* [7]. However, the minimum heat flux point temperature observed in the boiling curve, e.g. in the schematic boiling curve in Section 1.2 and in other boiling situations, has also been referred to as the Leidenfrost temperature (for pool boiling in [4] and for emergency reactor core cooling by falling water film and bottom reflooding in [23]).

In flow boiling, the term *Leidenfrost temperature* is not well defined. Terms such as rewetting, sputtering, quenching, calefaction or minimum film boiling temperature have been used interchangeably in the literature [15]. These terms, however, are not exactly synonymous as the causal mechanism for re-establishment of liquid-wall contact may differ based on the flow situation. Two approaches have been suggested for the estimation of this condition, namely, hydrodynamics-based and thermodynamics-based approaches. The hydrodynamic approach holds that the liquid-vapor interface remains separated from the wall only as long as the vapor generation rate is adequate to maintain a stable vapor film. As per this theory, hydrodynamic instabilities of the liquid-vapor interface cause rewetting. Based on this approach, Zuber [128] derived an expression for minimum film boiling heat flux for saturated pool boiling on a large horizontal surface. The formulation of Zuber was extended to determine the minimum heat flux temperature for saturated pool boiling on a large horizontal surface [15]. On the other hand, the thermodynamic approach holds that the maximum metastable liquid temperature is a thermodynamic property, and liquid can not exist beyond this temperature. If the liquid-wall interface temperature established by the sudden contact equals or exceeds this temperature, the vapor-liquid-solid triple interface can not form as the liquid will be repelled from the wall due to homogeneous nucleation. Thus, this liquid-wall interface temperature is the Leidenfrost temperature or the minimum heat flux temperature [50]. Chung and Lee [15] have compiled the experimentally determined minimum heat flux temperature data from many sources and have shown that these values deviate considerably from the predictions made using the above two approaches. A comprehensive review of the rewetting condition for quenching of the core of a light water reactor by bottom reflooding post-loss-of-coolant-accident is presented by Carbajo [11].

Filipovic et al. [27] defined two temperatures to quantify the rewetting condition because a local minimum corresponding to the change from film boiling to transition boiling is never seen in the boiling curve obtained from transient cooling measurements. They stated that apparent rewetting temperature, also referred to as the quench temperature in [34], corresponds to the onset of rapid surface cooling, while the rewetting temperature corresponds to the establishment of vapor-liquid-solid triple interface. Mathematically, the apparent rewetting temperature is the intersection point

of the tangent to the quenching curve at its point of largest slope with the tangent to the portion of the curve representing cooling before wetting occurs, i.e. film boiling. Downstream of the location of apparent rewetting temperature, wall is unaffected by heat conduction to the wetted region. The rewetting temperature is defined as the point of intersection of the tangent line to the quenching curve at its point of largest slope with the tangent to the inflection point of the quenching curve. However, Filipovic et al. [27] found that determining these informations from the quench curve may be cumbersome and error prone; hence an alternative procedure has been described in [27], which has been shown to relate closely with the before stated mathematical definitions. They found that, for the conditions of their study, the apparent rewetting temperature was always 30–40 K higher than the rewetting temperature.

Regarding the terminology used to refer the rewetting phenomenon in flow boiling, the rewetting temperature, Leidenfrost temperature, minimum film boiling temperature, etc. may be considered appropriate to define the rewetting condition. Moreover, as is shown by Filipovic et al. [27], the apparent rewetting temperature is very close to the rewetting temperature; therefore, experimentally determined rewetting conditions, including the apparent rewetting temperature, for various flow boiling situations reported in literature have been compiled in Table 2.1. Remarks have been added in the table, where the procedure to determine the rewetting condition is stated. As can be seen, the rewetting temperature is much higher than that for the saturated pool boiling of water at atmospheric pressure (about 245 °C), and even much higher than the critical temperature of water ($T_{cr} = 373.95$ °C). Carbejo [11] suggested that although the liquid temperature can not exceed the T_{cr} , the solid surface can. Assuming the solid and the liquid as semi-infinite slabs and the interface temperature equal to T_{cr} , Carbejo [11] suggested the following expression for the solid surface temperature or the rewetting temperature, $T_{s,rewet}$.

$$T_{s,rewet} = T_{cr} + (T_{cr} - T_L) \cdot \sqrt{\frac{(\lambda \cdot \rho \cdot c)_L}{(\lambda \cdot \rho \cdot c)_T}}. \quad (2.5)$$

From the above expression, it can be easily understood that steel will have higher $T_{s,rewet}$ than copper. For example, using Eq. (2.5) for water at 20 °C on stainless steel, rewetting temperature is 447 °C. If copper is the material, instead of stainless steel, $T_{s,rewet}$ is 389 °C. Besides this, $T_{s,rewet}$ will increase with liquid subcooling. Further, Carbejo [11] states that the above equation is true only for non-flow situations, and the $T_{s,rewet}$ is higher in flow situations than under non-flow situations. Accounting for the effect of flow rate, subcooling, pressure, liquid and solid material properties and surface condition, a correlation for estimating $T_{s,rewet}$ has been proposed by Carbejo [11]. Carbejo reported that $T_{s,rewet}$ estimates for bottom reflood conditions using the proposed correlation were in good agreement with the available data in literature.

For a wall jet, Filipovic et al. [27] found that their estimated rewetting temperatures deviated considerably from values calculated from the correlation by Carbejo [11], with the underprediction decreasing along the flow direction. The likely reason for the disagreement is that the flow velocity is typically two orders of magnitude higher in jet impingement quenching compared to bottom reflood condition, due to which rewetting is possible at much higher wall temperature.

Author(s)	Process	Material	T_I [°C]	$\Delta T_{sub}, l, v$	$T_{s,rewet}$ [°C]	Remarks
Ishigai et al. [49]	PJI	AISI 304	1000	5–55 K, 6.2 mm, 0.65–3.2 m/s,	245–1000♣	As v_J and ΔT_{sub} decrease, $T_{s,rewet}$ for the impingement region approaches $T_{s,rewet}$ for saturated pool boiling
Dhir et al. [21]	BRF	Zr	1127	50K–75 K, 1–30 cm/s	350–700◇	$T_{s,rewet}$ increases with v and ΔT_{sub}
Filipovic et al. [27]	WJ	Cu	750	45–75 K, 2–4 m/s	400–725♣	$T_{s,rewet}$ is 30–40 °C less than the apparent rewetting temperature. It decreases in the flow direction
Hall [36]	CJI	Cu	650–800	75 K, 5.1 mm, 2–4 m/s	150–450♣	
Elias et al. [24]	BRF	Zr	1600	10 K, 1.5 cm/s	≈ 527 ◇	
Liu and Wang [73]	CJI	AISI 316	1000	5–45 K, 10 mm, 1–3 m/s	300–1000♣	$T_{s,rewet}$ for the stagnation region increases with v_J and ΔT_{sub}
Robidou et al. [98]	PJI	Cu	Steady state	16 K, 1 mm, 0.8 m/s	450♣	$T_{s,rewet}$ is for a distance up to $3l$ from the stagnation line
Liu et al. [71]	CJI	CS, AISI 316	900	70–87 K, 18.9–30 mm, 5.6–6.5 m/s	900◇	$T_{s,rewet}$ at $r = 0$ mm
Zhang [127]	CJI	CS	850	60 K, 20 mm, 2.3 m/s	450–850♣	$T_{s,rewet}$ decreases with r
Juarsa et al. [51]	BRF	AISI 304	400–600	70 K, 20 mm, 0.7–2 cm/s	408–578♣	$T_{s,rewet}$ increases with v
Gradeck et al. [33]	CJI	Ni	450	80 K, 9 mm, 1.4 m/s	325–450◇	
Islam et al. [50]	CJI	CS	500	20 K, 2 mm, 5 m/s	474♣	
Gradeck et al. [32]	PJI	Ni	≈ 600	15 K, 4 mm, 1.2 m/s	580◇	Curved impingement surface

♣: Minimum film boiling point temperature, ◇: Apparent rewetting temperature, ♣: Rewetting temperature.
 l is the characteristic dimension, e.g. d_J or d_N for circular jet impingement, w_J or w_N for planar jet impingement, channel gap for bottom reflooding.

Table 2.1. Compilation of reported rewetting condition during quenching with flowing water at atmospheric pressure (arranged chronologically).

Islam et al. [50] have proposed a possible mechanism to explain the high heat transfer when liquid is in contact with a surface that is at a temperature higher than the thermodynamic limiting temperature. They hypothesized that long dry periods are interrupted by short intermittent periods of liquid-wall contacts; these contacts lead to homogeneous nucleation and heat transfer to the subcooled liquid. With decreasing surface temperature, such contacts become more frequent and the heat transfer increases.

2.3 Fundamentals of jet impingement heat transfer

The main focus of this thesis is to understand the heat transfer process during jet impingement quenching of large steel plates. Hence, the state of art related to jet impingement quenching will be

discussed in this section. Before that it is essential to understand the basics of jet impingement on an unheated surface.

2.3.1 Jet impingement hydrodynamics on an unheated surface

The jet impingement configurations are categorized as: free-surface jet, plunging jet, submerged jet, confined jet and wall jet [116]. Free-surface and plunging jet impingement configurations are commonly encountered in the aforementioned applications; the schematics of these two impingement configurations are shown in Fig. 2.6. Free-surface jet impingement is encountered when the jet impinges on a plate unrestricted by any containing walls on the sides, while plunging jet impingement configuration is observed when the jet impinges on to a pool of the same liquid accumulated on the plate. Free-surface jet impingement configuration is true during the early stages of cooling of large plates, while the plunging jet impingement configuration is true once the liquid starts to accumulate on the top surface of the plate.

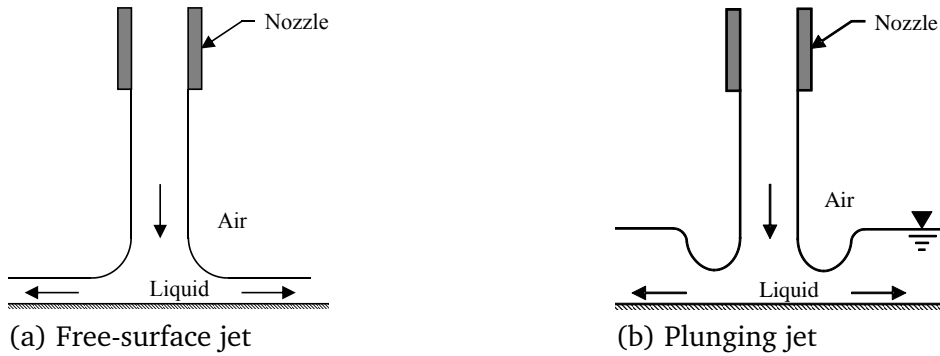


Figure 2.6. Schematic of jet impingement configurations relevant to this study.

Upon impingement, the flow is deflected by the wall and thereafter is made to flow parallel to the wall. Due to this diversion, the flow velocity and pressure distribution within the flow varies along the wall. These flow regions for a free-surface jet are schematically shown in Fig. 2.7. The inviscid pressure and streamwise velocity distributions for free-surface jet impingement with uniform velocity profile at the nozzle exit are also shown. The flow can be demarcated into three regions, depending on the pressure and velocity distribution, namely: *stagnation region* (A), *acceleration region* (B) and *radial flow region* (C). The pressure is maximum at the stagnation point (i.e. $r = 0$) and decreases monotonically away from it. The stagnation region coincides with the impinging jet and the streamwise velocity within this region increases almost linearly with radial distance from the stagnation point. The flow continues to accelerate in the acceleration region until its free-surface velocity approaches the jet velocity at the end of the acceleration region. Combined together, the stagnation and acceleration regions are referred to as the *impingement region*. In the radial flow region, the velocity decreases with radial distance from the stagnation point due to radial spread of the flow but no pressure gradient exists.

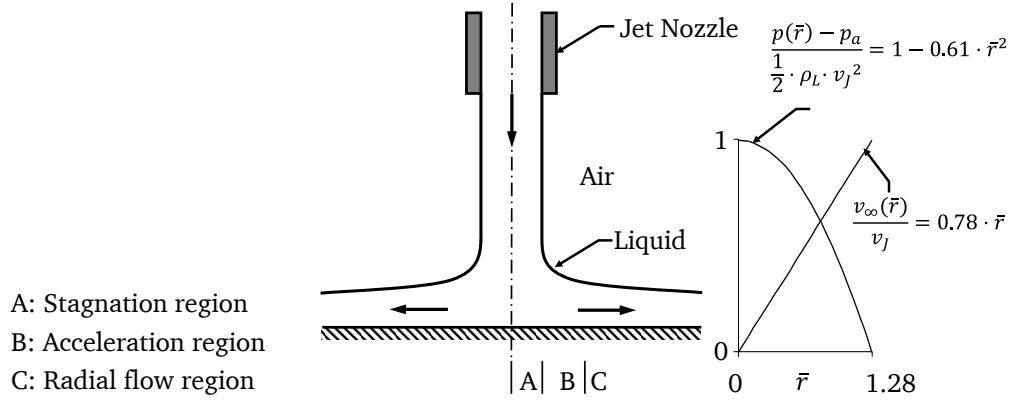


Figure 2.7. Schematic of a circular free-surface jet impingement showing the three flow regions along with the inviscid pressure and velocity distributions within the impingement region. These distributions are based on the equations for single-phase flow [60].

Watson [114] applied a similarity transformation to solve the boundary layer equations for the case of a circular laminar free-surface jet impinging over a horizontal surface and derived expression for liquid film thickness in the radial flow region. The liquid film thickness can be determined as

$$\bar{\delta}_f(\bar{r}) = \frac{0.125}{\bar{r}} + \left(\frac{\bar{r}}{\text{Re}_J} \right)^{1/2} \quad \text{when } \bar{r} \leq 0.183 \cdot \text{Re}_J^{1/3}, \quad (2.6a)$$

$$\bar{\delta}_f(\bar{r}) = \frac{0.1735}{\bar{r}} + \frac{4.82 \cdot \bar{r}^2}{\text{Re}_J} \quad \text{when } \bar{r} > 0.183 \cdot \text{Re}_J^{1/3}, \quad (2.6b)$$

where $\bar{r} = r/d_J$. The average liquid film velocity can be calculated as

$$v_f(\bar{r}) = \frac{v_J}{8 \cdot \bar{r} \cdot \bar{\delta}_f}. \quad (2.7)$$

The impingement phenomenon for plunging jet differs from free-surface jet due to the momentum exchange between the pool and the jet. The jet decelerates as it passes through the pool and expands radially prior to impingement. The jet flow in the pool leads to formation of a recirculation pattern in the pool, which advects the hot liquid away from the surface and replaces it with the colder fluid from the bulk of the pool [48]. The jet also entrains the surrounding air into the pool, which influences the heat transfer rate.

2.3.2 Single-phase jet impingement heat transfer

Single-phase jet impingement cooling regime occurs when the surface temperature is below the temperature required for vapor bubble nucleation, i.e. $T_s < T_{s,ONB}$. In this regime, the heat transfer rate is governed by the Newton's law of cooling.

$$q_s = h_s \cdot (T_s - T_L). \quad (2.8)$$

As stated in the previous section, the liquid hydrodynamics varies over the surface; as a result, the heat transfer coefficient is not uniform over the surface. Ma et al. [75] obtained an integral solution for the heat transfer in the boundary layer. They categorized the flow domain into four regions

based upon the relative thicknesses of liquid film, viscous boundary layer and thermal boundary layer (Fig. 2.8). For a laminar jet impinging on an uniformly heated flat surface, the following formulas for the Nusselt number distribution, $Nu_J = hd_J/\lambda_L$, have been derived .

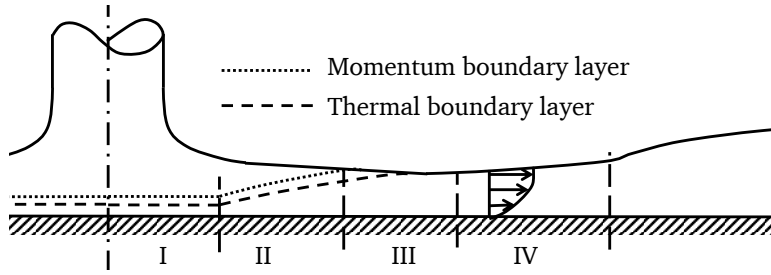


Figure 2.8. Development of viscous and thermal boundary layers on an uniformly heated flat surface (adapted from [68]). Based upon the relative size of the liquid film and the boundary layers, four heat transfer regions can be identified in the schematic.

Region I (Impingement region, $0 \leq \bar{r} < 1$)

$$Nu_J = 0.7212 \cdot Re_J^{1/2} \cdot Pr_L^{0.4} \text{ when } 0.7 \leq Pr \leq 3, \quad (2.9a)$$

$$Nu_J = 0.7212 \cdot Re_J^{1/2} \cdot Pr_L^{0.37} \text{ when } 3 \leq Pr \leq 10. \quad (2.9b)$$

Region II ($1 \leq \bar{r} < 0.1773 \cdot Re_J^{1/3}$)

In this region, both the thickness of the viscous and thermal boundary layers are less than the liquid film thickness.

$$Nu_J = 0.668 \cdot Re_J^{1/2} \cdot Pr_L^{1/3} / \bar{r}^{1/2}. \quad (2.10)$$

Region III ($0.1773 \cdot Re_J^{1/3} \leq \bar{r} < 0.5554 \cdot Re_J^{1/3} / (50 - 5.147 \cdot Pr_L)^{1/3}$)

In this region, the thickness of the viscous boundary layer is equal to the film thickness but the thermal boundary layer is still smaller than the liquid film.

$$Nu_J = 1.5874 \cdot Re_J^{1/3} \cdot Pr_L^{1/3} \left(25.735 \cdot \frac{\bar{r}^3}{Re_J} + 0.8566 \right)^{-2/3}. \quad (2.11)$$

Region IV ($\bar{r} > 0.5554 \cdot Re_J^{1/3} / (50 - 5.147 \cdot Pr_L)^{1/3}$)

In this region, both the viscous and the thermal boundary layers have reached the liquid free-surface.

$$Nu_J = \left(\frac{4 \cdot \bar{r}^2}{Re_J \cdot Pr_L} + C \right)^{-1}, \quad (2.12)$$

where

$$C = \frac{2.67 \cdot r^2}{Re_J} + \frac{0.089}{\bar{r}}. \quad (2.13)$$

The local Nusselt number predictions from above equations agree well with the experimental data of Stevens [31] (in Fig. 2.9). It is can be seen that the heat transfer coefficient is highest in the impingement region, outside which it reduces considerably. The large pressure gradient within the

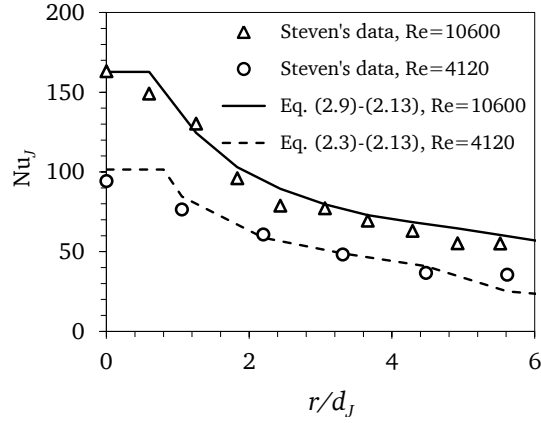


Figure 2.9. Comparison of the local Nusselt number predicted using the model by Ma et al. [75] with the experimental data by Stevens [31]).

stagnation region along with the higher velocity contribute to the enhancement in the heat transfer rate.

The Reynolds number range for the above given Nusselt number equations are not given by Ma et al. [75]. Similar correlation for the Nusselt number are given by Liu et al. [68]; they have shown that the correlation agrees well with their experimental data only when $Re_J \geq 25000$, below which the disagreement is significant and the applicability of these equations is doubtful.

2.4 Hydrodynamics of jet impingement quenching

The flow patterns observed when a subcooled free-surface jet impinges on the flat face of a metal plate heated to a temperature that is high enough to prohibit direct liquid contact with its surface are described in this section. The observations discussed here correspond to an initial plate temperature of about 900 °C. A schematic arrangement of a circular free-surface jet impinging on the top flat surface of a steel plate is shown in Fig. 2.10. All faces of the cylinder, except the impingement surface, are adiabatic. The flow patterns depend on the orientation of the jet with respect to the gravity vector, but here the general observations, combining observed flow patterns during free-surface jet impingement on an upward and a downward facing surface, are presented.

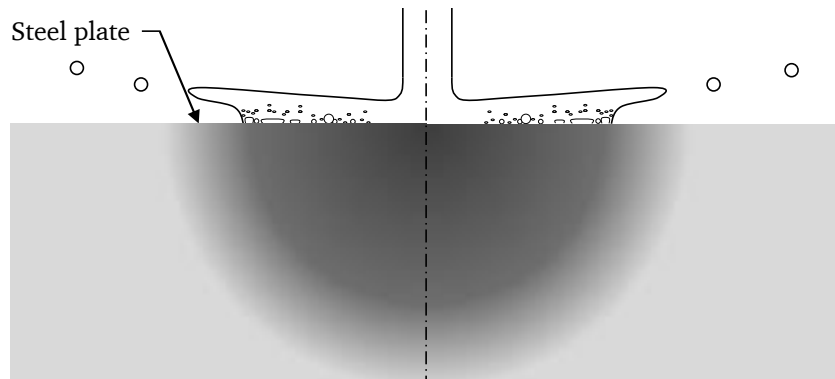


Figure 2.10. Schematic of a hot steel plate quenched by an impinging circular free-surface jet.

Since the initial high wall temperature makes it difficult for the liquid to wet the plate surface, immediate wetting of the impingement surface upon impingement may not happen. As soon as the jet strikes the hot surface, a vapor cushion is formed in the jet impingement region and stable film boiling occurs. Ishigai et al. [49] reported that during film boiling in the jet stagnation region, the impingement face is visible through the liquid and the vapor film, and the liquid-vapor interface is smooth. Brief solid-liquid contact may occur at the start of quenching; bubbles would then form, coalesce and make the jet slide over it, resulting in a shiny mirror-like flat liquid sheet [50]. The flat sheet breaks into droplets at its edges. Piggot [95] mentioned that the geometric limit of the sheet is set by a balance of fluid inertia and surface tension forces at the edge. Hall et al. [37] also reported similar flow patterns. The stable film boiling is reported to be quite [49, 50, 95]. A schematic depicting the possible flow pattern is shown in Fig. 2.11(a). Bogdanic et al. [9] measured the void fraction distribution under an impinging jet under steady state conditions and reported that intermittent wetting does not occur during the stable film boiling in the jet stagnation region. In their steady state experiments, Robidou et al. [99] observed no significant temperature fluctuations during stable film boiling in the jet stagnation region, which is in agreement with the measurements of Bogdanic et al. [9]. Visual and acoustic observations reported in other studies [1, 37, 49, 50, 95] provide enough evidence of the presence of stable film boiling in the jet stagnation region, though heat transfer measurements performed during transient quench tests have not revealed any evidences of stable film boiling in the stagnation region. During film boiling, heat is extracted from the impingement region and the surface temperature of the plate reduces. The film boiling duration depends on the jet velocity and subcooling, and on the thermal properties of the plate material. Mozumder et al. [86] reported that low conductivity metals, such as steels, are unable to conduct heat to the stagnation region quickly enough to sustain the high wall temperature necessary for stable film boiling, so the surface rapidly cools down and the vapor film collapses. Compared to steel, stable film boiling duration is longer for copper and brass. They showed that the duration of film boiling can be correlated with the thermal effusivity ratio of the plate material and the liquid $\sqrt{(\rho \cdot c \cdot \lambda)_T / (\rho \cdot c \cdot \lambda)_L}$.

At the end of film boiling, i.e. close to rewetting point, Robidou et al. [99] observed large surface temperature fluctuation due to a few intermittent liquid-wall contacts. Bogdanic et al. [9] reported that long periods of vapor near the wall are interrupted by a few short liquid contacts in the transition boiling regime close to the rewetting point. As the wall temperature decreases, a small wetted region is formed under the jet. Piggot et al. [95] suggested that transition boiling might occur in this wetted region. As the wall temperature decreases during transition boiling, the duration of vapor near the wall reduces, while the number and duration of liquid-wall contact increase [9]. Such intermittent contacts of liquid with the wall result in a sudden release of vapor, causing splashing of droplets away from the wall, as shown in Fig. 2.11(b).

As the surface temperature in the impingement region decreases further, complete wetting happens. Once wetted, the plate surface appears dark in color and this region has been referred to as the dark zone by Hatta et al. [42]. Since the heat transfer rate is considerably higher in the jet impingement region as compared to the radial flow region [131], the wetting remains restricted to a region approximately equal to the impingement region until the outside regions cools down by radial heat conduction to the wetted region. During this time, fully developed nucleate boiling and transition boiling exist at the edge of this wetted region (a region with finite width and called the *wetting*

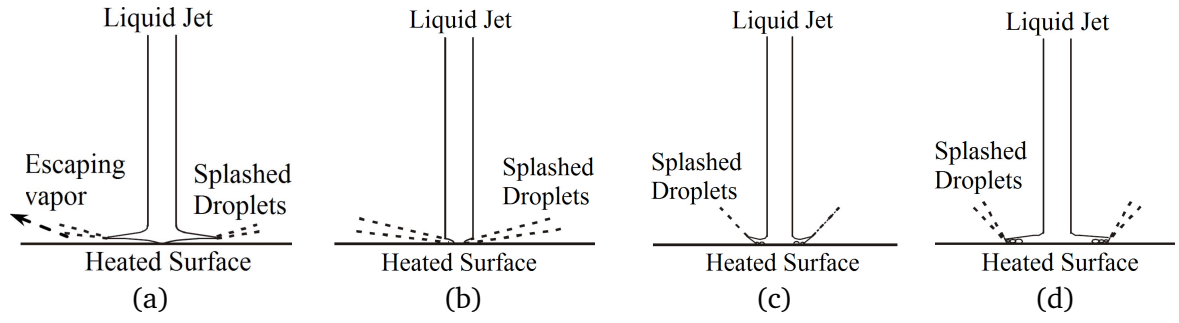


Figure 2.11. Schematic of observed flow patterns, with (a) to (d) arranged in the order of decreasing surface temperature (adapted from [50]).

front region) [39], and liquid is splashed away from the surface as a fine spray [50], Fig. 2.11(c). Depending on the thermal properties of the plate material, the wetted region can remain stagnant for few seconds to a few minutes [86]. This duration is called the *wetting delay*. It has been reported to be a function of the jet velocity, subcooling, initial plate temperature and thermal effusivity ratio of the plate material and the liquid $\sqrt{(\rho \cdot c \cdot \lambda)_T / (\rho \cdot c \cdot \lambda)_L}$ [86].

As the wall temperature around the wetted region reduces, the wetting region starts to grow in size with a wide wetting front region, Fig. 2.11(d). Maximum heat flux and transition boiling occur in the wetting front region, while partial nucleate boiling and single-phase forced convection heat transfer occurs in the wetted region [39, 87, 88, 123]. Film boiling occurs outside the wetting front region as the liquid flows over the surface as discrete drops, levitated by vapor and hot air. Slowly as the radial temperature distribution becomes less steep, the wetting front moves forward rapidly till the whole surface is completely wetted. Splattering sound is heard as the wetting front travels indicating the occurrence of transition boiling [122]. Longer wetting delay and higher radial heat conduction rates in case of copper compared to steel, result in a less steeper radial temperature distribution; hence the wetting front moves radially out much faster [86].

Due to the effect of gravity, some dissimilarities may exist between quenching the downward and the upward facing surfaces, however, the key flow features during quenching still remain the same.

2.5 Techniques for determining the heat transfer rate during quenching

As described in the previous section, many complex phenomena happen simultaneously during the quenching of a metal plate heated much above the liquid saturation temperature. Similar to the variation in hydrodynamics of the fluid with wall temperature at different radial positions, the heat transfer rate also varies significantly over the surface with time. In order to accurately measure the temporal variation of heat transfer distribution on the surface, various methods have been adopted by previous researchers. An overview of the measurement methods adopted by various researchers is being presented and reviewed. There are two widely accepted techniques to study boiling heat transfer: steady state measurement and transient measurement.

2.5.1 Steady state measurements

In steady state measurements, it is possible to study nucleate boiling and film boiling using heat flux controlled test specimen [111, 117], but a temperature-controlled test specimen is necessary to study the complete boiling curve [98, 99]. In a steady state experiment, instabilities occur in the system during the transition boiling regime owing to the negative slope of the boiling curve. To stabilize the system, a temperature feedback controlled heater was implemented by Robidou et al. [98]. In the test setup of Robidou et al. [98], the heat transfer surface is made from eight pieces of copper, each consisting of a separate and individually feedback controlled heater. Such implementations, though being suitable for studying the phenomenon, are quite different from the quenching process in the material processing and loss of coolant accident (LOCA) in the nuclear industry.

The heat flux in case of jet impingement quenching is typically around 10 MW/m^2 and maximum plate temperature is around $800\text{--}1000^\circ\text{C}$. Achieving such conditions is extremely difficult in a steady state measurement due to the unavailability of appropriate high temperature heaters. The maximum heat flux achieved by Wolf et al. [117] was around 7 MW/m^2 but the maximum surface superheat was only up to 40 K. Though Robidou et al. [98, 99] could reach surface superheat up to 400 K, but the maximum heat flux reached was less than 4.5 MW/m^2 . Since it is not possible to create realistic conditions as described above using steady state measurement systems, they are generally not preferred for investigating the jet impingement quenching process.

2.5.2 Transient measurements

Transient heat transfer measurements overcome the above described problems associated with steady state measurements, but the results have lower accuracy. The errors associated with the transient measurements are discussed later in this section.

A typical transient experiment involves heating a piece of metal to a high temperature and then exposing it to the coolant. The cooling proceeds at an uncontrolled rate, i.e. the cooling rate (in K/s) during the process is not constant but is determined by the conjugate interaction between the coolant and metal. In order to estimate the surface heat flux and temperature, thermocouples are located inside the metal plate close to the surface of interest [25, 36, 40, 45, 89, 127]. As the metal part cools down, the transient temperature distribution within the plate is measured by these thermocouples. The thermocouple temperature measurements can be then processed using inverse heat conduction method to estimate the surface temperature and heat flux [36, 40, 45, 89, 92, 127].

The transient experiments usually do not match the steady state measurements. In nucleate boiling, the transient heat transfer coefficients are generally found to be lower than those obtained under steady state conditions; the ratio of transient to steady state heat fluxes can be as low as 0.5 [22]. Dhir et al. [22] also mention that, although no quantitative basis exists in the literature for the estimation of the transient nucleate boiling curve from the steady state boiling curves, it is known that the magnitude of displacement of the boiling curve depends on the thickness and thermal properties of the metal. This finding means that the applicability of the results from steady state heat transfer measurements to the quenching process is severely restricted.

While the steady state measurements are not suitable to study the quenching phenomenon, the transient measurements are less accurate due to the non-uniqueness of the inverse heat conduction method. The following section discusses the non-uniqueness of inverse heat conduction solution.

2.5.2.1 The inverse heat conduction solution and its non-uniqueness

The generalized heat conduction equation for a rotationally symmetric cylindrical coordinate system is given as

$$\frac{1}{\alpha_T} \cdot \frac{\delta T}{\delta t} = \frac{1}{r} \cdot \frac{\delta}{\delta r} \left(r \cdot \frac{\delta T}{\delta r} \right) + \frac{\delta^2 T}{\delta z^2}. \quad (2.14)$$

For the case where the boundary conditions, initial condition and thermophysical property are specified, the problem defined by Eq. (2.14) is concerned with the determination of the temperature distribution $T(r, z, t)$ in the interior region of the solid. This is called the “direct problem” [92]. But if one or more of the boundary conditions are unknown and instead the measured temperatures at some interior points are available, then the problem given by Eq. (2.14) is concerned with the estimation of the unknown boundary condition. Such problem is called the “inverse problem”. In simple words, the direct problem is concerned with determining the effect due to a given cause, while the inverse method deals with estimating the cause by examining the effect. Since the measured temperature data used in the inverse heat conduction analysis contain measurement errors, the inverse heat conduction solution (i.e., the unknown boundary condition) is not exact. Therefore, Ozisik and Orlande [92] recommend the use of the terminology “estimation” in place of “determination”.

A major issue with the inverse heat conduction solution is its non-uniqueness [121]. For demonstrating this, the temperatures at the surface ($z = 0$) and at a depth of $z = 0.6$ mm are calculated by numerically solving the heat conduction equation for a 1 Hz sinusoidal surface heat flux variation given by Eq. (2.15) and a 1 Hz sinusoidal oscillating heat flux superimposed with a 100 Hz signal given by Eq. (2.16). The test specimen is a semi-infinite stainless steel plate ($\lambda_T = 21.9$ W/(m · K), $c_T = 640$ J/(kg · K) and $\rho_T = 7560$ kg/m³) with an initial temperature T_I of 1173.15 K.

$$q_s(t) = q_{s,max} \cdot \sin(2 \cdot \pi \cdot t). \quad (2.15)$$

$$q_s(t) = q_{s,max} \cdot [\sin(2 \cdot \pi \cdot t) + \sin(200 \cdot \pi \cdot t)]. \quad (2.16)$$

The variation of the temperature on the surface and at a depth $z = 0.6$ mm for the heat flux given by Eqs. (2.15) and (2.16) are shown in Fig. 2.12(a) and 2.12(b), respectively. It can be seen that while surface temperature oscillation varies with the change in the boundary condition, the temperature at a depth of $z = 0.6$ mm are identical in Figs. 2.12(a) and 2.12(b). This example demonstrates that different boundary conditions may lead to exactly the same time-temperature history at the measurement location inside the plate, and the resulting inverse heat conduction solution would be non-unique.

In order to mathematically describe the effect of the sensor distance from the boundary on the inverse heat conduction solution, the case of a semi-infinite solid whose boundary at $z = 0$ is subjected to a sinusoidal variation given in the following equation may be considered.

$$q_s(t) = q_{s,max} \cdot \sin(\omega \cdot t). \quad (2.17)$$

where $q_{s,max}$ and ω are the amplitude and angular frequency of oscillations for the heat flux, respectively, and t is the time variable. For a surface heat flux variation given by Eq. (2.17), the analytical solution for the temperature distribution at a depth z is given by Carslaw and Jaeger [12] as

$$T_z - T_I = \frac{q_{s,max}}{\lambda_T} \cdot \sqrt{\frac{\alpha_T}{\omega}} \cdot e^{-z \cdot \sqrt{\omega/(2 \cdot \alpha_T)}} \cdot \sin\left(\omega \cdot t - z \cdot \sqrt{\omega/(2 \cdot \alpha_T)} - \pi/4\right) - \frac{2 \cdot q_{s,max} \cdot \alpha_T}{\pi \cdot \lambda_T} \cdot \int_0^\infty \frac{-\omega \cdot \cos(u \cdot z)}{\omega^2 + \alpha_T^2 \cdot u^4} e^{-\alpha_T \cdot u^2 \cdot t} \cdot du. \quad (2.18)$$

From Eq. (2.18), the amplitude of the temperature oscillation is determined as

$$|\Delta T_z| = \frac{q_{s,max}}{\lambda_T} \cdot \sqrt{\frac{\alpha_T}{\omega}} e^{-z \cdot \sqrt{\omega/(2 \cdot \alpha_T)}}. \quad (2.19)$$

It can be seen that the amplitude of temperature fluctuation $|\Delta T_z|$ is attenuated with increasing depth of the sensor and increasing frequency by a factor of $\exp\left(-z \cdot \sqrt{\omega/(2 \cdot \alpha_T)}\right)$. This is specifically the reason why a 1 Hz disturbance is detected at a depth $z = 0.6$ mm in Fig. 2.12(a) but a 100 Hz disturbance is faintly detected in Fig. 2.12(b).

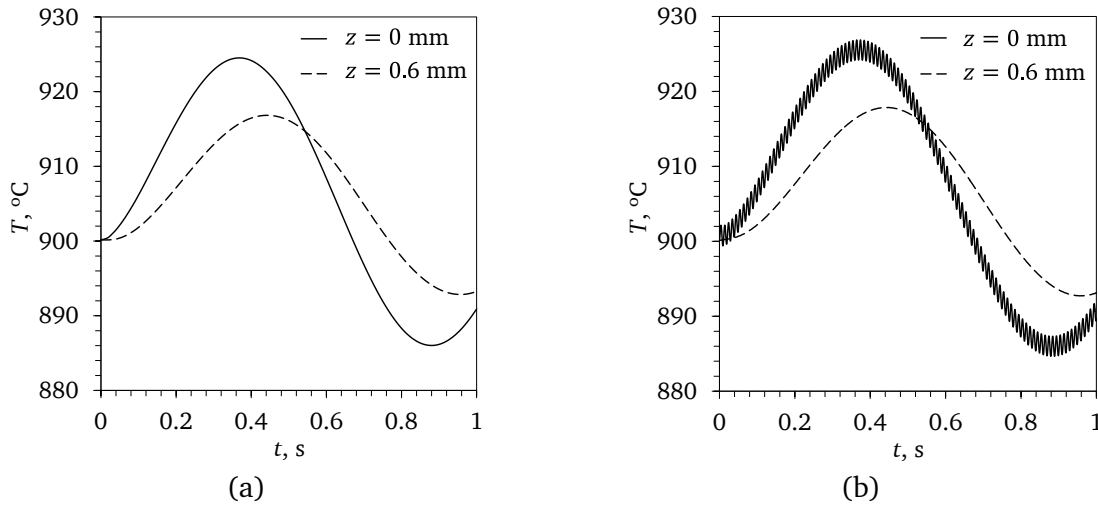


Figure 2.12. Temperature variation at the surface ($z = 0$ mm) and at a depth ($z = 0.6$ mm) for (a) a 1 Hz sinusoidal heat flux signal, and (b) a 1 Hz sinusoidal heat flux signal with a superimposed 100 Hz sinusoidal heat flux signal [63].

If an inverse heat conduction solution uses this time-temperature history in order to estimate the amplitude of the surface heat flux oscillation $q_{s,max}$, any measurement error on $|\Delta T_z|$ would be amplified by a factor of $\exp\left(z \cdot \sqrt{\omega/(2 \cdot \alpha_T)}\right)$. If the measurement error on $|\Delta T_z|$ becomes comparable to $|\Delta T_z|$, then it is impossible to determine if the estimated surface heat flux fluctuations are real or arising due to errors in the temperature measurement. Therefore, the inverse heat conduction solution is non-unique and is also susceptible to errors due to noise in temperature measurements.

In order to be able to estimate the boundary heat flux, a sensor must be located within a depth below the surface where the temperature oscillation due to the on-surface process is much more than the noise in the measurement. In many experimental designs, it is impossible to locate the

sensor very close to the surface of interest. Furthermore, in most cases, the time-temperature history is filtered and smoothed before performing the inverse heat conduction analysis in order to avoid spurious oscillations in the boundary condition estimations. This data manipulation limits the ability of the inverse heat conduction solution to estimate high frequency oscillations on the boundary.

Analogous to the case discussed above, short wavelengths in the radial direction are damped with the depth of the sensors away from the boundary. To elucidate this effect, consider the direct solution of the steady state heat conduction equation in Cartesian coordinate system when the surface is applied with a heat flux given as

$$q_s(x) = q_{s,max} \cdot \cos(2 \cdot \pi \cdot x/l). \quad (2.20)$$

where $q_{s,max}$ and l are the amplitude and wavelength of oscillations for the heat flux, respectively, and x is the space variable [121]. The solution of the heat conduction equation gives the temperature distribution at a depth z as

$$T_z - T_I = \frac{q_{s,max} \cdot l}{2 \cdot \pi \cdot \lambda_T} \cdot e^{-2 \cdot \pi \cdot z/l} \cdot \cos\left(\frac{2 \cdot \pi \cdot x}{l}\right). \quad (2.21)$$

Equation (2.21) shows that the magnitude of the fluctuation diminishes with depth in proportion to $\exp(-2 \cdot \pi \cdot z/l)$. Hence, short wavelengths may not be detected deep inside the solid. Besides this, if the wavelength in space is less than the sensor spacing, then the sensors cannot provide enough information about the heat flux distribution. In such a case, if an estimate of the wave amplitude is to be made, an assumption regarding the temperature distribution between the sensors has to be made. Different interpolation methods would lead to different inverse heat conduction solutions. Overall, it can be said that only large wavelength components are correctly estimated in the inverse heat conduction solutions.

The important conclusion that can be drawn here is that, due to non-uniqueness, all inverse heat conduction solutions will consist of low frequency and long wavelength components. The inverse heat conduction solution can also be seen as an average over a time interval defined as the *time resolution*, t_{res} , and over a spatial region defined as the *space resolution*, r_{res} .

2.5.2.2 Transient measurement setups

In order to estimate the boiling heat transfer with good space and time resolutions, Buchholz et al. [10] located fine thermocouples at a depth of 2.6 μm below the surface by spluttering a 2.5 μm copper layer on the embedded constantan wires. The thermocouples measurement locations were arranged in a 6×6 array spread over a $1 \times 1 \text{ mm}^2$ region. This approach would provide detailed information about the phenomenon, but can not be used for quenching studies because of the possibility of thermocouple damage due to differential thermal expansion of the various layers on the surface. Therefore, in all transient quenching studies, shielded thermocouples of diameter more than 0.5 mm are embedded in the plate in order to measure the temperature. Since the thermocouple can cause material inhomogeneity, they are located much below the surface. The thermocouple tip for jet impingement quenching studies are located in the range of 1 mm [124] to 2.1 mm [39]. In order to estimate the surface cooling rate during quenching, Hatta et al. [42] radially arranged 5 thermocouples on the back face of the 10 mm thick steel plate, with a radial

spacing of 20 mm between them. Similar experimental methods were adopted by the same authors in other studies [43, 44]. As has been discussed earlier, if the thermocouples are not close to the impingement surface or the thermocouples are not closely spaced, correct estimate of the surface heat flux and temperature distributions can not be made. It is easy to realize that these experiments would under-predict the heat transfer rates. As a result, these heat transfer measurements are not accurate and of doubtful useful. In other relevant studies, thermocouples with diameter of 1 mm or more are used. Larger thermocouples limit the minimum inter-sensor spacing or the pitch, which leads to poor space resolution in the measurements. Furthermore, bigger thermocouples have poor time response, which affects the accuracy of the boundary estimations. Woodfield et al. [123] simulated heat conduction due to a heat sink of constant width and a heat flux of 5 MW/m^2 with temperature measurements at depth of 2.1 and 5 mm from the surface and radially spaced by 5 mm. They compared the inverse heat conduction solution with the exact result. The result for different heat sink width are shown in Fig. 2.13. The heat flux for a heat sink width of less than 10 mm was underestimated. A combined effect of large sensor depth and sensor radial spacing led to a poor spatial resolution in their study.

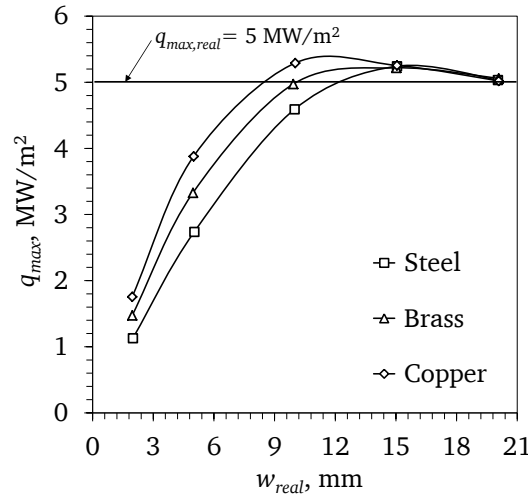


Figure 2.13. Effect of source width on heat flux estimation for three different materials with two rows of sensors at depths of 1.9 and 5 mm below the surface and a radial pitch of 5 mm [123].

It is clear that the heat transfer estimates for transient heat transfer measurements are prone to measurement errors, and accurate location of thermocouples as close as possible to the surface and close to each other is the key to a successful experiment. The previous experimental studies would be critically examined hereon from the inverse heat condition analysis perspective and the limitations of their studies would be stated thereof.

2.6 Jet impingement quenching heat transfer

First, the results from steady state measurement would be discussed, as they are more accurate. Next, the results of transient measurements would be discussed and also compared with the steady state measurement.

2.6.1 Steady state measurement results

Robidou et al. [98] performed steady state measurements in the stagnation and parallel flow region of a planar jet. Using a temperature feedback controlled heater, they obtained measurements for nucleate boiling, transition boiling and film boiling. The boiling curve in the stagnation region had a shoulder region between film boiling and transition boiling, with the heat flux magnitude similar to critical heat flux (refer Fig. 2.14).

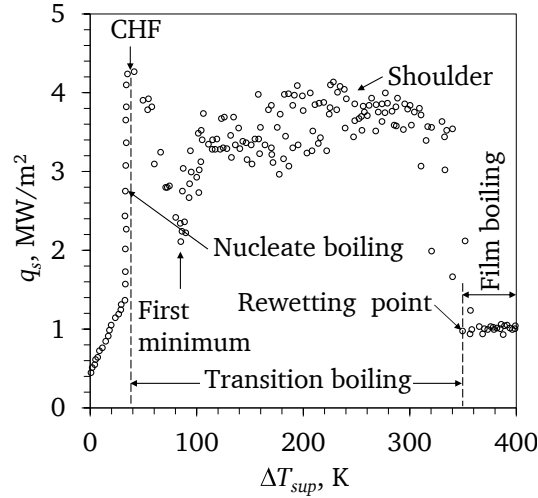


Figure 2.14. Boiling curve at the stagnation point of a planar free-surface impinging jet ($v_N = 0.8$ m/s, $w_N = 1$ mm, $S = 6$ mm and $\Delta T_{sub} = 16$ K) [98].

Ishigai et al. [49] and Gradeck et al. [32] also observed a shoulder region in the boiling curve for the jet stagnation region of a planar jet obtained by transient cooling experiments. Robidou et al. [98] explained this phenomenon using the microbubbles emission boiling process. The boiling phenomenon shows a transition from local nucleation to vapor spots after CHF. Till the first minimum, the jet is unable to burst these spots and the heat flux reduces. But after first minimum, due to increase in vapor spot size, the jet is able to burst them, causing excellent local mixing and spray-type wetting. With further increase in wall temperature, the vapor spots merge and the effective liquid-wall contact area is reduced. In these small contact areas, the heat flux is higher than in the contact areas at lower surface temperatures because of the larger available temperature difference. As a result, the overall heat flux remains constant in the shoulder region, though heat flux fluctuations are seen due to the explosive boiling. Beyond the rewetting temperature, these vapor spots merge to form a continuous film and the heat flux is low.

2.6.1.1 Onset of nucleate boiling and fully developed nucleate boiling

Miyasaka and Inada [79] obtained a dimensional correlation for the onset of nucleate boiling heat flux in a part of the stagnation region (ratio of width of heat transfer surface to the jet width 0.4) of a planar free-surface subcooled water jet as

$$q_{s,ONB} = 1.40 \cdot v_J^{0.56} \text{ MW/m}^2, \quad (2.22)$$

where $1.1 \text{ m/s} \leq v_J \leq 15.3 \text{ m/s}$ and $85 \text{ K} \leq \Delta T_{sub} \leq 108 \text{ K}$ (T_{sat} is based on the stagnation pressure).

Liu et al. [72] examined the effect of subcooling on nucleate boiling heat transfer in the stagnation region of a circular jet. The jet velocity was $0.5 \text{ m/s} \leq v_J \leq 6 \text{ m/s}$, nozzle diameter was $3 \text{ mm} \leq d_N \leq 12 \text{ mm}$ and jet subcooling was $15 \text{ K} \leq \Delta T_{sub} \leq 80 \text{ K}$. They reported that the heat flux in the single-phase regime and also the onset of nucleate boiling temperature $T_{s,ONB}$ increases with subcooling.

Monde and Katto [83] investigated the fully developed nucleate boiling regime on the flat end of a cylinder with diameter D in the range of 11 mm to 21 mm when impinged by a saturated water jet of diameter $d_N = 2 \text{ mm}$ and velocity v_N in the range of 3.9 m/s to 26.0 m/s. They found that the fully developed nucleate boiling curves were independent of the jet velocity and were an extension of the nucleate boiling data for pool boiling to larger surface heat flux and superheat. However, Monde and Okuma [85] found out that a lower velocity limit exists to this behavior observed by Monde and Katto [83]. When the heat flux is large enough such that the total amount of heat extracted from the wall is equal to the latent heat of evaporation of the saturated liquid, the fully developed nucleate boiling heat transfer is influenced by the jet velocity. It is important to note here that in both these studies, the plate diameter was much larger than the jet diameter ($D/d_N = 5.6$ to 10.1 in [83], $D/d_N = 9.6$ to 57.1 in [85]), and the estimated heat flux and temperature are based on the temperature variation along the axis of the heated cylindrical plate. One-dimensional heat conduction assumption is not true for such large D/d_N . Henceforth, the focus would be on studies that report space resolved boiling curves within the impingement and the radial flow regions. Besides this, results of boiling in the impingement region of a planar jet are considered to be applicable to the impingement region of a circular jet and vice versa, but the results of the parallel flow region of a planar jet are not applicable to the radial flow region of a circular jet and vice versa.

The boiling curves for various radial positions on a 80 mm diameter copper surface impinged by saturated water jet of diameter $d_N = 2.5 \text{ mm}$ were determined by Kamata [52]. Thermocouples were embedded inside the copper plate and were radially arranged in order to determine the surface heat flux and temperature distribution. Local boiling curves from $r = 0 \text{ mm}$ to $r = 25 \text{ mm}$ in steps of 5 mm are reported for jet velocity in the range of 0.6 to 2.1 m/s. They showed that in the jet stagnation region, the nucleate boiling heat flux increases with jet velocity. But in the radial flow region, the effects of the forced convection on the bubble dynamics would reduce, and the heat transfer augmentation is negligible for impinging jet velocity beyond 1.5 m/s. At a jet velocity of 1.8 m/s, the entire surface was covered with liquid film and the fully developed nucleate boiling curves for all the radial positions merged upon each other.

Miyasaka and Inada [79] proposed that the forced convection boiling can be considered as a superposition of single-phase forced convection and heat transfer due to bubble dynamics. The heat flux due to bubble dynamics was obtained from the difference of the applied heat flux and the single-phase convective heat flux obtained from an appropriate correlation. Data reported by Liu and Zhu [74] for saturated jet impingement also seems to agree with the finding of Miyasaka and Inada [79], i.e. the heat flux contribution due to bubble dynamics in jet impingement boiling is equal to the pool boiling heat flux.

Ishigai et al. [49] showed that the fully developed nucleate boiling curve is independent of the subcooling ($50 \text{ K} \leq \Delta T_{sub} \leq 70 \text{ K}$) in the stagnation region of a planar jet with $v_N = 2.1 \text{ m/s}$.

2.6.1.2 Critical heat flux

A large volume of literature exists relating to the critical heat flux (CHF) in jet subcooling, though most of these studies do not report local boiling curves on plates with large D/d_N . A detailed review of related literature published before 1993 has been presented by Wolf et al. [116]. They have shown significant inaccuracies and inconsistencies in the correlation by Ishigai and Mizuno and Miyasaka et al. [80].

Recently, Liu and Zhu [74] developed a correlation for critical heat flux in the stagnation region of a saturated water jet at atmospheric pressure as

$$\frac{q_{s,CHF,sat}}{\dot{m}_J h_{fg}} = 0.132 \cdot \left(1 + \frac{\rho_V}{\rho_L}\right)^{1/3} \cdot \left(\frac{\sigma \cdot \rho_L}{\dot{m}_J^2 \cdot d_N}\right)^{1/3} \cdot \left(\frac{\rho_V}{\rho_L}\right)^{1.4/3}, \quad (2.23)$$

where $v_N/d_N > 34.5$ 1/s, $0.5 \text{ m/s} \leq v_N \leq 6 \text{ m/s}$, $2 \text{ mm} \leq d_N \leq 10 \text{ mm}$ and \dot{m}_J is the mass flux in $\text{kg}/(\text{m}^2 \cdot \text{s})$. The nozzle to plate spacing was fixed at 10 mm. In this study, the plate was square in shape and it inscribed the jet, and they estimated a resulting uncertainty of about 5%. Additionally, they did not correct for the jet acceleration. Qui and Liu [97] found this correlation to be accurate over a wider range of jet velocity $0.5 \text{ m/s} \leq v_J \leq 10 \text{ m/s}$ and nozzle diameter $3 \text{ mm} \leq d_N \leq 12 \text{ mm}$ for water, ethanol, R-11 and R-113. Further, Liu et al. [72] investigated the effect of jet subcooling on critical heat flux in the stagnation region at atmospheric pressure for the following range of parameters: $0.5 \text{ m/s} \leq v_J \leq 6 \text{ m/s}$, $3 \text{ mm} \leq d_N \leq 12 \text{ mm}$ and $15 \text{ K} \leq \Delta T_{sub} \leq 80 \text{ K}$. They obtained the following correlation for critical heat flux in subcooled boiling.

$$q_{s,CHF,sub} = q_{s,CHF,sat} \cdot \left(1 + \frac{11.82 \cdot c_L \cdot \Delta T_{sub}}{h_{fg}}\right), \quad (2.24)$$

where $q_{s,CHF,sat}$ is given by Eq. (2.23). This correlation agrees well with the steady state measurements for the planar jet stagnation region in [49, 98].

Detailed measurements of heat flux and temperature variation in the radial flow region have not been performed till date. As a result, no correlation for critical heat flux in the radial flow region of a jet is available.

2.6.2 Transient measurement results

Owing to the difficulties in making steady state heat transfer measurements at high temperature as discussed previously in Section 2.5.1, most researchers have attempted to make transient heat transfer measurements during cooling of a hot metal plate. In this section, the literature has been subdivided into the measurements in the impingement region and the radial flow region. However, before discussing the results for these regions, the effect of initial plate temperature on the heat transfer results is being discussed.

2.6.2.1 Effect of initial plate temperature on the boiling curve

In all the studies, the selection of initial plate temperature for the quenching experiment has been governed either by the limitation of the experimental setup design in achieving a particular temperature level or by the intended application of the finding. An initial plate temperature of 900–1000 °C was chosen in [13, 30, 42–45, 65, 70, 71, 78, 124, 127], 600–800 °C in [37, 66], and 250–600 °C in [89]. Li et al. [67] estimated the boiling curve during spray cooling of a stainless steel plate heated

to an initial plate temperature between 400 and 1000 °C. Figure 2.15 shows the boiling curves for different initial plate temperatures. Comparing the boiling curve for $T_I = 400$ °C with the curve for $T_I = 1000$ °C, it is clear that the film boiling, transition boiling and part of the nucleate boiling regime can not occur for $T_I = 400$ °C. This means that when quenching a plate with $T_I = 400$ °C, the boiling curve can only be partially obtained. The study demonstrated that the initial plate temperature has a major influence on the shape and the magnitude of the boiling curve during quenching. Similar effect of initial plate temperature subcooling has been reported by Leocadio et al. [66].

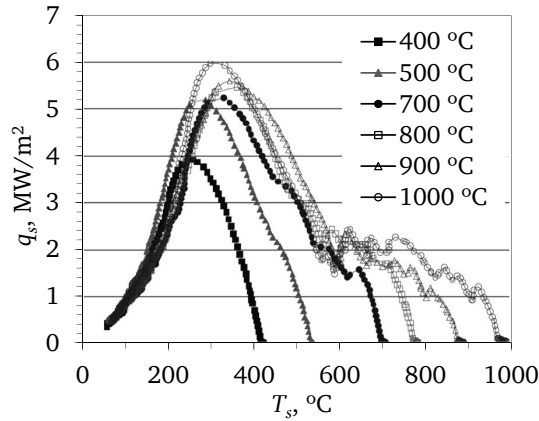


Figure 2.15. Boiling curves for spray cooling of a steel plate with different initial temperatures [67].

The question that arises here is, whether the maximum heat flux obtained from a transient experiments be compared with the critical heat flux or the burnout heat flux obtained by steady state experiments, as in the study by Mozumder et al. [87]. Mozumder et al. [87] ignored the difference between the maximum heat flux in the impingement region obtained in tests with $T_I = 300$ °C and $T_I = 400$ °C, and concluded that a weak correlation exists between the initial plate temperature and maximum heat flux. This conclusion is in contrast to the finding of Li et al. [67] and Leocadio et al. [66]. Possibly in the study of Mozumder et al. [87], the heat flux rapidly rises with a corresponding decrease in the surface temperature during the the first few milliseconds or more without the boiling mode reaching a quasi-steady state. This part of the boiling curve with a negative slope may give a false impression of the transition boiling regime; further, it may give a false indication that a boiling condition similar to the critical heat flux or burnout heat flux of a steady state experiment is existing at the maximum heat flux condition. Whether the two mechanism differ or not is an unanswered question in open literature because of the observed dependence of maximum heat flux on multiple factors, such as test specimen material, coolant properties, coolant thermo-hydrodynamic condition, initial temperature of the test specimen, geometric dimensions of the test specimen (diameter and thickness), etc. An overall implication of the argument stated above is that no quantitative basis exists to compare the maximum heat flux obtained from transient cooling experiments with the critical heat flux of a steady state measurement.

2.6.2.2 Heat transfer in the impingement region

Hall et al. [37] located nine thermocouples in a copper plate at a depth of 1.3 mm below the heat transfer surface and spaced them radially 6.4 mm apart. In the radial direction, these thermocou-

ple measurements were interpolated using an interpolation function. For a subcooled water jet ($\Delta T_{sub} = 75$ K at atmospheric pressure) with diameter $d_N = 5.1$ mm and velocity $v_N = 3$ m/s on the test specimen with initial temperature $T_I = 650$ °C, the estimated maximum heat flux is reported to be around 40 MW/m² and the surface temperature at the maximum heat flux condition is about 250 °C. They found a good agreement between the experimentally determined maximum heat flux and the critical heat flux correlation given by Monde [81] for saturated jet impingement along with a correction factor for subcooling. However, for the same flow parameters, the predicted critical heat flux using Eq. (2.24) is only 8.63 MW/m². The maximum heat flux reported for similar jet velocity and subcooling is significantly lower in the study of Mozumder [89] as compared to Hall et al. [37]. Mozumder [89] reported that the maximum heat flux obtained by transient cooling of a high thermal capacity copper test specimen matches with the critical heat flux of steady state measurement. As previously stated in Section 2.5.2, no quantitative basis for the deviation of the boiling curves obtained by steady state and transient experiments exists; few possible reasons for the deviation are discussed in the following paragraphs. The major studies related to steady state and transient cooling experiments for different test specimen materials and other conditions are summarized in Table 2.2.

Author(s)	Material	T_I [°C]	$\Delta T_{sub}, v_J, d_J$	$q_{s,MHF}$ [MW/m ²]	$T_{s,MHF}$ [°C]	Remarks
Kumagai et al. [64]	Cu	390	14–50 K, 3.5 m/s, 20 mm	≤ 17	200–300	
Hall [36]	Cu	650	75 K, 2–4 m/s, 5.1 mm	≤ 40	200–300	
Liu et al. [71]	CS, AISI 316	900	70–87 K, 5.6–6.5 m/s, 18.9–30 mm	≤ 13	300–500	$q_{s,MHF}$ and $T_{s,MHF}$ at $r = 0$ mm are lower for AISI 316 as compared to that for carbon steel.
Hammad [40]	Cu, CS, brass	250–300	5–80 K, 3–15 m/s, 2 mm	≤ 15	110–170	Data is for the radial flow region.
Hauksson [45]	CS	900	60 K, 5.7 m/s, 10.6 mm	≈ 8.5	500	Zhang [127] corrected the heat transfer estimations of Hauksson.
Gradeck et al. [33]	Ni	≈ 600	15–34 K, 1.2 m/s, 4 mm	3.5–8	200–400	$q_{s,MHF}$ and $T_{s,MHF}$ increase with ΔT_{sub} .
Mozumder [89]	Cu, CS, brass	250–400	5–80 K, 3–15 m/s, 2 mm	≤ 15	120–200	Data is for the radial flow region.
Gradeck et al. [32]	Ni	≈ 600	15 K, 1.2 m/s, 4 mm	≈ 3.5	200	Shoulder is seen in the surface temperature range of 350–530 °C.
Leocadio et al. [66]	AISI 304	600–900	78 K, 2.7 m/s, 6.8 mm	≈ 3	500	$q_{s,MHF}$ and $T_{s,MHF}$ depend on T_I .
Lee [65]	AISI 304	900	80 K, 5.6–10 m/s, 3 mm	≈ 2	≈ 500	

Table 2.2. Compilation of reported maximum heat flux condition, $q_{s,MHF}$ and $T_{s,MHF}$, for water jet impingement quenching at atmospheric pressure (chronologically arranged).

Hall et al. [37] also performed experiments with an initial test specimen temperature $T_I = 800\text{ }^\circ\text{C}$; in this experiment, a film boiling period was visually observed and at the stagnation point $T_{s,rewet} \approx 470\text{ }^\circ\text{C}$. However, for $T_I = 650\text{ }^\circ\text{C}$, film boiling regime was not observed in the boiling curve for the stagnation point due to the poor time response of the thermocouples. Akimenko [1] showed that the heat flux at the rewetting point increased monotonically with jet velocity up to 16 m/s until no film boiling was observed for an initial plate temperature of 1050 °C. Details regarding the jet dimensions, subcooling, experimental procedure, etc. are not mentioned by the author; hence these results must be considered only in a qualitative sense. The effect of jet subcooling and velocity on boiling heat transfer in the impingement region (includes the stagnation region and a part of the acceleration region) of a planar jet was studied by Ishigai et al. [49]. In their study, the nozzle width w_N was fixed at 6.2 mm, while the jet velocity ranged from 1 to 3.17 m/s and the subcooling ranged from 5 to 55 K. They reported that the boiling curve for the impingement zone of the jet is shifted to higher heat flux and temperature with the increase in the jet velocity and subcooling, which is in agreement with [79]. Enhanced convective heat transfer rates due to increase in local velocity gradients and liquid subcooling in the stagnation region is suggested as the possible reason for the increase in heat transfer. They observed a shoulder region in the boiling curve similar to Robidou et al. [98]. The correlation in Eqs. (2.23) and (2.24) under predicts the maximum heat flux as compared to the estimations of Ishigai et al. [49]. For subcooling greater than 55 K and jet velocity v_N in the range of 1–3.17 m/s, film boiling was not observed in the stagnation region for an initial plate temperature of 1000 °C. They obtained the following correlation for the minimum heat flux corresponding to the rewetting point $q_{s,rewet}$.

$$q_{s,rewet} = 5.4 \cdot 10^4 (1 + 0.527 \cdot \Delta T_{sub}) \cdot v_N^{0.604} \text{ W/m}^2, \quad (2.25)$$

where $1 \text{ m/s} \leq v_N \leq 3.17 \text{ m/s}$, $d_N = 6.2 \text{ mm}$ and $5 \text{ K} \leq \Delta T_{sub} \leq 55 \text{ K}$. They also compared the boiling curves obtained by steady state and transient experiments and found close agreement between the minimum and the maximum heat flux predicted by the two methods, but the temperature corresponding to the maximum heat flux was much higher for the transient experiments.

Zhang [127] performed quenching experiments on carbon steel plate heated to an initial temperature of 900 °C with a subcooled water jet ($1.17 \text{ m/s} \leq v_J \leq 3.27 \text{ m/s}$, $19.7 \text{ mm} \leq d_J \leq 23.3 \text{ mm}$, $50 \text{ K} \leq \Delta T_{sub} \leq 80 \text{ K}$). It has been reported that the slope of the boiling curve in the nucleate boiling regime deviated significantly from various correlations for the steady state nucleate boiling regime available in the literature, as can be seen in Fig. 2.16. Further, Zhang argued that due to the poor diffusivity of carbon steel, the heat transfer within the solid is slow; resultantly, the boiling curve shifts to higher temperature and lower heat flux.

The temperature corresponding to the maximum heat flux condition in steady state experiments is typically less than 200 °C for water at atmospheric pressure [9, 49, 98, 99]. However, in transient experiment, the reported values in literature vary in a wide range of 170–500 °C depending on the test specimen material, its initial temperature, jet diameter, liquid subcooling, etc. These values have been compiled in Table 2.2 along with the experimental conditions.

Zhang [127] also found that at constant subcooling, nucleate boiling heat flux showed no dependence on the jet velocity, as seen in Fig. 2.17; however, the maximum heat flux increased with jet

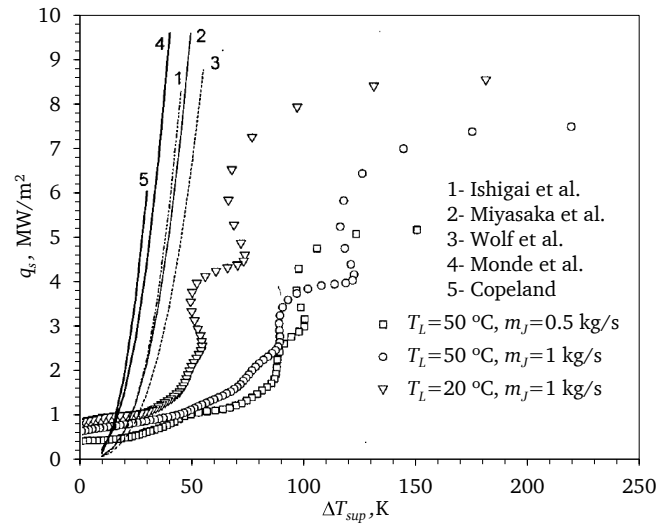


Figure 2.16. Comparison of predictions from various nucleate boiling correlations for stagnation point obtained by steady state measurements with the boiling data obtained by transient measurements [127].

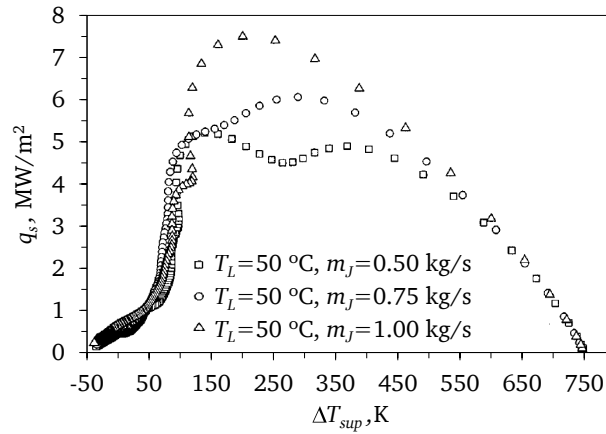


Figure 2.17. Effect of jet mass flow rate on the boiling curves at stagnation point [127].

velocity but the temperature at the maximum heat flux decreased. It is also noticeable in Fig. 2.17 that the curves for different velocities merge in the transition boiling regime; similar behavior was seen with the variation of liquid subcooling. On the other hand, they found that the liquid subcooling had a pronounced effect on both the nucleate boiling and maximum heat flux condition; with the maximum heat flux increasing with jet subcooling but the temperature at maximum heat flux reducing. The effect of jet subcooling seen by Zhang [127] contradicts the finding of Gradeck et al. [33], who found that subcooling had no effect on the nucleate boiling heat flux for the quenching of a nickel test specimen with a planar water jet. Besides this, Gradeck et al. [33] also saw a shoulder region in the boiling curve for the jet stagnation line, which was not observed by Zhang [127].

2.6.2.3 Heat transfer in the radial flow region

Only circular jet impingement heat transfer results are discussed here. There is a general agreement regarding the variation of heat transfer rate in the various regimes with the distance from the stagnation line [37, 87]. The heat flux in all the boiling regimes reduces downstream of the stagnation

line, though different researchers have reported different trends. The impingement region of the jet has significantly higher heat transfer than the radial/parallel flow region due to sharp pressure variation away from the stagnation line, which enhances the convective rates. The reduction in heat transfer with radial distance from the stagnation point is due to multiple factors: reduction in local liquid velocity owing to boundary layer growth and reduction in local subcooling due to the growth of thermal boundary layer. As discussed in Section 2.1, with the decrease in liquid velocity and local subcooling, the bubbles would grow to bigger sizes at much lower surface superheat. Thus, the boiling curves shifts to the lower wall superheat with distance from the stagnation point.

It has been observed that the velocity of movement of the maximum heat flux position is almost equal to the wetting front velocity, which is much lower than the velocity of the radially flowing liquid [87]. Drawing an analogy from steady state CHF experiments, where the CHF relates to the dry out of the surface, Mozumder et al. [87] argued that the boiling process reaches a crisis point (maximum heat flux) just upstream of the wetting front and the liquid is unable to wet the surface beyond it. Thus, during jet impingement quenching, rapid generation of vapor at the wetting front influences the hydrodynamics of liquid flow; as a result, the wetting front position is governed by the boiling process in the wetted region. They reported that just at the visible edge of the wetting front, the probable mode of heat transfer is transition boiling, while nucleate boiling occurs at the maximum heat flux position. Other researchers [37, 39] also reported similar findings. These observations can be misleading due to the effect of low initial temperature in these experiments, as discussed before. Despite the limited understanding of the phenomenon, it would be reasonable to say that intense boiling occurs in the wetting front region; the vapor generated here is able to deflect the liquid away from the surface, thereby keeping the outside surface dry. The maximum heat flux is just the maximum achievable heat flux obtained during quenching, and not essentially the burnout heat flux or the critical heat flux.

Mozumder et al. [87] made measurements on steel, brass and copper plates with 16 thermocouples placed in two rows that were 2.1 and 5 mm below the surface, with each row having 8 thermocouples radially spaced by 5 mm. The estimated maximum heat flux were significantly lower than the predictions using the correlation of Monde [81]. They concluded that the transient heat flux is always lower than steady state values due to the inability of the solid to conduct heat quickly enough to the surface and resultantly the boiling rates is lower. In support of their argument, they also showed that steel had the lowest maximum heat flux among the three metals. The maximum heat flux is correlated with the non-dimensional scaling parameter $\sqrt{(\rho \cdot c \cdot \lambda)_L / (\rho \cdot c \cdot \lambda)_T}$. Mann et al. [76] studied the influence of heat conduction in the wall on the heat transfer in a single bubble nucleate boiling system and reported that the boiling heat transfer rates on the steel surface were 2–12 % lower than on copper surface. König [61] experimentally determined that boiling heat flux on steel is 50–60 % lower than on copper. Stephan and Fuchs [107] commented that the capability of the wall and liquid to temporarily store energy is an important property of the boiling system that should be considered in numerical models as well as in boiling correlations.

While the argument of Mozumder et al. [87] is plausible and does find support in the single bubble literature, a major limitation exists in their experiments. Woodfield et al. [123] analyzed the limitations of these experiments. They showed that if the intense boiling region (maximum heat flux region) width was less than 10 mm, the heat flux is under-predicted. A close examination of the results of Mozumder [89] shows that the boiling region width on a copper plate with $T_l =$

400 °C impinged by a subcooled jet ($\Delta T_{sub} = 80$ K, $v_N = 15$ m/s) is generally smaller than 10 mm. Mozumder et al. [87] commented that as the boiling region width increases with distance from the stagnation region, the under-prediction in estimated maximum heat flux with respect to the correlation of Monde [81] reduces. For the same flow parameters, the intense boiling region width on steel was much smaller than copper, and hence the estimated heat flux is lower for steel compared to copper.

Similar to the deviation of transient and steady state nucleate boiling curves reported by Zhang [127] for the stagnation region, Islam et al. [50] found that, for the quenching of a carbon steel specimen with an initial temperature of 500 °C, the slope of their transient nucleate boiling curve for the radial flow region is significantly lower than the prediction made from the nucleate boiling correlation of Wolf et al. [117]; also, the maximum heat flux is reported to be about five times lower for the transient condition than the value predicted from the steady state correlation of Monde et al. [84]. The argument offered for this observation is consistent with that of Zhang [127].

2.7 Comments

Based on the above review of the state of the art, the following key comments can be made regarding the jet impingement quenching phenomenon:

1. Jet impingement quenching can be classified as a subcooled flow boiling process. Compared to pool boiling, bubble departure diameter and their lifetime is significantly smaller in subcooled flow boiling; therefore the boiling curve shifts to higher surface superheat. Moreover, as an outcome, it may become difficult to visually observe boiling activity with camera frame rate and resolution of the order of 10^3 frames per second and $10\text{ }\mu\text{m}$, respectively.
2. The rewetting temperature, generally refers to the temperature below which direct liquid-wall contact is re-established and the heat flux increases, varies over a very broad range depending on the flow velocity and subcooling; the highest rewetting temperature reported in literature is much higher than the critical temperature of the coolant. Studies related to the rewetting process have mostly focused on the quenching of the core of a nuclear reactor by bottom reflooding and falling film in a post-loss-of-coolant accident situation. The flow velocity in jet impingement quenching is normally two orders of magnitude higher than in these studies. It is therefore expected that the rewetting temperature in jet impingement quenching will be in much excess of that in a bottom reflood or falling film quenching.
3. Few major limitations in performing the jet impinging boiling studies at steady state for the conditions similar to that in the industry have become evident: (a) Instabilities associated with the negative slope of the transition boiling regime introduce complications in the design of the heater block; (b) Practical design issues restrict highest achievable temperature and heat flux to values much lower than is typical in the application; (c) The quenching process is understood to be a conjugate heat transfer process with flow boiling and transient heat conduction. The transient heat conduction process can not be simulated in a steady state experiment.
4. The above listed limitations of a steady state measurement system do not exist in a transient heat transfer (quenching) experiment. However, the uncertainties associated with the measurement inaccuracies, thermocouple time response, material inhomogeneity, inverse heat conduction analysis, etc. may lead to considerable inaccuracies in the heat transfer estimations from

these measurements. Despite these limitations, a transient heat transfer measurement is more closer to the actual process and therefore is suitable for studying the spatial distribution of boiling heat transfer for a wide range of surface temperature and is the easiest approach to study the transition boiling phenomenon.

5. To overcome the limitation of inverse heat conduction analysis, it is important to locate the thermocouples very close to the surface of interest and close to each other within the test specimen. However, practical design constraints exist in the installation of thermocouples within the test specimen. Similarly, the necessity to maintain high signal to noise ratio in the measurements means that the estimated heat transfer rate during a fast changing boiling process may be less accurate.
6. The published results are scarce and the various studies have little agreement. The boiling curves obtained from the transient quenching experiments differ significantly from the data and correlations available for steady state experiments; the slope of the nucleate boiling curve and the maximum heat flux are generally lower in transient boiling processes compared to steady state boiling processes. The conjugate interaction between the test specimen and the jet during the quenching process is supposed to be the likely reason for this behavior. Even when comparing the transient heat transfer measurement data from various studies, there is a general lack of agreement about the influence of the flow parameter on the various boiling regimes. It is clear that more experimental studies are necessary to determine the relation between the boiling heat transfer rate and the influencing parameters, such as thermal properties and initial temperature of test specimen, jet parameters, radial distance from the stagnation region, etc.
7. Physical understanding of this complicated quenching phenomenon is largely incomplete. Few studies have focused on understanding the jet impingement boiling mechanism in steady state conditions, but thermo-hydrodynamic mechanism during quenching of low conductivity metals, e.g. steel, is expected to be different due to rapid cooling and has been scarcely investigated.

2.8 Objectives of the present thesis

It is clearly apparent from the above drawn inferences that very few previous studies have focused on the estimation of heat transfer rates during jet impingement quenching of steels with thermal conditions close to those encountered in the steel industry. Consequently, little is understood about the complex phenomenon governing the cooling rates. Further, it is also realized that in a steady state experiment, the conjugate heat transfer nature of this heat transfer problem can not be studied and it is difficult to achieve high heat fluxes at temperatures of about 900 °C. Consequently, only transient experiment with uncontrolled cooling is suitable for the study of jet impingement quenching.

The objective of the present work is to experimentally study the phenomenon during transient jet impingement cooling of a stainless steel plate with initial temperature in the range of 800–900 °C. This study would complement a parallel study at the Institute of Fluid Mechanics and Aerodynamics, Technische Universität Darmstadt, in which the complex transport processes will be treated theoretically and validated against the experimental results. The physical processes occurring during circular free-surface subcooled water jet impinging normally on one flat end of a hot stainless steel cylinder would be investigated. The cooling rate would be measured by thermocouples embedded inside

the cylinder very close to the impingement surface. The heat transfer performance would then be estimated from these temperature measurements by solving the inverse heat conduction problem. The hydrodynamic phenomenon would also be studied using high-speed photography. These studies would help in understanding the heat transfer mechanism during jet impingement quenching. The parametric studies would be used to create a heat transfer database.

2.9 Closure

Based on the review of the state of the art, it is concluded that transient heat transfer experiments are most suitable for performing studies at the typical industrial conditions. However, limitations associated with the correct estimation of heat transfer rates in such experiments are clearly evident; therefore, due considerations will be given to the factors limiting the accuracy of the derived results in designing the test equipment, as described in the next chapter. The data analysis procedure for estimating the heat transfer performance has been previously applied by Woodfield et al. [120]. The basic mathematical model is presented in Chapter 4, following which the uncertainty in estimating heat transfer rate is presented.

3

Experimental Methodology

This chapter comprises the descriptions of the experimental setup, procedure and conditions.

3.1 Concept of the experiment

Based on the review of the literature, it has been commented in Section 2.7 that a transient heat transfer measurement is preferable for studying the quenching process. The concept of the transient heat transfer measurement setup used in this study is described here.

This thesis focuses on the quenching of a steel plate by circular liquid jets. When circular jets in a staggered arrangement impinge on a flat surface, hexagonal cells are formed on the plate surface (see Fig. 3.1). The area of influence of each jet is restricted to a regular hexagon. The net heat flux across the boundaries of a hexagon is zero (equivalent to a symmetry boundary condition). For fundamental understanding of the process, single jet impingement heat transfer process is prefer-

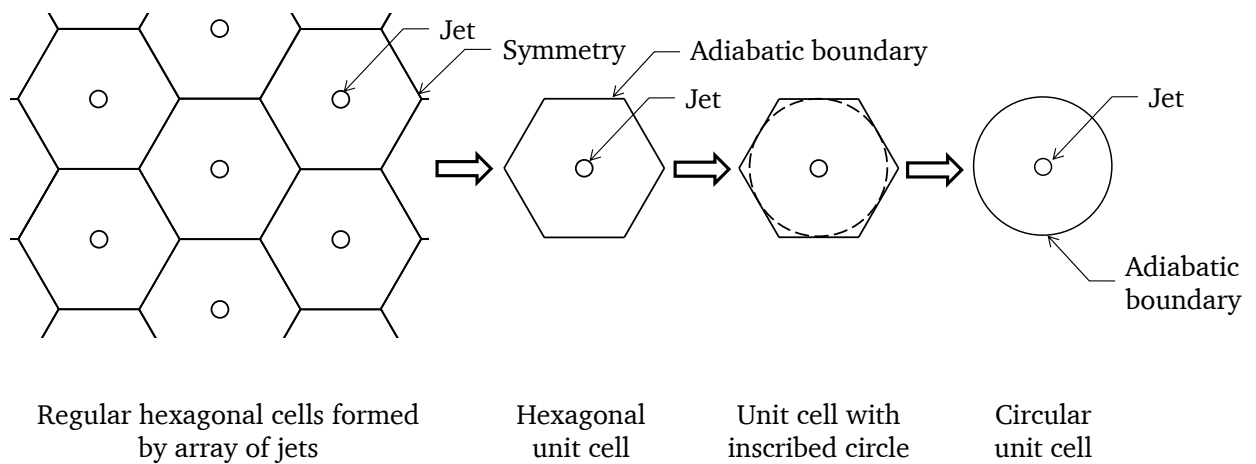


Figure 3.1. Identification of an unit cell.

able; hence, an unit cell of regular hexagonal shape is identified as a representative of the process. The symmetry boundary condition on the faces of the hexagon are aptly represented by an adiabatic boundary condition. However, a regular hexagon is not an axisymmetrical configuration; this makes the heat transfer analysis three-dimensional. In order to simplify the analysis, the hexagonal cell is replaced by a circular cell whose boundaries (shown as dashed line) inscribe the hexagon. Once again, adiabatic boundary condition is used to represent the symmetry boundary condition. A plate of cylindrical shape with a coaxially aligned jet is finally chosen as the geometry for investigation. The jet impinges on the upward facing flat face of this cylinder, called as the “impingement surface”, while the other faces are made adiabatic. A schematic of the test specimen is shown in Fig 3.2. In order to estimate the heat transfer rates during quenching, temperature sensors are embedded within the steel plate. Boundary conditions are well defined on the side and the bottom of the steel plate, and only one boundary condition, i.e. on the upward facing impinged surface, is to be determined from the experiments. For determining this boundary condition, temperature distribution in a single plane at a distance z_m below the impingement surface is sufficient. Hence, the thermocouples are arranged radially at the same depth below the impingement surface. To improve the time and space resolutions of the measurements, sensors with fast response are fixed very near the impingement surface and their spacing is kept as small as possible.

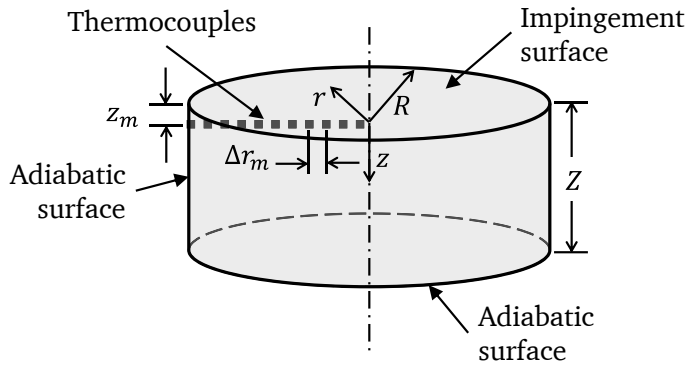


Figure 3.2. Schematic of the test specimen.

The quenching process is an uncontrolled cooling process, i.e. the liquid-wall interface cooling rate is controlled by the conjugate heat transfer between the liquid and the test specimen. The instrumented steel plate is uniformly heated to a desired high temperature and then the heating is turned off. The jet then impinges on the impingement surface and the quenching occurs. During quenching, the evolution of temperature at the sensor positions is measured. This data is then processed to determine the impingement surface boundary condition.

3.2 Overall experimental setup

Before describing the experimental setup in details, various terms used to describe components of the setup are discussed here. The various components have been schematically shown in Fig. 3.3. The overall experimental setup that includes the flow loop, instrumented test specimen along with the insulation assembly and the data acquisition system is called the test setup. At the heart of

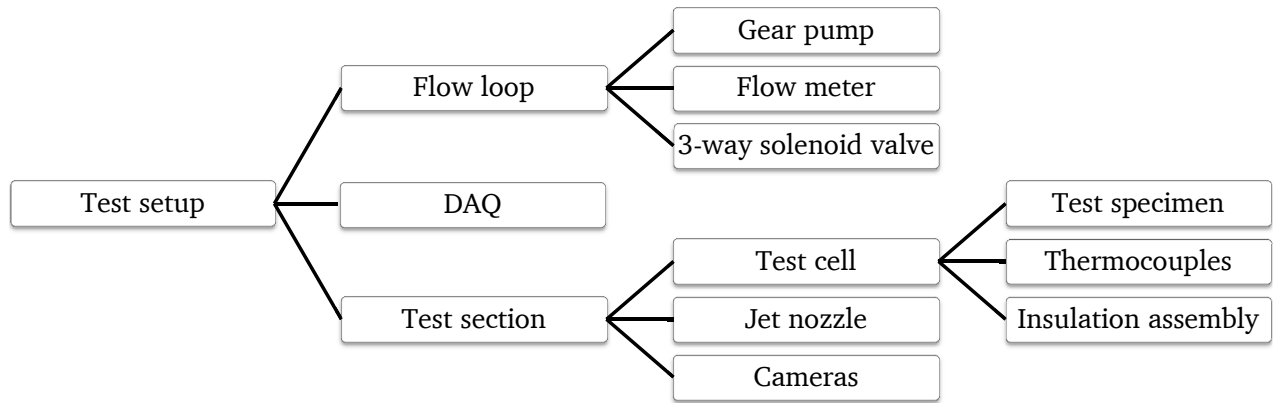


Figure 3.3. Block diagram showing the various components of the test setup.

the test setup is the test section where the quenching process happens. It consists of the test cell, the jet nozzle and the cameras. Figure 3.4 shows a basic schematic of the test section. In the test section, a stainless steel test specimen enclosed in a test cell is quenched by a normally impinging coaxial free-surface jet. The test cell includes the test specimen with embedded thermocouples and the insulation assembly. Upon impingement, the liquid jet flows over the top surface of the specimen or the impingement surface, and quenches it in the process. The liquid finally runs over the test cell into a drain.

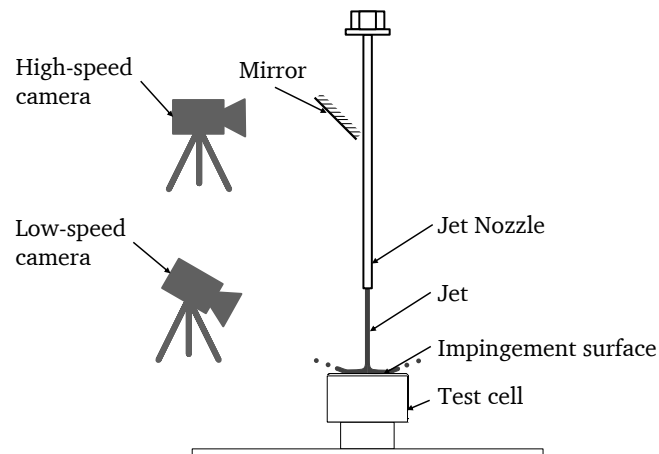


Figure 3.4. Schematic of the test section showing the arrangement of the test cell, jet nozzle and cameras.

The schematic of the experimental set-up used for investigation of thermo-fluid-dynamic phenomena during quenching of the test specimen is shown in Fig. 3.5. The main parts of the setup are the flow loop, test section and data acquisition system. The flow loop consists of a reservoir where the liquid temperature is maintained constant by a thermostat controlled cooling/heating coil, a variable speed gear pump¹, a turbine flow meter², a fast-response three-way solenoid valve³

¹Model: 8200 WM020R. Ernst Scherzinger GmbH and Co. KG, Furtwangen/Germany

²Model: NT3 turbine flow meter. Nixon Flowmeters Ltd, Cheltenham/UK

³Model: 0355. Bürkert GmbH and Co. KG, Egelsbach/Germany

(S) and a pipe-type jet nozzle. The working fluid (deionized water in this study) from the reservoir is pumped by the gear pump and the flow rate is set by regulating the pump speed using a potentiometer controller. The three-way solenoid valve continuously returns the working fluid through its outlet 1 back to the reservoir until it is triggered to route the same through outlet 2 to the jet nozzle. During quenching, the cameras capture the process and a DAQ system acquires the temperature and flow data. The process timing is accurately controlled using an 18-bit NI SCXI system and a virtual instrument in LabView 8.5. The high-speed camera⁴ captures the phenomenon for the first 2 s. Simultaneous, a low speed video camera⁵ captures the complete quenching phenomenon.

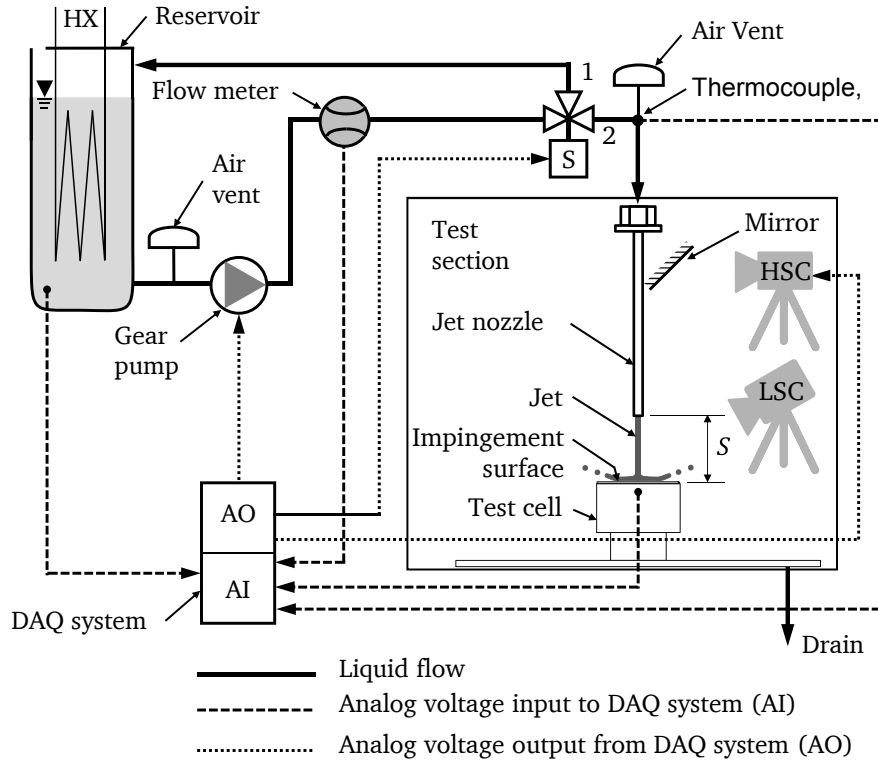


Figure 3.5. A schematic of the experimental setup.

3.2.1 Jet nozzle

The jet nozzle has a pipe-type design with an internal diameter $d_N = 3$ mm and length of 288 mm. In order to have an undisturbed jet, the following are done:

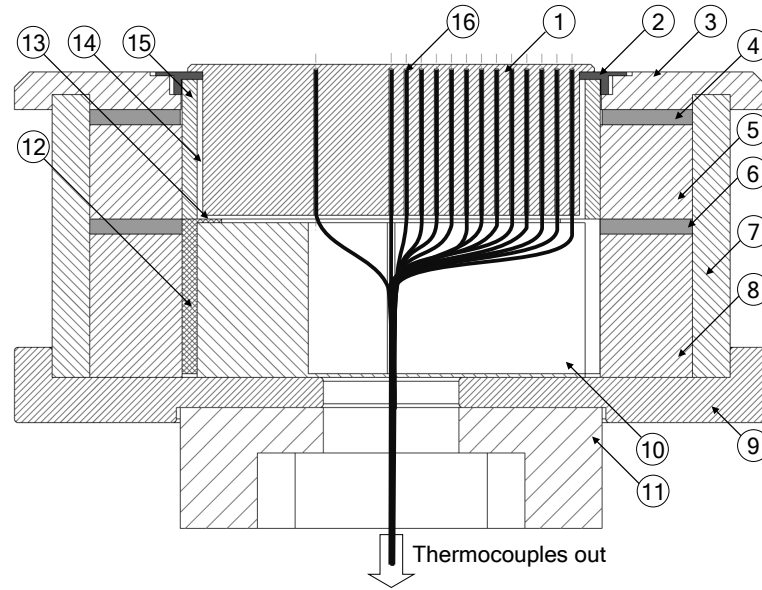
- Any trapped air is purged out of the liquid line just before of the jet nozzle inlet via an air vent.
- A fine mesh is placed before jet nozzle inlet to reduce the inlet disturbances.
- The jet nozzle is made of stainless steel seamless tubing⁶ with maximum average roughness of $0.5 \mu\text{m}$.

The jet nozzle exit is leveled using a set of four screws and is aligned with the axis of the test specimen using a 2-axis translation stage.

⁴FASTCAM-X 1024 PCI. Photron USA, Inc., San Diego/USA

⁵Model: DCR-PC9E. Sony Corporation, Japan

⁶Model: SS-T6M-S-1.5M-6ME. Swagelok Company, Germany



1: test specimen, 2: steel ring, 3: MACOR insulation cover, 4 and 6: mica gasket, 5, 8 and 10: Fiberfrax insulation, 7: ceramic insulation cover, 9: MACOR insulation support, 11: steel seat, 12: steel cylinder, 13 and 14: air gap, 15: quartz cylinder, 16: thermocouple embedded inside a hole.

Figure 3.6. The test cell assembly for free-surface jet impingement quenching studies.

3.2.2 Test cell

Figure 3.6 shows the test specimen assembled inside the test cell. Previous researchers used stainless steel AISI-type 304 to study jet impingement quenching. However, citing various metallurgical studies, Davis [18] suggested stainless steel AISI-type 314 (DIN 1.4841) for high temperature application as it has a stable austenitic structure and the best high temperature corrosion resistance among all the chromium-nickel steels. Trials done in the laboratory by the present author to compare the quench corrosion resistance of the two steels showed that stainless steel AISI-type 314 surface remained smooth while stainless steel AISI-type 304 developed pits due to repeated quenching. Wandelstorf et al. [115] studied the heat transfer rates during spray cooling of stainless steel AISI-type 314 sample from 900 to 200 °C. The cooling rate of stainless steel AISI-type 314 was compared with nickel, as nickel has negligible corrosion in this temperature range. They found that the heat transfer values were comparable for stainless steel AISI-type 314 and nickel, and concluded that the oxide scale layer on stainless steel AISI-type 314 surface has no effect on the heat transfer rates. Based on the findings in literature and the comparative studies on corrosion resistance performed in the laboratory (not reported here), stainless steel AISI-type 314 has been chosen for the test specimen. The elemental composition of AISI type 314 stainless steel specimen used in the study and the thermophysical properties are tabulated in Appendix A. The cylindrical test specimen has 50 mm diameter and 20 mm height. The cylindrical test specimen has an annular extension 1 mm thick and 2 mm wide at its impingement surface. Two M3 threaded holes of 4 mm depth are made through the bottom face of the test specimen in order to assemble the insulation around it. The side and the bottom of the test specimen are thermally insulated, while heat transfer takes place through the top surface. Even though a good corrosion resistance steel was used, some corrosion was unavoidable.

Hence, before each experiment, the surface was polished with 2000 grit emery paper. The average surface roughness of the top surface has been found to be 0.2 μm .

Thirteen holes of 0.5 mm diameter are drilled using EDM technique from the bottom surface of the test specimen to a depth of 19.4 ± 0.05 mm. The holes are located along a radial line and are spaced 2 mm apart. The thermocouples are fixed inside these holes. The hole-thermocouple annular tolerance is kept just enough to permit the sliding of the thermocouples till the dead end of the hole, thereby minimizing the thermal contact resistance.

Type-K class-I grounded thermocouples⁷ (0.5 mm sheath diameter and 0.075 mm wire diameter) encased in an AISI type 314 stainless steel sheath (sheath thickness is 0.05 mm) are fixed inside the holes. The thermocouples were calibrated using a calibration furnace⁸ with an accuracy of ± 1 K over the temperature range of 200–1000 °C. In order to minimize thermal contact resistance between the hole in the test specimen and the thermocouple, a high temperature thermal conductive paste⁹ ($\lambda = 9.1 \text{ W} \cdot \text{m}^{-1} \cdot \text{K}^{-1}$, maximum operating temperature in air of 927 °C) has been filled inside each hole using a syringe before pushing the thermocouple to the hole end. Next, hot air at 200 °C has been blown around the test specimen for around 2 hours in order to cure and strengthen the silver paste. The thermocouples have been reinforced in place at the bottom face of the test specimen using a metallic adhesive¹⁰. With this arrangement, the thermocouple end must be at a depth 0.6 mm from the impingement surface. The center of the thermocouple bead is geometrically determined to be 0.85 mm below the impingement surface. The overall time response of the hole-thermocouple system is expected to cause errors in the result. A sluggish thermocouple can not detect rapid temperature changes. Previously, Monde and co-workers [40, 89] used 1 mm diameter thermocouples for studying quenching of copper, brass and steel specimens. Since the rate of cooling and axial temperature gradients are lower for copper and brass, a sluggish measurement system would also give good results. However, in their study, the results for steel were influenced by the thermocouple time response and differed significantly with the data for copper and brass. In the present study, 0.5 mm thermocouples have been used to achieve overall fast time response of the measurement system, yet some influence on the results is expected. Sarnes and Schröfer [100] estimated a time constant of 0.03 s for the case where a thermocouple is plunged into a water bath at a speed of 0.4 m/s. Considering that the thermal contact resistance is unknown, the time contact for the thermocouple may be of the order of 0.05 s. Due to this uncertainty, the sensor time lag has not been considered in the inverse analysis.

The side and the bottom of the test specimen have been insulated using a combination of Pythagoras ceramic¹¹ ($\lambda = 2.0 \text{ W} \cdot \text{m}^{-1} \cdot \text{K}^{-1}$), OM 100 quartz¹² ($\lambda = 1.90 \text{ W} \cdot \text{m}^{-1} \cdot \text{K}^{-1}$ at 587 °C, opaque to both visible and infrared radiation), Fiberfrax Duraboard¹³ ($\lambda = 0.09 \text{ W} \cdot \text{m}^{-1} \cdot \text{K}^{-1}$ at 600 °C) and mica gasket sheets¹⁴. In this design, the principle insulation to the test specimen is provided by air gaps (width of the order of 0.2 mm) around the side and bottom of the test specimen. The two air gaps are shown in Fig. 3.6. The insulation assembly is made leak tight by pressing the insulation

⁷ES Electronic Sensor GmbH, Heilbronn/Germany

⁸Model: PTC 12/20/150, Carbolite GmbH, Ubstadt-Weiher/Germany

⁹PELCO High Performance Silver Paste. Ted Pella Inc., Redding/USA

¹⁰Durabond 954. Polytec Pt GmbH, Waldbronn/Germany

¹¹Morgan Technical Ceramics Haldenwanger, Waldkraiburg/Germany

¹²Heraeus Quarzglas GmbH and Co. KG, Kleinostheim/Germany

¹³Unifrax Deutschland GmbH, Duesseldorf/Germany

¹⁴IBK Wieseahn GmbH, Bottrop/Germany

assembly against the annular extension using two M3 bolts that are screwed into the threaded holes within the test specimen. The measured temperature and calculated cooling rate at the thermocouple depth $z = z_m$ at $r = 24$ mm is shown in Fig. 3.7. The details of the experiments F2, F3 and F4 are given in Table 3.1. Before the arrival of the wetting front, the temperature near the side surface changes much slowly compared to the maximum cooling rate, which verifies the assumption of an adiabatic boundary condition on the side surface. In separate tests done with another test specimen having additional thermocouples at 5 and 10 mm distance from the bottom surface, it is verified that an adiabatic boundary condition is maintained on the bottom surface through out the experiment.

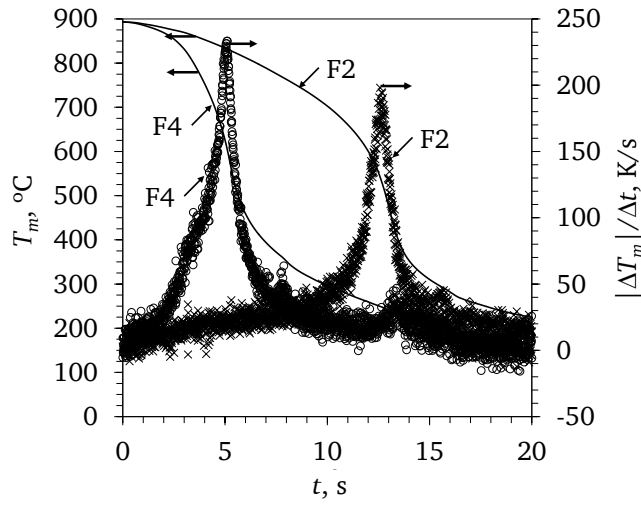


Figure 3.7. Measured temperature at $r = 24$ mm and calculated cooling rate at the thermocouple depth. For details of experiments F2 and F4, see Table 3.1.

3.2.3 Heating system

The test specimen is induction heated¹⁵ to the desired temperature. The induction heating is intermittently turned off during heating period to homogenize the temperature within the test specimen. During the complete heating period, the test cell is covered on the top surface with a Fiberfrax board to minimize radiation heat loss. The heating is stopped when the maximum temperature in the test specimen is around 25 °C above the desired temperature. After this, the heat is allowed to redistribute within the test specimen until the desired homogeneous temperature is reached. Following this, the jet is allowed to impinge on the impingement surface and cooling commences.

3.2.4 The data acquisition system

The 18-bit resolution data acquisition system does the following tasks simultaneously:

- triggers the three-way solenoid valve and thereby allows the jet to impinge on the impingement surface;
- triggers the high-speed camera;
- acquires and stores the process data.

¹⁵Model: Easyheat 0224. Cheltenham Induction Heating Ltd, Cheltenham/UK

Temperature data from the embedded thermocouples, liquid temperature in the tank and at the jet nozzle exit, and the liquid flow rate are acquired during quenching at 100 Hz with negligible time difference between their scanning. The DAQ system has a built-in reference cold-junction compensation and a 200 Hz low-pass filter. The integration time for each measurement is 3 μ s. For the range of calibration, the noise (3σ) in the temperature measurement or the resolution is ± 0.33 °C, while the overall measurement accuracy is ± 1.45 °C.

3.2.5 Visual observation

The arrangement of the cameras is shown in Fig. 3.4. During the experiments, a high-speed camera captured the quenching phenomenon looking from the top at 1000 frames/s with resolution of 1024×1024 pixels. Since the presence of the jet nozzle and the translation mechanism does not permit placing the camera directly over the surface, the camera looks into a mirror which is positioned at an angle of $\approx 50^\circ$ to the impingement surface. In the high-speed images, the impingement surface looks slightly elliptical, which is then corrected during analysis. Additionally, in few experiments, the quenching process has been captured from the side using a high-speed camera at 1000 frames/s with a resolution of 1024×512 pixels. The low speed video camera captures the whole process at 25 frames/s with a resolution of 640×480 pixels. The low speed video data has been converted into a sequence of images for further analysis.

From high-speed imaging, the time delay between the triggering of the three-way solenoid valve and the first impact of the jet on the impingement surface has also been determined. Depending on the flow rate, this time delay has been found to be in the range of 180 to 557 ms. The inverse analysis has been performed on the data right from the instant of triggering of the three-way solenoid valve. The data for the time before impingement has been included in the calculations in order to overcome the inaccuracies in the inverse calculations for the first few time steps arising due to lack of sufficient history data. Later, when discussing the results, time $t = 0$ s refers to the first impact of the jet on the impingement surface.

3.2.6 Plunging jet setup

In order to perform plunging jet impingement experiments, additional parts are assembled with the test cell described in Section 3.2.2. The assembly is shown in Fig. 3.8. The spent coolant accumulates inside an accumulation volume that is created by assembling a low conductivity ceramic cylinder of height h_p on top of the test cell. A steel disc is shrink fitted around the ceramic cylinder in order to improve its thermal shock resistance. In order to avoid any leakage of the accumulated liquid, the ceramic cylinder is pressed down on to a retaining ring and is reinforced into position using a ceramic cement. Additionally, a 2 mm thick mica sheet covers the top of the test cell outside the ceramic accumulation cylinder, thereby avoiding liquid seepage through the cracks in the MACOR insulation cover into the test cell. A snapshot of the test section with a ceramic cylinder of $h_p = 30$ mm assembled on top of the test cell is shown in Fig. 3.9.

The test specimen is heated to the desired temperature, after which the jet is allowed to impinge on the impingement surface. As the cooling progresses, the liquid accumulates within the accumulation volume. Once the accumulation volume is completely filled, the liquid spills over the edge of the ceramic cylinder.

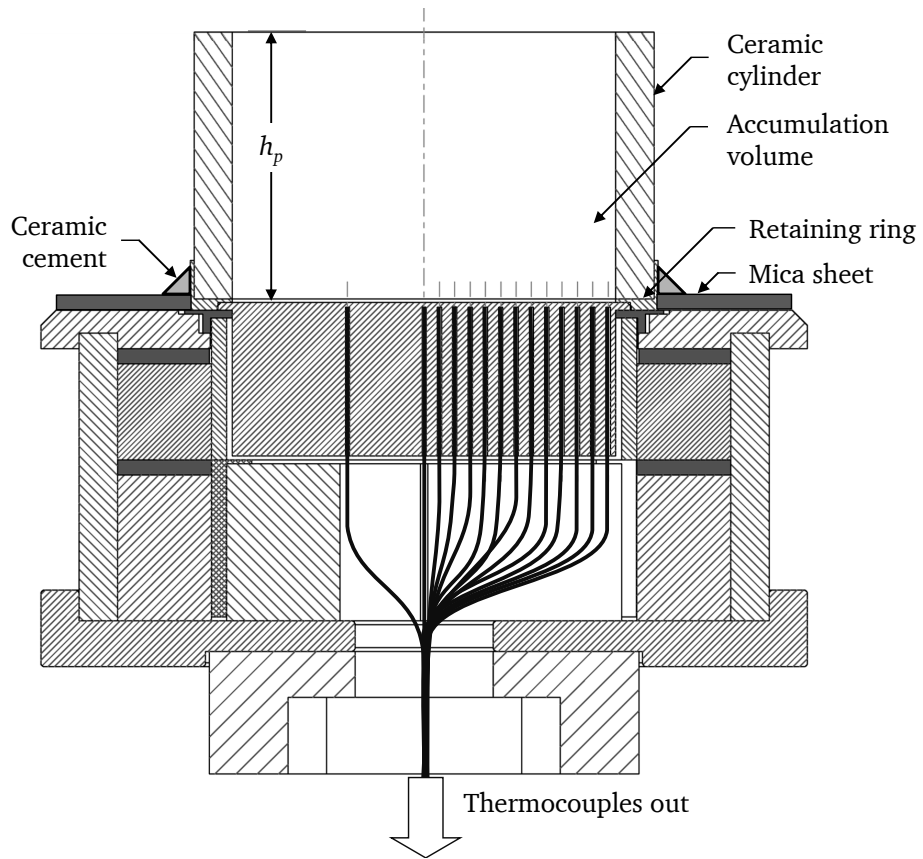
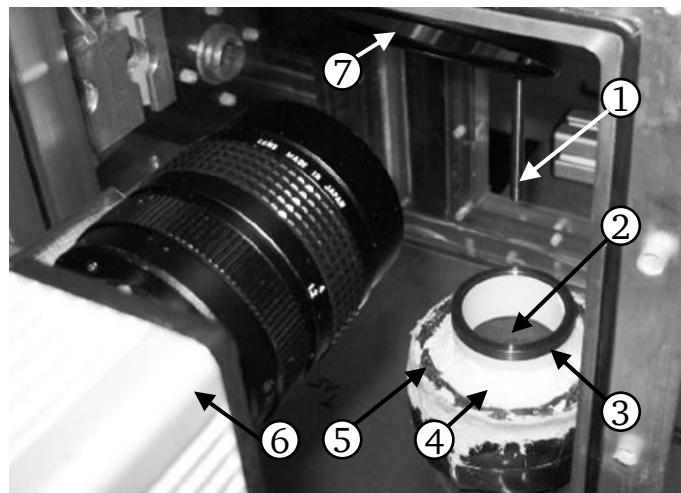


Figure 3.8. The test cell assembly for plunging jet impingement quenching studies.



1: jet nozzle, 2: impingement surface, 3: Ceramic accumulation cylinder with a shrink fitted stainless steel disc, 4: ceramic cement to reinforce the accumulation assembly in position, 5: mica sheet, 6: high speed camera, 7: mirror

Figure 3.9. A snapshot of the test section with a ceramic cylinder of $h_p = 30$ mm assembled on top of the test cell.

3.3 Experimental conditions

3.3.1 Free-surface jet impingement quenching

The working fluid in this study is deionized water. The experiments in this study are for a fixed jet nozzle diameter $d_N = 3$ mm and a fixed jet nozzle-to-surface spacing $S = 97.5$ mm ($S/d_N = 32.5$). The jet impingement velocity v_J is calculated as $v_J = \sqrt{v_N^2 + 2gS}$ and varies from 2.5 to 10 m/s, which corresponds to a mass flux based on the impingement area $\dot{m}_J = m_J/(\pi \cdot R^2)$, of 7.5-35 kg/(m² · s). The liquid temperature T_L is varied between 12 to 40 °C at atmospheric pressure. Over the range of liquid mass flow rate, the calibration accuracy is 0.5% at 25 °C, though additional errors in setting the pump voltage to get the desired flow rate occur due to the variation in liquid viscosity over the range of desired temperature. The maximum error in setting the liquid jet velocity v_J is estimated to be $\pm 4\%$. The mean initial test specimen temperature of the test specimen is fixed within 885-900 °C (within 1.6% of the desired starting temperature i.e. 900 °C) with the standard deviation within 1.8-5 °C (0.2-0.5% of $T_{I,avg}$).

The experimental conditions for the free-surface jet quenching studies are given in Table 3.1. The effect of jet velocity at constant subcooling is studied in experiments F1–F4. The effect of jet subcooling at a constant jet velocity $v_J = 5$ m/s is studied in experiments F2, F6 and F7, while at a constant jet velocity $v_J = 2.5$ m/s is studied in experiments F1 and F5.

Experiment #	T_I (°C)		T_L (°C)	v_J (m/s)	d_J (mm)	\dot{m}_J kg/(m ² · s)	Re_J
	$T_{I,avg}$	σ_{T_I}					
F1	890.0	5.05	25.8	2.5	2.738	7.5	7803
F2	895.2	3.16	25.9	5.1	2.943	17.67	17145
F3	891.5	1.8	25.2	7.5	2.974	26.54	25127
F4	895.0	3.22	25.3	9.75	2.985	34.75	32871
F5	885	3.12	12	2.5	2.728	7.5	5544
F6	893.2	3.5	13	4.77	2.93	16.43	11654
F7	901.5	2.58	39.9	5.2	2.945	18.05	23661

Table 3.1. Experimental conditions for the free-surface jet impingement quenching studies.

3.3.2 Plunging jet impingement quenching

The additional parameter in the study of plunging jet impingement quenching is the filling height of spend liquid h_p . The experimental conditions for the plunging jet impingement quenching studies are given in Table 3.2.

Experiment #	T_I (°C)		T_L (°C)	v_J (m/s)	\dot{m}_J kg/(m ² · s)	Re_J	h_p	Filling time (s)
	$T_{I,avg}$	σ_{T_I}						
P1	890	3.37	25.0	5.0	17.5	17140	30	1.7
P2	881	3	25.0	5.0	17.5	17140	80	4.5
P3	893	8.9	25.9	10	35	34482	80	2.3

Table 3.2. Experimental conditions for the plunging jet impingement quenching studies

3.4 Closure

The experimental setup, procedure and program have been described in this chapter. The result of these experiments are presented in Chapter 5. Inferences and conclusions drawn from these results along with supporting arguments and discussions are also presented in the same chapter. The inverse heat conduction analysis procedure and the uncertainty of the obtained results are discussed in the next chapter. These uncertainty estimates are duly considered when deriving any conclusions in Chapter 5.

4

Data Analysis and Uncertainty Estimation

This chapter briefly introduces the inverse heat conduction analysis procedure used for analysis of the experimental temperature data. The inverse heat conduction analysis tool “Inverse2d” used in the present study for the estimation of the heat transfer rate on the impingement surface has been developed by Monde (Saga University, Japan). Next, the uncertainty in the estimation of the surface heat transfer is discussed at length. The analysis of uncertainty and image analysis in the present study have been carried out by Kruse [63] and Schmidt [101], respectively, under the supervision of the present author.

4.1 Inverse heat conduction analysis

In this study, the temporal variation of temperature inside the test specimen has been measured by 13 embedded thermocouples. With the assumption that the thermocouple ends are in contact with the blind ends of their respective drilled holes, the center of all the thermocouple junction must be at an axial position of $z = 0.85$ mm. The thermocouple junctions were arranged along the radius of the test specimen on one side of its test specimen. In order to estimate the spatiotemporal variation of the surface heat transfer boundary condition, inverse heat conduction analysis has been performed. From both the high speed and low speed images, it has been confirmed that the wetting front was circular. Therefore, the inverse analysis of the heat conduction equation in cylindrical coordinates has been performed with the assumption of azimuthal symmetry. The thermocouple located at $r = 4$ mm had poor time response and therefore its data has not used in the inverse heat conduction analysis. The inverse heat conduction analysis has been performed in the 2-d inverse heat conduction tool “Inverse2D” using the data from the remaining 12 thermocouples. As is stated previously in Chapter 3, data from the instant of triggering the three-way solenoid valve has been used to calculate the inverse heat conduction solution. In Chapter 5, time $t = 0$ s refers to the instant when the jet first impinged in the impingement surface. The inverse heat conduction model implemented in Inverse2D is presented next. The choice of model parameters is discussed subsequently.

4.1.1 The inverse heat conduction model Inverse2D

The inverse heat conduction solution procedure is used to obtain surface heat flux and temperature distribution from temperature measured within the solid. Woodfield et al. [120] have developed an analytical inverse heat conduction solution procedure that is well suited for a 2-d system with adiabatic boundary condition on the back face, similar to the jet impingement heat transfer experiments performed in this study. The procedure can be divided into 4 steps:

1. Transformation of the 2-d heat conduction equation in cylindrical coordinate system and the boundary conditions into Laplace space.
2. Approximation of the measured temperature as a half-power polynomial series in time and as a Fourier-Bessel series in radial direction.
3. Solve the inverse heat conduction problem in Laplace space with the help of the approximated temperature distribution.
4. Apply the inverse Laplace transform to the solution.

The inverse heat conduction solution procedure for experiments in which temperatures are measured at a depth z_m below the surface is briefly discussed in the following paragraphs. More details can be seen in [120].

For a cylindrical plate (Fig. 4.1), the mathematical formulation of the 2-d heat conduction equation in cylindrical coordinate system can be written as

$$\frac{1}{\alpha_T} \cdot \frac{\partial T}{\partial t} = \frac{1}{r} \cdot \frac{\partial}{\partial r} \left(r \cdot \frac{\partial T}{\partial r} \right) + \frac{\partial^2 T}{\partial z^2} \quad (4.1)$$

Initial and boundary conditions for a cylindrical plate insulated at the side and the bottom faces are defined by the following equations. Only the boundary condition for the top surface is unknown.

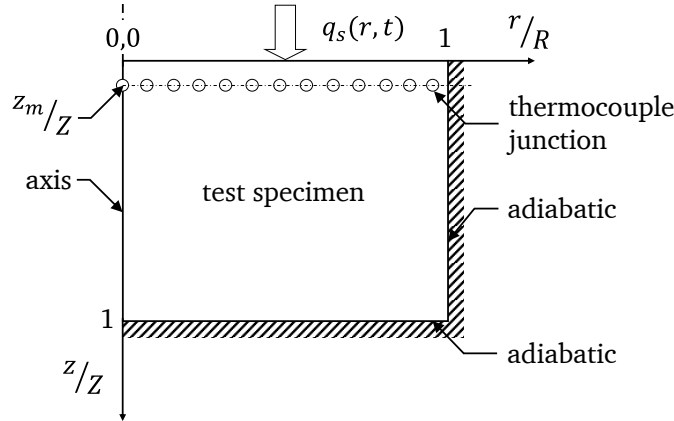


Figure 4.1. A schematic of the test specimen showing the boundary conditions.

$$T|_{t=0} = T_I, \quad (4.2)$$

$$\left. \frac{\partial T}{\partial z} \right|_{\frac{z}{Z}=1} = 0, \quad (4.3)$$

$$\left. \frac{\partial T}{\partial r} \right|_{\frac{r}{R}=0} = 0, \quad (4.4)$$

$$\left. \frac{\partial T}{\partial z} \right|_{\frac{r}{R}=1} = 0. \quad (4.5)$$

For simplification, the case of a one-dimensional semi-infinite plate with a single sensor at depth z_m below the surface is considered. Woodfield et al. [120] approximated the experimental data in the range from time t_0 ($t = 0$) to t_f (t_f is little more than t) as

$$(T - T_I)|_{t,z_m} = \sum_{k=0}^{N_k} \frac{P_{0,k} \cdot (t - t_i)^{\frac{k}{2}}}{\Gamma(\frac{k}{2} + 1)} + \sum_{i=1}^{N_{corr}} \sum_{k=0}^{N_k} \frac{P_{i,k} \cdot (t - t_i)^{\frac{k}{2}}}{\Gamma(\frac{k}{2} + 1)}. \quad (4.6)$$

Here, $\Gamma(\cdot)$ is the gamma function, and i and k are positive integers. A half-power polynomial series in time is chosen because of heat conduction equation's \sqrt{t} dependence, as seen in Eq. (2.19). Monde et al. [82] included a time lag in the half-power polynomial, which has been omitted by Woodfield et al. [120]. The temperature data in the time interval of t to t_f is included in the fit to account for the time delay required for a change on the surface to penetrate to depth z_m [120]. The first part on the right side of Eq. (4.6) approximates the measured data from time $t = 0$ to t_f with a k^{th} -degree half-power polynomial. This is necessary in order to retain the low frequency components from the long-term history. However, the use of low-degree polynomial over a large data windows would lead to low temporal resolution near the time of interest and therefore corrections needs to be added. The second summation is a set of corrections to the original fit, i.e. the one to retain low frequency components from the long-term history, to improve the temporal resolution. The successive windows (including experimental data in the time range of $t = t_i$ to t_f) for correction are shown in Fig. 4.2. The data window becomes smaller for each successive correction but the number of coefficients remain the same, thereby improving the local resolution of the approximating polynomial given by Eq. (4.6). The smallest data window size is limited by the order of the half-polynomial, which determines the number of corrections N_{corr} ; in the present study, the smallest window size is limited to 10 data points. The detailed procedure to determine these successive corrections is described in [120]. The heat conduction equation is solved in Laplace space, along with the boundary conditions and the approximate fit to the measured data in the i^{th} time window, to determine the surface temperature change. Finally, using the principle of superposition, the total surface temperature change is equal to the sum of surface temperature changes estimated using the measured temperature data in windows $i = 0$ to N_{corr} . The final solution is given as

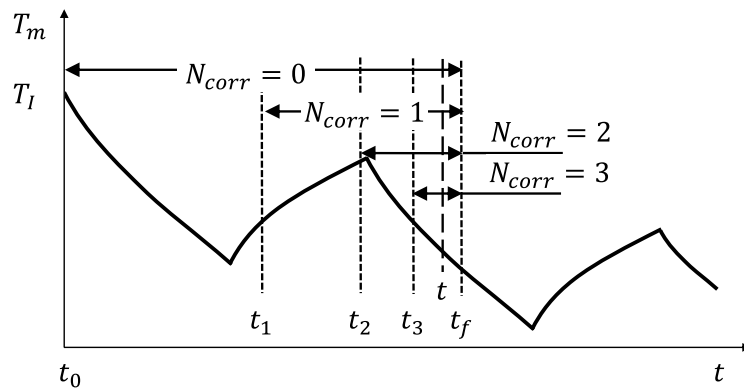


Figure 4.2. Data ranges used to calculate surface temperature and heat flux at time t [120].

$$T_s|_t - T_I = \sum_{i=0}^{N_{corr}} \sum_{k=-1}^{N_k} \frac{G_{i,k} \cdot (t - t_i)^{\frac{k}{2}}}{\Gamma\left(\frac{k}{2} + 1\right)}. \quad (4.7)$$

In principle, the surface heat flux can be obtained using the Fourier equation given below.

$$q_s|_t = -\lambda_T \cdot \left. \frac{\partial T}{\partial z} \right|_{t,z=0}. \quad (4.8)$$

The final solution is not given in [120]. They showed that the above model correctly estimates the surface heat flux, which is a square wave, for a finite plate up to Fourier number $\alpha_T \cdot t / Z^2 = 0.23$.

Woodfield et al. [120] further modified the semi-infinite solution for a thermally thick plate (boundary condition given in Eq. (4.3)). The solution is given as

$$\begin{aligned} T_s|_t - T_I = & \sum_{i=0}^{N_{corr}} \sum_{k=-1}^{N_k} \frac{G_{i,k} \cdot (t - t_i)^{\frac{k}{2}}}{\Gamma\left(\frac{k}{2} + 1\right)} \\ & + \sum_{i=0}^{N_{corr}} \sum_{n=1}^{\infty} \sum_{k=0}^{N_k} (-1)^n \cdot P_{i,k} \cdot (t - t_i)^{\frac{k}{2}} \cdot (2 \cdot i)^k \cdot \operatorname{erfc} \left(\frac{2 \cdot n \cdot Z - 2 \cdot n \cdot z_m - z_m}{2 \sqrt{\alpha_T \cdot (t - t_i)}} \right) \\ & + \sum_{i=0}^{N_{corr}} \sum_{n=0}^{\infty} \sum_{k=0}^{N_k} (-1)^n \cdot P_{i,k} \cdot (t - t_i)^{\frac{k}{2}} \cdot (2 \cdot i)^k \cdot \operatorname{erfc} \left(\frac{2 \cdot n \cdot Z - 2 \cdot n \cdot z_m + 2 \cdot Z - z_m}{2 \sqrt{\alpha_T \cdot (t - t_i)}} \right). \end{aligned} \quad (4.9)$$

Here, $\operatorname{erfc}(\cdot)$ is the complementary error function.

The 1-d thermally thick plate solution has been extended to a 2-d thick solid with boundary conditions given by Eqs. (4.3) and (4.4). The temperature at depth z_m is approximated as

$$(T - T_I)|_{t,r,z_m} = \sum_{i=0}^{N_{corr}} \sum_{j=0}^{N_j} J_0 \left(m_j \cdot \frac{r}{R} \right) e^{-\alpha_T \cdot m_j^2 \cdot (t - t_i) / R^2} \cdot \sum_{k=0}^{N_k} \frac{P_{i,j,k}}{\Gamma\left(\frac{k}{2} + 1\right)} \cdot (t - t_i)^{\left(\frac{k}{2} + 1\right)}, \quad (4.10)$$

where $J_0(\cdot)$ is a zero-order Bessel function of the first kind and the eigenvalue m_j is the j th positive root of $J_1(m_j) = 0$. Solving the problem defined by Eqs. (4.1)-(4.5) and (4.10) in Laplace domain and then making a inverse Laplace transform results in

$$T_s|_t - T_I = \sum_{i=0}^{N_{corr}} \sum_{j=0}^{N_j} J_0 \left(m_j \cdot \frac{r}{R} \right) e^{-\alpha_T \cdot m_j^2 \cdot (t - t_i) / R^2} \cdot \theta_{1D}|_t, \quad (4.11a)$$

$$\begin{aligned} \theta_{1D}|_t = & \sum_{k=-1}^{N_k} \frac{G_{i,j,k} \cdot (t - t_i)^{\frac{k}{2}}}{\Gamma\left(\frac{k}{2} + 1\right)} \\ & + \sum_{n=1}^{\infty} \sum_{k=0}^{N_k} (-1)^n \cdot P_{i,j,k} \cdot (t - t_i)^{\frac{k}{2}} \cdot (2 \cdot i)^k \cdot \operatorname{erfc} \left(\frac{2 \cdot n \cdot Z - 2 \cdot n \cdot z_m - z_m}{2 \sqrt{\alpha_T \cdot (t - t_i)}} \right) \\ & + \sum_{n=0}^{\infty} \sum_{k=0}^{N_k} (-1)^n \cdot P_{i,j,k} \cdot (t - t_i)^{\frac{k}{2}} \cdot (2 \cdot i)^k \cdot \operatorname{erfc} \left(\frac{2 \cdot n \cdot Z - 2 \cdot n \cdot z_m + 2 \cdot Z - z_m}{2 \sqrt{\alpha_T \cdot (t - t_i)}} \right). \end{aligned} \quad (4.11b)$$

The details for computation of $G_{i,j,k}$ are given in [119].

This model is implemented in Inverse2D. Woodfield et al. [120] classified a plate as thermally thick if the Fourier number based on the total time of experiment and height of the specimen is much less than one; for the test specimen used in the present study, the Fourier number is about 0.42 for the longest experiment (37 s). They showed that the model accurately determined the surface heat flux, which is a square wave, up to a Fourier number $\alpha_T \cdot t / Z^2 = 0.57$. Therefore, Inverse2D is appropriate for the inverse heat conduction analysis of the measured data in the present study.

4.1.2 Model parameters for Inverse2D

The choice of thermal properties and model constants for the present experiments are described here.

4.1.2.1 Thermal properties

The model in Inverse2D assumes that the thermo-physical properties of the solid are constant. Since the interest of this study is limited to $300\text{ }^{\circ}\text{C} \leq T_s \leq 900\text{ }^{\circ}\text{C}$, the solution has been determined using the thermal properties at $600\text{ }^{\circ}\text{C}$ ($\lambda_T = 21.9\text{ W} \cdot \text{m}^{-1} \cdot \text{K}^{-1}$, $c_T = 640\text{ J} \cdot \text{kg}^{-1} \cdot \text{K}^{-1}$ and $\rho_T = 7800\text{ kg} \cdot \text{m}^{-3}$).

4.1.2.2 Degree of half-polynomial to approximate the measured temperature history

The inverse model approximates the measured temperature data as a k^{th} -degree half-power polynomial series in time. Woodfield et al. [119] commented that increasing the degree of this half-polynomial would improve the time resolution of the inverse heat conduction solution. However, it should be noted that the fastest event that can be detected by the sensor is limited by its time-response. Hence, if a very high degree polynomial is used, it would just follow the higher frequency noise in the data. Woodfield et al. [119] recommended that the half-polynomial must be restricted to five terms ($N_k = 4$). Five terms in the half-polynomial, i.e. $N_k = 4$, has been found to be sufficient to approximate the temperature variation with time. With the use of a higher degree polynomial, only a minor change in the heat flux and temperature estimates is obtained. Hence, going with the recommendation by Woodfield et al. [119], $N_k = 4$ is chosen for approximating the time-temperature history.

4.1.2.3 Number of eigenfunctions to approximate the measured radial temperature distribution

Woodfield et al. [119] suggested that in order to improve the space resolution of the inverse heat conduction solution, radially up to 28 interpolation points can be used. In the present study, the measured cooling rate at the thermocouple location is much higher compared to the case discussed by Woodfield et al. [119]. As a result, even a slight difference in the time response of the thermocouples leads to non-physical temperature differences between neighboring thermocouples at any instant, especially near the jet impingement region. As stated in Section 2.5.2.1, detected disturbances at the depth are amplified by a factor of $\exp(2\pi z/l)$ to obtain the surface temperature, which induces errors in the surface heat flux distribution estimations. Hence, a careful selection of the value of N_j is critical to get a smooth and physically true surface heat flux distribution.

Figure 4.3 shows the effect of the value of N_j on the surface heat flux distribution at time $t = 1\text{ s}$ and the variation of the maximum heat flux with radius in experiment F2. Analysis with data points

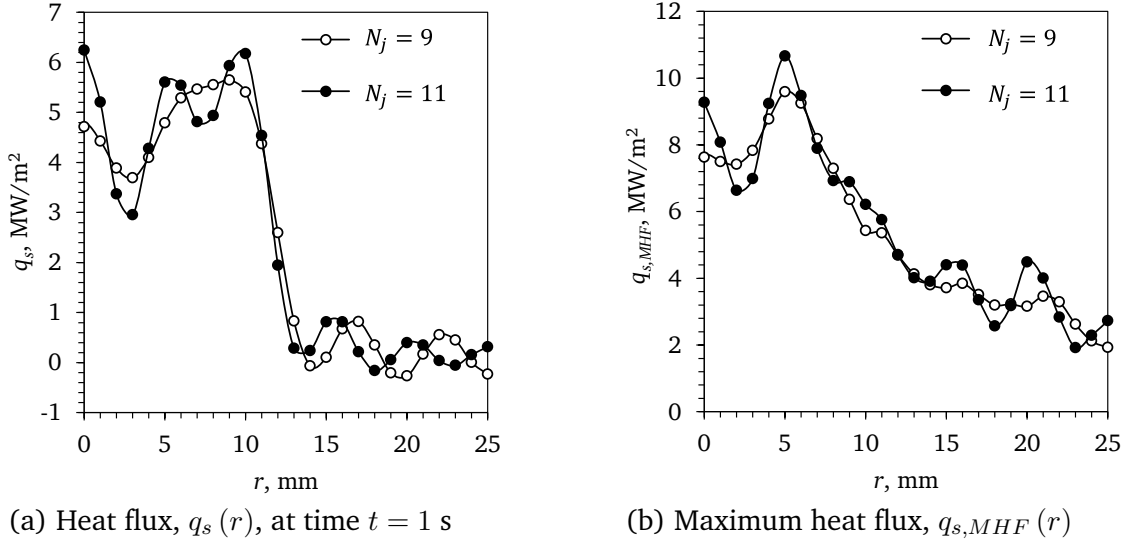


Figure 4.3. Effect of number of eigenfunctions used to approximate the radial temperature distribution at depth z_m for experiment F2.

equal to the number of thermocouples, i.e. $N_j = 11$, results in non-physical peaks in the heat flux distribution; with $N_j = 9$, these non-physical variations are mostly removed. Similar behavior is seen for other experiments as well. Hence, a value of $N_j = 9$ is chosen for the analysis.

4.2 Uncertainty in the heat transfer estimations

The reasons for the poor accuracy of transient heat transfer measurements have been discussed in Section 2.5.2.1. It has been commented that

“Due to non-uniqueness, all inverse heat conduction solutions will consist of low frequency components in time and long wavelength components in space. The inverse heat conduction solution can also be seen as an average over a time interval defined as the *time resolution*, t_{res} , and the over a width defined as the *space resolution*, r_{res} .”

The estimation of time and space resolutions are discussed in this section. It is to be noted that the choice of model constants is limited by the time response of the thermocouples and their radial pitch; hence, the time and space resolutions reflect the limitation of the measurement system and not the inverse model. In general, the resolution depends on the boundary condition [118]; here, the chosen representative values are the maximum of all the test cases. For estimating these limits, the direct heat conduction problem has been solved numerically in ANSYS-FLUENT for various heat flux boundary conditions, $q_{s,real}$, to calculate the temperature-time histories for the thermocouple junction's positions, i.e. at axial position z_m . Subsequently, the inverse heat conduction solution has been determined using Inverse2D. The inverse solution has been compared with the $q_{s,real}$ to estimate the time and space resolutions.

4.2.1 Time resolution and time shift

Woodfield and Monde [118] suggested a procedure to find the time resolution and time shift, where the approximation to the inverse heat conduction solution is given as

$$q_{s,inv}(t) \approx \frac{1}{t_{res}} \int_{t-\frac{t_{res}}{2}+t_{shift}}^{t+\frac{t_{res}}{2}+t_{shift}} q_{s,real}(t) \cdot dt. \quad (4.12)$$

To find the approximate value of the time resolution and the time shift, Eq. (4.12) is minimized as

$$\min F(t_{res}, t_{shift}) = \sum_{i=1}^n \left(q_{s,inv}(t_i) - \frac{1}{t_{res}} \int_{t_i-\frac{t_{res}}{2}+t_{shift}}^{t_i+\frac{t_{res}}{2}+t_{shift}} q_{s,real}(t) \cdot dt \right)^2. \quad (4.13)$$

In the present study, a simplified approach is used to determine the time resolution and the time shift. The time resolution and time shift are determined only at the time instant when the sign of the slope of real heat flux wave changes. The time resolution is determined by the following equation.

$$q_{s,inv,max} \cdot t_{res} = \int_{t-\frac{t_{res}}{2}+t_{shift}}^{t+\frac{t_{res}}{2}+t_{shift}} q_{s,real}(t) \cdot dt. \quad (4.14)$$

A schematic representation of Eq. (4.14) is shown in Fig. 4.4. It is essential to check the accuracy of the time resolution determined with the method in Eq. (4.14). The interpreted heat flux variation using the time resolution is given as

$$q_{s,int}(t) \approx \frac{1}{t_{res}} \int_{t-\frac{t_{res}}{2}+t_{shift}}^{t+\frac{t_{res}}{2}+t_{shift}} q_{s,real}(t) \cdot dt. \quad (4.15)$$

If the real heat flux variation is a non-symmetric perturbation, a time shift between the real distribution and the estimated distribution from the inverse analysis may occur. The time shift is schematically shown in Fig. 4.5 and is described as

$$t_{shift} = t|_{q_{s,inv,max}} - t|_{q_{s,real,max}}. \quad (4.16)$$

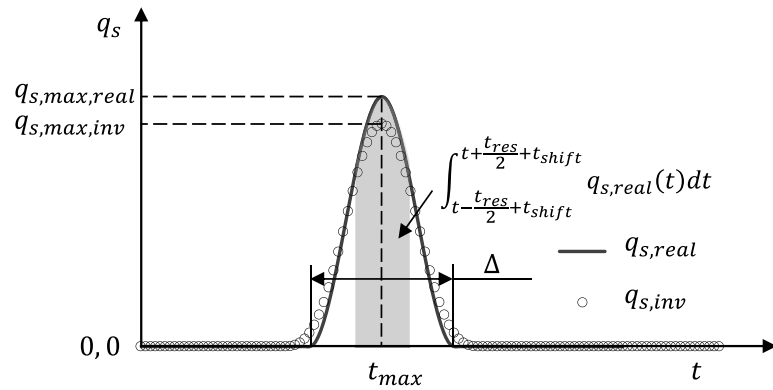


Figure 4.4. A schematic of the heat flux variation, $q_{s,real}(t)$, given by Eq. (4.17) and time resolution, t_{res} , described by Eq. (4.14).

The time resolution is determined for the following boundary conditions.

$$q_{s,real}(t) = \begin{cases} q_{s,max,real} \cdot \left[1 - 2 \cdot \left(\frac{t-t_{max}}{\frac{\Delta}{2}} \right)^3 - 3 \cdot \left(\frac{t-t_{max}}{\frac{\Delta}{2}} \right)^2 \right] & \text{if } (t_{max} - \frac{\Delta}{2}) \leq t < t_{max}, \\ q_{s,max,real} \cdot \left[1 + 2 \cdot \left(\frac{t-t_{max}}{\frac{\Delta}{2}} \right)^3 - 3 \cdot \left(\frac{t-t_{max}}{\frac{\Delta}{2}} \right)^2 \right] & \text{if } t_{max} \leq t < (t_{max} + \frac{\Delta}{2}), \\ 0 & \text{else.} \end{cases} \quad (4.17)$$

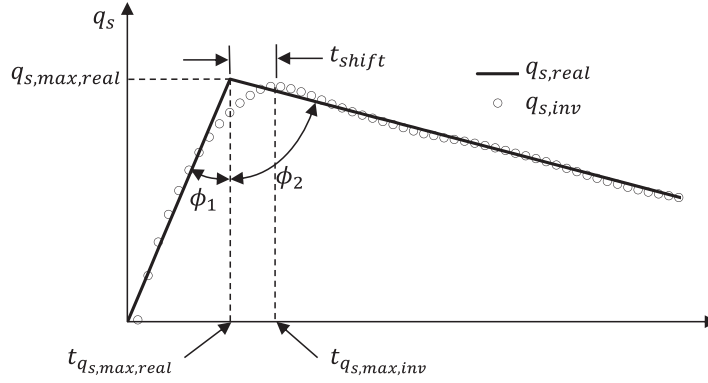


Figure 4.5. A schematic representation of the time shift, t_{shift} , described mathematically by Eq. (4.16).

The comparisons of the heat flux in the direct problem with the inverse heat conduction solution, and the interpreted heat flux with the inverse heat conduction solution are shown Fig. 4.6(a) and Fig. 4.6(b), respectively. The comparison has been shown for event of different time durations Δ . It can be seen that the interpreted solution is a good approximation of the inverse heat conduction solution. The error in the estimation of the peak heat flux value is plotted in Fig. 4.7. Table 4.1 shows the time resolution and the error in estimating the maximum value $q_{s,max,real}$ for duration Δ between 0.1 to 1 s. The largest value of time resolution is about 0.1 s, which is chosen as the representative value for this experimental study. Due to the symmetry of the thermal wave at t_{max} , time shift is zero for all the cases.

Δ	t_{res}	$\left \frac{q_{s,max,inv} - q_{s,max,real}}{q_{s,max,real}} \right \times 100\%$
0.05 s	0.09 s	71.77%
0.1 s	0.095 s	47.51%
0.2 s	0.098 s	17.85%
0.4 s	0.08 s	3.97%
0.5 s	0.08 s	2.37%
0.6 s	0.078 s	1.6%
1.0 s	0.078 s	0.574%

Table 4.1. Effect of the time duration Δ on the time resolution, t_{res} .

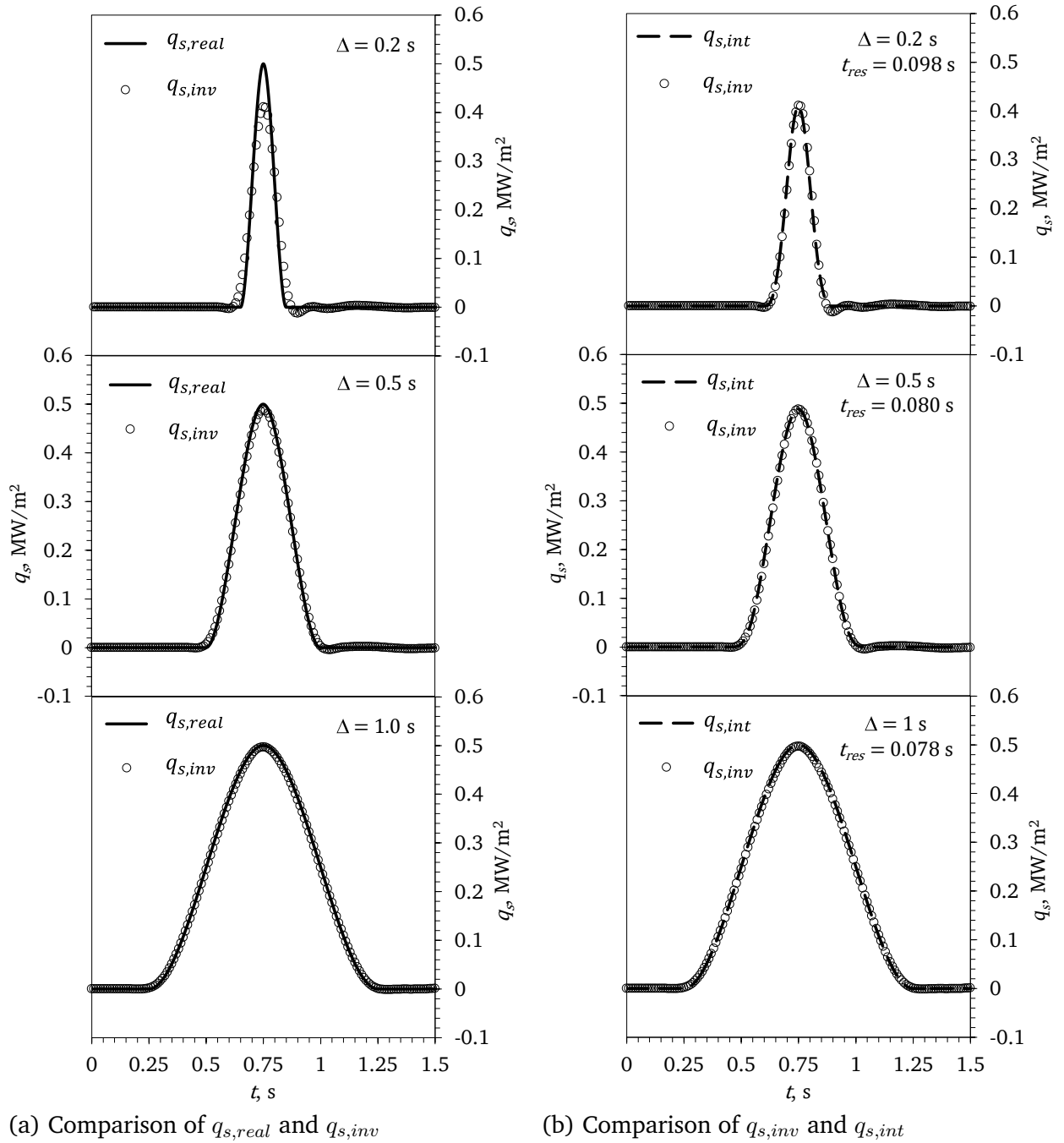


Figure 4.6. Effect of time duration Δ on the accuracy of the inverse heat conduction solution.

To determine the time shift, inverse heat conduction solution is determined when the actual event is a triangular thermal wave that is asymmetric at t_{max} (see Fig. 4.5). As is shown in Fig. 4.8, the time shift strongly depends on the shape of the thermal wave. The maximum time shift has been determined to be 0.06 s. It is difficult to choose a representative time shift value for the present experiment. As a conservative estimate, $t_{shift} = 0.06$ s is chosen as an appropriate representative value for the experiments.

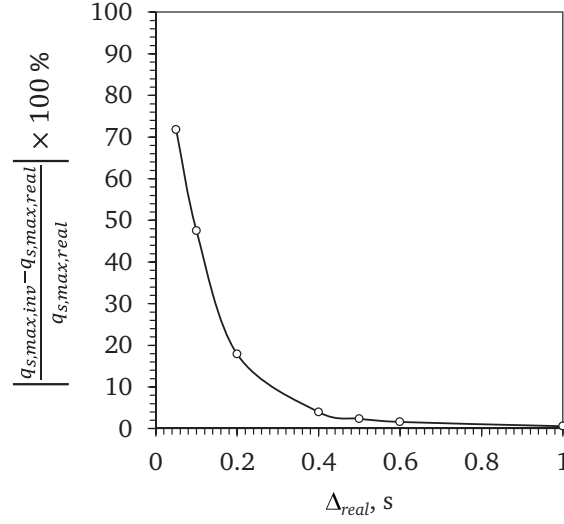
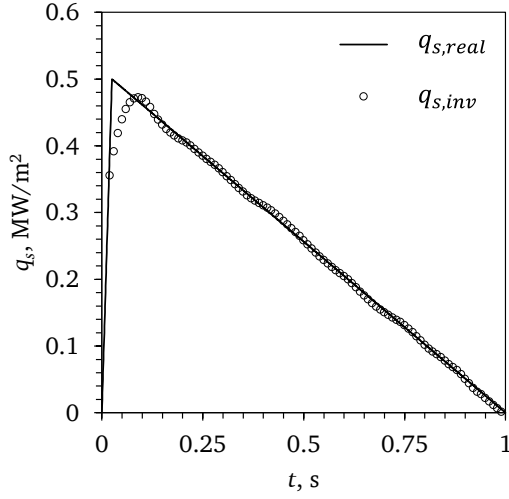
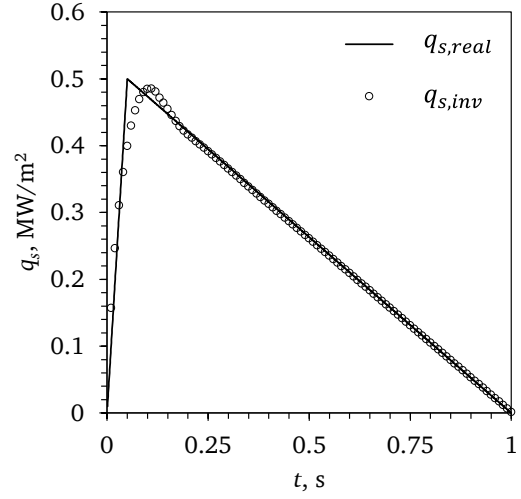


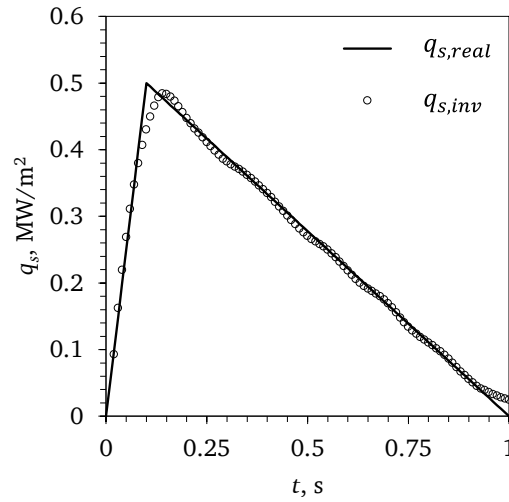
Figure 4.7. Error in estimating $q_{s,max}$ of a thermal wave.



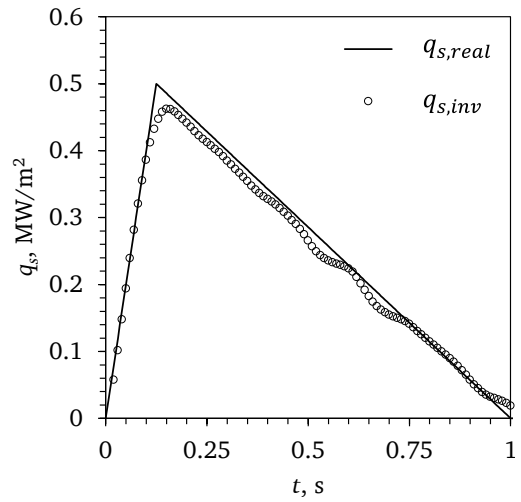
(a) $t_{max} = 0.025$ s



(b) $t_{max} = 0.05$ s



(c) $t_{max} = 0.1$ s



(d) $t_{max} = 0.125$ s

Figure 4.8. Comparison of $q_{s,real}(t)$ and $q_{s,inv}(t)$ showing the time shift in estimating a triangular thermal wave that is asymmetric at t_{max} .

4.2.2 Error in determining high frequency disturbances

In order to determine the fastest disturbance that can be resolved in the experiment, heat flux boundary condition described in the equation below is applied.

$$q_{s,real}(t) = q_{s,max,real} \cdot \left[1 - \frac{1}{10} \sin(2 \cdot \pi \cdot 2 \cdot t) + \frac{1}{10} \sin(2 \cdot \pi \cdot 3 \cdot t) + \dots + \frac{1}{10} \sin(2 \cdot \pi \cdot 29 \cdot t) \right]. \quad (4.18)$$

The signal spectrum is composed of prime number frequencies from 2 to 29.

Figure 4.9(a) shows the comparison of $q_{s,real}$ and $q_{s,inv}$. It can be seen that the inverse heat conduction solution consists only low frequency fluctuations. All high frequency fluctuations are damped by the inverse heat conduction solution. Results of a Fast Fourier Transformation (FFT) analysis of $q_{s,inv}$ is shown in Fig. 4.9(b). From the results of the FFT analysis, it can be concluded that surface disturbances with frequencies higher than 7 Hz can not be detected in the experiments.

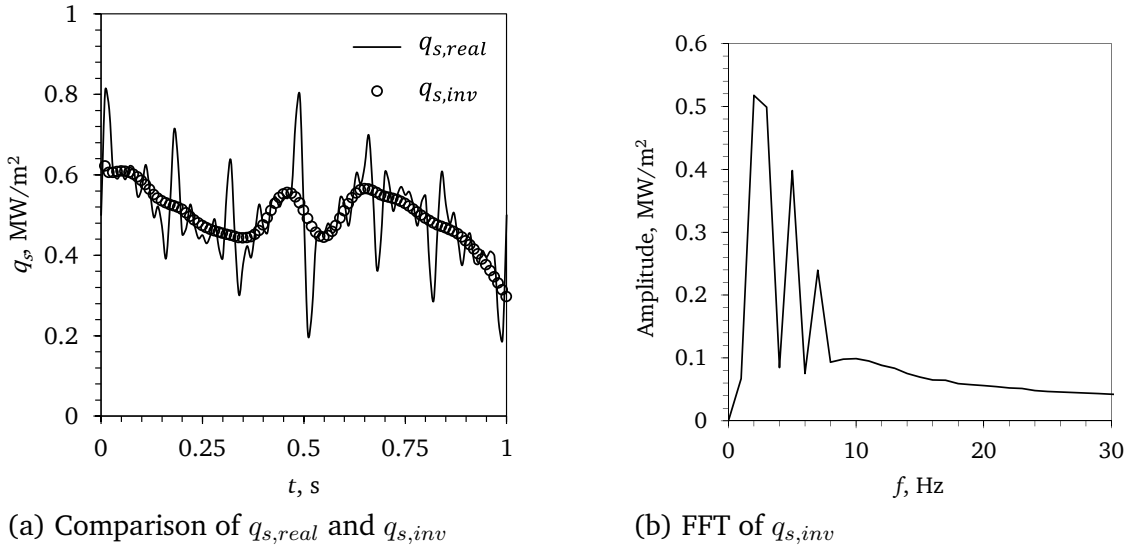
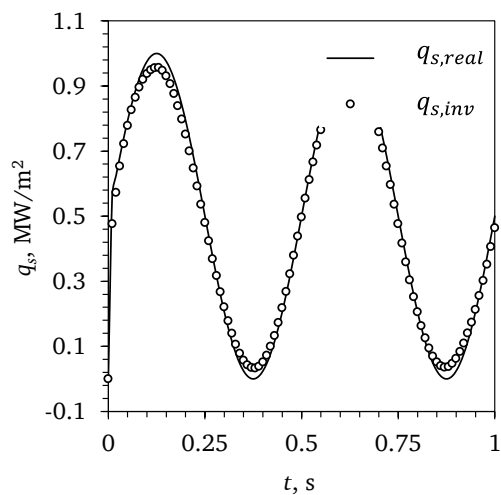


Figure 4.9. Limitations of the experiment in detecting high frequency components in thermal wave.

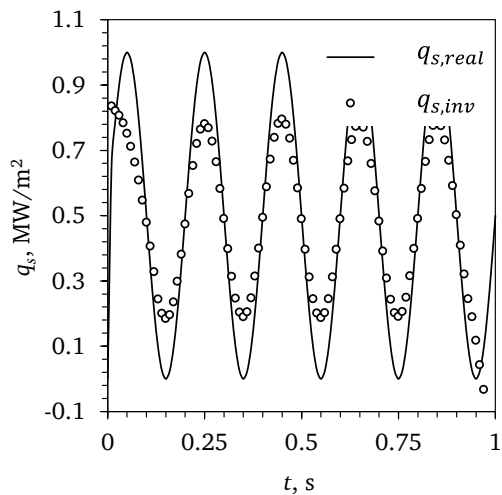
To determine the error in estimating the amplitude of high frequency disturbances, test cases with sinusoidal heat flux variation, as given by the following equation, are examined.

$$q_{s,real}(t) = q_{s,max,real} \cdot [1 - \sin(2 \cdot \pi \cdot f \cdot t)]. \quad (4.19)$$

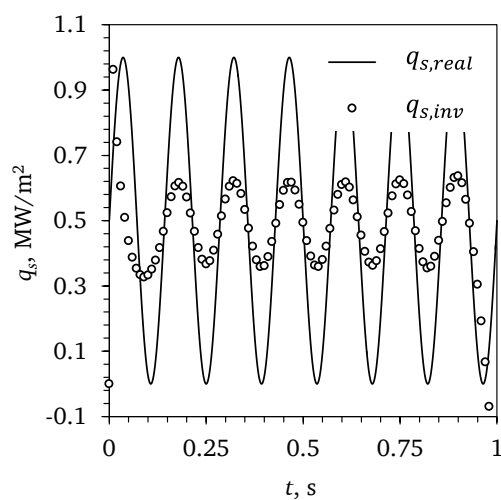
Figure 4.10 compares inverse heat conduction solution with real heat flux. As expected, the error in estimating the amplitude increases with the frequency of wave. Similar to the results shown in Fig. 4.9, 11 Hz disturbance can be hardly detected. However, the long term history, i.e. the non-periodic part of Eq. (4.19), is correctly determined. As shown in Fig. 4.11, the amplitude of a disturbance can be detected with an absolute error of less than 10% when the frequency is less than about 2 Hz.



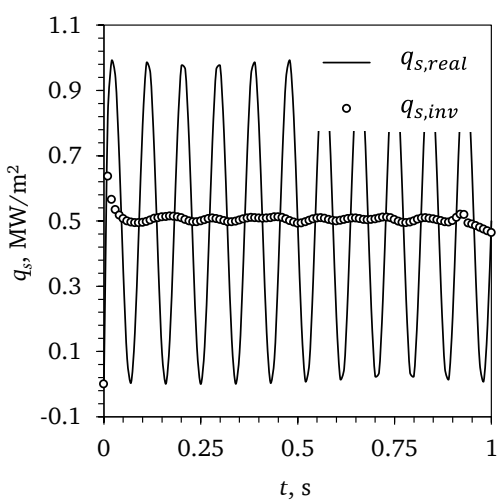
(a) $f = 2$ Hz



(b) $f = 5$ Hz



(c) $f = 7$ Hz



(d) $f = 11$ Hz

Figure 4.10. Effect of frequency, f , of the sinusoidal thermal wave on the accuracy of the inverse heat conduction solution.

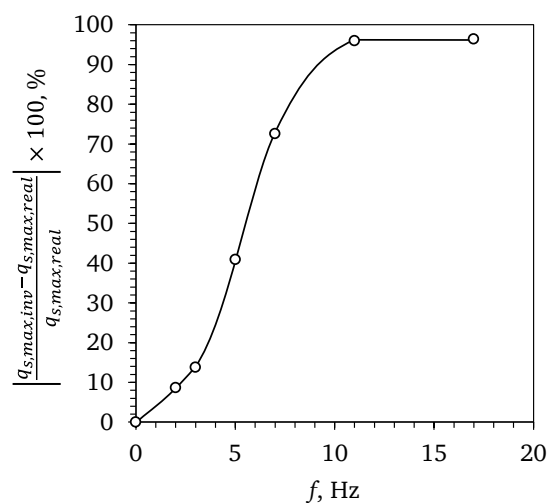


Figure 4.11. Error in estimation of the amplitude of a sinusoidal thermal wave.

4.2.3 Space resolution

Similar to the the method used to estimate the time resolution and time shift in Eqs. (4.14) and (4.16), the space resolution and space shift for a time-independent radial heat flux distribution are estimated by using the following equations.

$$q_{s,inv,max} \cdot r_{res} = \int_{r - \frac{r_{res}}{2} + r_{shift}}^{r + \frac{r_{res}}{2} + r_{shift}} q_{s,real}(r) \cdot dr. \quad (4.20)$$

$$r_{shift} = r|_{q_{s,inv,max}} - r|_{q_{s,real,max}}. \quad (4.21)$$

4.2.3.1 Stationary heat sink

To determine the space resolution, consider a finite width heat sink. The heat flux distribution within the heat sink is given as

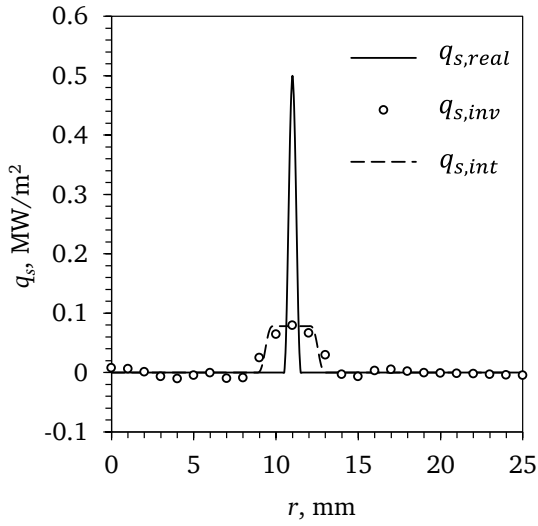
$$q_{s,real}(r) = \begin{cases} q_{s,max,real} \cdot \left[1 - 2 \cdot \left(\frac{r - r_{max}}{\frac{w}{2}} \right)^3 - 3 \cdot \left(\frac{r - r_{max}}{\frac{w}{2}} \right)^2 \right] & \text{if } (r_{max} - \frac{w}{2}) \leq r < r_{max}, \\ q_{s,max,real} \cdot \left[1 + 2 \cdot \left(\frac{r - r_{max}}{\frac{w}{2}} \right)^3 - 3 \cdot \left(\frac{r - r_{max}}{\frac{w}{2}} \right)^2 \right] & \text{if } r_{max} \leq r < (r_{max} + \frac{w}{2}), \\ 0 & \text{else.} \end{cases} \quad (4.22)$$

where $r_{max} = 11$ mm. The tests cases are divided into two categories based on the annular width: (a) $w \leq 2 \cdot \Delta r_m$, (b) $w > 2 \cdot \Delta r_m$.

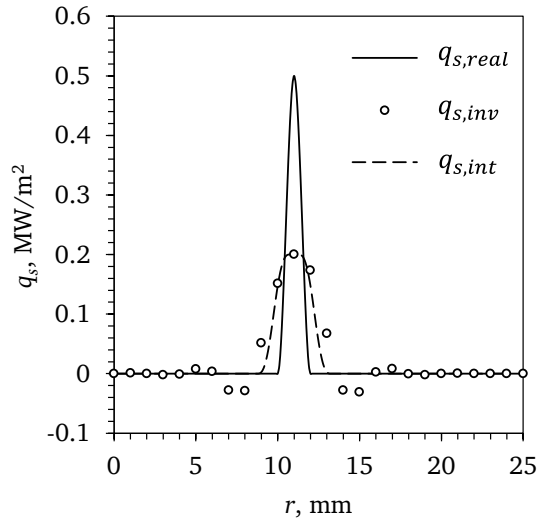
Figures 4.12(a)–4.12(d) show the comparison of the $q_{s,inv}$ with $q_{s,real}$ for $w \leq 2 \cdot \Delta r_m$. It can be seen that when the width w is less than the twice the thermocouple spacing Δr_m , the inverse heat conduction solution does not match with the real heat flux distribution. In addition, $q_{s,int}$ does not match well with $q_{s,inv}$. The reason for the large difference is that when $w < 2 \cdot \Delta r_m$, maximum up to 3 sensors are available within the heat sink, which are inadequate for the correct estimation of the heat transfer distribution within the heat sink. Figures 4.12(e) and 4.12(f) show the comparison of $q_{s,inv}$ and $q_{s,int}$ with $q_{s,real}$ for $w > 2 \cdot \Delta r_m$. It can be seen that the inverse heat conduction estimates are in a much better agreement with $q_{s,real}(r)$. Space resolution results for these cases are compiled in Table 4.2. Since the profile is symmetric, the space shift is 0 mm. Space resolution is in the range of 1.6 mm to about 3.2 mm. With increase in width the discrepancy between $q_{s,real}$ and $q_{s,inv}$ decreases. Similarly, the error in estimating $q_{s,max}$ reduces with increase in the heat sink width (see Fig. 4.13(a)). Table 4.2 also shows the predicted width of the heat sink, and the error in estimating the width (also shown in Fig. 4.13(b)). It can be seen that the inverse heat conduction solution always overpredicts the width, though the error in estimating the width of the heat sink reduces with increase in its width. A width of 5.6 mm is chosen for the determination of the space resolution for the case of a radially outwards moving heat sink.

4.2.3.2 Heat sink of constant width moving radially outwards at a constant speed

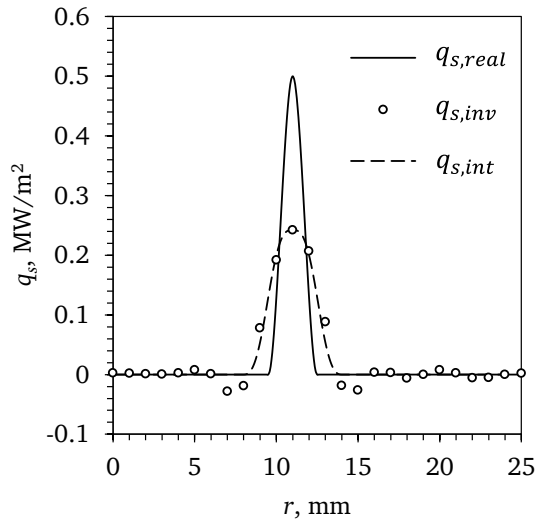
In the jet impingement quenching process, the wetted area grows in size with time, i.e. the maximum heat flux region moves radially outwards. A more realistic assumption of the surface boundary



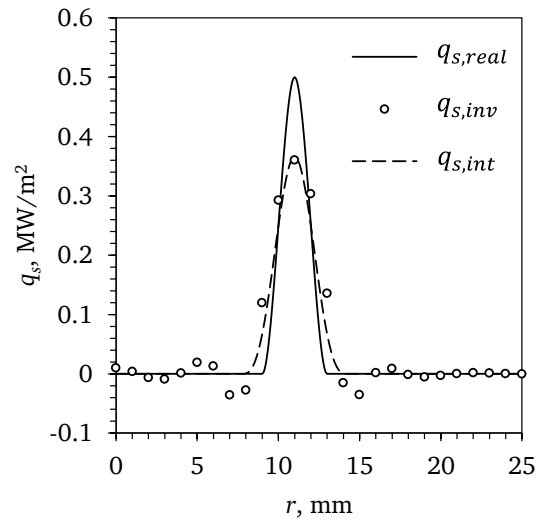
(a) $w = 1$ mm



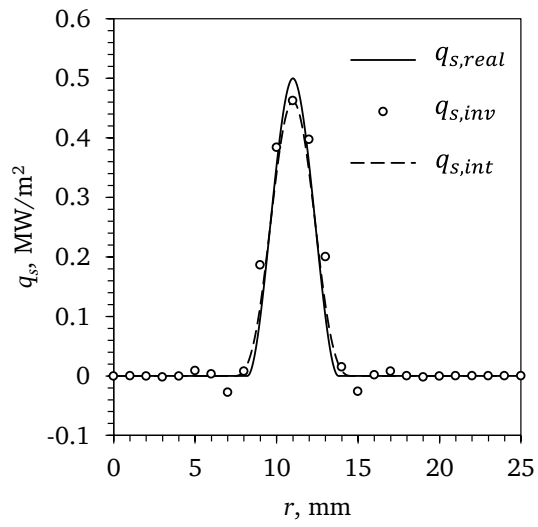
(b) $w = 2$ mm



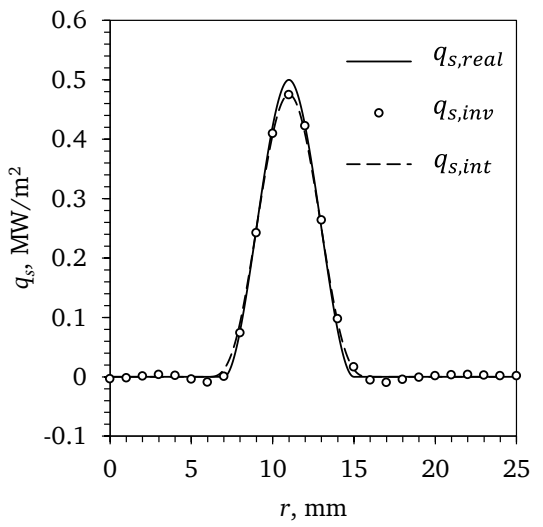
(c) $w = 3$ mm



(d) $w = 4$ mm



(e) $w = 5.6$ mm



(f) $w = 8$ mm

Figure 4.12. Comparison of $q_{s,real}(r)$, $q_{s,inv}(r)$ and $q_{s,int}(r)$ for different source widths w .

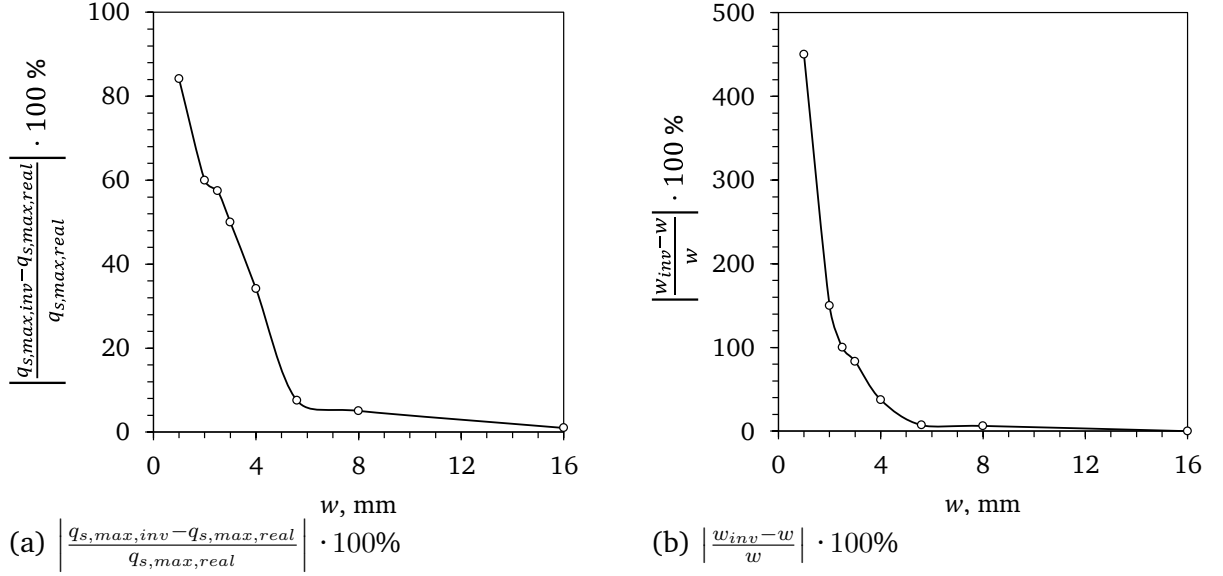


Figure 4.13. Uncertainty in the estimation of a stationary heat sink of width w .

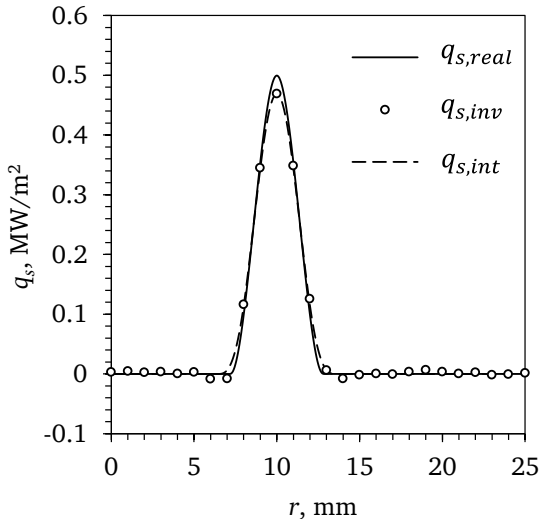
w	r_{res}	w_{inv}	$\left \frac{q_{s,max,inv} - q_{s,max,real}}{q_{s,max,real}} \right \times 100\%$	$\left \frac{w_{inv} - w}{w} \right \times 100\%$
1 mm	3.2 mm	5.5 mm	84.1%	260%
2 mm	2.4 mm	5 mm	59.9%	90%
2.5 mm	2.4 mm	5 mm	57.5%	84%
3 mm	3.0 mm	5.5 mm	51.6%	73.3%
4 mm	2.56 mm	5.5 mm	34.15%	45%
5.6 mm	1.6 mm	6 mm	7.5%	25%
8 mm	1.6 mm	8.5 mm	5.1%	5%
16 mm	1.6 mm	16 mm	1%	0%

Table 4.2. Variation of space resolution with the width of the heat sink, w .

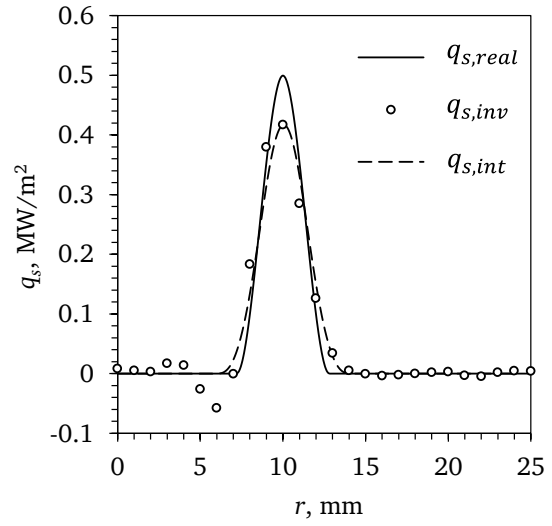
condition is a radially outwards moving finite width heat sink. To determine the space resolution, the inverse heat conduction solution performance is evaluated for a constant width heat sink of 5.6 mm, moving at a constant velocity v_w defined by

$$q_s(r, t) = \begin{cases} q_{s,max,real} \cdot \left[1 - 2 \cdot \left(\frac{r - v_w \cdot t}{\frac{w}{2}} \right)^3 + 3 \cdot \left(\frac{r - v_w \cdot t}{\frac{w}{2}} \right)^2 \right] & \text{if } (v_w \cdot t - \frac{w}{2}) \leq r < (v_w \cdot t), \\ q_{s,max,real} \cdot \left[1 + 2 \cdot \left(\frac{r - v_w \cdot t}{\frac{w}{2}} \right)^3 - 3 \cdot \left(\frac{r - v_w \cdot t}{\frac{w}{2}} \right)^2 \right] & \text{if } (v_w \cdot t) \leq r < (v_w \cdot t + \frac{w}{2}), \\ 0 & \text{else.} \end{cases} \quad (4.23)$$

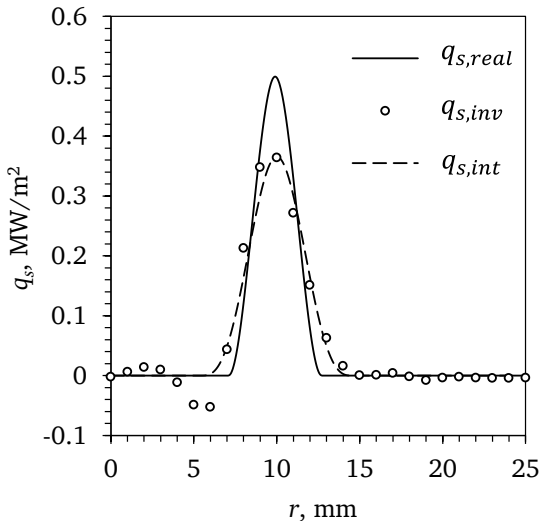
Figure 4.14 shows the estimated heat flux distribution when the peak of the thermal wave is at a radial position of 10 mm. With the increase in velocity, the difference between the inverse heat conduction solution and the real heat flux distribution increases, and the space resolution becomes poorer. Moreover, a space shift appears at higher velocity. Space resolution and space shift are compiled in Table 4.3.



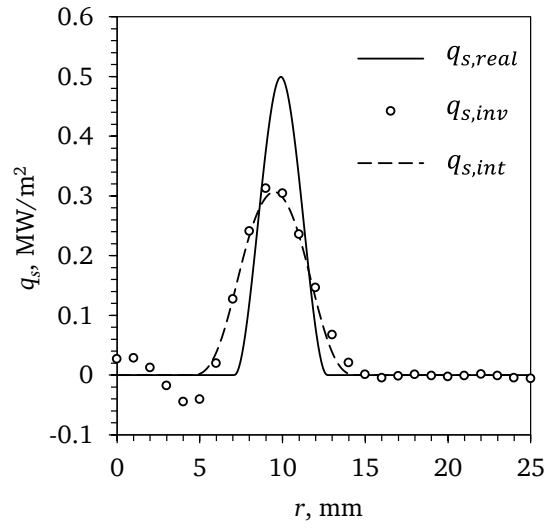
(a) $v_w = 5 \text{ mm/s}$



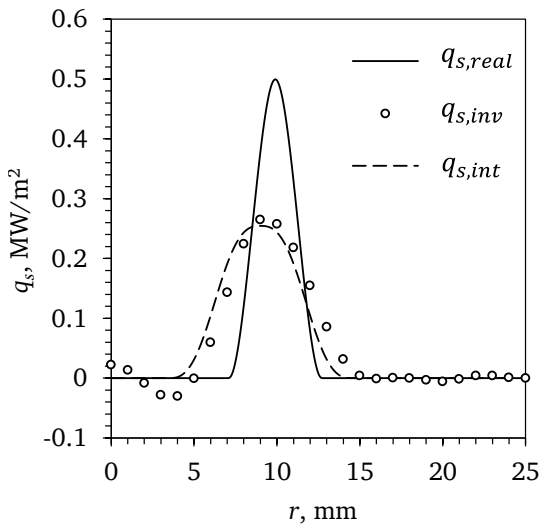
(b) $v_w = 25 \text{ mm/s}$



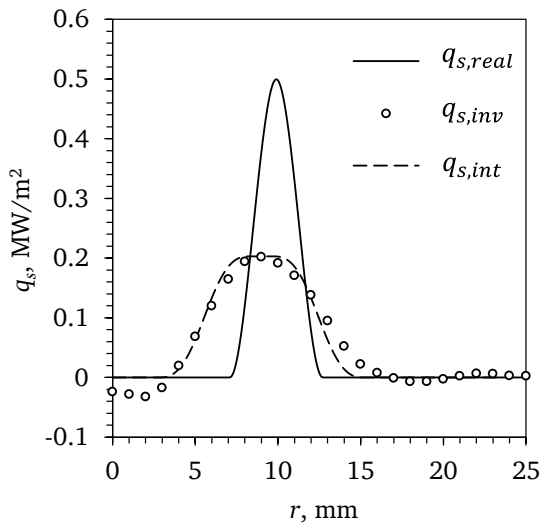
(c) $v_w = 35 \text{ mm/s}$



(d) $v_w = 45 \text{ mm/s}$



(e) $v_w = 55 \text{ mm/s}$



(f) $v_w = 75 \text{ mm/s}$

Figure 4.14. Comparison of $q_{s,real}$, $q_{s,inv}$ and $q_{s,int}$ when the peak of the radially outwards moving heat sink defined by Eq. (4.23) is at $r = 10 \text{ mm}$.

v_w	r_{res}	r_{shift}
0 mm/s	1.6 mm	0
5 mm/s	1.50 mm	0 mm
15 mm/s	1.7 mm	0 mm
25 mm/s	2.60 mm	0 mm
35 mm/s	3.5 mm	0 mm
45 mm/s	4.4 mm	-1 mm
55 mm/s	5.3 mm	-1 mm
75 mm/s	6.8 mm	-1 mm

Table 4.3. Effect of the movement of heat sink on the time resolution and shift.

4.2.4 Effect of temperature dependent properties

As already mentioned in Section 4.1, thermal properties at an average temperature of 600 °C are assumed in the inverse heat conduction solution. To test the error due to the assumption of constant thermal properties over the surface temperature range of 300–900 °C, the direct problem is solved using temperature-dependent thermal properties given by Eq. (A.1). A broad range of heat flux (0.5–5 MW/m²) has been considered. The heat flux in these cases is not varying with time or radius. The computed temperature-time history data is processed with Inverse2D using constant properties calculated at 600 °C ($\lambda = 21.9 \text{ W/m} \cdot \text{K}$, $c = 640 \text{ J/kg} \cdot \text{K}$ and $\rho = 7560 \text{ kg/m}^3$). Figure 4.15 shows $q_{s,real}$ and $q_{s,inv}$. For the range of surface heat fluxes considered here, the difference between the

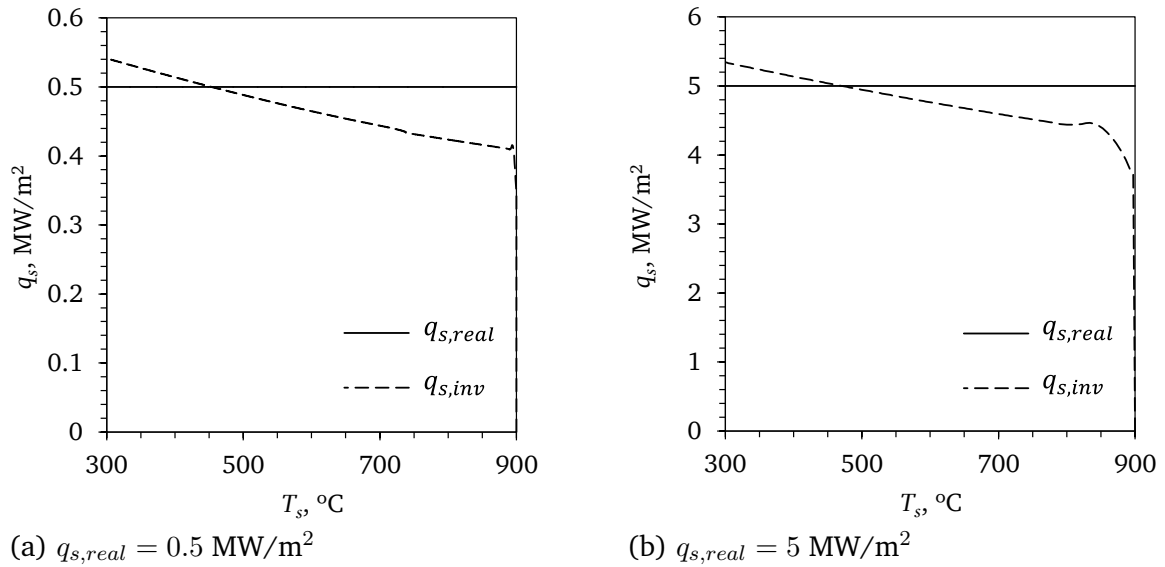


Figure 4.15. Error in the inverse heat conduction solution due to the use of constant thermal properties.

inverse heat conduction solution and the real heat flux for the surface temperature range of 300–900 °C is in the range of -20% to 10%. For the aforementioned temperature range, the thermal effusivity, $\sqrt{\lambda \rho c}$, is within $\pm 20\%$ of the value at 600 °C. In the case of transient heat transfer experiments, the thermal effusivity governs the heat transport rate and temperature distribution within

the solid. In this study, the error due to use of constant properties is found to be within the range of thermal effusivity variation of the stainless steel AISI-type 314.

4.2.5 Summary

From the analysis of uncertainty in the inverse heat conduction estimations, the following conclusions can be drawn.

1. A inverse heat conduction solution can be interpreted as a spatio-temporal average of the actual heat transfer variation.
 2. The time resolution is approximately 0.1 s.
 3. Frequencies higher than 7 Hz in the thermal waves can not be determined in the present experiment. The error in the estimation of the amplitude of thermal wave increases with the frequency. The error is more than 10% for frequencies higher than 2 Hz .
 4. The maximum time shift is estimated to be up to 0.06 s.
 5. The space resolution is in the range of 1.6–3.2 mm. The error in estimating the heat flux distribution within a moving heat sink increases with its velocity. Movement of heat sink also results in a space shift.
 6. The assumption of constant thermal properties leads to an uncertainty of up to $\pm 20\%$ over a surface temperature range of 300–900 °C. This error is within the range of variation in the thermal effusivity over the same temperature range.
-

4.3 Image analysis

The images captured by the high speed camera looking down over the impingement surface are post-processed in ImageJ and MATLAB image processing toolbox to determine the drop velocity. This procedure is described here and was developed by Schmidt [101] under the supervision of the present author.

The edges of many droplets are not sharp in these images due to the limitation of the lighting arrangement used for the measurement; hence, only a few droplets are chosen for analysis in any image. The chosen droplets are tracked in the image sequence from the instant of their first appearance till they go out of the field of view. A manual procedure is followed to track the droplet. The edges of the drops are highlighted using Sobel edge detector in ImageJ. Next, the images are transformed to binary with the careful selection of a gray threshold. Following this, the holes in the binary image are filled using MATLAB and the boundary of the chosen droplet is determined using the boundary tracing function in MATLAB [77]. Next, the center of mass of the droplet is determined. With the center of mass of the droplet known, the distance traveled by the droplets between subsequent images is determined and thereafter its drop velocity. It is found the velocity of splashed droplets is symmetric about the jet axis. In addition, the drop velocity is almost constant between consecutive images. The space resolution of the image is 75 μm and the time resolution is 1 ms.

4.4 Closure

In this chapter, the effectiveness of the inverse heat conduction model Inverse2D has been shown. Reasons for the uncertainties in the estimations are determined, though it is still not possible to quantify the overall uncertainty in the jet impingement quenching experiments. However, when

discussing and interpreting the results of the jet impingement quenching studies reported in the next chapter, these uncertainty estimates would be useful. The image analysis procedure developed by Schmidt [101] has been used for determining the splashed droplet velocity and these results are presented in Section 5.1.3. These results have been obtained by Schmidt [101] under the supervision of the present author.

5

Results and Discussion

This chapter is divided into three major section, with the first two sections dedicated to the observations, results and discussion of the free-surface jet impingement quenching. First in this chapter, the observed hydrodynamics of free-surface jet impingement quenching is described. Here, the distinct flow features and their evolution are discussed. Next, the heat transfer distribution upstream and downstream of the wetting front are presented. Results are presented in the form of estimated surface temperature, heat flux and boiling curves. Distribution of maximum heat flux, surface temperature at maximum heat flux and rewetting temperature are presented. The third section presents the results of plunging jet impingement quenching studies. It must be emphasized that repeated quenching studies on the same test specimen resulted in an eventual failure of the thermocouples below the impingement region, and therefore only a few plunging jet impingement quenching experiments have been performed. The effect of accumulated liquid on the surface heat flux and temperature distribution is discussed. The details of the experimental conditions for the free-surface and plunging jet impingement quenching experiments are given in Tables 3.1 and 3.2, respectively.

5.1 Free-surface jet impingement quenching: hydrodynamics

The hydrodynamics of the jet quenching process has been recorded using high-speed CMOS and low-speed video cameras. The low-speed videography provides information about the variation of the wetting front position as the quenching progresses, while the high-speed imaging provides information about the splashing patterns. Most of the high-speed measurements were done with the camera looking down on the impingement surface. Additionally, some high-speed images were recorded looking at the test specimen from the side and are reported in [57]. The general flow patterns observed in the experiments are presented and, wherever necessary, information about a specific experiment is given.

5.1.1 Flow patterns

Once the desired homogeneous initial temperature of the test specimen is reached, the jet impinges on the impingement surface. Immediately after impingement of the jet, the impingement surface in the stagnation region and around it appears dark, as can be seen in Fig. 5.1(a). At this time instant, the estimated impingement surface temperature, T_s , shown in Fig. 5.1(b), is still too high to permit stable liquid-wall contact; therefore, the cooling of the impingement surface is most likely not a reason for its dark appearance. One possible reason for the impingement surface to appear dark could be the absorption of the radiation emitted from the impingement surface by the liquid and vapor film. For $800\text{ }^{\circ}\text{C} \leq T_s \leq 900\text{ }^{\circ}\text{C}$, the peak of the gray body emission spectra is calculated using the Wien's displacement law to be within the range of 2471 to 2857 nm. Liquid water has a very high absorption coefficient in the wavelength range of 2700 to 3500 nm, while water vapor has a strong absorption band around a wavelength of 2400 nm; hence, the surface may appear dark.

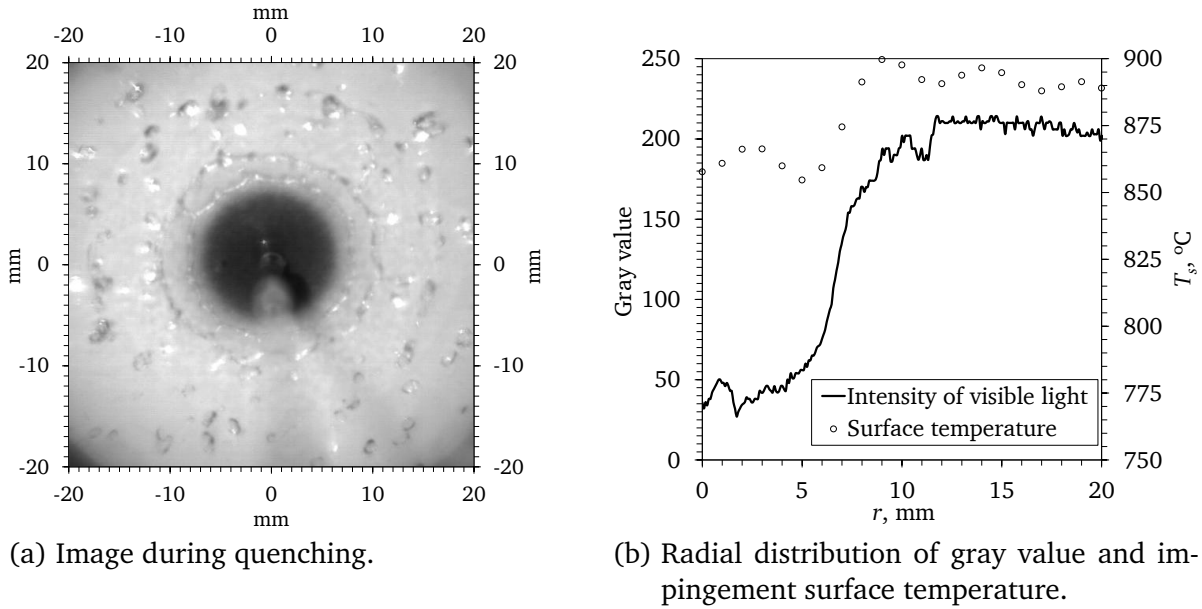


Figure 5.1. Formation of dark zone on the surface at time $t = 0.04\text{ s}$ in experiment F1.

A wetted zone appears around the stagnation region at about time $t = 100\text{ ms}$ in experiment F1. Since the boundary of this region is not very sharp at this moment, an image at time $t = 138\text{ ms}$ is shown in Fig. 5.2. For comparison, an image at $t = 76\text{ ms}$ is also shown, where no such zone could be identified. The impingement surface is at least partially wetted in this zone, which suggests that a boiling regime similar to film boiling might have existed the jet impingement region before the appearance of this zone. Unfortunately, since the time resolution of the heat transfer measurements is of similar duration, i.e. 0.1 s , the change from film boiling to transition boiling can not be resolved, e.g. in Fig. 5.3.

It is observed that the first appearance of wetted circle advances to $t = 58\text{ ms}$ in experiment F4 compared to $t = 100\text{ ms}$ in experiment F1 due to the increase in jet velocity. The wetted circle first appears at $t = 76\text{ ms}$ in experiment F2, which increases to $t = 150\text{ ms}$ in experiment F7 due to decrease in jet subcooling.

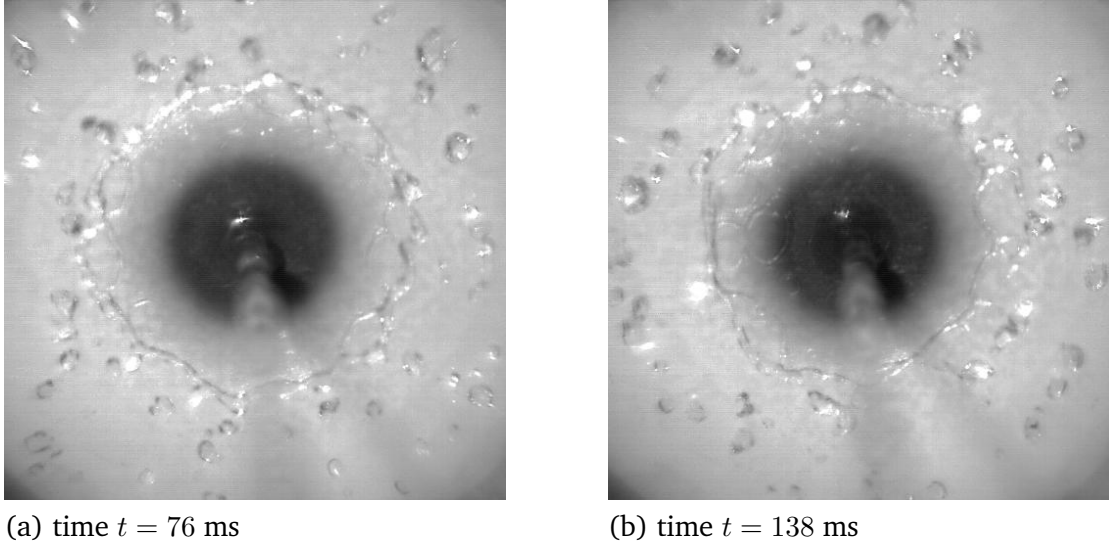


Figure 5.2. Formation of a wetted zone in experiment F1.

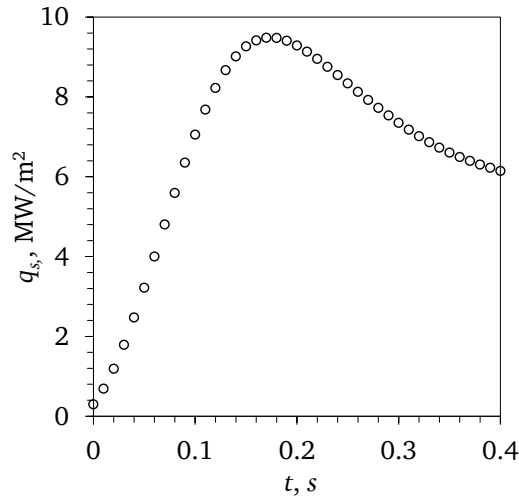


Figure 5.3. Heat flux, $q_s(t)$, at the stagnation point, $r = 0$ mm, in experiment F1. Since the time resolution of the inverse heat conduction solution is of the same order as the film boiling duration, the film boiling regime could not be identified.

Snapshots of the cooling process, showing the growth of the wetted region, are shown in Fig. 5.4. The wetted region is almost circular until it approaches the outer periphery of the surface, where some distortion of the wetted circle is seen. Three distinct regions on the quenched surface can be identified in the images obtained by high-speed imaging (see Fig. 5.5): (i) an expanding circular “wetted region” surrounding the jet (with its outer periphery named as the “wetting front”); (ii) an annular transition zone just outside the wetting front; and (iii) an “unwetted” or “dry region” outside this zone. The free-surface of the liquid appears smooth and shiny in the wetted region. No splashing of the liquid or disturbance of the free-surface is observed in this region and no visible evidence of boiling activity is available. Though both the wetted and annular transition region appear dark in color, the liquid free-surface in the annular transition region has a distinct disturbed liquid-gas interface. The disturbance is found to decrease with jet subcooling, which indicates that

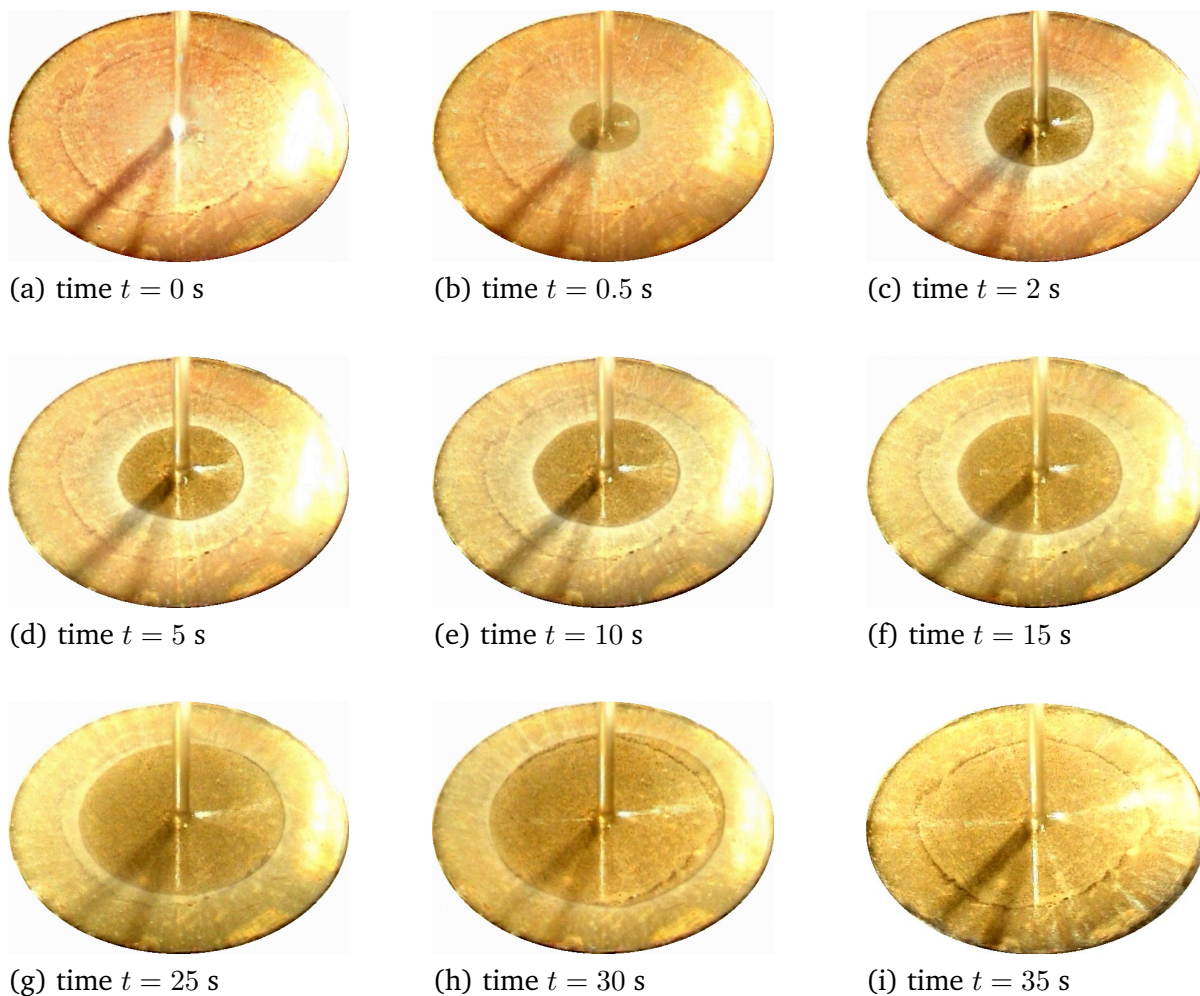


Figure 5.4. Low speed image sequence showing the wetted region growth in experiment F1.

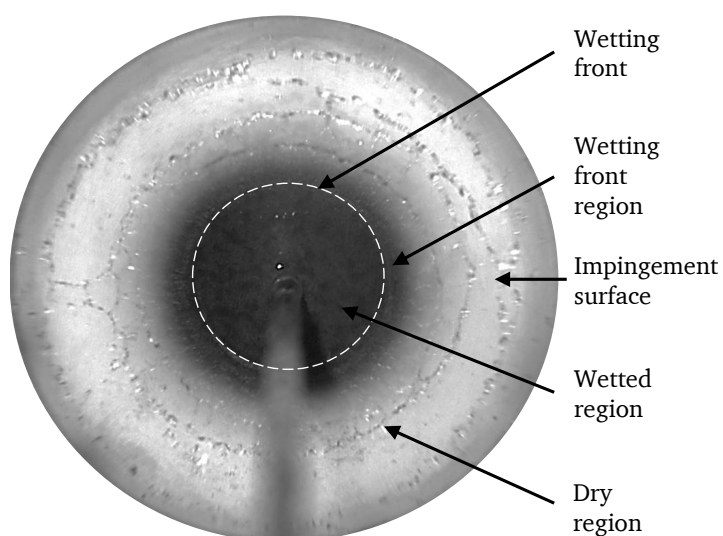


Figure 5.5. Identified heat transfer regions on the surface during quenching in experiment F6.

intense boiling activity happens in this region. At the outer periphery of this region, the liquid film is deflected away from the surface. Woodfield et al. [123] referred to this annular transition region as the “boiling region”. As is explained later in this thesis, it is determined from the estimated heat flux and surface temperature that boiling also happens in the wetted region. Therefore, the use of the terminology “boiling region” is a misnomer, and this region will be henceforth called as the “wetting front region”. The outer periphery of the wetting front region is difficult to define and it is not possible to determine its width. Hatta et al. [42] reported that during water jet ($d_N = 10$ mm, $v_N = 0.42$ m/s, $\Delta T_{sub} = 80$ K, $S = 0.2$ m) impingement quenching of a stainless steel plate, the wetting front region width increased from few mm to $r_w \approx 20$ mm as the wetted region expanded to a radius of 80 mm. Woodfield et al. [123] reported a wetting front region width of 6.1 mm at $r = 20$ mm for a water jet ($d_N = 2$ mm, $v_N = 3$ m/s, $\Delta T_{sub} = 20$ K) impinging on a carbon steel block with $T_I = 300$ °C. They also reported that the width decreased with increase in jet velocity and subcooling; it was suggested that the increase in the radial temperature gradient on the impingement surface with jet velocity and subcooling may be the likely reason for the decrease in the wetting front region width. In the present study, the initial temperature and thermal resistivity of the test specimen are higher than in the investigation of Woodfield et al. [123]. This would increase the radial temperature gradient and thereby reduce the wetting front region width.

At the outer edge of the wetted region, the liquid film is deflected away from the surface. The deflection happens due to forces exerted by the vapor generated in the wetting front region. Though the deflection angle is small, as seen in Fig. 5.6, no droplet contact with the dry surface is seen.

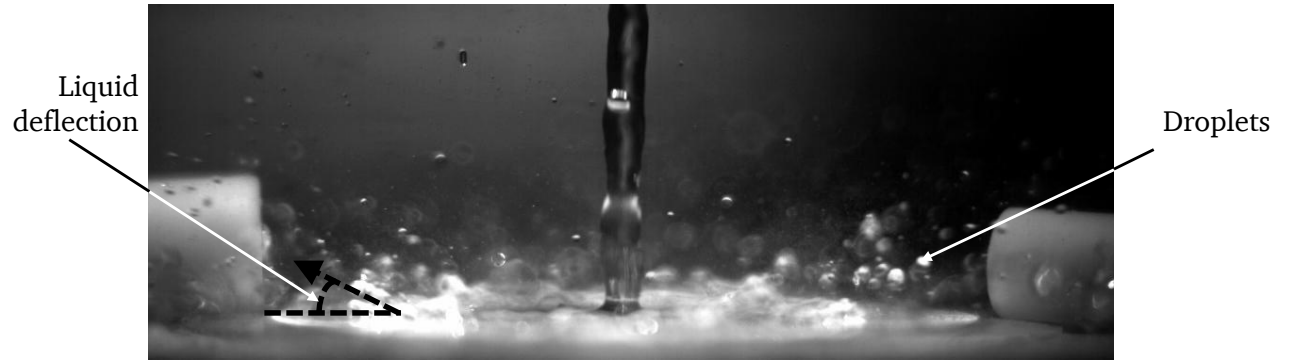


Figure 5.6. High-speed image showing the deflection of liquid film at time $t = 0.955$ s ($d_N = 3$ mm, $v_J = 2.85$ m/s, $\Delta T_{sub} = 80$ K) [57].

The rim of the deflected liquid sheet or lamella thickens due to surface tension forces, as is seen in Fig. 5.7, and then secondary jets are formed. These secondary jets then detach from the sheet to form ligaments, which eventually form droplets. Understanding the deflection phenomenon is of high significance to the jet quenching process because it limits the size of the wetted region. The quantitative assessment of the splashed droplet velocity has been made and its variation with time is discussed in Section 5.1.3. The image analysis procedure has been described in Section 4.3.

5.1.2 Wetting front dynamics

As the quenching progresses, the impingement surface within the wetted region and the wetting front region cools down by transferring its stored heat to the coolant. As an outcome, the boiling

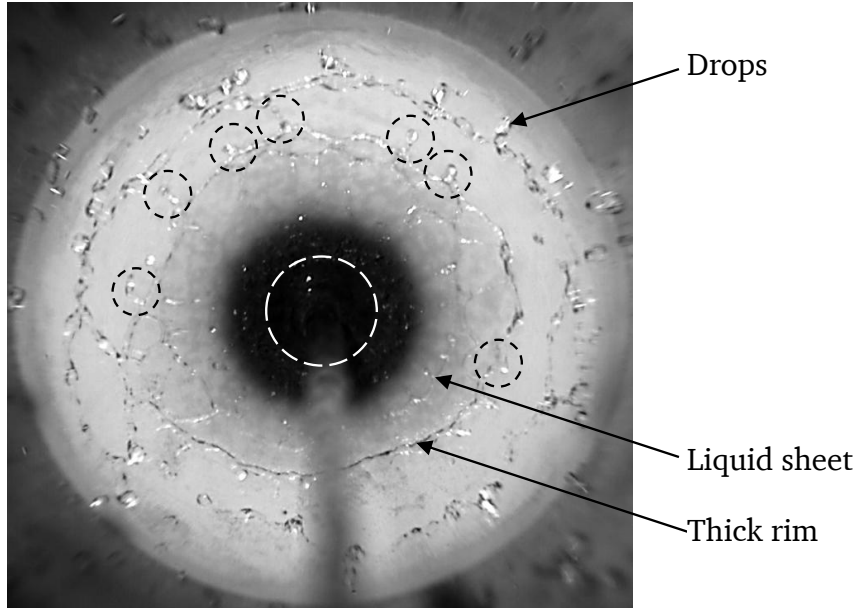


Figure 5.7. Lamella breakup and formation of secondary jets at time $t = 0.18$ s in experiment F6. The secondary jets are marked by enclosing black dotted circles.

activity reduces and the wetting front moves radially outwards, see Figs. 5.4 and 5.8(a). Here, r_w and v_w are the wetting front radius and velocity, respectively. The wetting front velocity decreases as the wetting front grows, as seen in Fig. 5.8(b). The propagation of the wetting front slows down with increasing radius, r_w , due to two reasons:

- The momentum of the liquid film reduces as it flows radially outwards; as a result, its ability to overcome the deflection force from the vapor bubbles reduces.
- The liquid subcooling reduces as it travels radially outwards, so its ability to condense the vapor bubbles in the wetting front region reduces. This leads to an increase in the net vapor efflux, which then leads to an increase in the deflection force on the liquid.

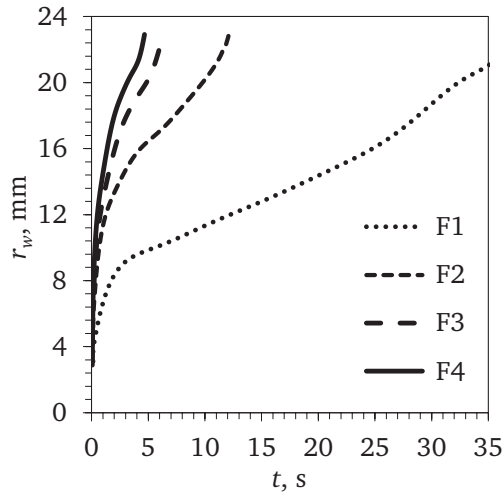
The wetting front velocity, v_w , increases with the jet velocity, v_J , and subcooling, ΔT_{sub} , as shown in Fig. 5.8. Since the liquid momentum increases with the jet velocity, the wetting front velocity also increases, as shown in Fig. 5.8(b). Similarly, the vapor efflux is reduced with increase in jet subcooling; as a result, the wetting front velocity increases, as shown in Fig. 5.8(d).

A power law relationship between the wetting front radius and time, i.e. $r_w = Ct^n$, has been suggested in [2, 42]. Hatta et al. [42] found that $n \approx 0.5$, while Akmal et al. [2] showed that the value of n depends on the jet subcooling and velocity. In this study, the n is 0.3 ± 0.05 . Constant C increases with jet velocity and subcooling, and is in the range of 6 to 14.

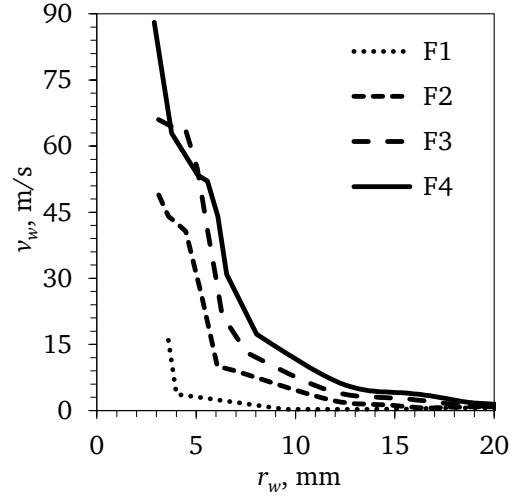
5.1.3 Boiling activity and wetting limits

The results presented in this section were obtained by Schimdt [101] while working under the supervision of the present author.

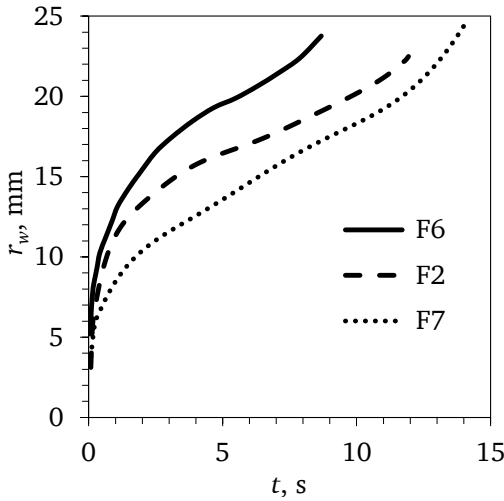
As stated previously, the liquid free-surface in the wetted region is smooth and no visual evidence of boiling is available. Figure 5.9 shows the surface heat flux, $q_s(r)$, and temperature, $T_s(r)$, in experiment F6. The average surface temperature in the wetted region is about 450 °C and the average heat flux is about 6.5 MW/m², which are typical of boiling heat transfer. When heat transfer



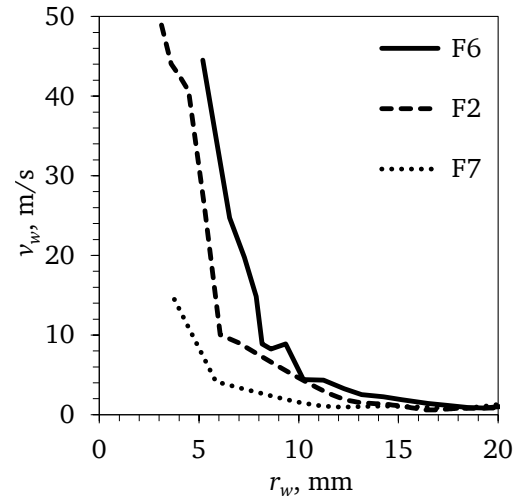
(a) Effect of jet velocity, v_J , on wetting front radius, r_w , at constant sub-cooling $\Delta T_{sub} = 75$ K.



(b) Effect of jet velocity, v_J , on wetting front velocity, v_w , at constant sub-cooling $\Delta T_{sub} = 75$ K.



(c) Effect of jet subcooling, ΔT_{sub} , on wetting front velocity, r_w , at constant jet velocity $v_J = 5$ m/s.



(d) Effect of jet subcooling, ΔT_{sub} , on wetting front velocity, v_w , at constant jet velocity $v_J = 5$ m/s

Figure 5.8. Effect of jet velocity, v_J , and subcooling, ΔT_{sub} , on wetting front growth.

measurements clearly suggest that boiling is happening, why does the wetted region looks bubble-less? Referring to Section 2.1, previous studies of bubble dynamics in flow boiling suggest that the bubbles that are formed in the wetted region must be very small and short lived. In the case of subcooled jet impingement heat transfer, the expected bubble departure diameter is $O(10) \mu\text{m}$ and the bubble lifetime of $O(0.1)$ ms. Since the temporal and spatial resolution of high-speed imaging in this study is only 1 ms and $75 \mu\text{m}$, respectively, and the shutter opening time is $40 \mu\text{s}$, it is not possible to observe these small bubbles. It is also possible that the bubble quickly condense in the subcooled liquid film after detachment; hence, the bubbles never grow up to reach the free-surface of liquid. Near the wetting front, some evidence of boiling is available. It is expected that the liquid free-surface within the wetting front region is most likely disturbed due to intense boiling activity.

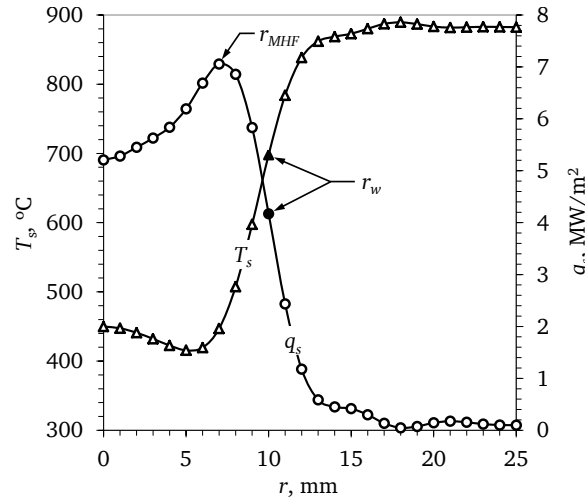


Figure 5.9. Heat flux, $q_s(r)$, and surface temperature, $T_s(r)$, at time $t = 0.5$ s in experiment F6.

As has been discussed earlier in this section, though the wetted region appears devoid of any bubble, extremely small bubbles may exist in this region. A question that remains unanswered is the role the bubbles in the wetted region might play in the overall phenomenon, specifically the wetting front growth. It is expected that as the bubbles slide along the impingement surface, they would alter the liquid flow, though the extent to which these bubbles alter the flow and their influence on the wetting front position is not known. It is difficult to experimentally determine the volume fraction of these bubbles in the liquid film and the resistance these bubble offer to the flow of liquid. The measurement of the liquid film thickness in the wetted region and comparing it with isothermal/single-phase liquid film measurements for the same jet parameters (v_J and d_J) can provide an estimate of the viscous resistance in the two-phase flow. However, the high temperatures involved in the experiments discourage the use of a film thickness measurement sensor. The other possible alternative is to measure the splashed droplet velocity and then make indirect estimations of the liquid film velocity in the wetted region. The velocity can be determined by processing the images obtained by high-speed photography looking from the top. Hence, to assess the condition of the flow, the splashed droplet velocity has been determined; indirect interpretation regarding the flow in the wetted region and its role in determining the wetting front position are then made from the determined splashed droplet velocity variation.

The variation of splashed droplet velocity, v_d , as the quenching proceeds in experiment F6 is shown in Fig. 5.10. It can be seen in Fig. 5.10(a) that the splashed droplet velocity is low in the first 0.1 s after the commencement of cooling. The splashed droplet velocity increases rapidly in the period from 0.1–0.3 s. After this, the splashed droplet velocity remains high at about 3 m/s with considerable fluctuations in the range of 2.6–3.4 m/s. For the same time instances, the wetting front position is also determined from these images. The splashed droplet velocity variation in relation to the wetting front position is shown in Fig. 5.10(b). It can be seen that when the wetting front is at position of up to 8 mm, the splashed droplet velocity is low. Similar variations of splashed droplet velocity are observed for the experiments F2 and F7, as shown in Fig. 5.11.

In order to understand the influence of boiling occurring in the wetted region on the liquid film flow, the liquid film velocity, $v_f(r)$, is determined for each radial position using Eqs. (2.6) and (2.7), assuming single-phase flow within the wetted region. The variation of $v_f(r)$ computed for the jet

parameters in experiment F6 is shown in Fig. 5.10(c). The film velocity decreases as the liquid flows radially outwards. If the flow in the wetted region is single-phase and no shear forces act on the liquid sheet after deflection from the impingement surface, then the splashed droplet velocity must be equal to $v_f(r)$. But the splashed droplet velocity shows a different trend in Fig. 5.10(b). The difference in the measured splashed droplet velocity, v_d , and estimated film velocity for single phase flow, v_f , is shown in Fig. 5.10(d). Similar results have been obtained for other experiments, as shown in Fig. 5.11. It is found that the splashed droplet velocity, v_d , is much lower than the analytically determined liquid film velocity at the wetting front for single-phase flow. This deficit decreases as the quenching progresses, before becoming zero approximate at wetting front position $r_w = 10$ mm. In the following paragraphs, an explanation for the observed splashed droplet velocity variation is given. Finally, a hypothesis regarding the state of flow in the wetted region and its influence on the quenching phenomenon is proposed.

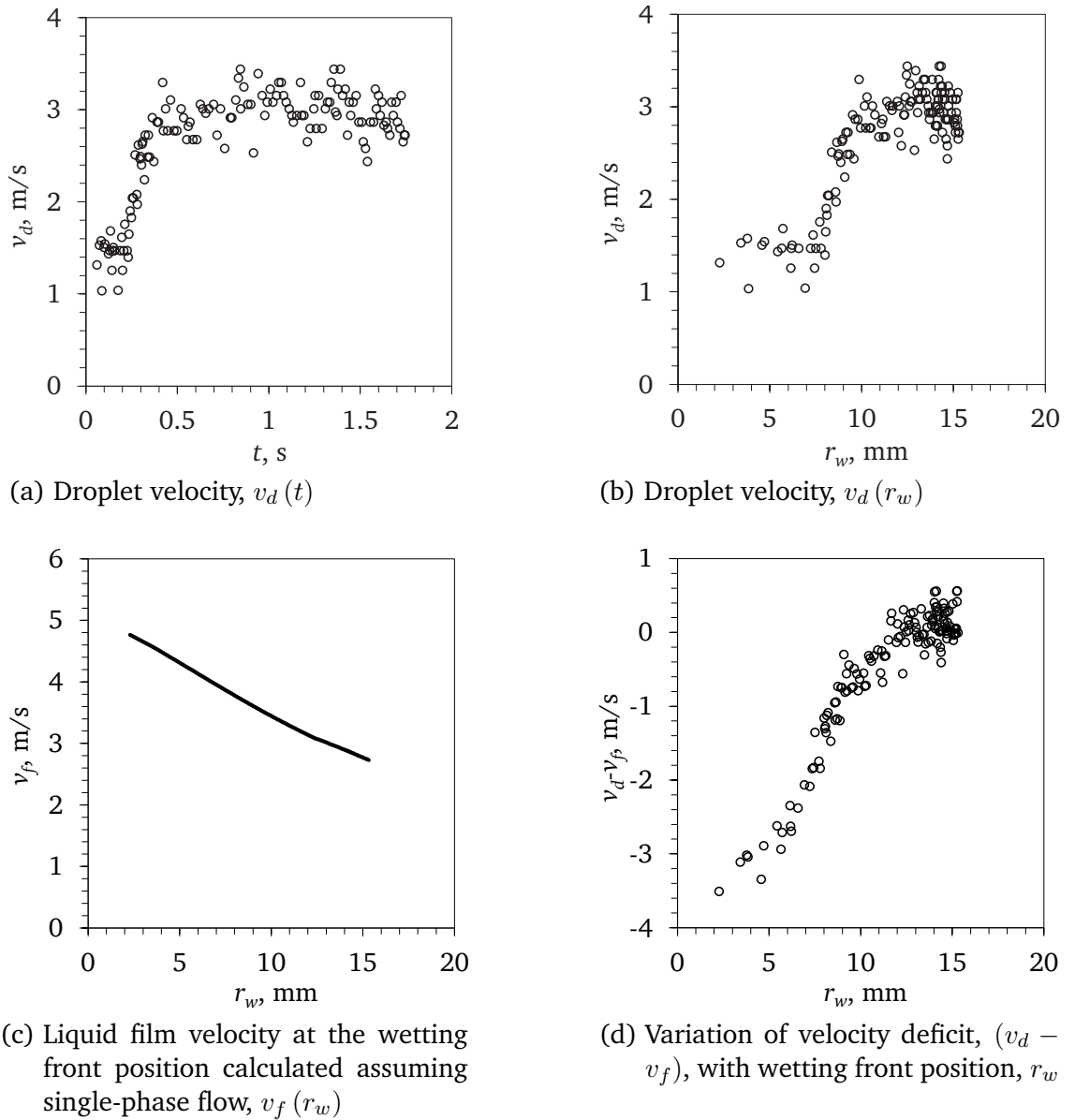


Figure 5.10. Splashed droplet velocity, v_d , in experiment F6 and its comparison with the theoretically determined single-phase film velocity, $v_f(r_w)$.

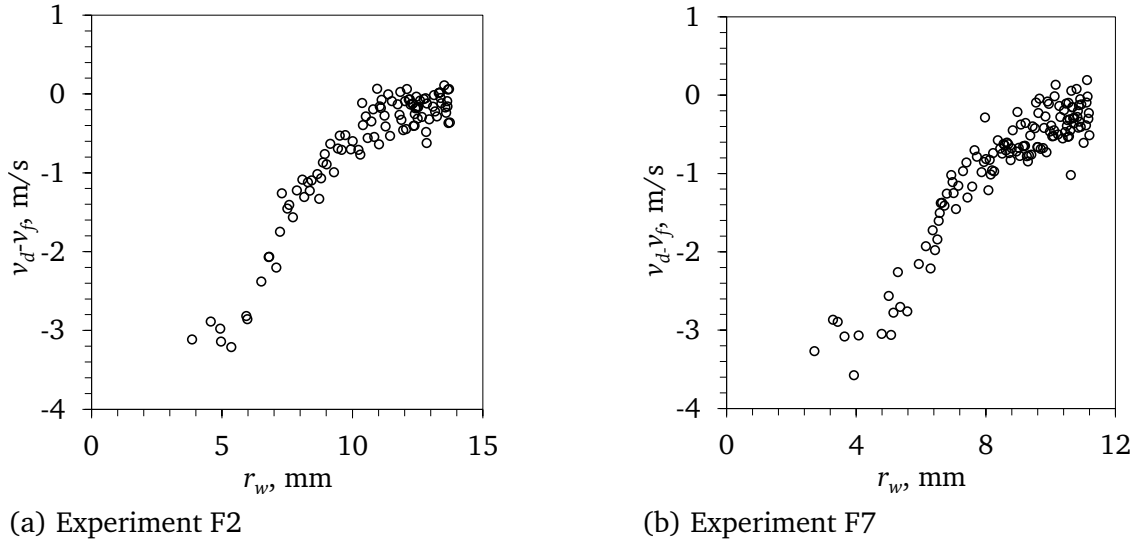


Figure 5.11. Variation of the velocity deficit, $(v_d - v_f)$, with the wetting front position, r_w , for $v_J = 5$ m/s.

It is seen in Fig. 5.12(a) that the heat flux at the stagnation point, $r = 0$ mm, is maximum in the time interval $0.15 < t < 0.25$ s, approximately the time when the droplet velocity is increasing. Similarly, up to radius $r = 6$ mm, the maximum heat flux, $q_{s,MHF}$, is reached when time $t < 0.3$ s. It is possible that the boiling activity in the wetted region provides resistance to the liquid film flow, thereby reducing the film velocity compared to the predicted value from the single-phase flow model of Watson [114]. At a certain radial position, the liquid film momentum reduces to the extent that the vapor is able to deflect it away from the surface. Figure 5.12(b) shows the variation of the maximum heat flux, $q_{s,MHF}$, with radial position, r , in experiment F6. The maximum heat flux, $q_{s,MHF}$, reduces with radius after $r = 6$ mm. This means that with increasing distance from the

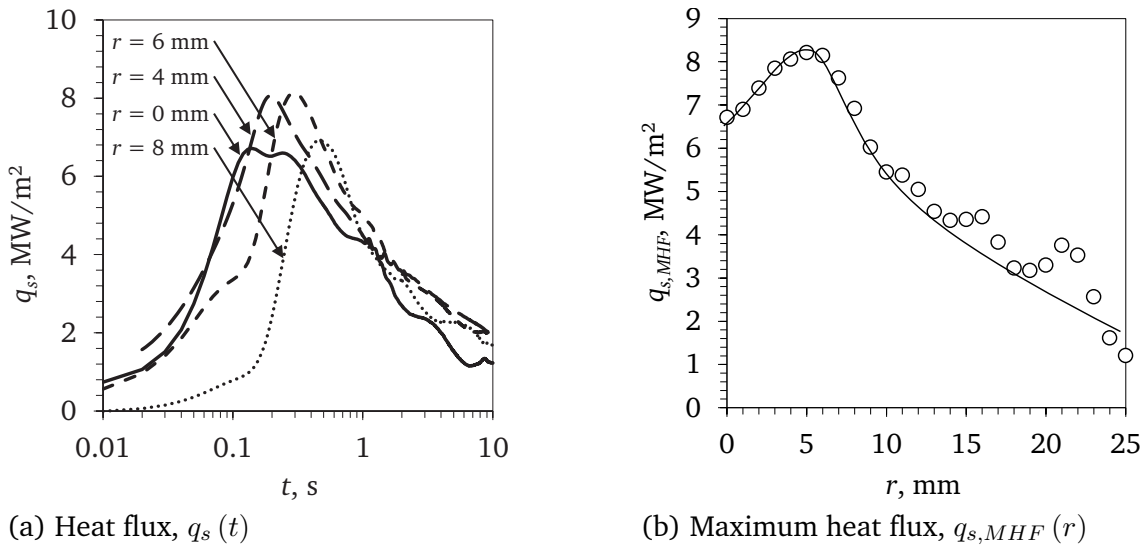


Figure 5.12. Heat transfer in experiment F6. Up to a radial position of 6 mm, the maximum heat flux, $q_{s,MHF}$, is reached when time $t < 0.3$ s. The maximum heat flux, $q_{s,MHF}$, reduces with radius after $r = 6$ mm, which means that the latent heat transfer increases with distance from the stagnation point.

impingement region, the latent heat transfer increases; hence, larger volume of vapor would be generated as the wetting front moves radially outwards. Larger volume of vapor would increase the deflection force on the liquid film and hence slow down the wetting front. Simultaneously, the vapor would accelerate the deflected liquid sheet. As a net balance between the deceleration effect of bubbles in the wetted region and the acceleration forces of the vapor efflux in the wetting front region, the droplet velocity first increases as the wetting front moves out before reaching an almost constant value. Another very important conclusion that can be drawn from the failure of the single-phase model of Watson [114] to predict the droplet velocity is that a strong two-phase flow regime exists in the wetted region, though it visually appears bubbles-less.

Figure 5.13 shows the variation of difference between the droplet velocity and computed single-phase liquid film velocity in experiment F5. It can be seen that the velocity deficit is much lower in this case compared to experiments F6. It should be noted here that larger volume of vapor is released in the wetting front region in experiment F5 compared to experiment F6 due to the lower liquid mass flow rate. This means that while significant deceleration of the liquid film might happen in the wetted region in experiment F5, the acceleration due to the vapor released in the wetting front region significantly reduces the velocity deficit.

Finally, a hypothesis is proposed as an outcome of this study. The film thickness and the resulting film velocity prediction using the model in [114] are only valid for a single-phase boundary layer developing within the liquid film in an isothermal system. During quenching, additional resistance to the liquid flow within the wetted region is due to the micrometer diameter vapor bubbles. The resistance of wall-attached bubbles in flow boiling has been discussed in brief in Section 2.1.2. Thus, a thicker two-phase film is formed in the wetted region as compared to the predicted film thickness from the model in [114] and the film velocity reduces. The boiling activity increases as the liquid approaches the wetting front, which results in rapid deceleration of the liquid film within the wetted region. At a certain radial position, the liquid momentum reduces to the extent that the force of the vapor released in the wetting front region is able to deflect the liquid away from the surface. Once deflected from the surface, the liquid film is accelerated by the large volume of vapor released in the wetting front region and it finally breaks into droplets. As the wetting front moves radially outwards, larger volume of vapor is released in the wetting front region, which increases the forces on the deflected sheet. Thus, while the approach velocity of the liquid film to the wetting front reduces as the wetting front moves radially outward, the droplet velocity increases or remains constant.

Though a slight increase in the splashed droplet velocity with increase in jet temperature from 12 to 40 °C is seen at jet velocity $v_J = 5$ m/s, there is no substantial evidence in support of the hypothesis presented above. Hence, the experiment at $v_J = 5$ m/s and $T_L = 70$ °C ($\Delta T_{sub} = 30$ K) has been carried out. From the variations of r_w and v_d with t shown in Fig. 5.14, it can be seen that the wetting front stops growing beyond $r_w = 6.5$ mm after time $t = 0.25$ s. The liquid sheet disturbance in the wetting front region is found to be more intense than during the experiments at high jet subcooling (experiment F2, F6 and F7 with jet subcooling of 87, 75 and 60 K, respectively); this means that very large volume of vapor is generated that provided enough force to deflect the liquid film and stop the wetting front growth. The droplet velocity is also significantly higher in this situation at radial position $r = 6.5$ mm compared to experiment F6. The effect of decrease in the liquid viscosity, with jet subcooling, on the film velocity is calculated to be small (only up to 10%).

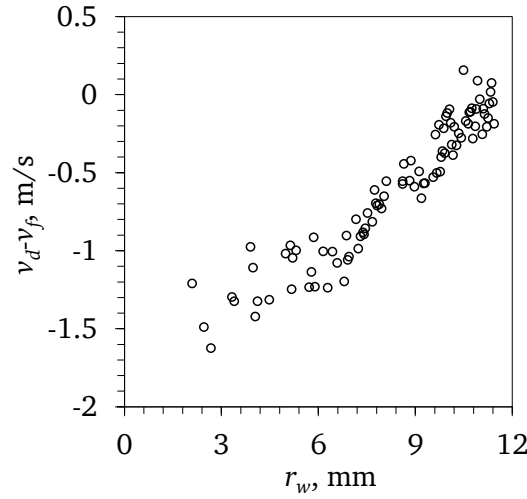


Figure 5.13. Variation of velocity deficit, $(v_d - v_f)$, in experiment F5 ($v_J = 2.5$ m/s). Here, the velocity deficit is much lower compared to that in experiment F6 ($v_J = 5$ m/s).

This means that the acceleration of the deflected liquid sheet increases significantly with the liquid temperature. This result provides supporting evidence to the proposed hypothesis. Furthermore, with increase in the liquid temperature, the splashing was observed to be more intense, which resulted in the droplets being spread far away from the test section.

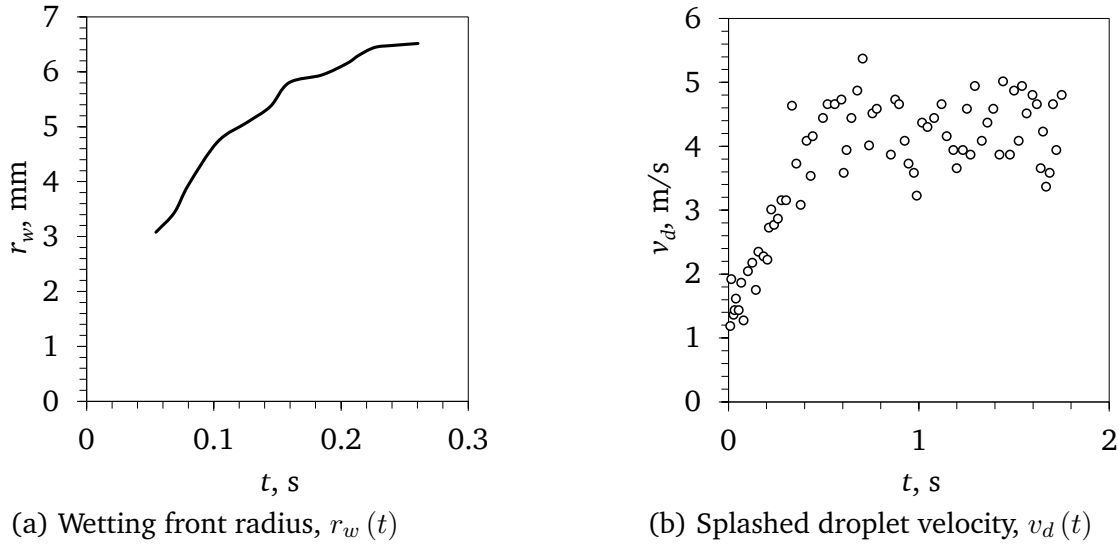


Figure 5.14. Variation of wetting front radius, $r_w(t)$, and droplet velocity, $v_d(t)$ ($T_I = 900$ °C, $v_J = 5$ m/s and $\Delta T_{sub} = 30$ K).

Due to the extremely high temperatures involved in the present experiments, limited measurements of the film hydrodynamics could be performed in this study. Besides this, the measurement of film thickness in the wetted region could not be made. Further investigations are needed in order to understand more about the role of the two-phase flow in the wetted region in determining the wetting limits. Such measurements probably must be made at a reduced pressure with fluids having low boiling point, thereby reducing the maximum system temperature. The lower temperature would allow the use of film thickness sensors such as Confocal chromatic sensor [112].

5.1.4 Summary

The following conclusions can be drawn from this study:

1. Three distinct heat transfer regions can be identified over the impingement surface based on the state of liquid-wall contact: (i) a central wetted region with a smooth free-surface of liquid; (ii) an annular wetting front region surrounding the wetted region; (iii) an outside dry region. Around the wetting front region, the liquid is deflected from the surface as a lamella, which then breaks into droplets due to surface tension and shear forces.
2. The wetting front velocity increases with jet velocity and subcooling.
3. As the quenching progresses, the average splashed droplet velocity increases and then takes a constant value. The droplet velocity is strongly governed by the jet velocity, while a moderate dependence on jet subcooling is seen.
4. The droplet velocity is significantly lower compared to the liquid film velocity at the wetting front position as calculated using the single-phase flow model of Watson [114]. The difference between these velocities reduces as the wetting front moves radially outwards. It is hypothesized that a two-phase flow occurs in the wetted region, though it could not be visually confirmed, and the liquid is decelerated as it reaches the wetting front. At the wetting front, the flow resistance from the vapor released in the wetting front region is strong enough to deflect the liquid film from the hot steel surface. The deflected liquid sheet is then accelerated by the vapor generated at the wetting front. The generation of the vapor increases as the wetting front moves radially outwards, causing an increased acceleration of the lamella, which causes the droplet velocity to increase.

5.2 Free-surface jet impingement quenching: heat transfer

The transient surface temperature and heat flux distributions have been obtained by solving the inverse heat conduction problem using the measured temperature. In this section, the results of the heat transfer studies are presented.

5.2.1 Uncertainty in the heat transfer estimations

In the previous chapter, the limitations of the present measurements owing to sensor distance from the impingement surface and radial spacing have been described. It has been stated that the heat transfer results must be interpreted as an average over time and space (radius). The objective of this section is to understand these limitations in perspective with the jet impingement quenching experiments reported in this thesis. It is to be noted here that the propagation of error technique frequently used to access the overall uncertainty of steady state heat transfer results is different from the uncertainty analysis reported in the previous chapter. The propagation of error technique determines the sensitivity of the results to the measurement errors and, therefore, is deterministic. On the other hand, the analysis reported in the previous chapter only determines the limits within which any information can be determined from a transient experiment and it is not possible to quantify the errors in the experiment. This analysis, however, can be used as a guide by other researchers to devise techniques for faithful temperature measurement, whereby the rapid heat transfer changes can be predicted.

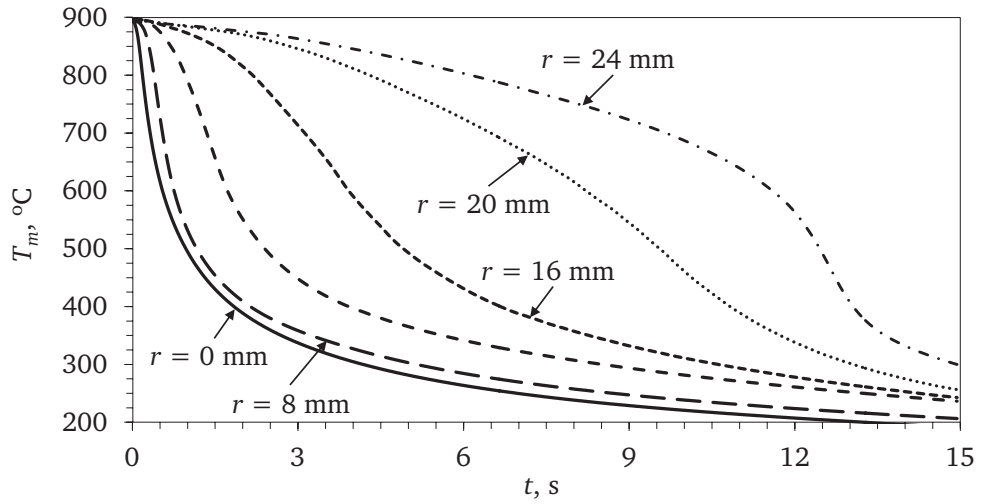
It has been determined previously that if the heat transfer rate changes rapidly or the annular region of intense heat transfer is narrow, the maximum heat flux is underestimated. Some examples of possible erroneous results are given here, however the extent of error could not be assessed.

- The first appearance of the wetted circle in the impingement region is visually determined to be in the time interval $0.05 \leq t \leq 0.15$ s. It was not possible to determine the sensor time response for the embedded configuration used in this study, but it can be safely assumed to be up to 0.1 s; if the frequency of thermal wave during the initial few seconds of quenching is comparable, the used thermocouples would lag behind and therefore the correct temperature can not be measured and considerable errors may be expected in the heat flux estimations. Further it has been shown in Chapter 4 that if the temperature changes are very rapid, the inverse heat condition analysis result lags behind the actual heat flux variation (see Fig. 4.8). However, it must be noted that slower changes are well determined and therefore the long term history is well predicted in this study.
- It has been determined that if the width of the heat sink is less than about 6 mm, the peak heat flux can not be correctly determined, see Section 4.2.3.1. Furthermore, the predicted width of this intense boiling region is wider; however, the total heat transfer on the impingement surface is expected to be well predicted. The width of the intense boiling region, i.e. region just around the wetted region, is difficult to determine from the high-speed images and it is not possible to determine the uncertainty in the estimated maximum heat flux, $q_{s,MHF}$.
- The wetting front movement leads to additional errors in the estimation of the maximum heat flux within the intense boiling region, see Section 4.2.3.2. The wetting front velocity increases with jet velocity, as shown in Fig. 5.8(b); resultantly, the error in estimating the maximum heat flux, $q_{s,MHF}$, is expected to increase with jet velocity. Similarly, the wetting front velocity is higher near the impingement region (e.g. $v_w \geq 15$ mm/s when $r_w \leq 9$ mm in experiment F4) and it is expected that the underestimation of maximum heat flux must be higher within this region.

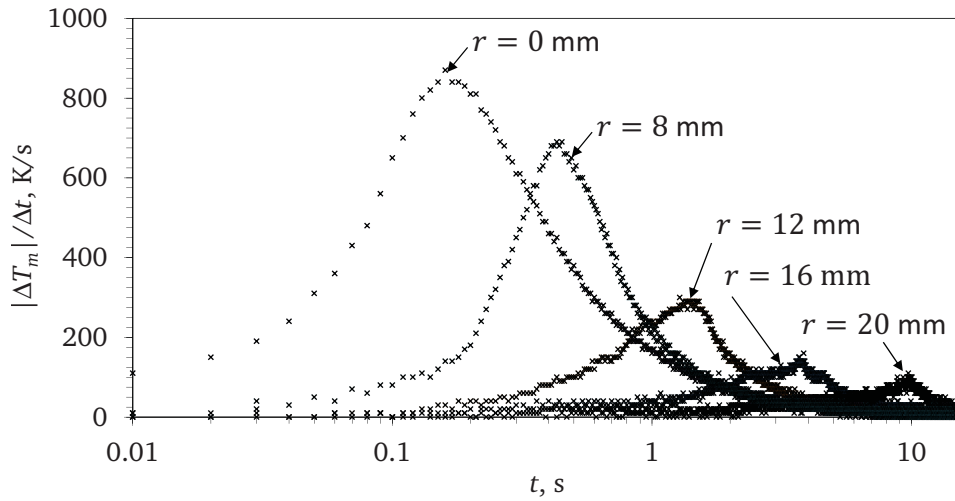
5.2.2 Measured temperature

As has been discussed in Section 5.1 and shown in Fig. 5.5, three distinct regions could be visually identified during quenching, with the extent of liquid-wall contact being different in these regions. It is well known that the heat transfer rates are higher when the wall is in contact with liquids than with vapor. Furthermore, the heat transfer rate increases with the three-phase contact line length [105]. It is then logical that the heat transfer rates in these regions would be different. The variation of the measured surface temperature with the wetting front movement is discussed here.

Variation of measured temperature, $T_m(t)$, and cooling rate at the thermocouple positions, $\frac{|\Delta T_m|}{\Delta t}(t)$, in experiment F2 are shown in Figs. 5.15(a) and 5.15(b), respectively. It should be noted here that the measurement data is shown in Fig. 5.15(a) as a curve instead of a scatter diagram because of the large number of data points. Consider the temperature evolution at radial position $r = 16$ mm. Up to time $t \approx 1.5$ s, the cooling rate measured by the thermocouple is low (the wetting front radius at time $t = 1.5$ s is $r_w = 12.5$ mm). Since the surface at $r = 16$ mm is dry during this period, the surface cools mostly by radial heat conduction to the wetted region. Film boiling heat transfer rate is low in the dry region, as is discussed later in this chapter. As the wetting front moves radially outwards, this radial position comes within the wetting front region, where direct liquid-wall contact occurs and the cooling rate significantly increases. Later at about $t = 4.4$ s the wetting



(a) Measured temperature, $T_m(t)$



(b) Measured cooling rate, $\frac{|\Delta T_m|}{\Delta t}(t)$

Figure 5.15. Variation of measured temperature, $T_m(t)$, and cooling rate, $\frac{|\Delta T_m|}{\Delta t}(t)$, at various radial positions in experiment F2. The temperature drops much faster within the impingement region as compared to the radial flow region. The maximum cooling rate at $r = 0$ mm is almost nine times of that at $r = 20$ mm.

front reaches this radial position and the cooling rate is almost maximum. After the wetting front has crossed this position, the cooling rate once again starts to drop. The variation in the cooling rate, thus, indicates the change in the heat transfer process occurring on the surface and its relation to the wetting front position. Depending on the radial position, the duration of these events might be different. The temperature drops much faster within the impingement region compared to radial flow region, with the cooling rate at $r = 0$ mm being almost nine times of that at $r = 20$ mm, see Fig. 5.15(b).

The variation of measured temperature, T_m , with the radial position, r , for two different jet velocities is shown in Fig. 5.16. Due to the rapid growth of the wetted region, the measured temperatures are lower in experiment F4 compared to experiment F1. No significant difference is seen within the impingement region for the two experiments, but the difference is prominent within the radial flow region. A very noticeable jump is seen in the variation with the radial position, r , due to the large

difference in the heat transfer rates between the wetted and dry regions. Once the complete surface is wetted (about $t = 8$ s in experiment F4), the impingement region is almost isothermal, while the temperature gradually increases with the radius in the radial flow region.

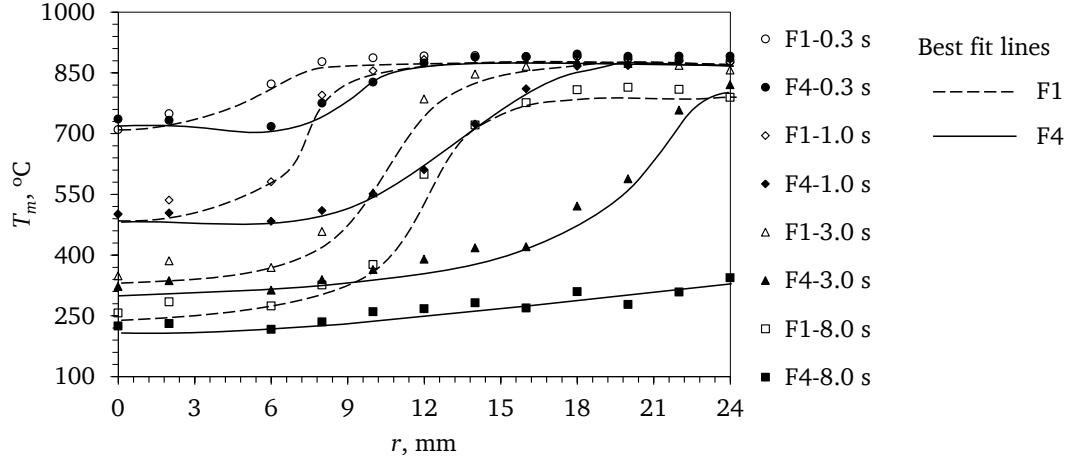


Figure 5.16. Comparison of measured temperature, $T_m(r)$, in experiments F1 and F4. The best fit lines have been approximately drawn and are just for assistance in reading the chart.

The effect of jet velocity, v_J , on the measured temperature, T_m , at $r = 10$ mm is shown in Fig. 5.17. A period of slow cooling (up to $t \approx 1.5$ s) is seen in experiment F1, but the temperature drops rapidly in experiment F2 and F4 without any noticeable duration of film boiling. On the other hand, the cooling rate at the stagnation point is found to be slightly lower in experiment F4 compared to F1 (Fig. 5.18). The cooling is expected to be faster at higher velocity, but the changes in temperature can not be detected by the sensor due to their poor time response. Besides this, some aging of the thermocouples, especially in the stagnation region, may have taken place due to the repeated rapid quenching experiments. The aging may change the voltage-temperature characteristics. These measurement system limitations leads to an uncertainty in the heat transfer estimation within the impingement region, which will be presented later in this chapter.

5.2.3 Surface temperature and heat flux

Figure 5.19(a) shows the variation of surface heat flux, $q_s(t)$, and temperature, $q_s(t)$, at radius $r = 20$ mm in experiment F2. Tangents to the estimated surface temperature variation have been approximately drawn; intersection of these tangents approximately mark a change in the heat transfer mechanism, as seen in the heat flux variation. Such a procedure has been previously used by Filipovic et al. [27]. The surface temperature at time $t \approx 6$ s, i.e. the intersection point on the left, is the approximate rewetting temperature. The surface temperature at time $t \approx 11.5$ s, i.e. the intersection point on the right, is approximately the temperature corresponding to the maximum heat flux, $T_{s,MHF}$. Similar interpretations about the boiling mechanisms can be made elsewhere, e.g. in Fig. 5.19(b).

Figure 5.20 shows the time shift of the estimated maximum surface cooling rate and maximum heat flux with respect to the measured maximum cooling rate by the thermocouple. The wetting front passes the radial position $r = 8$ mm at time $t = 0.37$ s. The maximum surface cooling rate

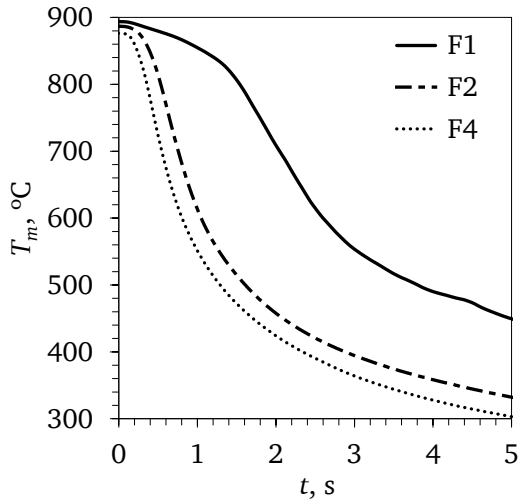


Figure 5.17. Effect of jet velocity, v_J , on the measured temperature, $T_m(t)$, at $r = 10$ mm. The jet velocities are 2.5 m/s, 5.1 m/s and 9.75 m/s in experiments F1, F2 and F4, respectively.

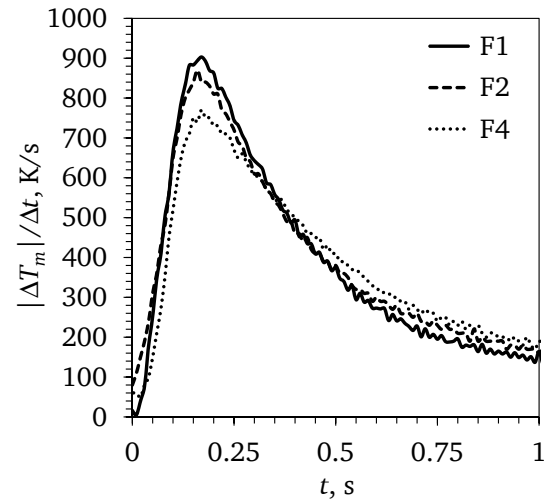
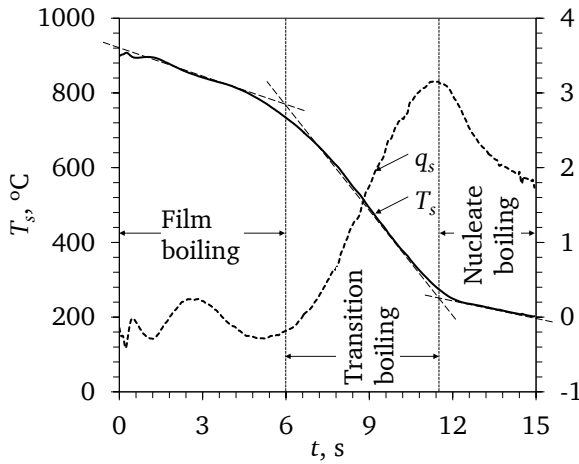
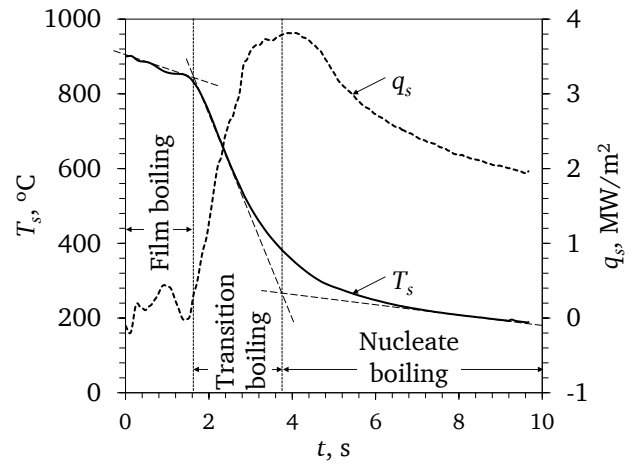


Figure 5.18. Effect of jet velocity, v_J , on the measured cooling rate, $\frac{|\Delta T_m|}{\Delta t}(t)$, at $r = 0$ mm. The jet velocities are 2.5 m/s, 5.1 m/s and 9.75 m/s in experiments F1, F2 and F4, respectively.



(a) Experiment F2



(b) Experiment F4

Figure 5.19. Surface temperature, $T_s(t)$, and heat flux, $q_s(t)$, at a radial position of $r = 20$ mm in experiments F2 and F4. Tangents to the surface temperature variation have been approximately drawn to illustrate that changes in the heat transfer mechanism can be interpreted from the change in the slope of the temperature history.

occurs slightly before the wetting front arrival. However, the maximum heat flux (MHF) condition is delayed with respect to the estimated maximum surface cooling rate. Therefore, it is interesting to compare the MHF position with the wetting front position.

5.2.3.1 Maximum heat flux position

The estimated surface heat flux, $q_s(r)$, and temperature, $T_s(r)$, at time $t = 0.37$ s in experiment F2 are shown in Fig. 5.21. The wetting front position is shown with filled markers. A local peak in

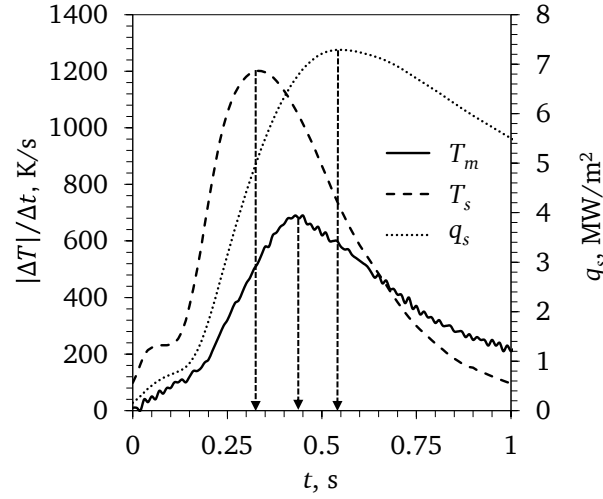


Figure 5.20. Measured cooling rate, $\frac{|\Delta T_m|}{\Delta t}(t)$, surface cooling rate, $\frac{|\Delta T_s|}{\Delta t}(t)$, and heat flux, $q_s(t)$, at $r = 8$ mm in experiment F2. The maximum heat flux (MHF) condition is delayed with respect to the estimated maximum surface cooling rate.

the heat flux distribution can be seen at radial position $r \approx 6$ mm, which is inside the wetting front position. This local peak corresponds to the maximum heat flux condition (similar to the critical or burnout heat flux in steady state pool boiling). The liquid extracts large amount of heat from the test specimen around the maximum heat flux region, which results in inwards radial heat conduction from the wetting front region and the dry region. The surface heat flux gradually reduces outside the maximum heat flux position, while the heat flux within the wetting front region is typical of boiling heat transfer. The surface heat flux is negligible outside a radial position $r \approx 14$ mm, which indicates the beginning of film boiling region. The maximum heat flux position, r_{MHF} , is compared with the wetting front position in Fig. 5.22. The data for the maximum heat flux position, r_{MHF} , is obtained from the estimated heat flux history of each radial position by determining the time instant when the maximum heat flux is achieved. It can be seen that the maximum heat flux position always lies within the wetted region. Similar observations have been made in other experiments as well. Hammad et al. [39] also found that the maximum heat flux position was upstream of the wetting front, i.e. within the wetted region. Up to the maximum heat flux position, the mode of heat transfer is nucleate boiling, while transition boiling happens outside it. Figure 5.23 shows a snapshot of the quenching process with the local boiling modes marked on the schematic boiling curves. Further, the boiling process is shown schematically in Fig. 5.24. Here, single-phase convection region is also marked, which may be true at a later stage of the quenching process.

As has been stated earlier, the maximum cooling takes place just before the arrival of the wetting front. To explain this, surface temperature distributions at few instants during quenching are shown in Fig. 5.25(a). The wetting front positions at the same instants are shown with filled markers. The wetting front always lies in the annular region with the largest radial temperature gradient, e.g. $6 \text{ mm} \leq r \leq 10 \text{ mm}$ at $t = 0.37$ s. As shown in Fig. 5.25(b), the maximum heat flux position at time $t = 0.37$ s is 6 mm, which is inside the wetting front position. Similar observations can be made at other time instants in Fig. 5.25. Large radial temperature gradient means that large amount of heat is conducted radially inwards to the maximum heat flux position. Therefore, the fastest surface cooling happens at just about the wetting front position due to the combination of radial

heat conduction to the maximum heat flux position and transition boiling. The radial distribution of surface heat flux, $q_s(r)$, at various time instants is shown in Fig. 5.25(b). The local peaks in the heat flux distributions corresponding to the maximum heat flux position are seen at different time instants and the position of the peaks move radially outwards as the quenching proceeds. It is also noticeable that as the wetting front grows, the local maximum heat flux reduces, which is in line with the observations of other researchers [25, 88].

Karwa et al. [57] measured the cooling rate during quenching of an AISI 314 stainless steel test specimen, 50 mm in diameter and 20 mm in height, with a 3 mm diameter subcooled water jet. They measured the temperature at a depth of 1.18 mm below the surface using 1 mm diameter thermocouples that were radially spaced 4 mm apart. This resulted in much a inferior time and space resolution as compared to this study. Heat flux distribution estimated in experiment F1 can be compared with the results of Karwa et al. [57] as the experimental conditions are almost similar (see Fig. 5.26). At time instants $t = 3$ s and 8 s, the heat flux is comparable within the impingement region of the two experiments, but they differ significantly near the wetting front, where local peaks

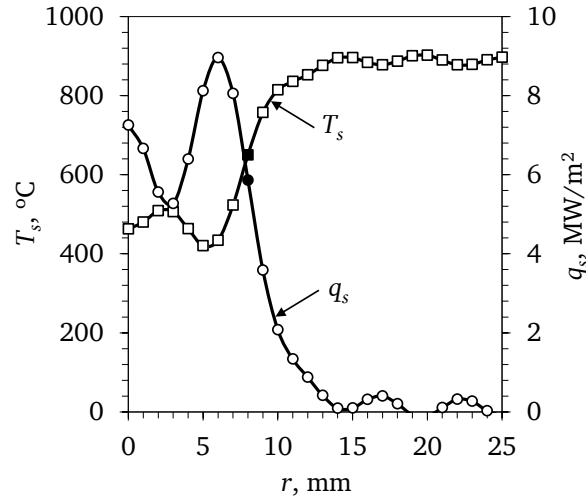


Figure 5.21. Heat flux, $q_s(r)$, and surface temperature, $T_s(r)$, at time $t = 0.37$ s in experiment F2. At this time instant, $r_{MHF} = 6$ mm and $r_w = 8$ mm.

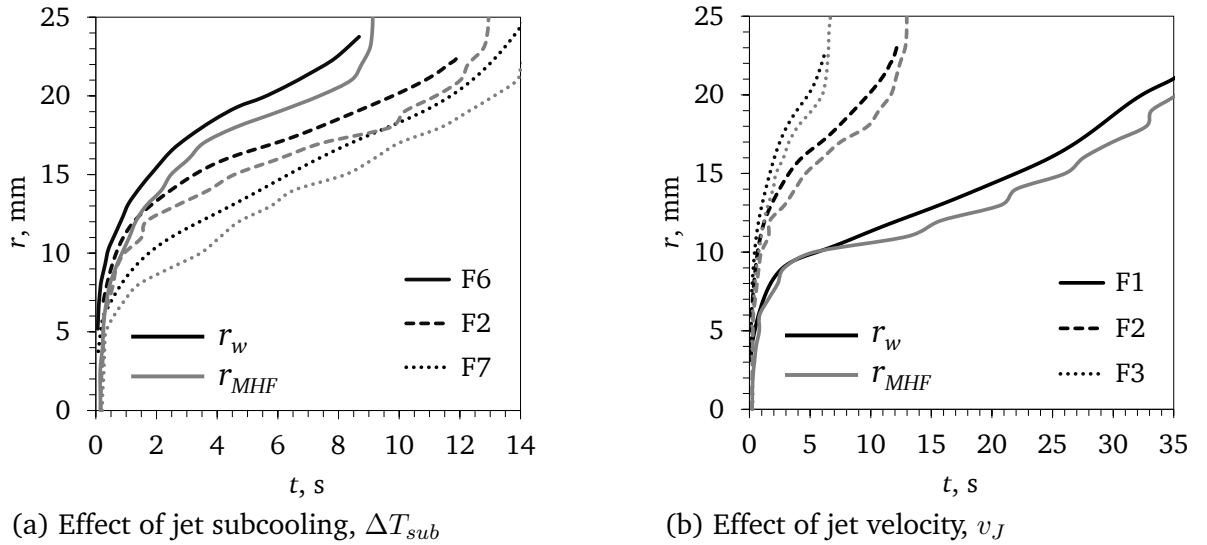


Figure 5.22. Comparison of wetting front radius, r_w , and maximum heat flux position, r_{MHF} , showing that the maximum heat flux position is within the wetted region.

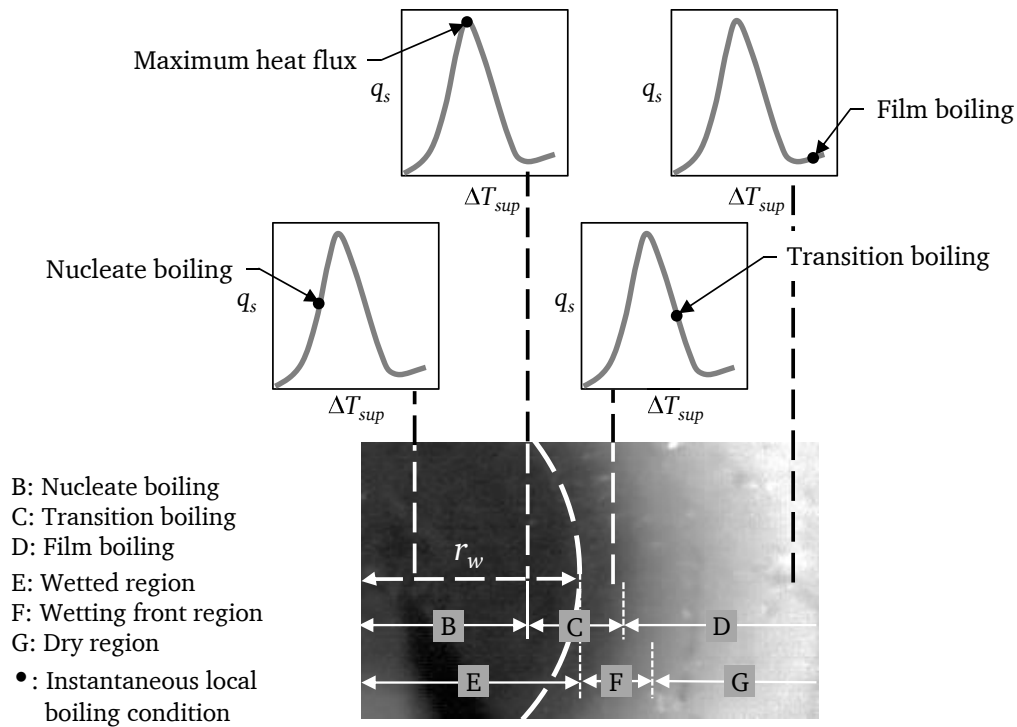


Figure 5.23. A snapshot of the quenching process with the instantaneous local boiling modes shown on schematic boiling curves.

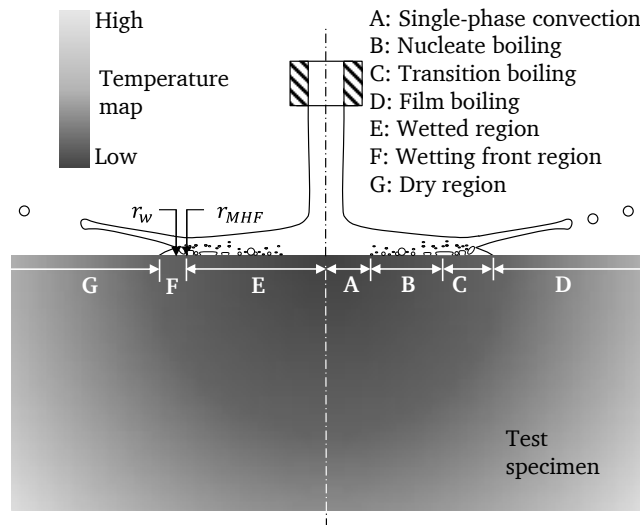
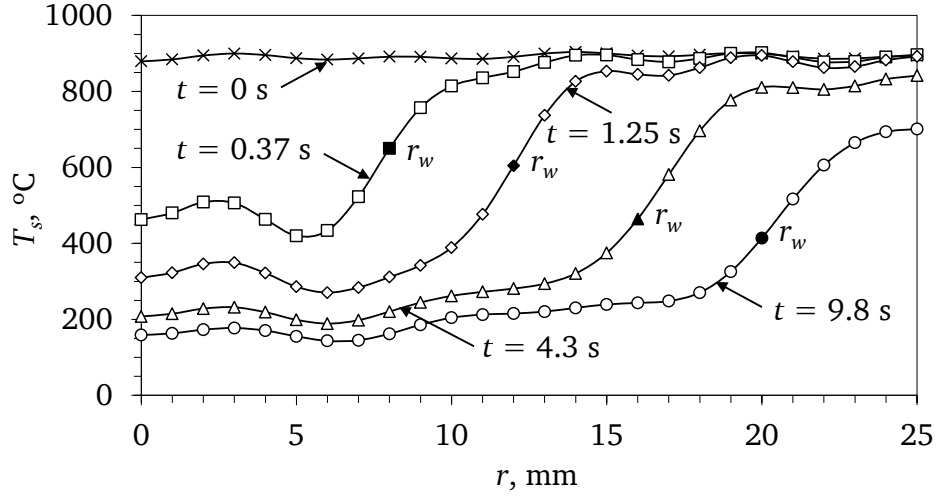
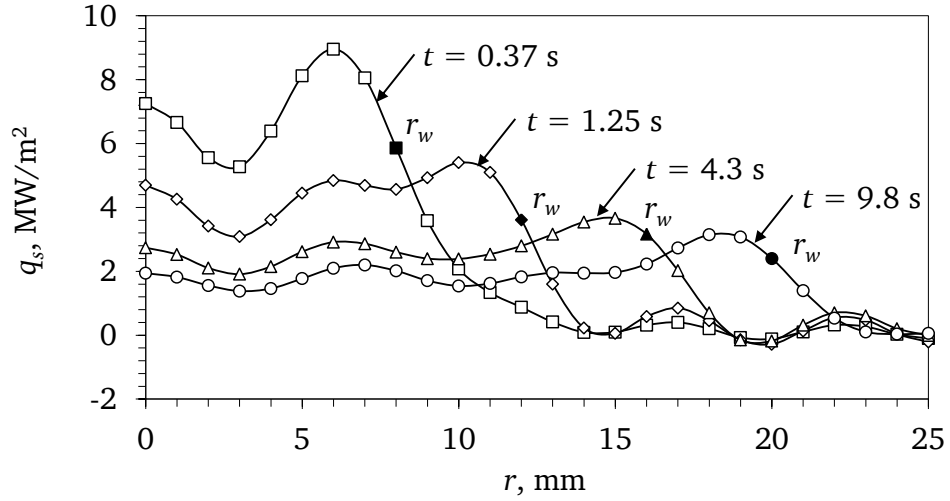


Figure 5.24. A schematic of the jet quenching process showing the boiling activity in the wetted region and the liquid deflection in the wetting front region.

near the wetting front cannot be identified in the study of Karwa et al. [57]. This difference in the results of the two studies shows that the results are negatively affected by the time and space resolution limitations of the experiment. In reality, the local heat flux peak might have been higher even in the present study (shown schematically in Fig. 5.27) but for the above mentioned limitations of a transient heat transfer experiment. This error can be expected to more in and around the impingement region.



(a) Surface temperature, $T_s(r)$



(b) Heat flux, $q_s(r)$

Figure 5.25. Surface temperature, $T_s(r)$, and heat flux, $q_s(r)$, at various time instants in experiment F2. The wetting front positions at the same instants are marked with closed symbols. Local peaks near the wetting front position are seen in the heat flux distribution.

It is necessary to highlight the sensitivity of the inverse solution on the differences in the hole-thermocouple thermal contact resistance, exact thermocouple position below the top surface and the thermocouple time constant; these differences may result in non-physical local peaks and troughs in the surface heat flux distribution. A low value of N_j is chosen for the inverse analysis study specifically to reduce this sensitivity. However, even with $N_j = 10$, the effect of this sensitivity is seen within the impingement region. To illustrate the overall effect of these errors in the measurement on the quality of the inverse solution, the measured temperature data along with the interpolated temperature profile in experiment F1 at $t = 1.5$ s is shown in Fig. 5.28. The thermocouple measurement at $r = 2$ mm deviates slightly from what otherwise should have been a smooth radial measured temperature distribution. This results in a local trough at $r = 2$ mm in the heat flux distribution, as seen in Fig. 5.29. Similar local trough is seen in Figs. 5.25(b) and 5.30.

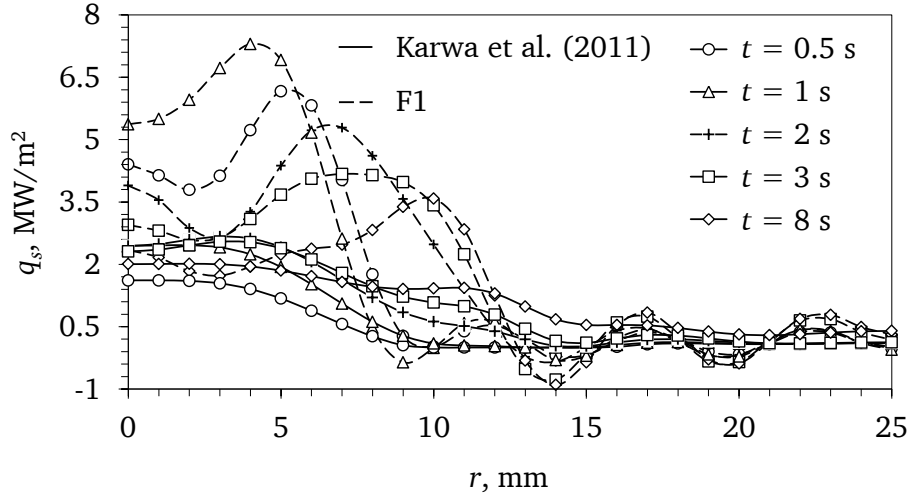


Figure 5.26. Heat flux, $q_s(r)$, at different time instants during quenching of an AISI type 314 stainless steel specimen ($T_I = 900\text{ }^\circ\text{C}$) with an impinging water jet ($v_J = 2.85\text{ m/s}$, $d_J = 2.8\text{ mm}$ and $\Delta T_{sub} = 80\text{ K}$) [57]. Heat flux, $q_s(r)$, at same time instants in experiment F1 is shown for comparison. For almost similar experimental conditions, the local peaks near the wetting front cannot be identified in the study of Karwa et al. [57] because of inferior space and time resolution compared to this study.

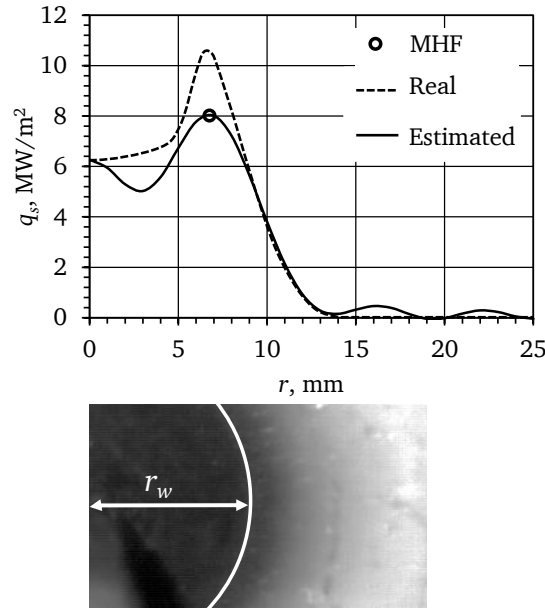


Figure 5.27. A schematic representation of the error arising due to the time and space resolutions of the inverse solution. Here, a snapshot from experiment F2 at $t = 0.5\text{ s}$ is shown along with the estimated heat flux distribution. If the time and space resolutions of the inverse solution were almost negligible, the real heat flux distribution (schematically shown here) would have had a sharper peak just inside the wetting front boundary than is estimated in this study.

5.2.3.2 Effect of jet velocity and subcooling

As shown earlier, the wetting front velocity increases with jet velocity. The heat transfer results are in congruence with this observation. Fig. 5.29 shows that at the same time instant, the heat flux distribution is broader in experiment F4 compared to F1. Similar effect is seen with increase in jet

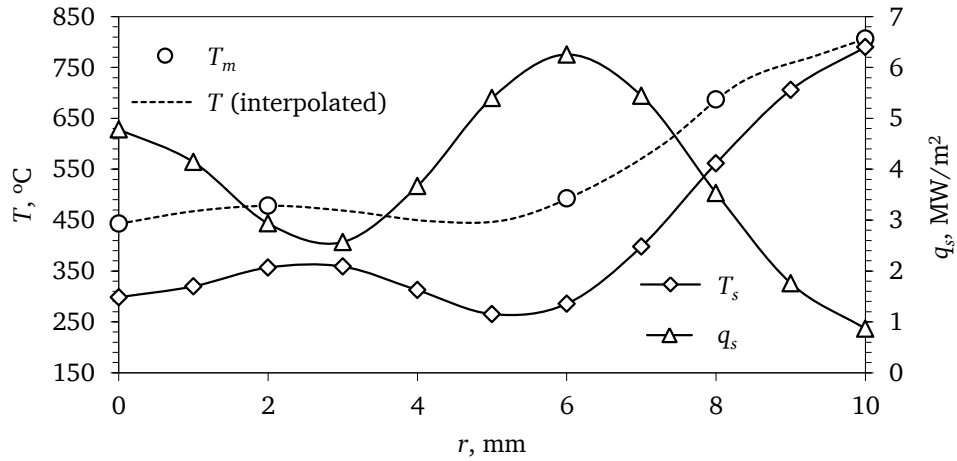


Figure 5.28. Effect of difference in thermocouple time response on the inverse solution at $t = 1.5$ s in experiment F1.

subcooling, ΔT_{sub} , (Fig. 5.30). Furthermore, similar to Fig. 5.25(b), local peaks are seen near the wetting front position.

5.2.3.3 Mechanism of heat transfer near the wetting front

In the section of hydrodynamics, it has been stated that the rate of wetting front growth is limited by the ability of the liquid to overcome the deflection force of the vapor released near the wetting front. Deflection of the liquid seems to start at the wetting front position, which would mean that heat transfer must be extremely low outside this position. However, the heat transfer estimates show that the heat flux in the wetting front region is not low and transition boiling might be occurring. In this section, a hypothesis about the heat transfer mechanism near the wetting front is presented.

A schematic representation of the flow near the wetting front is shown in Fig. 5.31. The nucleate boiling activity increases as the liquid flows along the heated surface. The high degree of liquid subcooling and flow velocity inhibit the accumulation of vapor near the impingement surface and within the liquid film. If vapor bubbles are not allowed to accumulate, a vapor barrier can not form between the the liquid and the impingement surface. However, at a certain position from the impingement point, the bubbles grow to large sizes and the maximum heat flux condition is reached. Outside the maximum heat flux position, these bubbles merge to form a vapor film and deflect the liquid away from the surface. This position has been observed in the high-speed images as the wetting front. Though the liquid is deflected away from the surface, a thin superheated liquid layer remains on the impingement surface within the wetting front region (as suggested by Filipovic et al. [25]), with the deflected liquid separated from it by a layer of vapor. Filipovic et al. [25] also observed that outside this thin film region, the surface was distinctly luminous, which meant that the surface was not wetted. Similar observation has been made in the present study. Hence, the liquid film completely disappears at the outer periphery of the wetting front region and heat transfer happens by film boiling. Heat transfer within the wetting front region happens by evaporation of this thin liquid film. Islam et al. [50] suggested that heterogeneous and homogeneous nucleation, which are explosive in nature, occur during transition boiling in the jet stagnation region. It is possible that the similar explosive boiling mechanism might be active within the wetting front region, which results

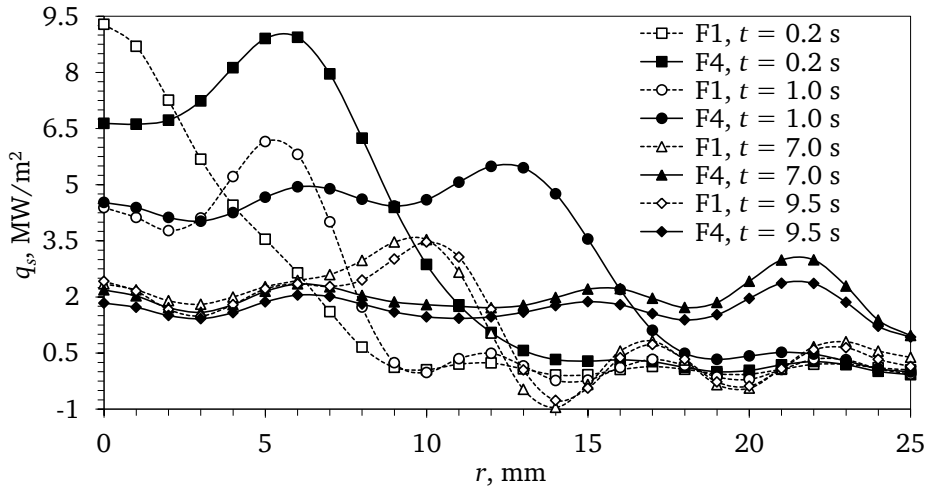


Figure 5.29. Effect of jet velocity, v_J , on heat flux, $q_s(r, t)$.

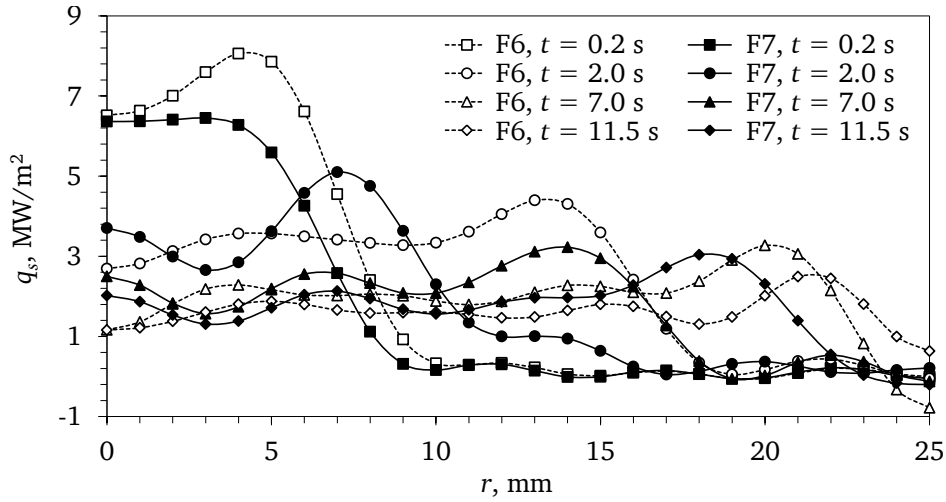


Figure 5.30. Effect of jet subcooling, ΔT_{sub} , on heat flux, $q_s(r, t)$.

in the disturbed appearance of the deflected liquid film. As this film evaporates, it is replenished by the liquid from the wetted region. The annular width of this thin film region, therefore, depends on the balance between the evaporation rate and the rate of replenishment from the main flow. The rapid evaporation and replenishment phenomenon is responsible for the high heat transfer rate in the wetting front region. As the heat is removed in the wetted region, the surface temperature reduces and the bubble activity reduces. The wetting front can then move radially outwards.

5.2.4 Boiling curves

From the temporal evolution of heat flux and surface temperature, the local boiling curves have been determined and are presented in this section. The measured temperature data has not been analyzed once the impingement surface is completely covered by liquid, as after that the adiabatic boundary condition on the sides can no longer be maintained. This restricts the lowest surface superheat to 100 K.

5.2.4.1 Impingement region

Figure 5.32 shows the boiling curve for the stagnation point, $r = 0$ mm, in experiment F1. This curve is similar to the classical pool boiling curve (see Fig. 1.2), though film boiling regime and rewetting point can not be identified. The maximum heat flux condition (MHF), analogous to the critical heat flux condition (CHF), and nucleate boiling can be seen. Immediately after impingement, the surface temperature starts to reduce rapidly, with a simultaneous increase in the heat flux. At a surface superheat $\Delta T_{sup} \approx 500$ K, the maximum heat flux condition (MHF) is obtained. Here, the heat transfer regime for $\Delta T_{sup} > \Delta T_{sup, MHF}$ is named as “initial cooling” because the probable thermo-hydraulic mechanism of heat transfer is not known. This “initial cooling” regime has been discussed in details in the next paragraph. Below $\Delta T_{sup, MHF}$, nucleate boiling occurs and the slope of the boiling curve is gradual. The single-phase convection regime is not estimated in the experiments as the analysis has not been done for $\Delta T_{sup} \leq 100$ K.

What mode of boiling occurs within the stagnation region during the initial cooling period? In Section 5.1, it has been noted that a wetted circle appeared in experiment F1 at about $t = 100$ ms, while the maximum heat flux condition occurs later. Did any transition of the boiling mode happen with the appearance of the wetted circle? If any transition did happen, why is it not seen in the boiling curve?

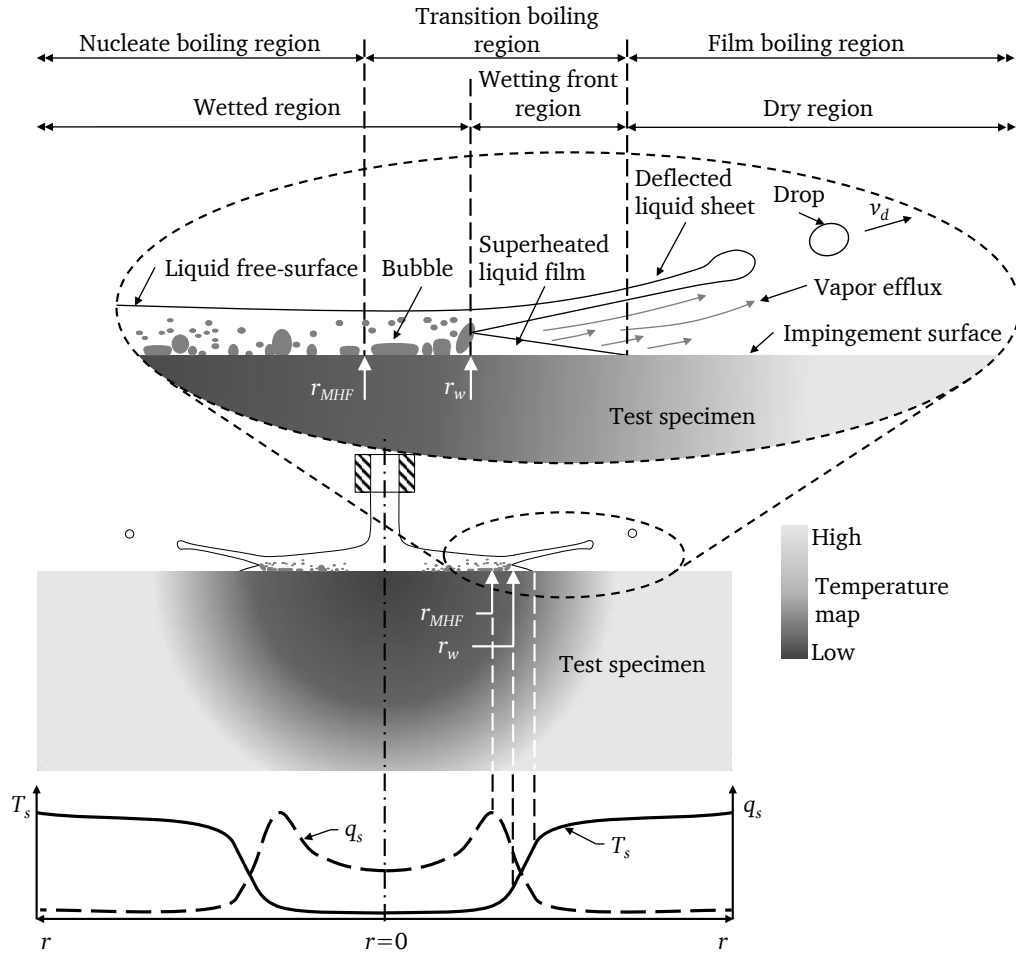


Figure 5.31. Schematic of the flow structure near the wetting front region.

To understand more about the initial cooling phase, an experiment has been conducted with the same conditions as experiment F1 but with the initial test specimen temperature of 800 °C. Figure 5.33 compares the boiling curve for this experiment with that of experiment F1 ($v_J = 5$ m/s and $\Delta T_{sub} = 75$ K). In both the experiments, film boiling regime could not be identified from the boiling curves. Moreover, the initial rate of cooling in both the cases is almost similar. Both the boiling curves merge upon each other below $\Delta T_{sup} \approx 450$ K. Perhaps the initial rate of cooling is not governed just by the plate temperature but also by the thermo-physical properties of the solid and the liquid ($\sqrt{(\rho \cdot c \cdot \lambda)_T / (\rho \cdot c \cdot \lambda)_L}$) as the time is too short for the boiling to reach a quasi-steady condition. These observations are in line with the results reported by Li et. al. [67], who determined that the initial slope of the spray cooling boiling curves with different initial plate temperatures were almost similar (see Fig. 2.15). The negative slope of the boiling curve looks similar to the characteristic slope of boiling curve in the transition boiling regime, though more studies are needed to understand the governing heat transfer mechanism. It is likely that the liquid is in a metastable

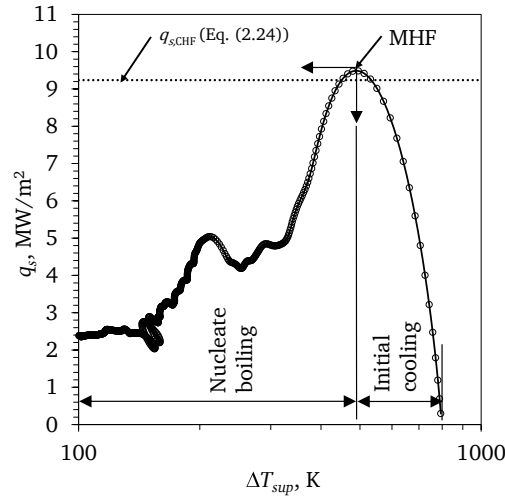


Figure 5.32. Boiling curve for the stagnation point in experiment F1. Critical heat flux, $q_{s,CHF}$, calculated using Eq. (2.24) is also shown for comparison.

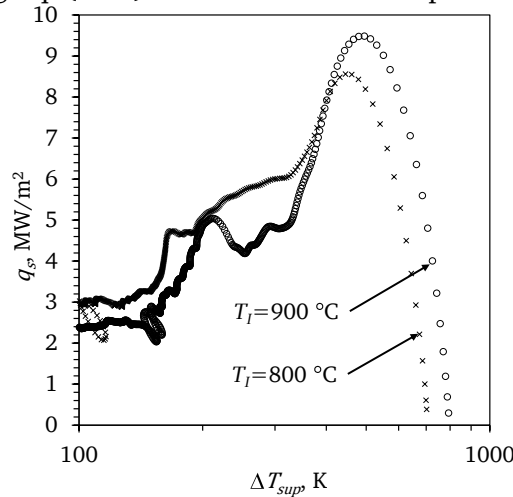


Figure 5.33. Boiling curve for the stagnation point, $r = 0$ mm, with different initial test specimen temperature, T_I , but same jet velocity and subcooling ($v_J = 2.5$ m/s and $\Delta T_{sub} = 75$ K). The curve's slope during the initial cooling period is similar in both the experiments.

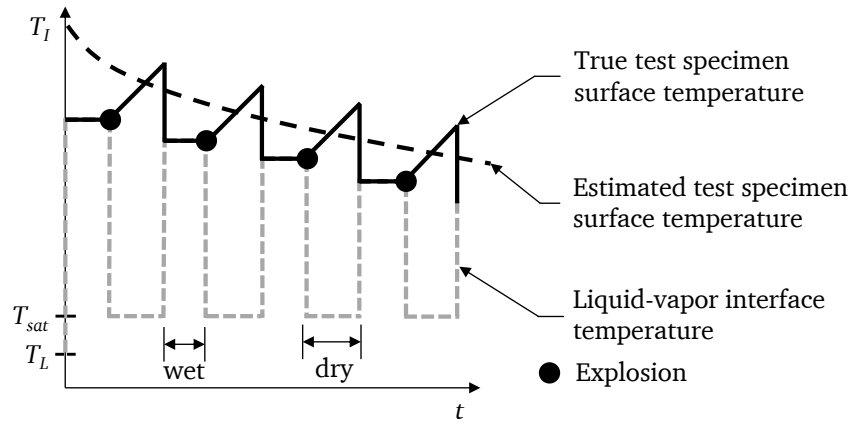


Figure 5.34. A schematic representation of the possible oscillations of the impingement surface temperature and liquid-vapor interface temperature during the initial cooling period.

state during this period, which results in an unstable boiling regime during this phase. Since the initial surface temperature of the test specimen is too high to permit stable liquid-wall contact, spontaneous bubble nucleation occurs at the liquid-solid interface. The bubble nucleation can be either heterogeneous or homogeneous [6]. Homogeneous nucleation, which occurs within the liquid due to density fluctuations, is more likely to be responsible for the explosive boiling. Due to explosive vapor generation, the liquid is deflected away from the impingement surface in the wetting front region. Once the vapor is generated, liquid-wall contacts are not possible. Now, if the rate of evaporation at the liquid-vapor interface is high enough, metastable film boiling can exist for some time. However, this vapor film is probably swept away from the impingement region by the jet; as a result, the vapor layer becomes thinner and, eventually, liquid-wall contact happens again. Once again, the liquid-wall contact would result in explosive vapor generation, followed by film boiling. This cycle would repeat until the surface temperature is low enough to allow stable liquid-wall contact. A schematic of this cycle is shown in Fig. 5.34. During the homogeneous nucleation process, some heat would be removed from the test specimen and the surface temperature would drop. The heat transfer rates are comparatively lower during the film boiling period, so the surface temperature of the test specimen would again recover to a value slightly lower than the initial block temperature. As the process goes on, the surface temperature of the test specimen would gradually reduce. Overall, during the initial cooling period, it is likely that an unsteady boiling process similar to transition boiling, i.e. a mixture of nucleate boiling and film boiling, occurs. With time, as the surface temperature reduces during this period of initial cooling, the duration for which the surface remains wetted increases. The heat flux increases while the surface temperature reduces as the quenching progresses. Finally, the boiling process reaches a quasi-steady condition at $T_{s,MHF}$ and fully-developed nucleate boiling occurs.

Another question that remains unanswered is that whether film boiling occurs before the appearance of a wetted circle. Most likely, the appearance of a wetted circle indicates a change from film boiling (with some homogeneous nucleation events) to a more stable transition boiling mode. In the present study, the film boiling process and the change from film boiling to stable transition boiling could not be estimated due to the comparable time resolution of the inverse solution. However, the high heat fluxes before the appearance of the wetted circle mean that intermittent liquid-wall contact would also occur during film boiling. Bogdanic et al. [9] were unable to observe any liquid-

wall contact during film boiling in the stagnation region of a subcooled jet using a micro-probe, but their estimated heat flux value during film boiling were much higher than that computed assuming heat conduction through the vapor film (measured to be about $10 \mu\text{m}$). This means that intermittent liquid-wall contacts leading to explosive boiling did occur during film boiling in the study of Bogdanic et al. [9]; Auracher (H. Auracher, personal communication, Dec 2010) communicated that the liquid-vapor interface oscillated up and down during the stable film boiling process close to the rewetting point in the experiment of Bogdanic et al. [9]. Indeed, due to natural instabilities of a cylindrical free-jet, such as the Plateau-Rayleigh instability, the flow in the impingement region fluctuates; therefore, it is highly unlikely that stable film boiling can exist in the impingement region. Studies with detailed measurement of bubble activity near the impingement surface along with impingement surface temperature measurement with fast response sensors are necessary to confirm the above hypothesis. However, to the best of the author's knowledge, no such measurement technique for high temperature environments exists at present.

Maximum heat flux, $q_{s,MHF}$, is reached at $\Delta T_{sup,MHF} \approx 500 \text{ K}$. In steady-state measurements, $50 \text{ K} < \Delta T_{sup,MHF} < 100 \text{ K}$ [79, 98]. Hauksson [45] reported $300 \text{ K} < \Delta T_{sup,MHF} < 400 \text{ K}$ for quenching of a stainless steel plate ($T_I \approx 900 \text{ }^\circ\text{C}$) with a subcooled water jet ($\Delta T_{sub} = 70 \text{ K}$, $v_J = 5.7 \text{ m/s}$). Comparable estimations are reported in other comparable jet impingement quenching studies and have been compiled in Table 2.2. For quick reference, these reported values are listed here in Table 5.1. Two possible reasons for the deviation between steady state and transient measurements are:

1. Referring to Fig. 2.14, a shoulder region in the boiling curve for the jet stagnation region is seen at surface superheat higher than $\Delta T_{sup,CHF}$. In this shoulder region, micro-emission boiling may be happening and the heat flux is comparable to critical heat flux, $q_{s,CHF}$ [98]. A similar boiling phenomenon might be responsible for the better wetting of the surface in a quenching experiment, thereby increasing $T_{s,CHF}$. The comment by Dhir et al. [22] about the lack of congruence between the boiling heat transfer results obtained in quenching studies and steady state (see Section 2.5.2) is reemphasized here. They stated that in nucleate boiling, the transient heat transfer coefficients are generally found to be lower than those obtained under steady state; the ratio of transient to steady state heat fluxes can be as low as 0.5. Further, they also mention that although no quantitative basis exists in the literature for the estimation of the transient nucleate boiling curve from the steady state boiling curves, it is known that the magnitude of displacement of the boiling curve depends on the thickness and thermal properties of the metal.
2. The heat transfer estimations in the jet stagnation region have lower accuracy as discussed in Section 5.2.1. Hence, the heat flux may have been underestimated, which may also lead to overestimation of the surface temperature. However, in the absence of information about the energy spectrum of the boiling process, it is not possible to quantify this error.

The estimated maximum heat flux, $q_{s,MHF}$, agrees well with $q_{s,CHF}$ calculated using Eq. (2.24). No other reliable correlation for $q_{s,MHF}$ is available in open literature (refer [116] for critical review of the other correlations and their shortcomings). Mozumder et al. [87] reported significant differences between their jet quenching data and the steady state correlation of Monde et al. [84], and suggested that finite thermal effusivity of the test specimen reduces the heat flux during boiling. Besides this, disagreement between the maximum heat flux obtained in transient measurements and the critical heat flux obtained in steady state measurements has been reported in other boiling stud-

Author(s)	Process	Material	T_I [°C]	$\Delta T_{sub}, l, v$	$\Delta T_{sup,MHF}$ [K]
Ishigai et al. [49]	PJI	AISI 304	1000	5–55 K, 6.2 mm, 0.65–3.2 m/s	400*
Kumagai et al. [64]	PJI	Cu	390	14–50 K, 20 mm, 3.5 m/s	100–200
Filipovic et al. [25]	WJ	Cu	750	45–75 K, 2–4 m/s	250–300
Hall [36]	CJI	Cu	650–800	75 K, 5.1 mm, 2–4 m/s	100–2300
Liu and Wang [73]	CJI	AISI 316	1000	5–45 K, 10 mm, 1–3 m/s	100–200
Hauksso [45]	CJI	CS	850	60 K, 10.6 mm, 5.7 m/s	400
Liu et al. [71]	CJI	CS, AISI 316	900	70–87 K, 19–30 mm, 5.6–6.5 m/s	200–400
Hammad [40]	CJI	Cu, CS, brass	250–300	5–80 K, 2 mm, 3–15 m/s	10–70
Mozumder [89]	CJI	Cu, CS, brass	250–400	5–80 K, 3–15 m/s, 2 mm	20–100
Leocadio et al. [66]	CJI	AISI 316	900	78 K, 6.7 mm, 2.7 m/s	406
Gradeck et al. [32]	PJI	Ni	600	15 K, 4 mm, 1.2 m/s	\approx 50–100
Lee [65]	CJI	SS 304	900	80 K, 5.6–10 m/s, 3 mm	\approx 400

*: shoulder region temperature, where heat flux is comparable to CHF.

l is the characteristic dimension: e.g. d_J or d_N for circular jet impingement, w_J or w_N for planar jet impingement.

CJI: circular jet impingement. PJI: plunging jet impingement. WJ: wall jet.

Table 5.1. Compilation of reported surface superheat at maximum heat flux, $\Delta T_{sup,MHF}$, during quenching with impinging water jet at atmospheric pressure (arranged chronologically).

ies as well, though the reason is not known. No comparative steady-state measurements have been done in this study and further discussion is not possible.

Most nucleate boiling correlations found in the literature for jet impingement boiling are only valid up to a surface superheat of about 50 K [116], with a general form given as

$$q_s = C \cdot \Delta T_{sat}^n. \quad (5.1)$$

The various available correlations have been compiled by Wolf et al. [116]. These correlations have been developed from steady state measurements and differ significantly from the nucleate boiling curve obtained in transient experiments, e.g. in the studies of Ishigai et al. [49]. In this study, the slope of the boiling curve in the nucleate boiling regime is significantly lower than given by these correlations, as also reported by Zhang [127] and discussed earlier in Chapter 2. Other researchers [45, 50] have also reported similar differences.

Another observation that can be made in Fig. 5.35 is that the nucleate boiling data is noisy at lower surface superheat. The noise is due to the fact that the measured cooling rate becomes comparable to the measurement noise after about 1.5 s, as is shown in Fig. 5.36. Therefore, the heat flux estimates beyond $t = 1.5$ s are of doubtful accuracy. The surface superheat at this time is about 200 K and, specifically for this reason, the single-phase heat transfer data has not been discussed in this thesis.

The boiling curves at constant jet subcooling, $\Delta T_{sub} = 75$ K, but varying jet velocities, v_J , are shown in Fig. 5.37. The boiling curves merge upon each other at very high surface superheat, which spans over a part of the initial cooling phase, and at low surface superheat, which spans over a part of the nucleate boiling regime. Similar merging of the boiling curves in the initial cooling and

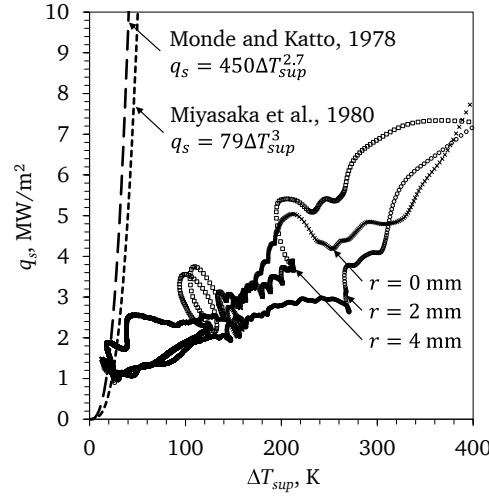


Figure 5.35. Comparison of boiling curves for the impingement region in experiment F1 and correlations for nucleate boiling compiled in [116]. These correlations, obtained from steady state measurements, overpredict the slope of the nucleate boiling curve.

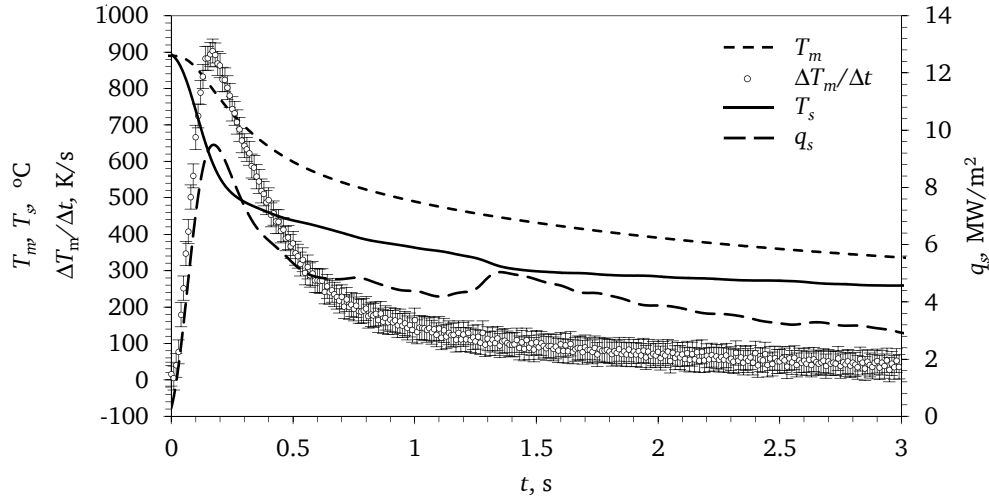


Figure 5.36. Comparison of the measured cooling rate, $\frac{|\Delta T_m|}{\Delta t}$, at the stagnation point, $r = 0$ mm, with the noise in the measured temperature. The noise level in the temperature measurement is determined to be $3\sigma = 0.33$ K. The cooling rate becomes comparable to noise in the measurement after about $t = 1.5$ s. As a result, the heat flux estimates for $\Delta T_{sup} < 200$ K are of doubtful accuracy.

nucleate boiling regime have been reported by Zhang [127] (see Fig. 2.17). Interestingly, contrary to observations in [72], the maximum heat flux, $q_{s,MHF}$, reduces with jet velocity. In the next paragraph, two possible explanations are offered for this observation. It is to be noted that these explanations are still conjectures and further studies are necessary to understand the mechanism responsible for the maximum heat flux condition.

1. Such an observation is most likely due to the limitations of the experiment. With the increase in jet velocity, the wetting front velocity increases; as a result, the space resolution becomes poor (see Section 4.2.3). Further, if the rate of temperature change is very high, as expected for higher jet velocity, the temperature changes are not correctly detected by the thermocouples; as

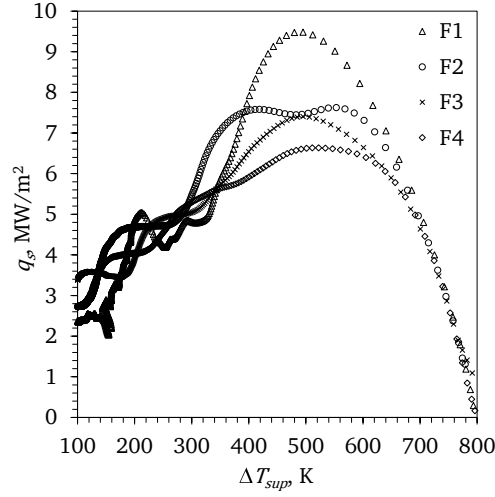


Figure 5.37. Boiling curves for the stagnation point, $r = 0$ mm, in experiments F1, F2, F3 and F4. The boiling curves for different jet velocities merge upon each other in the initial cooling and nucleate boiling regime. Contrary to the observation of Liu et al. [72], the maximum heat flux decreases with increasing jet velocity.

a result, the heat transfer rates are underestimated (see Fig. 4.10). The outcome of both these limitations is that the maximum heat flux, $q_{s,MHF}$, may be underpredicted and the estimated peak of the boiling curve also gets delayed with respect to the actual event (see Fig. 4.8). Overall, the underestimation in heat flux value increases with the jet velocity. The underestimation is more near the maximum heat flux condition, while the nucleate boiling heat flux is usually well estimated.

2. An alternative explanation for the observations in Fig. 5.37 is that since quenching is a conjugate heat transfer process, faster cooling of the surface with increase in jet velocity may not necessarily results in higher heat flux. Faster cooling event results in the propagation of high frequency thermal waves into the test specimen. Since the damping of the thermal wave increases with its frequency, the penetration depth of the thermal wave decreases (for details, see Eqs. (2.17)–(2.19) and the following discussion in Section 2.5.2.1). Pool boiling heat transfer rates have been reported to be dependent on the thickness of the solid, with the deviation from quasi-steady conditions increasing with decreasing thickness [94]. Further, Mann et al. [76] numerically confirmed the dependence of isolated bubble nucleate boiling heat flux on the penetration depth of the thermal wave, with the boiling heat transfer rates on a thin steel foil being 2–12 % lower than that on a copper foil of the same thickness. For jet impingement quenching, a similar dependence of the boiling heat flux on the penetration depth is possible, which may explain the decrease of maximum heat flux, $q_{s,MHF}$, with increase in the jet velocity, v_J .

The boiling curves at constant jet velocity $v_J = 5$ m/s but varying jet subcooling, ΔT_{sub} , are shown in Fig. 5.38. Here again, merging of the two boiling curves in parts of the initial cooling and nucleate boiling regime are seen. The maximum heat flux, $q_{s,MHF}$, for $\Delta T_{sub} = 75$ K is higher than for $\Delta T_{sub} = 87$ K.

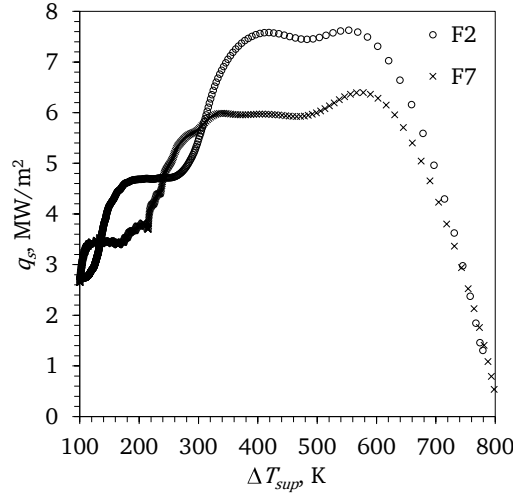


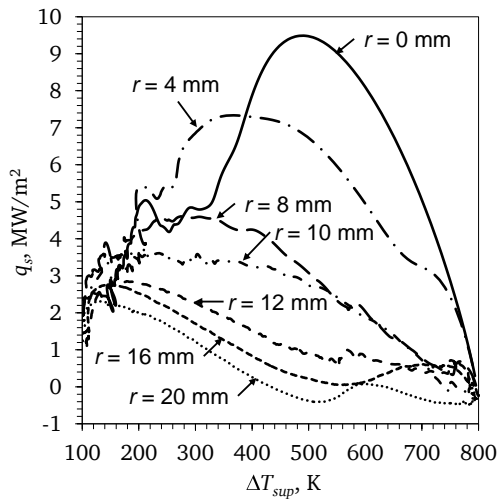
Figure 5.38. Boiling curves for the stagnation point, $r = 0$ mm, in experiments F2 and F7. The boiling curve for different jet velocity merge in the initial cooling and nucleate boiling regime, while the the maximum heat flux increases with jet subcooling.

5.2.4.2 Radial flow region

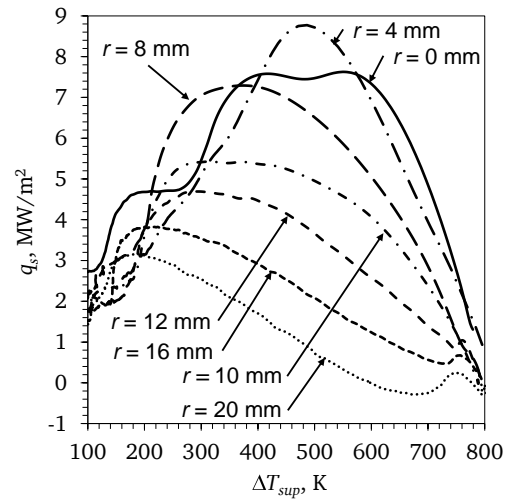
The boiling curves for the radial flow region are shown in Fig. 5.39. The boiling curve shifts to lower surface superheat and the heat flux reduces with increasing distance from the jet stagnation point. This happens because the liquid subcooling and velocity reduce with the radial distance from the stagnation point; as a result, the heat transfer rate reduces and the boiling curve shifts to lower surface superheat. Comparing the boiling curves in Fig. 5.39, it is evident that the higher velocity of the liquid film increases the heat flux in the radial flow region. The rewetting temperature also increases significantly with jet velocity.

It is interesting to see if film boiling can be identified in these curves or not. Examining the boiling curve for $r = 10$ mm, the heat flux is almost zero when the surface superheat is more then 740 K. Below this surface superheat, the heat flux shows a monotonous increase as the impingement surface temperature reduces and finally the maximum heat flux condition is reached. Can the heat transfer mode between surface superheat range of 740–800 K be classified as film boiling? To answer this, the variation of heat flux and surface temperature at $r = 10$ mm with time, t , is shown in Fig. 5.40. As can be seen that up to $t = 1.2$ s, the heat transfer rate is low and the surface temperature drops really slowly. At $t = 1.2$ s, the wetting front is at 7 mm and the surface temperature at $r = 10$ mm is 840 °C ($\Delta T_{sat} = 740$ K). As the wetting front grows further, this radial position ($r = 10$ mm) comes within the wetting front region and the heat transfer rate increases due to transition boiling. Hence the likely mode of heat transfer in the surface superheat range of 740-800 K is film boiling or simply radiation heat transfer. However, since the temperature change due to film boiling is appreciably lower than that due to radial heat conduction to the wetted region, the estimated film boiling heat transfer rate is almost negligible. Film boiling can be seen clearly at $r > 12$ mm, as shown in Fig. 5.41.

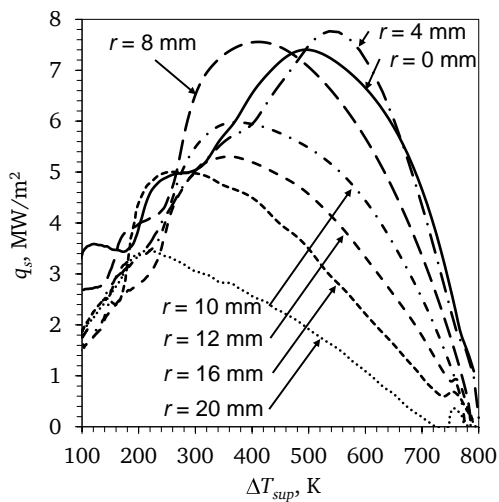
The variation heat transfer coefficient, h_s , with surface superheat, ΔT_{sat} , for various radial positions, r , is shown in Fig. 5.42. The heat transfer coefficient first increases with decrease in impingement surface temperature in the transition boiling regime and then decreases in the nucleate



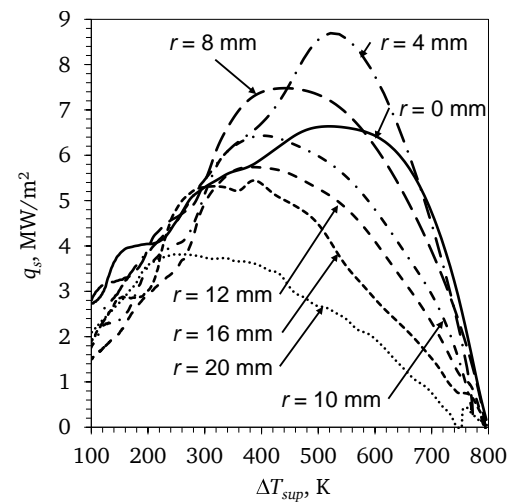
(a) Experiment F1



(b) Experiment F2



(c) Experiment F3



(d) Experiment F4

Figure 5.39. Boiling curves for the impingement and radial flow regions. The boiling curve shifts to lower surface superheat and heat flux with distance from the stagnation point.

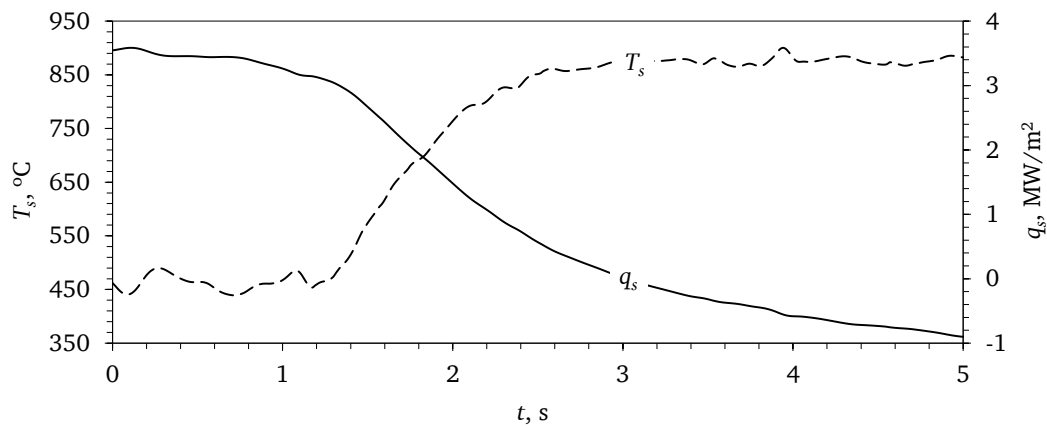


Figure 5.40. Heat flux, $q_s(t)$, and surface temperature, $T_s(t)$, at $r = 10$ mm in experiment F1.

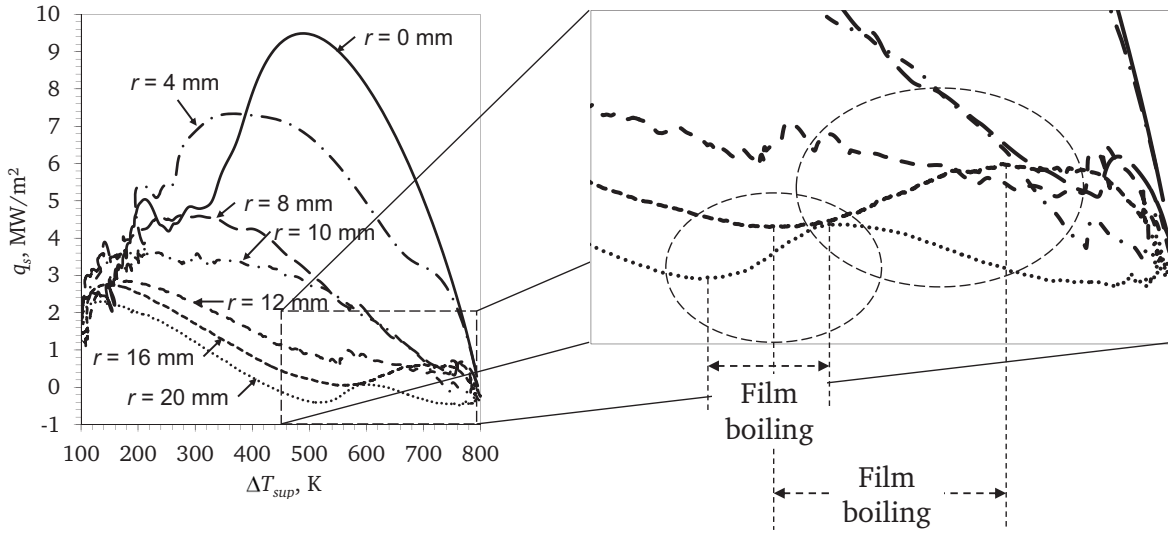


Figure 5.41. Boiling curve for experiment F1 clearly showing film boiling in the radial flow region.

boiling regime. In the impingement region, the heat transfer coefficient increases with decreasing surface superheat even in the nucleate boiling regime, though it should be mentioned that the data is noisy at low surface superheat. Similarly, the heat transfer coefficient decreases with radial distance from the impingement point. Further, the heat transfer coefficient increases with jet velocity in the radial flow region, as shown in Fig. 5.43. Similar influence of the jet subcooling is seen, though the influence is less pronounced compared to the influence of jet velocity.

5.2.4.3 Area-weighted average boiling curves

To determine the overall influence of the jet parameters on the heat transfer, area-weighted average heat transfer values have been calculated as

$$\bar{q}_s(t) \cdot 25^2 = q_{s,r=0}(t) \cdot 0.5^2 + q_{s,r=1}(t) \cdot (1.5^2 - 0.5^2) + q_{s,r=2}(t) \cdot (2.5^2 - 1.5^2) + \dots + q_{s,r=24}(t) \cdot (24.5^2 - 23.5^2) + q_{s,r=25}(t) \cdot (25^2 - 24.5^2), \quad (5.2)$$

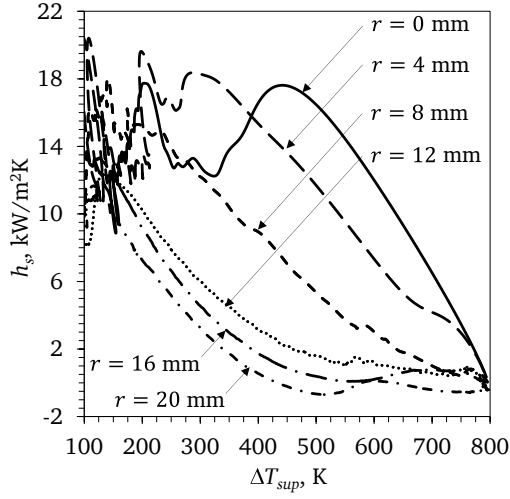
$$\bar{T}_s(t) \cdot 25^2 = T_{s,r=0}(t) \cdot 0.5^2 + T_{s,r=1}(t) \cdot (1.5^2 - 0.5^2) + T_{s,r=2}(t) \cdot (2.5^2 - 1.5^2) + \dots + T_{s,r=24}(t) \cdot (24.5^2 - 23.5^2) + T_{s,r=25}(t) \cdot (25^2 - 24.5^2), \quad (5.3)$$

$$\bar{h}_s(t) = \bar{q}_s(t) / [\bar{T}_s(t) - T_L]. \quad (5.4)$$

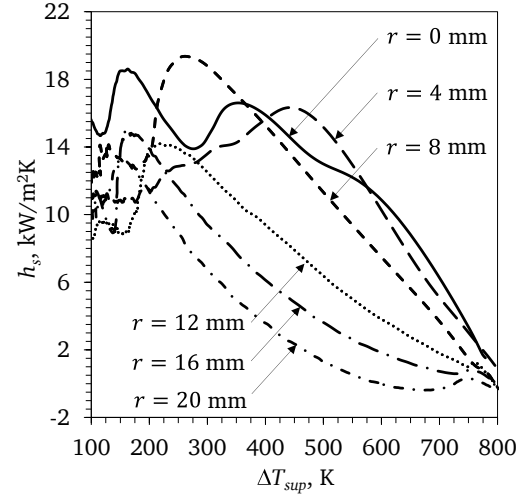
Figure 5.44 shows the variations of area-weighted average heat flux, \bar{q}_s , and area-weighted average heat transfer coefficient, \bar{h}_s , with the area-weighted average surface superheat, $(\bar{T}_s - T_L)$. Both \bar{q}_s and \bar{h}_s increase with jet velocity, v_J . Furthermore, the maximum heat flux, $\bar{q}_{s,MHF}$, and temperature at this condition, $\bar{T}_{s,MHF}$, also increase with jet velocity, v_J . \bar{q}_s increases with ΔT_{sub} , but \bar{h}_s shows less dependency on subcooling.

5.2.5 Maximum heat flux condition

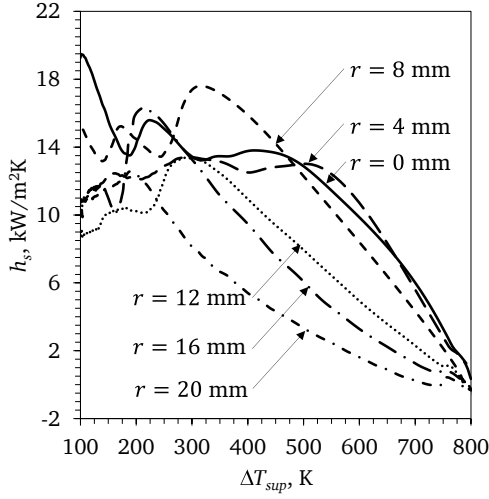
As stated previously, the maximum heat flux position is estimated to be always just inside the wetting front boundary. Hence, it is reasonable to say that condition determining the maximum heat flux



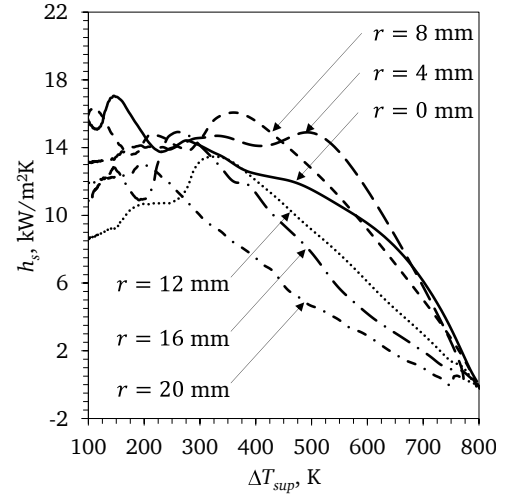
(a) Experiment F1



(b) Experiment F2



(c) Experiment F3



(d) Experiment F4

Figure 5.42. Heat transfer coefficient, $h_s(\Delta T_{sup})$ at various radial positions.

position, r_{MHF} , and the wetting front position, r_w , are more or less the same. Therefore, the maximum heat flux condition, $q_{s,MHF}$ and $T_{s,MHF}$, give a clearer picture of what happens before the liquid gets deflected away from the surface in the wetting front region. Variation of the maximum heat flux condition, $q_{s,MHF}$ and $T_{s,MHF}$, over the surface and its dependence on jet parameters is a very important information that can be derived from this study. In this section, the variation of the maximum heat flux condition with radial position is discussed.

5.2.5.1 Variation of maximum heat flux condition with radial position

Figure 5.45(a) shows the variation of maximum heat flux, $q_{s,MHF}$, with radial distance from the stagnation point for different jet velocities. The maximum heat flux reduces as the liquid travels radially outwards due to decrease in liquid velocity and subcooling. The variation of surface temperature at the maximum heat flux, $T_{s,MHF}$, with radial distance from the stagnation point, r , for different jet velocities is shown in Fig. 5.45(b). Here again, surface temperature at maximum heat flux decreases with radial distance from the stagnation point. Further, it can be seen that both maximum heat flux position, $q_{s,MHF}$, and surface temperature at maximum heat flux increase with

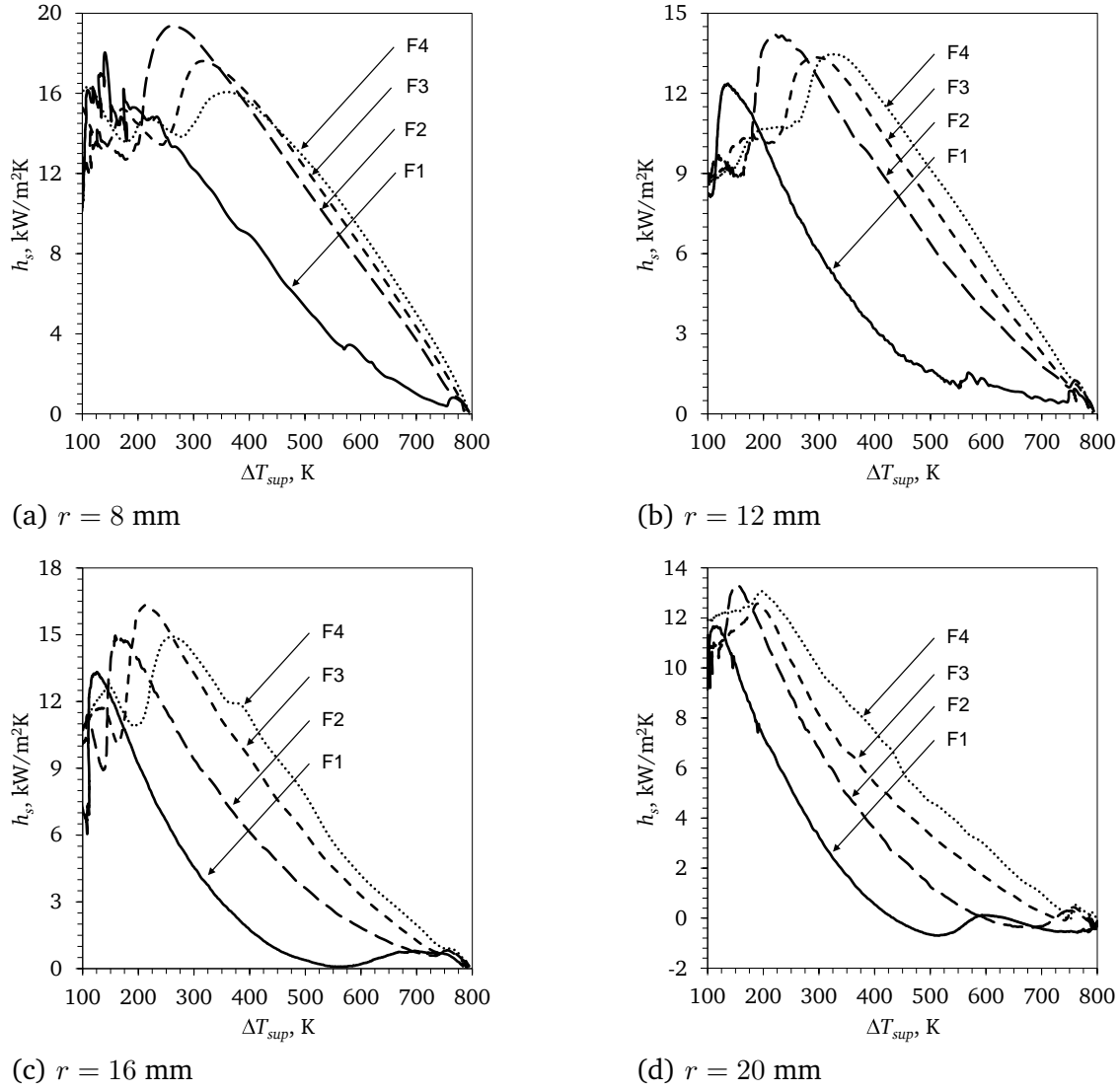
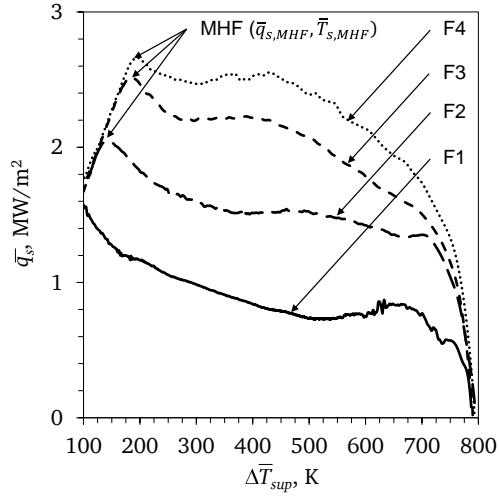


Figure 5.43. Effect of jet velocity, v_J , on heat transfer coefficient, $h_s(\Delta T_{sup})$, at various radial positions.

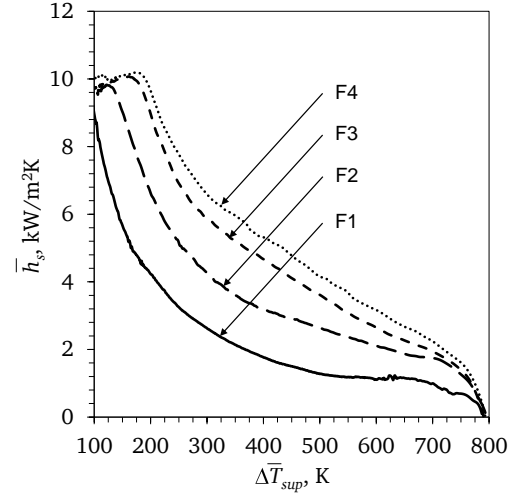
jet velocity. As has been discussed in Section 2.2, the rewetting temperature increases with the jet velocity but the mechanism is still not understood. Nevertheless, simultaneous enhancement in rewetting temperature and temperature at maximum heat flux condition with flow velocity have been reported by various researchers and it can be safely argued that the underlying mechanism for the two phenomenon is closely related.

Ma et al. [75] classified the Nusselt number distribution on the surface into the following regions based on the state of the boundary layer compared to the film thickness.

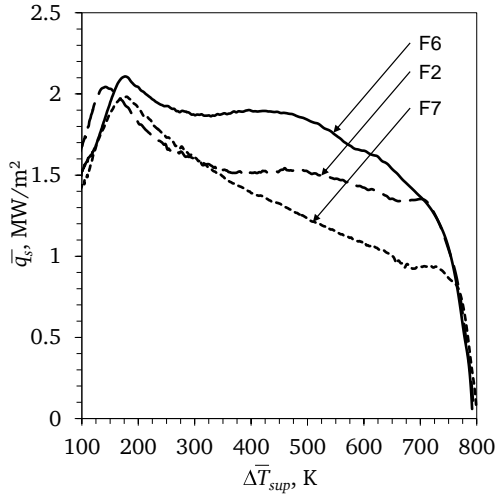
- Region I (Impingement region, $0 \leq \bar{r} < 1.28$): Though Ma et al. [75] specifies the impingement region up to $\bar{r} = 1$, the same has been specified to be 1.28 times the jet diameter by Koldin and Platanov [60]. The modification has been made accordingly.
- Region II (Boundary layer region, $1.28 \leq \bar{r} < 0.5554 \cdot \text{Re}_J^{1/3} / (50 - 5.147 \cdot \text{Pr}_L)^{1/3}$): In this region, the viscous boundary layer has not reached the liquid free-surface. For water at 25°C , the thermal and viscous boundary layers reach the free-surface at almost the same location. The position at which the thermal boundary layer merges with the liquid free-surface marks the end of region II.



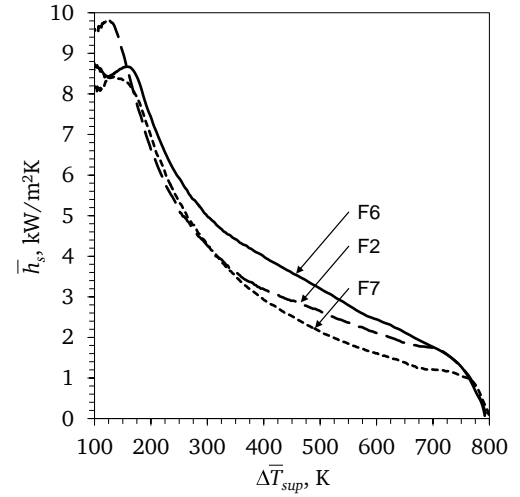
(a) Effect of jet velocity, v_J , on area-weighted average heat flux, \bar{q}_s



(b) Effect of jet velocity, v_J , on area-weighted average heat transfer coefficient, \bar{h}_s



(c) Effect of jet subcooling, ΔT_{sub} , on area-weighted average heat flux, \bar{q}_s



(d) Effect of jet subcooling, ΔT_{sub} , on area-weighted average heat transfer coefficient, \bar{h}_s

Figure 5.44. Variation of area-weighted average heat transfer, $\bar{q}_{s,MHF}$ and \bar{h}_s , with area-weighted average surface superheat, $(\bar{T}_s - T_L)$.

- Region III (Similarity regions, $\bar{r} > 0.5554 \cdot \text{Re}_J^{1/3} / (50 - 5.147 \cdot \text{Pr}_L)^{1/3}$): In this region, the thermal boundary layer has reached the free-surface of the liquid film, and the free-surface liquid temperature increases in the flow direction.

On similar lines, the maximum heat flux, $q_{s,MHF}$, variation with radial position, r , in the present study has been categorized into three regions. The three regions are marked in Fig. 5.46. Within region I, ideally $q_{s,MHF}$ must be more or less uniform but for the reasons concerning the heat flux variation in the stagnation region discussed previously in Section 5.2.4.1. In the region II, the MHF value reduces sharply as the boundary layer develops. Here, the MHF value shows an inverse relationship to \bar{r} . In contrast to the result of this study, Mozumder et al. [87] reported an inverse relation to \bar{r} in the region III, where the boundary layer reaches the free-surface. In the region

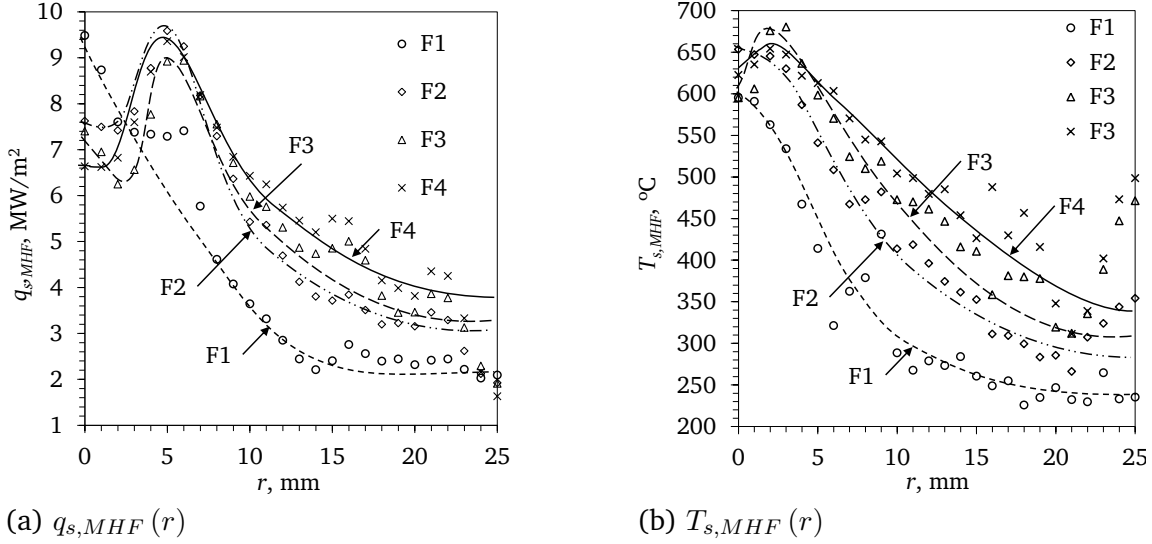


Figure 5.45. Effect of jet velocity, v_J , on maximum heat flux condition, $q_{s,MHF}(r)$ and $T_{s,MHF}(r)$. For clarifying the trend, tentative best fit lines have been drawn here, while ignoring the sudden changes in $q_{s,MHF}(r)$ and $T_{s,MHF}(r)$ when $r \geq 22$ in experiments F2, F3 and F4.

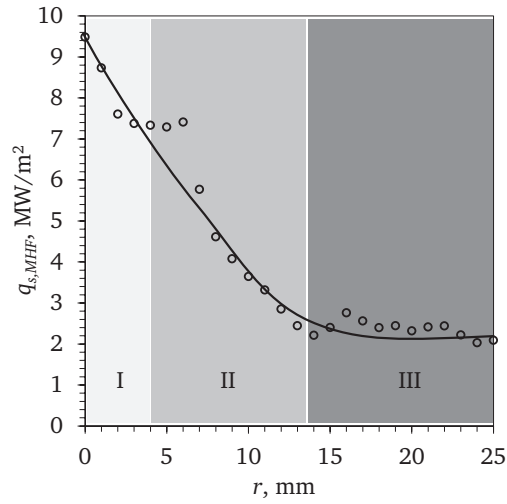
III, the maximum heat flux is almost constant or decreases gradually with radial distance from the stagnation point as compared to that in region II.

The above mentioned three region classification has also been applied to the radial distribution of $T_{s,MHF}$ (see Fig. 5.47), and different slopes in the radial distribution of $T_{s,MHF}$ can be identified in these regions. This shows the efficacy of the suggested three region classification for the development of correlations. This information can be the starting point for development of a correlation. However, since the number of experiments performed in this study are not enough to have a reasonable correlation, it has been not been presented as an outcome of this study.

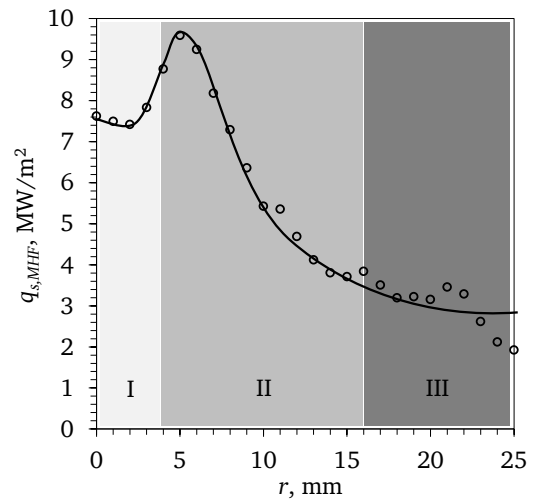
5.2.5.2 Variation of maximum heat flux condition with jet velocity and subcooling

Revisiting Fig. 5.45(a), it is seen that the maximum heat flux, $q_{s,MHF}$, in the radial flow region increases with the jet velocity. The variation of $q_{s,MHF}$ with Re_J is shown for a few radial positions in Fig. 5.48. Monde [81] found that the maximum heat flux, $q_{s,MHF}$, is proportional to $v_J^{1/3}$ for saturated jets, and the exponent increases with jet subcooling, ΔT_{sub} . For the data plotted in Fig. 5.48, this exponent is found to vary between 0.38 to 0.5 (except for $r = 6$ mm and $r = 14$ mm, where the exponents are 0.14 and 0.6, respectively), which is in good agreement with the slope reported by Mozumder [89]. The variation of surface temperature at maximum heat flux, $T_{s,MHF}$, with jet Reynolds number, Re_J , is shown for the radial flow region in Fig. 5.49. The exponent is found to vary between 0.25 to 0.48.

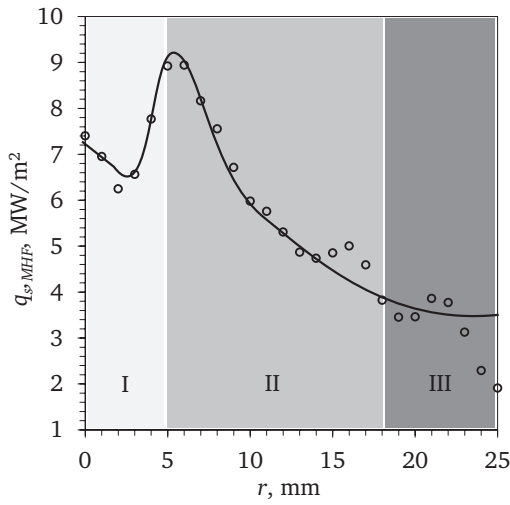
The effect of jet subcooling, ΔT_{sub} , on the maximum heat flux condition, $q_{s,MHF}$ and $T_{s,MHF}$, is shown in Fig. 5.50(a). Comparing experiments F2 and F7 in Fig. 5.45(b), it can be seen that both maximum heat flux, $q_{s,MHF}$, and the surface temperature at maximum heat flux, $T_{s,MHF}$, increase with the jet subcooling, ΔT_{sub} . However, this influence is not clear at lower jet subcooling, i.e. when



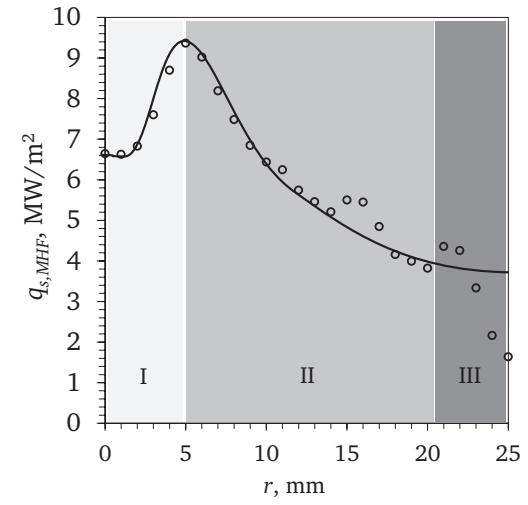
(a) Experiment F1



(b) Experiment F2



(c) Experiment F3



(d) Experiment F4

Figure 5.46. Distribution of maximum heat flux, $q_{s,MHF}(r)$. Three regions have been marked based on the relative size of boundary layer to the liquid film. Region I (Impingement region, $0 \leq \bar{r} < 1.28$), Region II (Boundary layer region, $1.28 \leq \bar{r} < 0.5554 \cdot \text{Re}_J^{1/3} / (50 - 5.147 \cdot \text{Pr}_L)^{1/3}$), Region III (Similarity region, $\bar{r} > 0.5554 \cdot \text{Re}_J^{1/3} / (50 - 5.147 \cdot \text{Pr}_L)^{1/3}$). Tentative best fit lines have also been drawn here.

comparing experiments F2 and F6. More investigations are necessary to understand the influence of jet subcooling.

5.2.6 Rewetting temperature

Outside the wetting front region, the impingement surface is dry and film boiling is the heat transfer mode. The rewetting temperature (analogous to the Leidenfrost temperature for a sessile droplet) is the condition deciding whether the surface is wet or dry, and is, therefore, the boundary between two boiling regimes characterized by quite different heat transfer rates. A state of art on the subject of rewetting temperature is discussed in much details previously in Section 2.2. The following major conclusions that were drawn are:

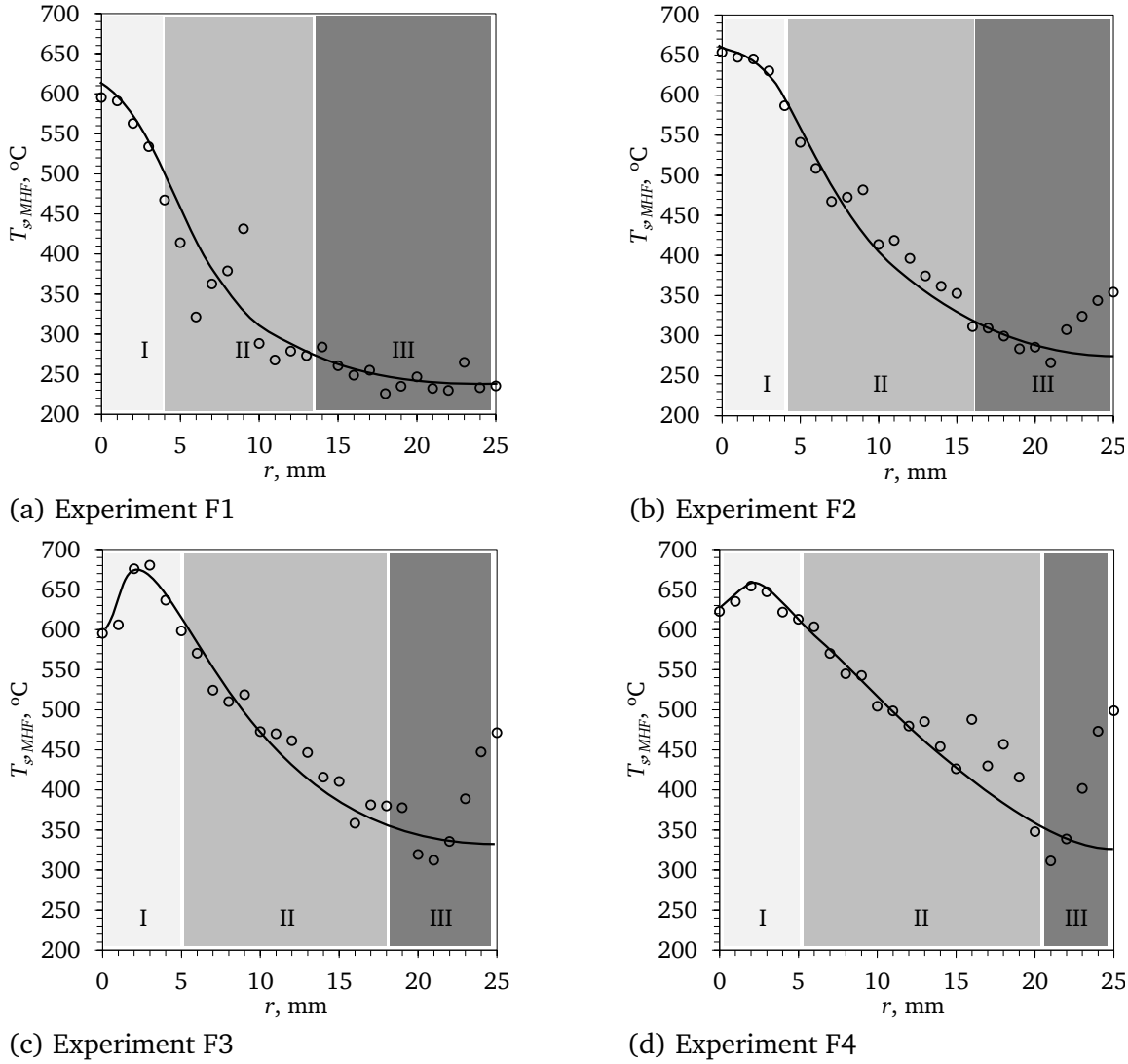


Figure 5.47. Distribution of surface temperature at maximum heat flux, $T_{s,MHF}(r)$. Three regions have been marked based on the relative size of boundary layer to the liquid film. Region I (Impingement region, $0 \leq \bar{r} < 1.28$), Region II (Boundary layer region, $1.28 \leq \bar{r} < 0.5554 \cdot \text{Re}_J^{1/3} / (50 - 5.147 \cdot \text{Pr}_L)^{1/3}$), Region III (Similarity regions, $\bar{r} > 0.5554 \cdot \text{Re}_J^{1/3} / (50 - 5.147 \cdot \text{Pr}_L)^{1/3}$). Tentative best fit lines have also been drawn here.

- The rewetting temperature depends on the properties of the liquid and the solid, condition of the impingement surface, flow velocity and subcooling.
- Measured rewetting temperature have been reported in much excess of the critical temperature of the liquid. The mechanism, however, is not clear.
- No well established method for estimation of the rewetting temperature is available. However, most of the methods define rewetting temperature as the temperature below which the heat flux increases considerably. While some researchers have interpreted this information from the temperature history [21, 24, 27, 37], others have interpreted it from the boiling curve [50, 51, 73, 127]. In the present study, due to the rapid growth of the wetting front and predominant cooling of the dry region by radial heat conduction to the wetted region, and it is difficult to accurately determine from the temperature history when the surface heat flux becomes considerable. Further adding

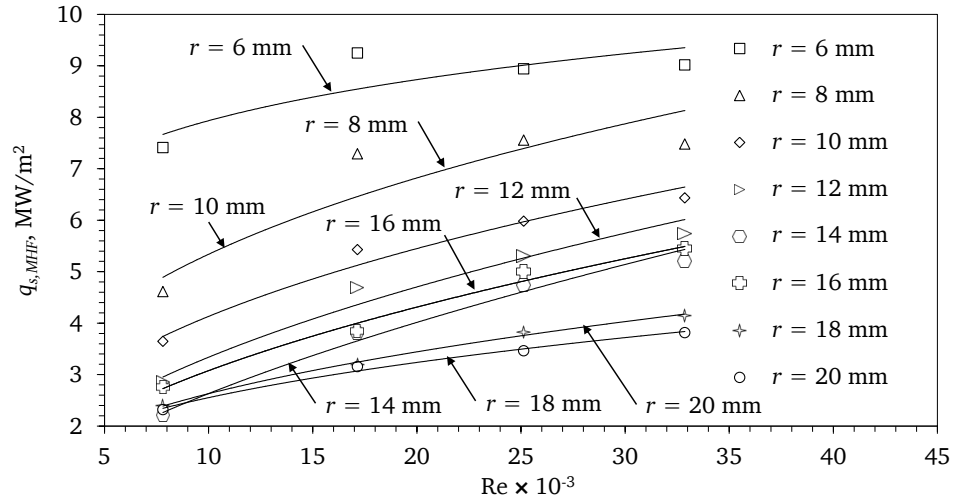


Figure 5.48. Variation of maximum heat flux, $q_{s,MHF}$, in the radial flow region with jet Reynolds number, Re_J , at $\Delta T_{sub} = 75$ K.

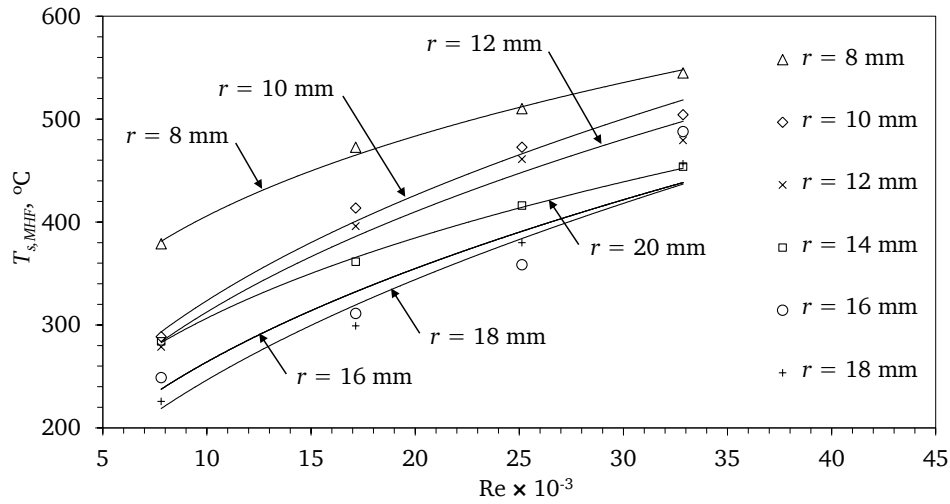


Figure 5.49. Variation of temperature at maximum heat flux, $T_{s,MHF}$, in the radial flow region with jet Reynolds number, Re_J , at $\Delta T_{sub} = 75$ K.

to the difficulty is the observation that during the initial contact between the hot impingement surface and the cold liquid, liquid-wall interface cools down without the establishment of a well describable boiling regime; as a results, it becomes difficult to determine the minimum heat flux point on the boiling curve. To summarize, the suggested approaches neither provide a reliable procedure nor a certain estimate of the rewetting temperature. Therefore, only approximate values can be interpreted from the change in the shape of the boiling curve (e.g. in Fig. 5.41) or from the change in the slope of the temperature history (e.g. in Fig. 5.19). The values reported here have been approximately judged from the change in the shape of the boiling curve, and, therefore, are contestable.

The estimated values of rewetting temperature are shown in Fig. 5.51. These estimated rewetting temperature are in much excess of the critical temperature of water. Similar high values have been reported previously for flow boiling situations and have been reproduced in Table 5.2 from Section 2.2 for quick referencing. Further, it can be seen that the rewetting temperature value depends on the jet velocity. Why does the rewetting temperature depend on the jet velocity? To understand

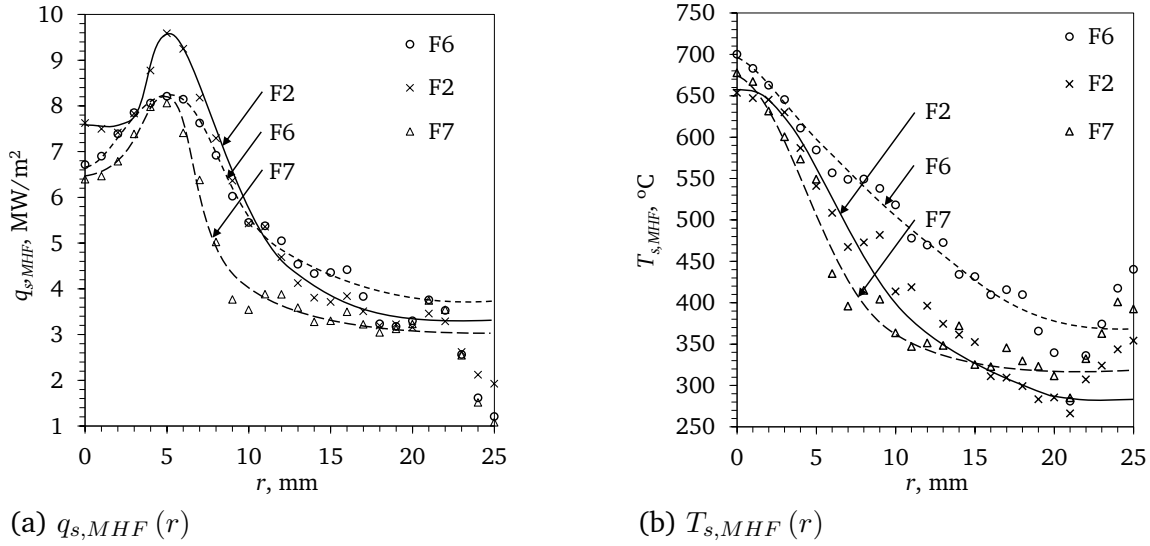


Figure 5.50. Effect of jet subcooling, ΔT_{sub} , at $v_J = 5$ m/s on the variation of maximum heat flux condition, $q_{s,MHF}(r)$ and $T_{s,MHF}(r)$, with radial position. Tentative best fit lines have been drawn here for better visualization of the variation, while ignoring the sudden drop in $q_{s,MHF}(r)$ or the sudden rise in $T_{s,MHF}(r)$ when $r \geq 22$.

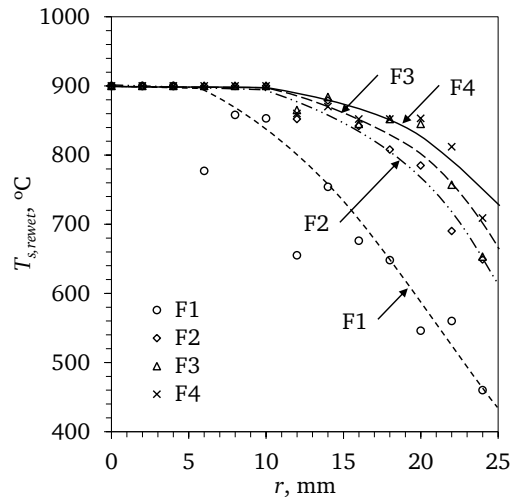


Figure 5.51. Effect of jet velocity, v_J , on the rewetting temperature, $T_{s,rewet}$.

this, let us revisit the discussion on the heat transfer in the wetting front region Section 5.2.3.3. The width of the superheated liquid film depends on the relative rate of evaporation and replenishment. With increase in jet velocity, the replenishment rate increases. As a result, the width of the wetting front region and the temperature at its outer periphery, i.e. the rewetting temperature, increase.

5.2.7 Summary

The following conclusions can be drawn from this study:

1. During quenching, three distinct heat transfer regions can be identified based on the estimated surface heat flux and temperature: (i) a central wetted region with nucleate boiling being the

Author(s)	Process	Material	T_I [°C]	$\Delta T_{sub}, l, v$	$T_{s,rewet}$ [°C]
Ishigai et al. [49]	PJI	AISI 304	1000	5–55 K, 6.2 mm, 0.65–3.2 m/s,	245–1000
Dhir et al. [21]	BRF	Zr	1127	50K–75 K, 1–30 cm/s	350–700
Filipovic et al. [27]	WJ	Cu	750	45–75 K, 2–4 m/s	400–725
Hall [36]	CJI	Cu	650–800	75 K, 5.1 mm, 2–4 m/s	150–450
Elias et al. [24]	BRF	Zr	1600	10 K, 1.5 cm/s	≈ 527
Liu and Wang [73]	CJI	AISI 316	1000	5–45 K, 10 mm, 1–3 m/s	300–1000
Liu et al. [71]	CJI	CS, AISI 316	900	70–87 K, 18.9–30 mm, 5.6–6.5 m/s	900
Zhang [127]	CJI	CS	850	60 K, 20 mm, 2.3 m/s	450–850
Gradeck et al. [32]	PJI	Ni	≈ 600	15 K, 4 mm, 1.2 m/s	580

l is the characteristic dimension: e.g. d_J or d_N for circular jet impingement, w_J or w_N for planar jet impingement, channel gap for bottom reflooding.

BRF: Bottom reflooding. CJI: circular jet impingement. PJI: Plunging jet impingement. WJ: Wall jet.

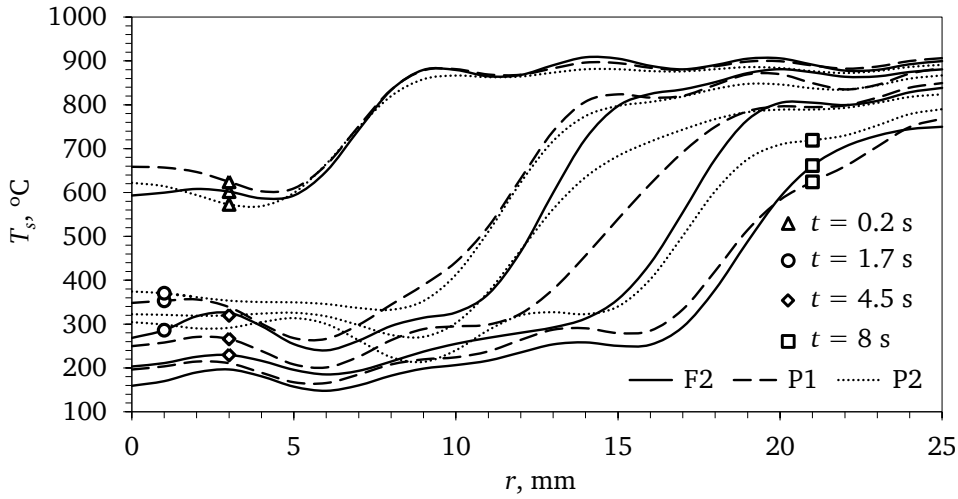
Table 5.2. Compilation of reported rewetting temperature, $T_{s,rewet}$, during quenching with flowing water at atmospheric pressure (arranged chronologically).

- main heat transfer mode, (ii) an annular wetting front region surrounding the wetted region with transition boiling being the main heat transfer mode, and (iii) an outside dry region with the surface cooling down due to radial heat conduction to the wetted region and film boiling. The wetting front always lies in the region with the largest temperature gradient. The maximum heat flux position lies slightly upstream of the wetting front.
2. The impingement surface temperature increases sharply outside the maximum heat flux position. As the quenching progresses, this radial temperature gradient becomes gradual.
 3. The boiling curve shifts to lower surface superheat and heat flux with distance from the impingement point. A similar shift of the boiling curve is seen with decrease in jet velocity and subcooling.
 4. The maximum heat flux and surface temperature at maximum heat flux reduce with distance from the stagnation point. Based on the boundary layer theory, it is possible to classify the distribution into three regions. Such a classification has been made for the range of operating parameters in the present study.
 5. The temperature corresponding to the maximum heat flux position and the rewetting temperature have been found to be in much excess of the homogeneous nucleation temperature of water. Film boiling regime could not be identified within and around the impingement region in either the boiling curve or the temperature history.
 6. Area-weighted average surface heat flux, surface temperature and heat transfer coefficient have been calculated, which clearly show the improvement in heat transfer with jet velocity over the complete temperature range of 200–900 °C. The dependence of the area-weighted averaged cooling on jet subcooling, ΔT_{sub} , has been estimated to be less prominent as compared to jet velocity.

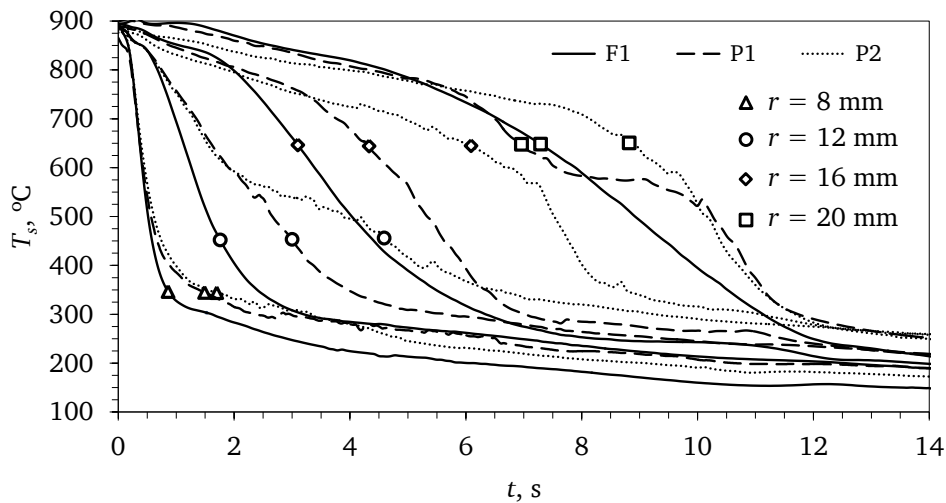
5.3 Plunging jet impingement heat transfer

In this section, the effect of accumulated liquid in the plunging jet impingement quenching on the surface heat flux and temperature is compared with that of free-surface jet impingement quenching. Free-surface jet impingement experiment F2 is comparable to plunging jet impingement experiments P1 and P2, as the jet velocity, v_J , and subcooling, ΔT_{sub} , are the same in all the three experiments, i.e. 5 m/s and 75 K, respectively. The accumulation heights in experiments P1 and P2 are 30 and 80 mm, respectively. Based on the mass flow rate of the jet, the filling time in experiments P1 and P2 are calculated to be 1.7 s and 4.5 s, respectively. Similarly, experiment P3 can be compared to experiment F4, as the jet velocity, v_J , and subcooling, ΔT_{sub} , of 10 m/s and 75 K, respectively, are the same among both the experiments. The filling time in experiment F4 is 2.3 s.

Figure 5.52(a) compares the variation of surface temperature with time for plunging jet impingement experiments P1 and P2 with the free-surface jet experiment F2. In general, the growth of the



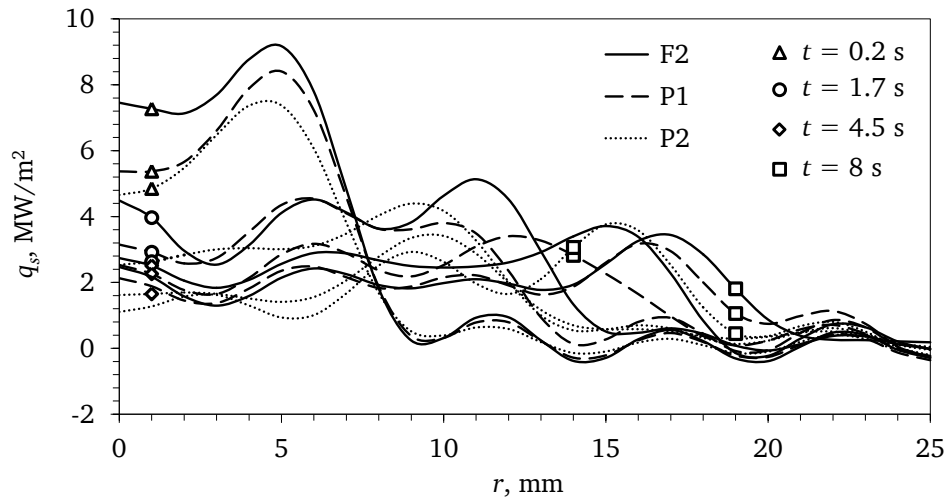
(a) Surface temperature, $T_s(r)$



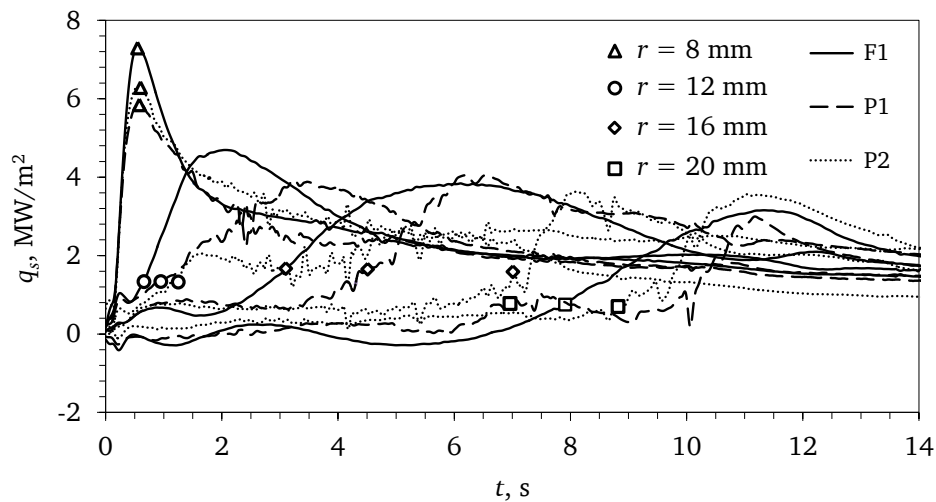
(b) Surface temperature, $T_s(t)$

Figure 5.52. Effect of liquid accumulation on the evolution of surface temperature, $T_s(r, t)$. Based on the mass flow rate of the jet, the filling time in experiments P1 and P2 are calculated to be 1.7 s and 4.5 s, respectively.

high heat transfer region, i.e. the wetted region, is slightly slowed down due to accumulation. The radial distribution of surface temperature is almost similar in the three experiments during the early stages of quenching, i.e. when the accumulated liquid height is small, but then the cooling starts to lag behind in the plunging jet impingement experiments as the accumulated liquid height increases. Comparison of experiments P1 and P2 shows that the radial surface temperature distribution is similar up to $t = 1.7$ s (i.e filling time in experiment P1). Following this, as the height of accumulated liquid increases in experiment P2, the cooling in experiment P2 starts to lag behind experiment P1. The temperature histories at selected radial positions within the radial flow regions are shown in Fig. 5.52(b), where it can be seen that the effect of accumulation is most prominent at radial positions much away from the impingement region. The influence at a radial position of $r = 20$ mm is negligible, which is likely due to improved cooling by liquid rebounding from the ceramic cylinder wall. Similar observations regarding the influence of liquid accumulation can be made in the heat flux variations shown in Fig. 5.53.

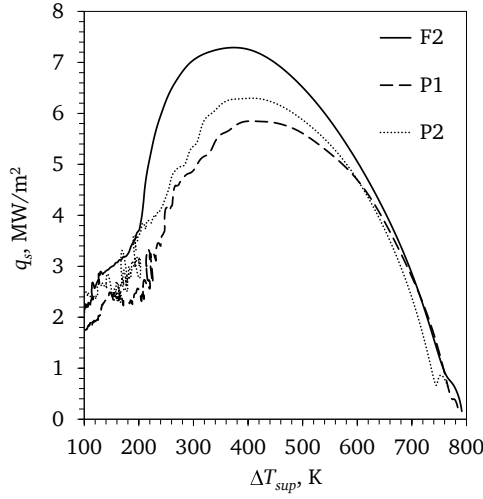


(a) Surface heat flux, $q_s(r)$

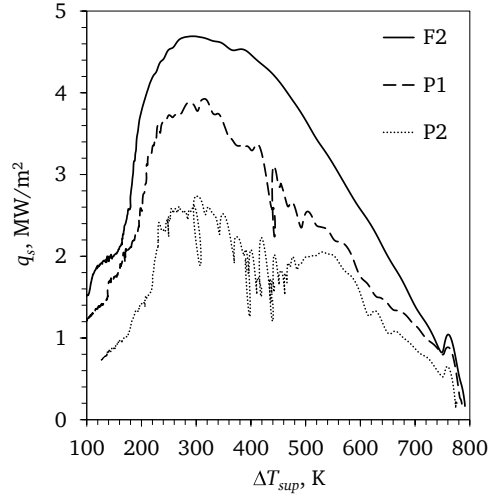


(b) Surface heat flux, $q_s(t)$

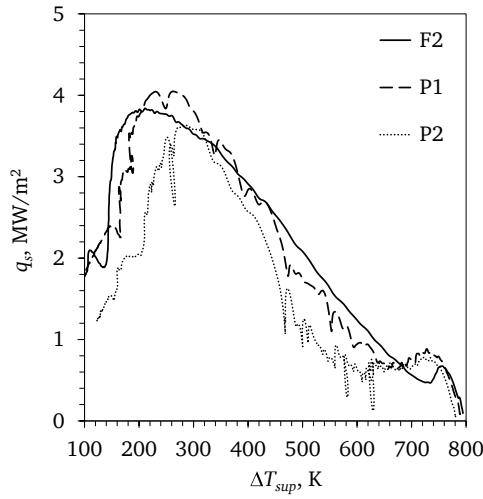
Figure 5.53. Effect of coolant accumulation over the impingement surface on the heat flux, $q_s(r)$.



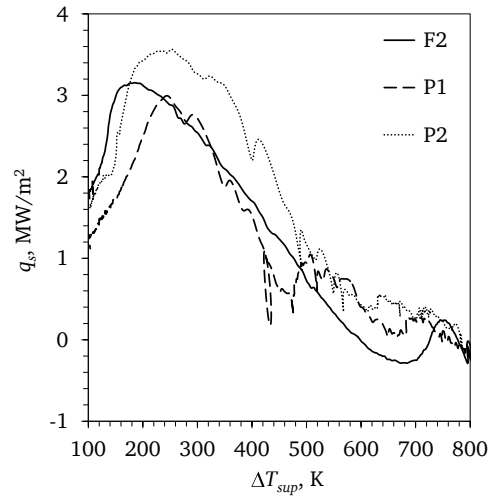
(a) $r = 8$ mm



(b) $r = 12$ mm



(c) $r = 16$ mm

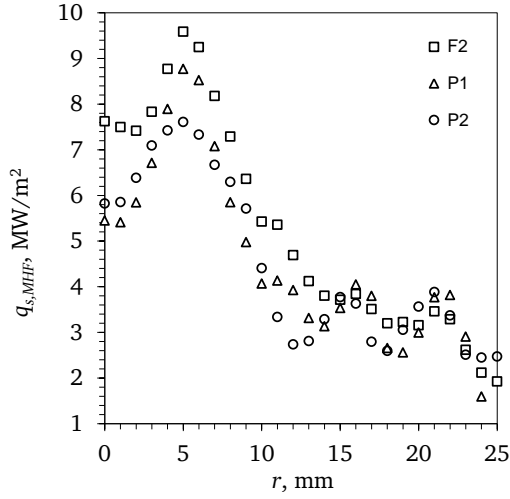


(d) $r = 20$ mm

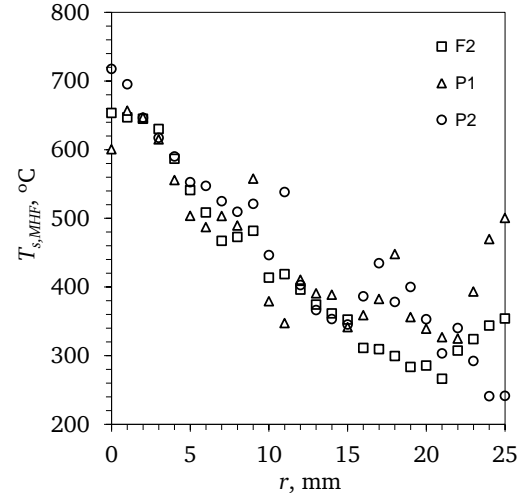
Figure 5.54. Comparison of the boiling curves for the radial flow region of the plunging jet and free-surface jet impingement quenching experiments shows that no clear trend regarding the variation of boiling heat transfer rate with the accumulated liquid height can be made.

The boiling curves for selected radial positions are shown in Fig. 5.54. No clear trend regarding the variation of boiling heat transfer rate with the accumulated liquid height can be made here. The maximum heat flux, $q_{s,MHF}$, reduced due to accumulation, though the temperature corresponding to the maximum heat flux shows little dependence on the accumulation. Similarly, from the variation of $q_{s,MHF}$ and $T_{s,MHF}$ shown in Fig. 5.55, it can be seen that the effect of accumulation is not considerable.

The comparison of the maximum heat flux condition for the plunging jet impingement experiment P3 and free-surface jet experiment F4 are shown in Fig. 5.56. While the deterioration of maximum heat flux, $q_{s,MHF}$, due to accumulation can be seen, no such effect on the temperature at maximum heat flux is seen. Why the similar influence can not be seen at a jet velocity $v_J = 5$ m/s? This remains an open question, and many more studies are necessary to quantify the effect of accumulation on boiling heat transfer. Area weighted heat transfer coefficient has been shown in

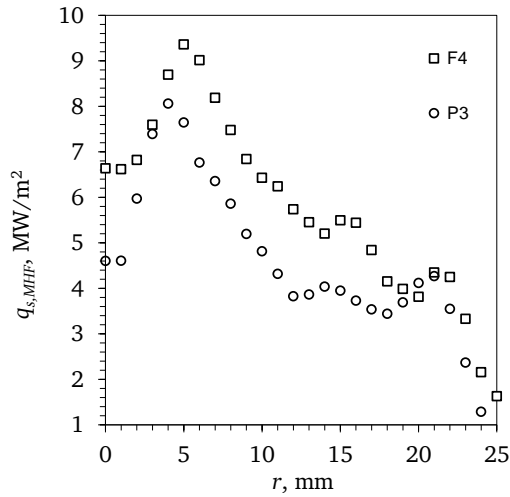


(a) $q_{s,MHF}(r)$

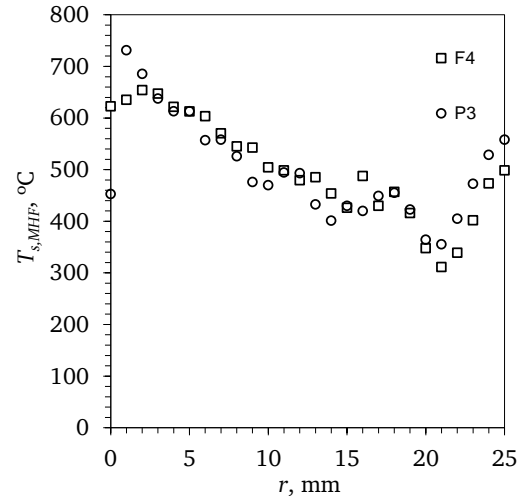


(b) $T_{s,MHF}(r)$

Figure 5.55. Comparison of the maximum heat flux condition, $q_{s,MHF}(r)$ and $T_{s,MHF}(r)$, for the plunging jet and free-surface jet impingement quenching experiments. It can be seen that the effect of accumulation is not considerable.



(a) $q_{s,MHF}(r)$

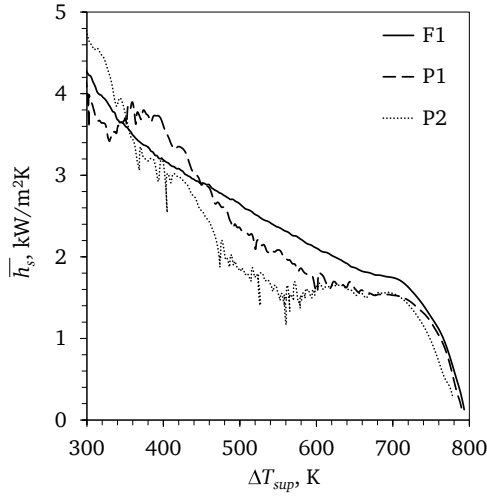


(b) $T_{s,MHF}(r)$

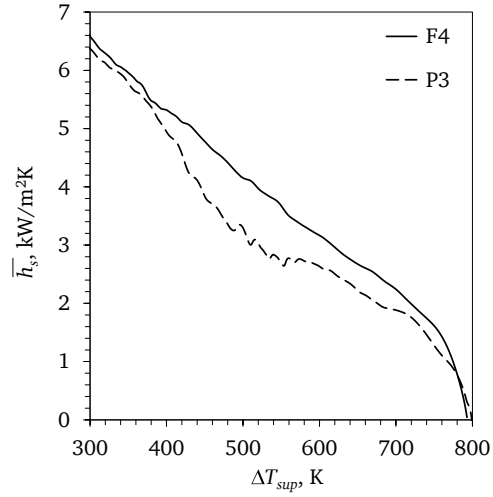
Figure 5.56. Comparison of the maximum heat flux condition, $q_{s,MHF}(r)$ and $T_{s,MHF}(r)$, for the plunging jet and free-surface jet impingement quenching experiments. While the deterioration of maximum heat flux, $q_{s,MHF}$, due to accumulation can be seen, no such effect on the temperature at maximum heat flux is seen.

Fig. 5.57. Here it can be seen that the heat transfer coefficient decreases due to accumulation in the surface superheat range of approximately 450-700 K.

It is definite that the flow in the case of a plunging jet impingement would be much more complex than in the case of a free-jet impingement. Due to the visual obstruction from the ceramic cylinder, it was not possible to visualize the flow in this study. Further, as has been stated previously, only a limited number of plunging jet impingement quenching experiments have been performed. These studies were exploratory in nature and further studies are necessary to clarify the effect of coolant accumulation.



(a) Jet velocity $v_J = 5$ m/s



(b) Jet velocity $v_J = 10$ m/s

Figure 5.57. Variation of area-weighted average heat transfer coefficient, \bar{h}_s , with area-weighted average surface superheat, $(\bar{T}_s - T_L)$.

5.4 Closure

This study presents a systematic procedure to measure and estimate the temporospatial variations of heat transfer on the impingement surface during jet impingement quenching of an extremely hot steel plate. The observations presented in this chapter confirm that high heat fluxes can be removed at large surface superheats by impinging liquid jets, as practiced in the industry. Important and unique heat transfer data regarding the variation of heat transfer due to such a rapid quenching phenomenon has been obtained from these experiments. The obtained results assist in clarifying the underlying boiling heat transfer mechanism and support in the development of mechanistic models for quenching or flow boiling by creating a heat transfer database. The major outcomes of this study are summarized in the next chapter.

6

Summary and Outlook

6.1 Summary

The ability of liquids jets to extract high heat flux from metal parts, with temperatures as high as 800-1000 °C, at moderate flow rates has made them indispensable in many applications. Due to the complexity of the problem, the mechanism of flow boiling heat transfer is not well understood. The present experimental work has been carried out to understand the thermo-hydrodynamic phenomenon occurring during the quenching of hot stainless steel plate with a free-surface water jet. Uncontrolled transient cooling experiments have been performed on an instrumented stainless steel AISI-type 314 cylinder, heated to an initial homogeneous temperature of about 900 °C, with a single circular coaxial subcooled water jet impinging on its top flat face.

A two-dimensional axi-symmetric inverse heat conduction analysis using the measured temperature data has been performed to determine the temporospatial variations of the temperature and heat flux on the impingement face. Furthermore, both low and high speed images to visualize the two-phase flow have been recorded and compared with the heat transfer distribution to understand the boiling mechanism. The effect of jet parameters, namely subcooling and impingement velocity, on the free-surface jet impingement heat transfer has been studied. Additionally, plunging jet impingement quenching, where the spent liquid accumulates over the impingement surface, has been explored. The major findings of the study are:

1. The measurements and estimates of both temporal and spatial variations of heat transfer on the impingement surface during the rapid quenching of extremely hot steel plates are possible.
2. Three distinct regions with difference in the extent of liquid-wall contact have been identified on the impingement surface:
 - i) A wetted region where single phase convection and nucleate boiling are the principle heat transfer modes. However, no boiling activity has been observed in the high speed images, as the bubbles are small and do not reach the liquid free-surface. The maximum heat flux position is determined to be within this region. As wetted region grows in size with time,

the maximum heat flux position also moves radially outwards. The wetted region growth rate increases with the jet velocity and subcooling.

- ii) The liquid gets deflected at the outer periphery of the wetted region due to the efflux of large vapor bubbles near the maximum heat flux position. Transition boiling within a thin liquid film that is continuously replenished by the bulk flow is hypothesized to be the heat transfer mode in the wetting front region.
 - iii) The impingement surface outside the wetting front region is dry and the heat transfer rate is very low. After deflecting away from the impingement surface, the liquid breaks into droplets. The velocity of the splashed droplet velocity has been analyzed from the high speed images and it has been found that the drop velocity is much lower than the liquid film velocity calculated using single-phase flow relations because the bubbles growing on the impingement surface within the wetted region decelerate the liquid film.
3. The rewetting temperature, the temperature below which the direct liquid-wall contact is re-established and the heat flux increases, is significantly higher in both the impingement and radial flow regions than for the pool boiling. Removal of bubbles in the early stages of their growth by the flowing liquid and then their rapid condensation within the subcooled liquid avoids the buildup of vapor near the impingement surface, which is the likely reason for the enhancement of the rewetting temperature.
 4. It has been found that more heat flux can be removed at large surface superheats by liquid jet impingement as compared to pool boiling and bottom reflooding. The maximum heat flux and the temperature at maximum heat flux decrease with distance from the stagnation point before reaching a constant value, and increase with the jet velocity and subcooling. The boiling curve shifts to higher heat flux and surface superheat with the increase in the jet velocity and subcooling.
 5. Boiling curve based on area-weighted average heat flux and surface temperature shifts to higher surface superheat with jet velocity, but the effect of liquid subcooling is small.
 6. The area-weighted heat transfer coefficient decreases due to the accumulation of spent coolant over the impingement surface.

This work can complement a theoretical and numerical study of the complex transport processes during jet impingement quenching. The models can be validated against the experimental results of this work.

6.2 Outlook

In the present thesis, the first insight into the complex thermo-hydrodynamic phenomenon has been reported. Using high-resolution photography, interesting information about the liquid deflection at the wetting front has been obtained. A hypothesis has been proposed in order to explain the rewetting process. The collected heat transfer data in this investigation incubates the process of detailed thermo-hydrodynamic measurements in this subject. Limitations of the study have been identified, which principally points to the fact that an improved procedure of embedding fast response temperature sensors inside the test specimen would go a long way in generating confidence in the results. Further, due to the extreme difficulty in performing measurements at such high temperatures, few

trials could be performed in this study. In the future, increased confidence in the results can also be achieved by repeating the measurements and performing trials over a much broader parameter range.

As has been mentioned in Chapter 1, the actual operating conditions in the application is much more complex than the flow configuration studied in this thesis. Due to aforementioned difficulties in performing such experiments, limited studies are available on this subject. Here some future steps are being suggested. These steps have been divided into three major categories: reduce uncertainty; understand the physics; and correlate. Such a categorization should lead to the development of a comprehensive jet impingement quenching model and a design methodology for the development of improved accelerated cooling system is suggested.

1. Reduce Uncertainty:

- a) Use of high temperature thermocouples
- b) Estimate the thermocouple decalibration due to repeated quenching
- c) Use fast response thermocouples
- d) Minimize thermal contact resistance between the embedding hole and the thermocouple
- e) Quantify the overall time response of the embedded thermocouple

2. Understand:

- a) Conjugate heat transfer nature of the boiling process
- b) Rewetting process
- c) Boiling within the wetted region and associated flow structure
- d) Effect of surface condition on boiling (it is worthwhile to note here that the steel plates at the end of hot rolling are quite rough)
- e) Effect of surface orientation, plate motion and accumulation of spent liquid

3. Correlate:

- a) Heat transfer to the flow parameters, plate material, plate motion, surface condition, spent liquid accumulation, etc.
- b) Wetting front growth to the above mentioned factors.

Bibliography

- [1] Akimenko, A. D. Features of film boiling in surface water cooling. *NASA Rep. TT F-10184*, N66-33689, 1966.
- [2] Akmal, M., Omar, A. M. T., and Hamed, M. S. Experimental investigation of propagation of wetting front on curved surfaces exposed to an impinging water jet. *Int. J. Microstruct. Mat. Prop.*, 3(4–5):654–681, 2008.
- [3] Basu, N., Warriar, G. R., and Dhir, V. K. Onset of nucleate boiling and active nucleation site density during subcooled flow boiling. *ASME J. Heat Transfer*, 124(4):717–728, 2002.
- [4] Bejan, A. *Convective Heat Transfer*. John Wiley and Sons, Inc., New York, USA, 2nd edition, 1995.
- [5] Bergles, A. E. and Rohsenow, W. M. The determination of forced-convection surface-boiling heat transfer. *ASME J. Heat Transfer*, 1:365–372, 1964.
- [6] Bernardin, J. D. and Mudawar, I. The leidenfrost point: Experimental study and assessment of existing models. *ASME J. Heat Transfer*, 121(4):894–903, 1999.
- [7] Biance, A.-L., Clanet, C., and Quéré, D. Leidenfrost drops. *Phy. Fluid*, 15(6):1632–1637, 2003.
- [8] Bibeau, E. L. and Salcudean, M. A study of bubble ebullition in forced-convective subcooled nucleate boiling at low pressure. *Int. J. Heat Mass Transfer*, 37(15):2245–2259, 1994.
- [9] Bogdanic, L., Auracher, H., and Ziegler, F. Two-phase structure above hot surfaces in jet impingement. *Heat Mass Transfer*, 45:1019–1028, 2009.
- [10] Buchholz, M., Lüttich, T., Auracher, H., and Marquardt, W. Experimental investigation of local processes in pool boiling along the entire boiling curve. *Int. J. Heat Fluid Flow*, 25(2):243–261, 2004.
- [11] Carbajo, J. J. A study on the rewetting temperature. *Nucl. Eng. Des.*, 84:21–52, 1985.
- [12] Carslaw, H. and Jaeger, J. *Conduction of Heat in Solids*. Oxford University Press, New York, USA, 2nd edition, 2008.
- [13] Chester, N. L. A study of boiling heat transfer on a hot steel plate cooled by an inclined circular bottom water jet. Master’s thesis, University of British Columbia, Vancouver, Canada, Dec. 2006.
- [14] Cho, M., Thomas, B., and Lee, P. Three-dimensional numerical study of impinging water jets in runout table cooling processes. *Metall. Mater. Trans. B*, 39:593–602, 2008.
- [15] Chung, M. K. and Lee, Y. W. Description and discussion of the current state of the knowledge about the leidenfrost phenomenon. *J. Korean Nucl. Soc.*, 14(4):204–218, 1982.
- [16] Cornwell, K. and Schüller, R. B. A study of boiling outside a tube bundle using high speed photography. *Int. J. Heat Mass Transfer*, 25(5):683–690, 1982.

-
-
- [17] Davis, E. J. and Anderson, G. H. The incipience of nucleate boiling in forced convection flow. *AIChE J.*, 12(4):774–780, 1966.
- [18] Davis, J. R. *Alloy Digest Sourcebook: Stainless Steels*. ASM Int., Ohio, USA, 2000.
- [19] Del Valle, V. H. and Kenning, D. B. R. Subcooled flow boiling at high heat flux. *Int. J. Heat Mass Transfer*, 28(10):1907–1920, 1985.
- [20] Dhir, V. K. Boiling heat transfer. *Ann. Rev. Fluid Mech.*, 30(1):365–401, 1998.
- [21] Dhir, V. K., Duffey, R. B., and Catton, I. Quenching studies on a zircaloy rod bundle. *ASME J. Heat Transfer*, 103(2):293–299, 1981.
- [22] Dhir, V. K., Kandlikar, S. G., Fujita, Y., Iida, Y., and Heist, R. Nucleate boiling. In Kandlikar, S. G., Masahiro, S., and Dhir, V. K., editors, *Handbook on Phase Change: Boiling and Condensation*, pages 71–120, Taylor and Francis, Philadelphia, PA, 1999.
- [23] Duffey, R. B. and Porthouse, D. T. C. The physics of rewetting in water reactor emergency core cooling. *Nucl. Eng. Des.*, 25:379–394, 1973.
- [24] Elias, E., Sanchez, V., and Hering, W. Development and validation of a transition boiling model for RELAP5:MOD3 reflood simulation. *Nucl. Eng. Des.*, 183:269–286, 1998.
- [25] Filipovic, J., Incropera, F. P., and Viskanta, R. Quenching phenomenon associated with a water wall jet: I. transient hydrodynamics and thermal conditions. *Exp. Heat Transfer*, 8(2):97–117, 1995.
- [26] Filipovic, J., Incropera, F. P., and Viskanta, R. Quenching phenomenon associated with a water wall jet: II. comparison of experimental and theory and theoretical results for the film boiling region. *Exp. Heat Transfer*, 8(2):119–130, 1995.
- [27] Filipovic, J., Incropera, F. P., and Viskanta, R. Rewetting temperature and velocity in a quenching experiment. *Exp. Heat Transfer*, 8(4):257–270, 1995.
- [28] Filipovic, J., Viskanta, R., and Incropera, F. P. Similarity solution for laminar film boiling over a moving isothermal surface. *Int. J. Heat Mass Transfer*, 36(12):2957–2963, 1993.
- [29] Filipovic, J., Viskanta, R., and Incropera, F. P. An analysis of subcooled turbulent film boiling on a moving isothermal surface. *Int. J. Heat Mass Transfer*, 37(17):2661–2673, 1994.
- [30] Franco, G. Boiling heat transfer during cooling of a hot moving steel plate by multiple top jets. Master’s thesis, University of British Columbia, Vancouver, Canada, Dec. 2008.
- [31] Fujimoto, H., Hatta, N., and Viskanta, R. Numerical simulation of convective heat transfer to a radial free surface jet impinging on a hot solid. *Heat Mass Transfer*, 35:266–272, 1999.
- [32] Gradeck, M., Kouachi, A., Lebouché, M., Volle, F., Maillet, D., and Borean, J. L. Boiling curves in relation to quenching of a high temperature moving surface with liquid jet impingement. *Int. J. Heat Mass Transfer*, 52(5–6):1094–1104, 2009.
- [33] Gradeck, M., Kouachi, A., Volle, F., Borean, J. L., Gardin, P., and Lebouché, M. Cooling of a hot cylinder with an impinging planar water jet. *Int. Heat Transfer Conf., Sydney, Australia*, pages JET-11, August, 2006.
- [34] Gunnerson, F. S. On the prediction of quench and rewet temperatures. *Am. Nucl. Soc. Annu. Meeting, Las Vegas, NV, USA*, June 8, 1980.
- [35] Gunther, F. C. Photographic study of surface-boiling heat transfer to water with forced convection. *ASME J. Heat Transfer*, 73:115–124, 1951.
-

-
-
- [36] Hall, D. E. *Transient and Steady State Measurement of Boiling Heat Transfer from Impinging Jets*. PhD thesis, Purdue University, West Lafayette, IN, USA, May 1998.
- [37] Hall, D. E., Incropera, F. P., and Viskanta, R. Jet impingement boiling from a circular free-surface jet during quenching: part 1 – single-phase jet. *ASME J. Heat Transfer*, 123(5):901–910, 2001.
- [38] Hall, D. E., Incropera, F. P., and Viskanta, R. Jet impingement boiling from a circular free-surface jet during quenching: part 1 – two-phase jet. *ASME J. Heat Transfer*, 123(5):911–917, 2001.
- [39] Hammad, J., Mitsutake, Y., and Monde, M. Movement of maximum heat flux and wetting front during quenching of hot cylindrical block. *Int. J. Therm. Sci.*, 43(8):743–752, 2004.
- [40] Hammad, J. A. *Characteristics of Heat Transfer and Wetting Front During Quenching High Temperature Surface by Jet Impingement*. PhD thesis, Saga University, Jpn., Mar. 2004.
- [41] Hanus, F., Schröter, F., and Schütz, W. State of art in the production and use of high-strength heavy plates for hydropower applications. *Proc. High Strength Steel for Hydropower Plants, Graz, Austria*, July 05–07 2005.
- [42] Hatta, N., Kokado, J.-I., and Hanasaki, K. Numerical analysis of cooling characteristics for water bar. *Trans. ISIJ*, 23:555–564, 1983.
- [43] Hatta, N. and Osakabe, H. Numerical modeling for cooling process of a moving hot plate by laminar water curtain. *ISIJ Int.*, 29(11):912–925, 1989.
- [44] Hatta, N., Tanaka, Y., Takuda, H., and Kakado, J.-I. A numerical study on cooling of hot steel plate by a water curtain. *Trans. ISIJ*, 29:673–679, 1989.
- [45] Hauksson, A. T. Experimental study of boiling heat transfer during water jet impingement on a hot steel plate. Master's thesis, University of British Columbia, Vancouver, Canada, Nov. 2001.
- [46] Houston, S. D. and Cornwell, K. Heat transfer to sliding bubbles on a tube under evaporating and non-evaporating conditions. *Int. J. Heat Mass Transfer*, 39(1):211–214, 1996.
- [47] Hsu, Y. Y. On the size range of active nucleation cavities on a heating surface. *ASME J. Heat Transfer*, 84:207–216, 1962.
- [48] Ishida, R., Mizuta, A., Korida, K., Yasunaga, S., and Takisawa, K. Basic characteristics of pipe nozzle cooling with retaining water on plate. *ISIJ Int.*, 29(4):339–344, 1989.
- [49] Ishigai, S., Nakanishi, S., and Ochi, T. N. Boiling heat transfer for a plane water jet impinging on a hot surface. *Proc. 6th Int. Heat Transfer Conf., Toronto, Canada*, pages 445–450, August 1978.
- [50] Islam, M. A., Monde, M., Woodfield, P. L., and Mitsutake, Y. Jet impingement quenching phenomena for hot surfaces well above the limiting temperature for solid-liquid contact. *Int. J. Heat Mass Transfer*, 51(5–6):1226–1237, 2008.
- [51] Juarsa, M., Antariksawan, A. R., Joko, P., Ismu, W., Edys, S., and Kiswanta. Study on boiling heat transfer during reflooding process in "queen" test section. *Proc. Int. Cong. Adv. Nucl. Power Plants, Seoul, Korea*, page Paper 5402, May 15-19, 2005.
- [52] Kamata, C. Experimental study on boiling heat transfer with an impinging jet on a hot block. *Heat Transfer – Asian Res.*, 28(5):418–427, 1999.

-
-
- [53] Kandlikar, S. G. Bubble nucleation, growth and departure in flow boiling. *Soc. Eng. Sci. Conf., New Orleans*, November 1995.
- [54] Kandlikar, S. G., Cartwright, M. D., and Mizo, V. R. Investigation of bubble departure mechanism in subcooled flow boiling of water using high-speed photography. *Proc. Int. Conf. on Convective Flow Boiling, Banff, Alberta, Canada*, pages 161–166, 30 April–5 May 1995.
- [55] Kandlikar, S. G., Cartwright, M. D., and Mizo, V. R. A photographic study of nucleation characteristics of cavities in flow boiling. *Proc. Int. Conf. on Convective Flow Boiling, Banff, Alberta, Canada*, pages 73–78, 30 April–5 May 1995.
- [56] Kandlikar, S. G., Mizo, V. R., Cartwright, M. D., and Ikenze, E. Bubble nucleation and growth characteristics in subcooled flow boiling of water. *Proc. 32nd Nat. Heat Transfer Conf., Baltimore, Maryland*, pages 11–18, August 8–12, 1997.
- [57] Karwa, N., Gambaryan-Roisman, T., Stephan, P., and Tropea, C. Experimental investigation of circular free-surface jet impingement quenching: transient hydrodynamics and heat transfer. *Exp. Therm. Fluid Sci.*, 35(7):1435–1443, 2011.
- [58] Klausner, J. F., Mei, R., Bernhard, D. M., and Zeng, L. Z. Vapor bubble departure in forced convection boiling. *Int. J. Heat Mass Transfer*, 36(3):651–662, 1993.
- [59] Klemens, P. G. and Neuer, G. Thermal conductivity of alloys. In *Landolt-Börnstein: III/15c*, page 374, Berlin, Germany, 1991. Springer-Verlag.
- [60] Koldin, A. V. and Platonov, N. I. A study of heat transfer in the surface layer of metal during the impingement of a liquid jet. *Therm. Eng.*, 55(3):223–227, 2008.
- [61] König, A. W. The influence of the thermal properties of the heating-surface on the heat-transfer of bubble boiling. *Heat Mass Transfer*, 1:38–44, 1973.
- [62] Kreith, F. and Bohn, M. *Principles of Heat Transfer*. West Pub Co., MN, 1993.
- [63] Kruse, U. Estimation of uncertainty in transient heat transfer experiments. Bachelor’s thesis, Technische Universität Darmstadt, Darmstadt, Germany, Jan. 2011.
- [64] Kumagai, S., Suzuki, S., Sano, Y., and Kawazoe, M. Transition cooling of hot metal plate with impinging water jet. *Trans. JSME (in Japanese)*, 61-590B:3749–3754, 1995.
- [65] Lee, J. Effects of surface roughness on stagnation heat transfer of impinging liquid jet on metal surface. *J. Fluid Sci. Tech.*, 5(1):64–74, 2010.
- [66] Leocadio, H., Passos, J. C., and da Silva, A. F. C. Heat transfer behavior of a high temperature steel plate cooled by a subcooled impinging circular water jet. *Proc. 7th ECI Int. Conf. on Boiling Heat Transfer, Sao Paulo, Brazil*, 2009.
- [67] Li, D., Wells, M. A., Cockcroft, S. L., and Caron, E. Effect of sample start temperature during transient boiling water heat transfer. *Metall. Mater. Trans. B*, 38:901–910, 2007.
- [68] Liu, X., Lienhard V, J. H., and Lombara, J. S. Convective heat transfer by impingement of circular liquid jets. *ASME J. Heat Transfer*, 113(3):571–582, 1991.
- [69] Liu, Z. D. *Experiments and Mathematical Modeling of Controlled Runout Table Cooling in a Hot Rolling Mill*. PhD thesis, University of British Columbia, Vancouver, Canada, March 2001.
- [70] Liu, Z. D., Fraser, D., , Samarasekera, I. V., and Lockhart, G. T. Experimental observations and modelling of thermal history within a steel plate during water jet impingement. *Can. Metall. Q.*, 41(1):75–96, January, 2002.

-
- [71] Liu, Z. D., Fraser, D., and Samarasekera, I. V. Experimental study and calculation of boiling heat transfer on steel plates during runout table operation. *Can. Metall. Q.*, 41(1):63–74, January, 2002.
- [72] Liu, Z.-H., Tong, T.-F., and Qiu, Y.-H. Critical heat flux of steady boiling for subcooled water jet impingement on the flat stagnation zone. *ASME J. Heat Transfer*, 126(2):179–183, 2004.
- [73] Liu, Z.-H. and Wang, J. Study of film boiling heat transfer for water jet impinging on high temperature flat plate. *Int. J. Heat Mass Transfer*, 44(2):2475–2481, 2001.
- [74] Liu, Z.-H. and Zhu, Q.-Z. Prediction of critical heat flux for convective boiling of saturated water jet impinging on the stagnation zone. *ASME J. Heat Transfer*, 124(6):1125–1130, 2002.
- [75] Ma, C., Tian, Y. P., Tian, Y. C., and Lei, D. H. Liquid jet impingement heat transfer with and without boiling. *J. Therm. Sci.*, 2(1):32–49, 1993.
- [76] Mann, M., Stephan, K., and Stephan, P. Influence of heat conduction in the wall on nucleate boiling heat transfer. *Int. J. Heat Mass Transfer*, 43(12):2193–2203, 2000.
- [77] The MathWorks Inc. *Image Processing Toolbox User's Guide*, 2004.
- [78] Meng, Q. Experimental study of transient cooling of a hot steel plate by an impinging circular jet. Master's thesis, University of British Columbia, Vancouver, Canada, Oct. 2002.
- [79] Miyasaka, Y. and Inada, S. The effect of pure forced convection on the boiling heat transfer between a two-dimensional subcooled water jet and a heated surface. *J. Chem. Eng. Jpn.*, 13(1):22–28, 1980.
- [80] Miyasaka, Y., Inada, S., and Owase, Y. Critical heat flux and subcooled nucleate boiling in transient region between a two-dimensional water jet and a heated surface. *J. Chem. Eng. Jpn.*, 13(1):29–35, 1980.
- [81] Monde, M. Critical heat flux in saturated forced convective boiling on a heated disk with an impinging jet. *Heat Mass Transfer*, 19:205–209, 1985.
- [82] Monde, M., Arima, H., Liu, W., Mitsutake, Y., and Hammad, J. An analytical solution for two-dimensional inverse heat conduction problems using laplace transform. *Int. J. Heat Mass Transfer*, 46(12):2135–2148, 2003.
- [83] Monde, M. and Katto, Y. Burnout in a high heat-flux boiling system with an impinging jet. *Int. J. Heat Mass Transfer*, 21(3):295–305, 1978.
- [84] Monde, M., Kitajima, K., Inoue, T., and Mitsutake, Y. Critical heat flux in a forced convective subcooled boiling with an impinging jet. *Inst. Chem. Eng. Sym. Series Heat Transfer*, 7:515–520, 1994.
- [85] Monde, M. and Okuma, Y. Critical heat flux in saturated forced convective boiling on a heated disk with an impinging jet—chf in l-regime. *Int. J. Heat Mass Transfer*, 28(3):547–552, 1985.
- [86] Mozumder, A. K., Monde, M., and Woodfield, P. L. Delay of wetting propagation during jet impingement quenching for a high temperature surface. *Int. J. Heat Mass Transfer*, 48(25–26):5395–5407, 2005.
- [87] Mozumder, A. K., Monde, M., Woodfield, P. L., and Islam, M. A. Maximum heat flux in relation to quenching of a high temperature surface with liquid jet impingement. *Int. J. Heat Mass Transfer*, 49(17–18):2877–2888, 2006.

-
-
- [88] Mozumder, A. K., Woodfield, P. L., Islam, M. A., and Monde, M. Maximum heat flux propagation velocity during quenching by water jet impingement. *Int. J. Heat Mass Transfer*, 50(7–8):1559–1568, 2007.
- [89] Mozumder, M. *Thermal and Hydrodynamic Characteristics of Jet Impingement Quenching for High Temperature Surface*. PhD thesis, Saga University, Jpn., Sep. 2006.
- [90] Ochi, C. Development of steel plates by intensive use of TMCP and direct quenching processes. *ISIJ Int.*, 41(6):542–553, 2001.
- [91] Omar, A. M. T., Hamed, M. S., and Shoukri, M. Modeling of nucleate boiling heat transfer under an impinging free jet. *Int. J. Heat Mass Transfer*, 52(23–24):5557–5566, 2009.
- [92] Ozisik, M. N. and Orlande, H. R. B. *Inverse Heat Transfer-Fundamentals and Applications*. Taylor and Francis, New York, USA, 2000.
- [93] Park, I. S. Numerical analysis for film boiling heat transfer of a moving hot steel plate. *ISIJ Int.*, 51(5):743–747, 2011.
- [94] Peyayopanakul, W. and Westwater, J. W. Evaluation of the unsteady-state quenching method for determining boiling curves. *Int. J. Heat Mass Transfer*, 21(11):1437–1445, 1978.
- [95] Piggott, B. D. G., White, E. P., and Duffey, R. B. Wetting delay due to film and transition boiling on hot surfaces. *Nucl. Eng. Des.*, 36(2):169–181, 1976.
- [96] Prodanovic, V., Fraser, D., and Salcudean, M. Bubble behavior in subcooled flow boiling of water at low pressures and low flow rates. *Int. J. Multiphase Flow*, 28(1):1–19, 2002.
- [97] Qiu, Y.-H. and Liu, Z.-H. Critical heat flux of steady boiling for saturated liquids jet impinging on the stagnation zone. *Int. J. Heat Mass Transfer*, 48(21–22):4590–4597, 2005.
- [98] Robidou, H., Auracher, H., Gardin, P., and Lebouché, M. Controlled cooling of a hot plate with a water jet. *Exp. Therm. Fluid Sci.*, 26(2–4):123–129, 2002.
- [99] Robidou, H., Auracher, H., Gardin, P., Lebouché, M., and Bogdanić, L. Local heat transfer from a hot plate to a water jet. *Heat Mass Transfer*, 39(10):861–867, 2003.
- [100] Sarnes, B. and Schrüfer, E. Determination of the time behavior of thermocouples for sensor speedup and medium supervision. *Proc. Estonian Acad. Sci. Eng.*, 13(4):295–309, 2007.
- [101] Schmidt, L. Experimental study of the hydrodynamics of water jet impingement cooling of hot steel plates. Bachelor’s thesis, Technische Universität Darmstadt, Darmstadt, Germany, Jan. 2011.
- [102] Schweizer, N. *Multi-Scale Investigation of Nucleate Boiling Phenomena in Microgravity*. PhD thesis, Technische Universität Darmstadt, Darmstadt, Germany, Dec. 2010.
- [103] Seiler, N., Seiler, J.-M., and Simonin, O. Transition boiling at jet impingement. *Int. J. Heat Mass Transfer*, 47(23):5059–5072, 2004.
- [104] Situ, R., Mi, Y., Ishii, M., and Mori, M. Photographic study of bubble behaviors in forced convection subcooled boiling. *Int. J. Heat Mass Transfer*, 47(17–18):3659–3667, 2004.
- [105] Sodtke, C. and Stephan, P. Spray cooling on micro structured surfaces. *Int. J. Heat Mass Transfer*, 50(19–20):4089–4097, 2007.
- [106] Steiner, H., Kobor, A., and Gebhard, L. A wall heat transfer model for subcooled boiling flow. *Proc. ASME-ZSIS Int. Therm. Sci. Seminar, Bled, Slovenia*, pages 643–650, June 13–16, 2004.

-
-
- [107] Stephan, P. and Fuchs, T. Local heat flow and temperature fluctuations in wall and fluid in nucleate boiling systems. *Proc. 6th ECI Int. Conf. on Boiling Heat Transfer, Spoleto, Italy*, 7–12 May 2006.
- [108] Thorncroft, G. E. and Klausner, J. F. The influence of vapor bubble sliding on forced convection boiling heat transfer. *ASME J. Heat Transfer*, 121(1):73–79, 1999.
- [109] ThyssenKrupp Mater. Int. *Material Data Sheet TK 1.4841*, 2007.
- [110] Tsung-Chang, G. and Bankoff, S. G. On the mechanism of forced-convection subcooled nucleate boiling. *ASME J. Heat Transfer*, 112(1):213–218, 1990.
- [111] Vader, D. T., Incropera, F. P., and Viskanta, R. Convective nucleate boiling on a heated surface by and impinging, planar jet of water. *ASME J. Heat Transfer*, 114(1):152–160, February 1992.
- [112] van Hinsberg, N. P., Budakli, M., Göhler, S., Berberovic, E., Roisman, I. V., Gambaryan-Roisman, T., Tropea, C., and Stephan, P. Dynamics of the cavity and the surface film for impingements of single drops on liquid films of various thicknesses. *J. Colloid Interface Sci.*, 350(1):336–343, 2010.
- [113] Wagner, W. and Kretzschmar, H.-D. Properties of water and steam. In *VDI Heat Atlas*, page 154, Springer-Verlag, Berlin, Germany, 2010.
- [114] Watson, E. J. The radial spread of a liquid jet over a horizontal plane. *J. Fluid Mech.*, 20(3):481–499, 1964.
- [115] Wendelstorf, R., Spitzer, K.-H., and Wendelstorf, J. Effect of oxide layers on spray water cooling heat transfer at high surface temperatures. *Int. J. Heat Mass Transfer*, 51(19–20):4892–4901, 2008.
- [116] Wolf, D. H., Incropera, F. P., and Viskanta, R. Jet impingement boiling. In Hartnett, J. P. and T. F. Irvine, J., editors, *Advances in Heat Transfer*, volume 23, pages 1–132. Elsevier, 1993.
- [117] Wolf, D. H., Incropera, F. P., and Viskanta, R. Local jet impingement boiling heat transfer. *Int. J. Heat Mass Transfer*, 39(7):1395–1406, 1996.
- [118] Woodfield, P. L. and Monde, M. Estimation of uncertainty in an analytical inverse heat conduction solution. *Exp. Heat Transfer*, 22(3):129–143, 2009.
- [119] Woodfield, P. L., Monde, M., and Mitsutake, Y. Implementation of an analytical two-dimensional inverse heat conduction technique to practical problems. *Int. J. Heat Mass Transfer*, 49(1–2):187–197, 2006.
- [120] Woodfield, P. L., Monde, M., and Mitsutake, Y. Improved analytical solution for inverse heat conduction problems on thermally thick and semi-infinite solids. *Int. J. Heat Mass Transfer*, 49(17–18):2864–2876, 2006.
- [121] Woodfield, P. L., Monde, M., Mitsutake, Y., and Islam, M. A. Time and space resolution of analytical solution for two-dimensional inverse heat conduction problem. *Int. Heat Transfer Conf., Sydney, Australia*, pages CND–05, August, 2006.
- [122] Woodfield, P. L., Monde, M., and Mozumder, A. K. Observations of high temperature impinging-jet boiling phenomena. *Int. J. Heat Mass Transfer*, 48(10):2032–2041, 2005.
- [123] Woodfield, P. L., Mozumder, A. K., and Monde, M. On the size of the boiling region in jet impingement quenching. *Int. J. Heat Mass Transfer*, 52(1–2):460–465, 2009.

-
-
- [124] Xu, F. and Gadala, M. S. Heat transfer behavior in the impingement zone under circular water jet. *Int. J. Heat Mass Transfer*, 49(21–22):3785–3799, 2006.
 - [125] Yonezawa, T. and Sumitomo, H. Method of cooling thick steel plates. *Patent US 3629015*, Dec. 21, 1971.
 - [126] Zeng, L. Z., Klausner, J. F., Bernhard, D. M., and Mei, R. A unified model for the prediction of bubble detachment diameters in boiling systems–ii. flow boiling. *Int. J. Heat Mass Transfer*, 36(9):2271–2279, 1993.
 - [127] Zhang, P. Study of boiling heat transfer on a stationary downward facing hot steel plate cooled by a circular water jet. Master’s thesis, University of British Columbia, Vancouver, Canada, Dec. 2004.
 - [128] Zuber, N. *Hydrodynamic Aspects of Boiling Heat Transfer*. PhD thesis, University of California, Los Angeles, USA, June 1959.
 - [129] Zumbrunnen, D. A., Incropera, F., and Viskanta, R. Method and apparatus for measuring heat transfer distributions on moving and stationary plates cooled by a planar liquid jet. *Exp. Therm. Fluid Sci.*, 3(2):202–213, 1990.
 - [130] Zumbrunnen, D. A., Incropera, F. P., and Viskanta, R. A laminar boundary layer model of heat transfer due to a nonuniform planar jet impinging on a moving plate. *Heat Mass Transfer*, 27(5):311–319, 1992.
 - [131] Zumbrunnen, D. A., Viskanta, R., and Incropera, F. P. The effect of surface motion on forced convection film boiling heat transfer. *ASME J. Heat Transfer*, 111(3):760–766, 1989.



Thermophysical Properties of Materials

Thermophysical properties of water are given in Table A.1.

T_L [°C]	ρ_L [kg/m ³]	c_L [J/(kg · K)]	λ_L [W/(m · K)]	α_L [m ² /s]	μ_L [kg/(m · s)]	Pr_L
12	999.50	4193	0.5857	$1.398 \cdot 10^{-7}$	$1.234 \cdot 10^{-3}$	8.834
25	997.05	4182	0.6075	$1.457 \cdot 10^{-7}$	$8.900 \cdot 10^{-4}$	6.127
40	993.22	4179	0.6368	$1.516 \cdot 10^{-7}$	$6.527 \cdot 10^{-3}$	4.339

Table A.1. Thermophysical properties of water [113].

The elemental composition of the stainless steel AISI-type 314 test specimen are given in Table A.2.

Element	C	Si	Mn	Ni	Cr	N	S	P
Composition	0.240	2.10	1.77	19.07	24.3	0.018	0.0015	0.025

Table A.2. Elemental composition of stainless steel AISI-type 314 (as per the supplier's report).

Detailed thermal properties of this stainless steel are not available. Therefore, the data for the thermophysical properties over the temperature range of interest in the present study has been compiled from various sources (λ_T and c_T are compiled from [59], while ρ_T has been determined from the linear thermal expansion coefficient values provided in [109]). The data is then correlated with the following set of equations:

$$\lambda_T = 0.0151 \cdot T + 12.438, (27^\circ\text{C} \leq T \leq 927^\circ\text{C}). \quad (\text{A.1a})$$

$$c_T = 0.1654 \cdot T^2 + 122.54 \cdot T + 505003, (27^\circ\text{C} \leq T \leq 927^\circ\text{C}). \quad (\text{A.1b})$$

$$\rho_T = -0.4274 \cdot T + 7817.4, (27^\circ\text{C} \leq T \leq 927^\circ\text{C}). \quad (\text{A.1c})$$

T [°C]	λ_T [W/(m·K)]	c_T [J/(kg·K)]	ρ_T [kg/m³]	α_T [m²/s]	$\sqrt{\rho_T \cdot c_T \cdot \lambda_T}$ [J²/(m⁴·K²·s)]
300	17.2	556.6	7689	$4.014 \cdot 10^{-6}$	8579
600	21.9	638	7561	$4.542 \cdot 10^{-6}$	10278
900	26.7	749.3	7433	$4.794 \cdot 10^{-6}$	12194

Table A.3. Thermophysical properties of stainless steel AISI-type 314 at select temperatures.

Publications

In Journals

N. Karwa, T. Gambaryan-Roisman, P. Stephan, C. Tropea. A hydrodynamic model for subcooled liquid jet impingement at the Leidenfrost condition, *Int. J. Therm. Sci.*, 50(6):993–1000, 2011.

N. Karwa, T. Gambaryan-Roisman, P. Stephan, C. Tropea. Experimental investigation of circular free-surface jet impingement quenching: transient hydrodynamics and heat transfer, *Exp. Therm. Fluid Sci.*, 35(7):1435–1443, 2011.

N. Karwa, L. Schmidt, P. Stephan. Hydrodynamics of quenching with impinging free-surface jet, *Int. J. Heat Mass Transfer*, 55 (13): 3677–3685, 2012.

In Conferences

N. Karwa, T. Gambaryan-Roisman, P. Stephan, C. Tropea. A hydrodynamic model for planar jet impingement at the Leidenfrost condition, *Proc. 20th Nat. and 9th Int. ISHMT-ASME Heat Mass Transfer Conf., Mumbai, India*, 4–6 January 2010.

M. Subhash, S. Jakirlic, N. Karwa, I. Roisman, C. Tropea, D. Greif. Computational study of the heat transfer due to normal water jet impingement onto a hot steel plate, *Proc. 7th Int. Conf. Computational Heat Mass Transfer, Istanbul, Turkey*, 18–22 July 2011.

N. Karwa, P. Stephan. Experimental investigation into the boiling processes during jet impingement quenching of a stainless steel plate, *ECI 8th Int. Conf. Boiling Condensation Heat Transfer, Lausanne, Switzerland*, June 3–7, 2012.

N. Karwa, P. Stephan. Jet impingement quenching: effect of spent coolant accumulation, Article accepted for 6th *European Thermal Sciences Conference, Poitiers-Futuroscope, France*, September 4–7, 2012.

Posters

N. Karwa, T. Gambaryan-Roisman, P. Stephan, C. Tropea, K.-H. Tacke, K. Eberwein. Experimental investigation of jet impingement quenching, *Jahrestreffen des ProcessNet-Fachausschusses Wärme- und Stoffübertragung, Frankfurt am Main*, 21–22 March 2011.

Résumé

Nitin Karwa, M. Tech.

Personal

Date of birth	01.01.1982
Place of birth	Churu, India
Family status	Married
Nationality	Indian

Academic

1985 – 1995	Elementary education, St. Anne's School, Jodhpur (India)
1995 – 1999	Secondary education, Board of Secondary Education, Rajasthan (India)
1999 – 2003	Bachelor of Engineering (Mechanical Engineering), Jai Narain Vyas University, Jodhpur (India) Thesis: Experimental study of heat transfer enhancement in an asymmetrically heated rectangular duct with perforated baffles.
2003 – 2005	Master of Technology (Thermal Engineering), Indian Institute of Technology, Delhi (India) Thesis: Experimental investigation of heat transfer from surfaces by sprays.

Professional

07.2003 – 05.2005	Teaching assistant at Department of Mechanical Engineering, Indian Institute of Technology, Delhi (India) Research area: Spray impingement cooling.
07.2005 – 02.2008	Technologist at Applied Computational Fluid Dynamics Laboratory, Energy and Propulsion Technology Global Technology Organization, General Electric Global Research, Bangalore (India) Research area: Air-blast atomization.
03.2008 – 12.2012	Research assistant at the Institute of Technical Thermodynamics, Department of Mechanical Engineering, Technische Universität Darmstadt, Darmstadt (Germany) Research area: Jet impingement quenching.
Since 01.2012	Research assistant at the Institute of Technical Thermodynamics, Department of Mechanical Engineering, Technische Universität Darmstadt, Darmstadt (Germany) Research area: Convective evaporation.

